# THREE-DIMENSIONAL CARBON ARCHITECTURES FOR ENERGY CONVERSION AND STORAGE

EDITED BY: Tianyu Liu, Kaiyuan Shi, Teng Zhai and Hyun-Kyung Kim
PUBLISHED IN: Frontiers in Energy Research

frontiers Research Topics

ISSN 1664-8714
ISBN 978-2-88966-335-4
DOI 10.3389/978-2-88966-335-4

## About Frontiers

Frontiers is more than just an open-access publisher of scholarly articles: it is a pioneering approach to the world of academia, radically improving the way scholarly research is managed. The grand vision of Frontiers is a world where all people have an equal opportunity to seek, share and generate knowledge. Frontiers provides immediate and permanent online open access to all its publications, but this alone is not enough to realize our grand goals.

## Frontiers Journal Series

The Frontiers Journal Series is a multi-tier and interdisciplinary set of open-access, online journals, promising a paradigm shift from the current review, selection and dissemination processes in academic publishing. All Frontiers journals are driven by researchers for researchers; therefore, they constitute a service to the scholarly community. At the same time, the Frontiers Journal Series operates on a revolutionary invention, the tiered publishing system, initially addressing specific communities of scholars, and gradually climbing up to broader public understanding, thus serving the interests of the lay society, too.

## Dedication to Quality

Each Frontiers article is a landmark of the highest quality, thanks to genuinely collaborative interactions between authors and review editors, who include some of the world's best academicians. Research must be certified by peers before entering a stream of knowledge that may eventually reach the public - and shape society; therefore, Frontiers only applies the most rigorous and unbiased reviews.
Frontiers revolutionizes research publishing by freely delivering the most outstanding research, evaluated with no bias from both the academic and social point of view.
By applying the most advanced information technologies, Frontiers is catapulting scholarly publishing into a new generation.

## What are Frontiers Research Topics?

Frontiers Research Topics are very popular trademarks of the Frontiers Journals Series: they are collections of at least ten articles, all centered on a particular subject. With their unique mix of varied contributions from Original Research to Review Articles, Frontiers Research Topics unify the most influential researchers, the latest key findings and historical advances in a hot research area! Find out more on how to host your own Frontiers Research Topic or contribute to one as an author by contacting the Frontiers Editorial Office: researchtopics@frontiersin.org

# THREE-DIMENSIONAL CARBON ARCHITECTURES FOR ENERGY CONVERSION AND STORAGE

Topic Editors:
**Tianyu Liu,** Virginia Tech, United States
**Kaiyuan Shi,** Sun Yat-Sen University, China
**Teng Zhai,** Nanjing University of Science and Technology, China
**Hyun-Kyung Kim,** Kangwon National University, South Korea

**Citation:** Liu, T., Shi, K., Zhai, T., Kim, H.-K., eds. (2021). Three-Dimensional Carbon Architectures for Energy Conversion and Storage. Lausanne: Frontiers Media SA. doi: 10.3389/978-2-88966-335-4

# Table of Contents

frontiers
in Energy Research

EDITORIAL
published: 12 November 2020
doi: 10.3389/fenrg.2020.611537

# Editorial: Three-Dimensional Carbon Architectures for Energy Conversion and Storage

*Tianyu Liu*[1]*, *Teng Zhai*[2], *Kaiyuan Shi*[3] *and Hyun-Kyung Kim*[4]

[1] *Department of Chemistry, Virginia Polytechnic Institute and State University, Blacksburg, VA, United States,* [2] *School of Materials Science and Engineering, Nanjing University of Science and Technology, Nanjing, China,* [3] *School of Materials Science and Engineering, Sun Yat-sen University, Guangzhou, China,* [4] *Department of Materials Science and Engineering, Kangwon National University, Chuncheon, South Korea*

**Keywords: three-dimensional, carbon, energy conversion, energy storage, batteries, supercapacitors, electrocatalysis**

OPEN ACCESS

***Edited by:***
*Jun Yan,*
*Harbin Engineering University, China*

***Reviewed by:***
*Xu Xiao,*
*Drexel University, United States*

****Correspondence:***
*Tianyu Liu*
*tliu23@vt.edu*

***Specialty section:***
*This article was submitted to Electrochemical Energy Conversion and Storage,*
*a section of the journal Frontiers in Energy Research*

***Received:*** *29 September 2020*
***Accepted:*** *19 October 2020*
***Published:*** *12 November 2020*

***Citation:***
*Liu T, Zhai T, Shi K, Kim H-K (2020) Editorial: Three-Dimensional Carbon Architectures for Energy Conversion and Storage.*
*Front. Energy Res. 8:611537.*
*doi: 10.3389/fenrg.2020.611537*

**Editorial on the Research Topic:**

**Three-Dimensional Carbon Architectures for Energy Conversion and Storage**

Meeting our expectation, this Research Topic has served as a global forum to report, communicate, and discuss the state-of-the-art of three-dimensional (3D) carbon materials in the context of energy conversion and storage. By the closing date in mid-September, 2020, the Research Topic has collected nine manuscripts contributed from 58 authors and gathered over 13000 views in total. These data unequivocally demonstrate the impact and popularity of 3D carbon materials in electrochemical energy conversion and storage.

The six research articles highlight the versatility of 3D carbon architectures in a plethora of applications associated with energy conversion and storage. Luo et al. demonstrated a 3D network consisting of helical carbon nanotubes and reduced graphene oxide nanosheets. This material functioned as sulfur hosts in Li-sulfur batteries. Nawwar et al. reported 3D $Fe_3O_4$-decorated carbon nanotube assemblies for capacitive charge storage. Yang et al. anchored Rh nanoparticles on 3D graphene aerogels to synthesize methanol oxidation catalysts in direct methanol fuel cells. Wang et al. fabricated symmetric supercapacitors using 3D porous graphene nanosheets derived from chitosan. Guo et al. sandwiched fluorophosphate $NaVPO_4F$ nanoparticles between amorphous carbon/reduced graphene oxide 3D hosts, which led to high-performance cathode materials for sodium-ion batteries. Liu et al. supported sulfur-deficient $MoS_{2-x}$ nanoflakes onto 3D macroporous carbon paper and made efficient oxygen-reduction catalysts to promote the electrochemical charge-storage performance of Li-$O_2$ batteries.

Additionally, the Research Topic also includes two review articles. Galek et al. surveyed the 3D hierarchically porous carbon materials as electrodes in electrochemical capacitors. Feng et al. reviewed the 3D, ordered porous carbon materials for applications in electrocatalysis, rechargeable batteries, and supercapacitors. Both reviews timely summarized the state-of-the-art development of 3D porous carbon materials in energy conversion and storage.

Last but not least, Liu commented on several overlooking issues about 3D porous carbon supercapacitor electrodes, as well as discussed potential solutions to guide future researchers in relevant research fields.

The successful conclusion of this Research Topic is impossible without the consistent support from the professional editorial team of *Frontiers in Energy Research*, our authors, reviewers, and readers. We, as the guest editors of this Research Topic, are grateful for the in-house editors. They have provided us step-by-step instructions on how to initiate, disseminate, promote, and maintain our Research Topic. We appreciate all the authors to choose our Research Topic to publish their high-quality research works, thorough reviews, and thoughtful comments. We thank all the reviewers for keeping high bars to ensure the scientific rigidity, data integrity, and presentation clarity of all the submitted manuscripts. We hope that readers of our Research Topic will find the collected articles informative, insightful, and inspiring.

## AUTHOR CONTRIBUTIONS

TL drafted and polished the editorial. All other authors proofread and approved the submission of this editorial.

**Conflict of Interest:** The authors declare that this editorial is written without any commercial or financial relationships that could be construed as a potential conflict of interest.

frontiers
in Energy Research

ORIGINAL RESEARCH
published: 24 January 2020
doi: 10.3389/fenrg.2019.00157

# Ferroconcrete-Like Helical Carbon Nanotube/Reduced Graphene Oxide Heterostructure 3D Networks as Sulfur Hosts for High-Performance Li-S Batteries

***Zhangbin Luo*[†], *Zengren Tao*[†], *Xinyu Li**, *Dandan Xu, Congxu Xuan, Zhun Wang, Tao Tang, Jianfeng Wen**, *Ming Li and Jianrong Xiao****

*Ministry-Province Jointly-Constructed Cultivation Base for State Key Laboratory of Processing for Non-Ferrous Metal and Featured Materials & Key Laboratory of Nonferrous Materials and New Processing Technology, College of Science, Guilin University of Technology, Guilin, China*

**Edited by:**
*Teng Zhai,*
*Nanjing University of Science and Technology, China*

**Reviewed by:**
*Tianyu Liu,*
*Virginia Tech, United States*
*Xifei Li,*
*Xi'an University of Technology, China*
*Qiubo Guo,*
*Nanjing University of Science and Technology, China*

***Correspondence:**
*Xinyu Li*
*lixinyu5260@163.com*
*Jianfeng Wen*
*wjfculater@163.com*
*Jianrong Xiao*
*xjr@glut.edu.cn*

[†] *These authors have contributed equally to this work*

**Specialty section:**
*This article was submitted to Electrochemical Energy Conversion and Storage,*
*a section of the journal Frontiers in Energy Research*

***Received:*** *24 October 2019*
***Accepted:*** *09 December 2019*
***Published:*** *24 January 2020*

**Citation:**
*Luo Z, Tao Z, Li X, Xu D, Xuan C, Wang Z, Tang T, Wen J, Li M and Xiao J (2020) Ferroconcrete-Like Helical Carbon Nanotube/Reduced Graphene Oxide Heterostructure 3D Networks as Sulfur Hosts for High-Performance Li-S Batteries. Front. Energy Res. 7:157.*
*doi: 10.3389/fenrg.2019.00157*

A novel helical Carbon nanotubes (HCNT) network with a reduced graphene oxide (rGO) coating was designed and fabricated through a synergistic self-assembly and sulfuration strategy for use as an effective sulfur (S) host. A ferroconcrete frame structure with a hierarchical 3D nanostructure composed of 1D HCNT and 2D rGO nanosheets was obtained. The rGO wraps around the HCNT to form a heterostructure and provide an apparent coating that protects S. HCNT in the composite is boosted to create a 3D network architecture and reinforce the structural stability. Moreover, the heterostructures and rGO coatings, which are rich in wrinkles, can greatly minimize direct contact between the polysulfide and electrolyte; they also provide an abundance of active sites and boundary defects. Furthermore, the 3D interconnected structure creates effective ion diffusion channels and allows effective trapping of S and Li polysulfides. When used as a cathode, the HCNT/rGO/S cathode exhibits a high initial specific capacity of 1,196 mAh $g^{-1}$ at 0.1 C. The capacity decay rate of the HCNT/rGO/S is only 0.075% per cycle after cycling for 200 times at a rate of 0.1 C. This unique hybrid HCNT/rGO/S electrode design may motivate the development of other high-performance electrodes with excellent electrochemical properties.

**Keywords: helical carbon nanotube, reduced graphene oxide, heterostructure, 3D hybrid materials, lithium–sulfur batteries**

## INTRODUCTION

Under the situation of new energy, electric vehicles based on Li-ion power batteries are widely considered a development thrust for next-generation automobiles (Kim et al., 2013; Manthiram et al., 2013; Song et al., 2013). Li-ion batteries, which commonly use $LiCoO_2$ or $LiFePO_4$ as a cathode material, are limited by their low practical energy density. Thus, intensive studies have been conducted to develop rechargeable batteries with high energy density, good cycle performance, and low cost to meet the market demand for energy storage. Among the numerous battery systems currently available, Li-S batteries (LSBs) were proposed as a promising candidate for power batteries and have attracted considerable attention. LSBs have high theoretical specific capacity

(1,675 mAh $g^{-1}$); their energy density (2,600 Wh $kg^{-1}$) is 2–3 times of current Li-ion batteries, are inexpensive, and employ low-toxicity active materials. Despite the recent great progress in LSBs, however, the applications of these batteries are restrained by several critical challenges (Liu et al., 2017; Gu et al., 2018; Xiaofei et al., 2018). These problems mainly originate from volume expansion, the extremely low conductivity of S, and the shuttle effect and limit the electrochemical stability and coulombic efficiency of the cell during cycling and resting.

Numerous strategies, such as novel nanostructured S cathodes (Wang C. et al., 2014), modification of the electrolyte adjustment separator (Yan et al., 2013; Wang et al., 2015), and protected Li metal anodes (Zhang H. et al., 2018), have been proposed to enhance the LSBs' electrochemical performance. Various C structures, such as C nanotubes (CNTs) and graphene oxide (GO), have been developed as highly promising hosts for S cathodes (Hu et al., 2017; Tan et al., 2018). In particular, GO is highly suitable for coating the surface of C–S nanocomposites to form a cladding structure because the unique 2D structure and excellent physicochemical properties of GO improve the cycle performance of LSBs (Kim et al., 2012). CNTs present unique nanostructures with excellent electrical conductivity and can form heterostructure in three dimensions (Gulzar et al., 2018). However, both forms of CNT and GO easily aggregate due to strong van der Waals interactions, thereby degrading the effective specific surface area (SSA) and available space. Thus, it is essential to design composite carbon materials that integrate CNTs and GO with 3D structural carbon matrix as host materials for sulfur cathodes. And these hybrid cathodes with CNTs and GO exhibit enhanced electrochemical performance on account of their synergistic effect (Ding et al., 2016; Wang et al., 2016; Yang et al., 2018). Heterostructures can be formed by synthesizing mixed 1D CNTs and 2D GO, and these structures can be assembled into 3D superstructures. The constructed heterostructures can not only hasten the transport kinetics in the crystal structures but also preserve the nanocrystal structures. The construction of heterostructures has immense potential in improving energy conversion and storage properties (Sun et al., 2011; Zhang et al., 2019).

Modification of S cathodes with graphene and CNTs is still in its initial stages, and more structural designs are needed to obtain S cathodes with improved electrochemical performance. Chiral C-based nanotubes with helical structures (HCNT), large specific surface areas, and numerous surface grooves are highly desired in LSBs because of their outstanding electrochemical performance, extraordinary self-weaving behavior, and light weight. HCNTs are used to construct interwoven conductive networks for the rapid transfer of electrons, and the 3D mesh structure formed provides attachment sites for S (Akagi et al., 1995; Tang et al., 2010; Li et al., 2018). These characteristics inhibit the dissolution and diffusion of polysulfides and adapt to the volume expansion effect in the discharge process. Thus, these characteristics improve the cycling life of the S cathode (Jin et al., 2016). In addition, compared with straight CNTs, HCNT can be more easily twisted, bent, and stretched (Di et al., 2016). HCNT can also have a nested structure because graphene stacks up to form multilayer structures. The rational design and fabrication of graphene films with optimized 3D architectures are an effective approach to avoid the restacking of graphene and shorten ion-diffusion paths. These films possess a large surface area, porous structures, and excellent electrical conductivity. Moreover, the films can be easily formed by introducing HCNTs to the GO framework. Thus, the electrochemical performance is enhanced (Peng et al., 2014; Su et al., 2017). Twisted CNT yarns, for example, have been developed to harvest electrical energy. Kar (Cherusseri et al., 2016) prepared hierarchical HCNT/C fiber structure electrodes for use as flexible supercapacitors and obtained a maximum gravimetric capacitance of 125.7 F $g^{-1}$ at a current density of 0.28 mA $cm^{-2}$. Although helical structures have been well-studied for converting tensile or torsional mechanical energy into electrical energy, the use of HCNT and GO in LSBs has rarely been reported.

In this work, we designed and fabricated a cathode composed of a rGO-coated HCNT heterostructure composite with a 3D ferroconcrete-like structure as a S container (HCNT/rGO/S) through a facile and scalable solution-based self-assembly method. Here, the HCNTs and rGO serve as the ferroconcrete-like frame structure, and rGO provides an external coating that protects S and forms a heterostructure. The S particles are well-coated and confined to the 3D ferroconcrete-like nanostructures. The HCNTs prompt the formation of an interconnected 3D network architecture with highly robust conductive networks that can boost electron transport and maintain structural integrity. The rGO coatings with abundant wrinkles and voids can greatly increase both surface area and interfaces contact, which are beneficial for accommodating volume expansion and minimize direct contact between the polysulfide with the electrolyte. The unique 1D/2D HCNT/rGO heterostructure provides abundant active sites and boundary defects while ameliorating the nucleation/conversion redox kinetics and decreasing the overpotential of polysulfide nucleation. When used as a cathode, a battery made of the proposed HCNT/rGO/S heterostructure can achieve high initial specific capacities of 1,196, 1,130, and 1,009 mAh $g^{-1}$ at 0.1, 0.2, and 0.5 C, respectively. Furthermore, the HCNT/rGO/S cathode provides a high specific capacity of 1,016, 971.8, and 872 mAh $g^{-1}$ at 0.1, 0.2, and 0.5 C, respectively, after 200 cycles. These results suggest that the fabricated cathode is a promising candidate for ultrafast charge/discharge applications.

# EXPERIMENTAL SECTION

## Preparation of Helical Carbon Nanotubes and the 1D/2D Helical Carbon Nanotube/Graphene Oxide Heterostructure

Pristine HCNTs were synthesized via catalytic CVD as reported previously (Tang et al., 2010). The catalyst precursor was prepared from citric acid and $Ni(NO_3)_2$. The CVD method used the catalyst precursor as a raw material to change the temperature and gas flow rate to control the material morphology. In order to enhance chemical compatibility with a suitable solvent, we performed a typical mixed acid ($H_2SO_4$ and $HNO_3$ in a 3:1 ratio) and produced a hydrophilic O group on the surface of the HCNT. GO was prepared via a modified Hummers' method (Xu et al., 2017). 0.1 g GO powder and 0.1 g acid-treated HCNTs were separately dispersed into the 100 ml N-Methyl pyrrolidone (NMP) and sonicated for 2 h. Then, the GO dispersions and HCNT dispersions were mixed together at a volume ratio of 3:1 and ultrasonicated for 1 h to prepare a mixture of HCNT/GO. During the ultrasound process, the temperature is maintained within 50°C.

## Preparation of the Helical Carbon Nanotubes/Reduced Graphene Oxide/Sulfur, Helical Carbon Nanotube/Sulfur, and Reduced Graphene Oxide/Sulfur Active Material

In a typical synthesis procedure, 6.9 g $Na_2S_2O_3$ was first dissolved into the 100 ml HCNT/GO NMP dispersion, ultrasonicated, and then magnetically stirred. Thereafter, 2.7 g concentrated HCl was diluted into an aqueous solution of 0.1 mol $l^{-1}$, and added dropwise to the above solution at a rate of 10 ml $min^{-1}$ and stirred for 10 min. HCl (0.1 M) was added dropwise into the above well-mixed solution under strong magnetic stirring to obtain an HCNT/GO-S solution and sonicated for 2 h at 90°C to obtain an HCNT/rGO/S solution. Simultaneous sulfuration of GO and elimination of the O-containing functional groups on the GO rendered the formation of the HCNT/rGO/S hybrid material. Finally, the HCNT/rGO/S composite was obtained by centrifugation and drying. HCNT/S and rGO/S were synthesized via the same procedures applied to obtain the HCNT/rGO/S.

## Fabrication of the Helical Carbon Nanotubes/Reduced Graphene Oxide/Sulfur, Helical Carbon Nanotubes/Sulfur, and Reduced Graphene Oxide/Sulfur Cathodes

For preparing HCNT/rGO/S working electrodes, a mixture of HCNT/rGO/S composite, Super P, and poly-(vinyl difluoride) (PVDF) binder in the NMP at a mass ratio of 80:10:10 was pasted on an Al foil. The cathode slurry was spread onto Al foil with a doctor blade and then dried for 12 h at 60°C under vacuum. Finally, the cathode was punched into disks with a diameter of 16 mm with an active-material loading of about 1 mg $cm^{-2}$ for assembly, and the HCNT/rGO/S cathode was obtained. HCNT/S and rGO/S were synthesized via the same procedures applied to obtain the HCNT/rGO/S.

## Electrochemical Characterization

CR-2025 button cell was used to test the electrochemical properties of the S cathode, and the cell was assembled in the glove box filled with Ar. A Li sheet was used as the anode electrode. The working cathodes and Li anodes were connected to an Al foil and Ni foil, respectively. Celgard 2400 was used to separate the cathodes and anodes. The electrolyte contained a mixture of 1,3-dioxolane and 1,2-dimethoxyethane with 1 M bis sulfonamide Li salt and $LiNO_3$ (1 wt%) dissolved into it. The electrolyte volume for each cell was ~50 μl. Before electrochemical measurements, the assembled coin-type cells were kept at 25°C for 30 min. A CHI750E electrochemical measurement system was used for cyclic voltammetry (CV) and electrochemical impedance spectroscopy (EIS) measurements. CV was conducted at a scan rate of 0.1 mV $s^{-1}$ in the potential window from 1.5 to 3.0 V. EIS spectra were recorded over frequencies ranging from 0.01 Hz to 100 kHz. The cells were charged/discharged in the potential range from 1.5 to 2.8 V. The specific capacity values were calculated based on the mass of sulfur in the cathode. All experiments were carried out and analyzed at room temperature.

## Materials Characterization

The crystal structure and state of the samples were detected by X-ray diffraction (XRD) with Cu K$\alpha$ radiation in the range of 5–65°. The topographical characteristics of the sample were determined by scanning electron microscopy (SEM) and Transmission electron microscope (TEM). Elemental analysis and distributions were characterized by energy dispersive spectroscopy (EDS), and the crystalline structures of the samples were determined by Raman spectra. X-ray photoelectron spectroscopy (XPS) was conducted to survey the chemical states of the composites. The mass of active material in the electrode was characterized by thermogravimetric analysis (TGA).

# RESULTS AND DISCUSSION

## Configuration and Morphology

The preparation of HCNT/rGO/S composite with 3D ferroconcrete-like heterostructure is shown in **Figure 1a**. Briefly, GO was prepared via a modified Hummers' method. HCNTs were synthesized by CVD as reported previously (Tang et al., 2010; Xu et al., 2017). In order to enhance the chemical compatibility between components, we treated the HCNTs with a typical mixed acid ($H_2SO_4$ and $HNO_3$ at a volume ratio of 3:1), and hydrophilic O groups were produced on the surface of the HCNTs. The HCNTs were first loaded onto the GO by simple bath sonication to increase the conductivity of the GO sheets and the final composite material. Thereafter, π-π bonds were created via H bonding on the carboxyl groups on the GO and acid-treated HCNT surfaces. This step facilitates tight bonding of the two materials (Yu et al., 2014). Then, the HCNTs and GO were dispersed in NMP to form a homogeneous mixture via vigorous ultrasonication treatment. Because the GO sheets contained hydrophobic aromatic regions that could interact with HCNT and highly hydrophilic regions for dispersion in water, therefore the HCNTs and GO were dispersed in NMP to form a homogeneous mixture via vigorous ultrasonication treatment. Given intrinsic van der Waals forces among the HCNT and GO components, the scaffolds supported the porous C nanosheets, and the 2D structures were transformed into 3D interconnected hierarchical porous structures. To synthesize the S particles, $Na_2S_2O_3$ was dissolved in the HCNT/GO dispersions, and HCl was added to this mixture. After ultrasonic hydrothermal reduction, the S nanoparticles attached to the GO sheet were wrapped by the shrunken rGO sheets, and the HCNTs formed electron channels between the inclusions. In

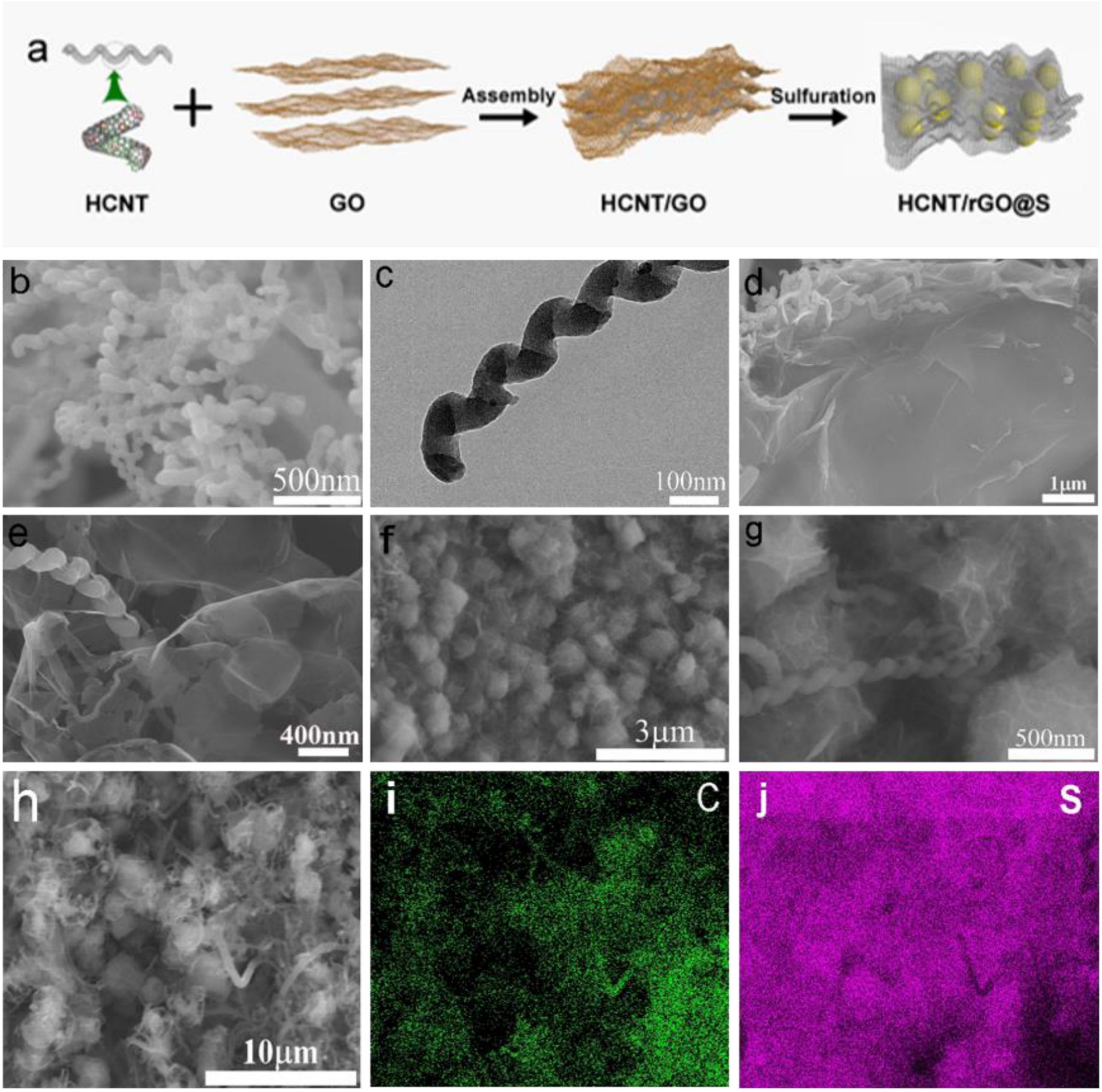

**FIGURE 1 | (a)** Schematic of the synthetic process of the helical carbon nanotubes (HCNT)/reduced graphene oxide (rGO)/sulfur (S) electrode. The SEM **(b)** and Transmission electron microscope (TEM) **(c)** image of HCNTs. The SEM **(d,e)** of HCNT/GO. The SEM **(f,g)** of HCNT/rGO/S. **(h)** SEM images and **(i,j)** elemental mapping of the HCNT/rGO/S cathode.

our approach, a mildly oxidized HCNT/GO material was used to form composites with the S particles. The GO surfactant was used as a capping agent for the S particles and limited the size of these particles to the submicrometer region during synthesis. Small S particle sizes favor the high specific capacity and rate capability of the S cathodes. The HCNT/GO suspension was mixed with S particles to afford the final S–GO composite. S, which was mainly encapsulated into the abundant hierarchical pores of rGO and HCNT, clearly provides a highly robust conductive pathway for electron transport. The HCNT and rGO were weaved into porous framework, forming a self-obtained 3D interconnected HCNT/rGO.

The morphology and microstructure of the HCNT, HCNT/GO, and HCNT/rGO/S were investigated by SEM. **Figure 1b** shows a SEM image of the pristine HCNTs, in which most of the samples have spiral structures. Sufficient void spaces and micron-sized spatial dimensions of HCNT with an average length of 5–8 μm are generated by the randomly interconnected HCNTs, which can hold a large amount of active material. This process maintains high electrolyte absorbability and effectively accommodates the volume expansion of S during discharge. TEM images in **Figure 1c** and in our previous work show that HCNTs have hollow structures with a wall thickness of a few nanometers. The hollow part of the HCNT has numerous defects, which can buffer the electrolyte within the tube and facilitate fast charge transfer. The wrinkle-like structure as observed can be seen more clearly in HCNT in **Figure S1**. Correspondingly, the as-prepared HCNTs possess abundant opened edges with geometrical defects. As depicted in **Figures 1d,e**, the 1D/2D HCNT/GO heterostructure is constructed from a self-assembly process rather than from a rough surface. Numerous 1D HCNT and 2D GO are closely entangled. This feature endows the heterostructure with high stability, flexibility, and interconnected porous channels. The heterostructure effectively prevents polysulfide diffusion and accelerates electron transfer for the polysulfide conversion reactions. Thus, the shuttling effect of LSB is remitted. The 3D ferroconcrete-like phenomenon occurs here because of the combination of the special helical structures of HCNTs and O functional groups on the GO surface, which can reinforce their connections. The large rGO not only acts as substrate for the uniform dispersion of the S but also greatly favors the rapid charge transfer in the whole electrode. The HCNTs also improve the electrical conductivity of the material for electron transport. **Figures 1f,g** show that the S particles are well-coated and confined by the GO sheets and HCNT/rGO heterostructures; S is also interfaced with the HCNT sheets. Thus, the fabrication benefited from the synergistic, applicable self-assembly and sulfuration strategy. Therefore, 3D ferroconcrete-like HCNT/rGO/S can reduce dissolution and protect S from decomposition by the electrolyte. The HCNT/rGO heterostructure layer in HCNT/rGO/S, which features a hydrophilic surface, not only prevents polysulfide dissolution but also improves the wettability of the electrolyte with the electrode.

The elemental mapping images in **Figures 1h–j** confirm the uniform distribution of C and S elements within a single HCNT/rGO/S particle. This form reduces dissolution and protects S from electrolyte decomposition. In addition, it can increase the interface contact and surface area, which can enhance the electron transfer pathway. These results indicate that 1D/2D HCNT/rGO heterostructures are successfully constructed. The larger distribution of C points compared with S points confirms that the outer shells of the material consist of C.

XRD is commonly used to study the crystallization of materials. The XRD patterns of HCNT/S, rGO/S, HCNT/rGO/S are shown in **Figure 2**. The three samples show obvious diffraction peaks, and the results indicate that the mixed materials of the samples form a relatively complete crystal structure. HCNT and rGO show a "steamed bread" peak at $2\theta = 20–30^\circ$, indicating that the two C-based materials are present in the sample in an amorphous state (Zhang Y. Z. et al., 2018). The three samples reveal sharp elemental S peaks at $2\theta = 23.187^\circ$, which indicates a typical $S_8$ bond structure. This characteristic reveals that the material has a remarkable crystal structure in all three samples (Zhang et al., 2014; Xu et al., 2017). The difference is that the sharpness of the S peak decreased in the three samples of HCNT/S, rGO/S, and HCNT/rGO/S. This characteristic indicates that the degree of dispersion and encapsulation of elemental S in the three composite materials increases. The XRD results demonstrate that this structure will exert a very strong inhibitory effect on S diffusion.

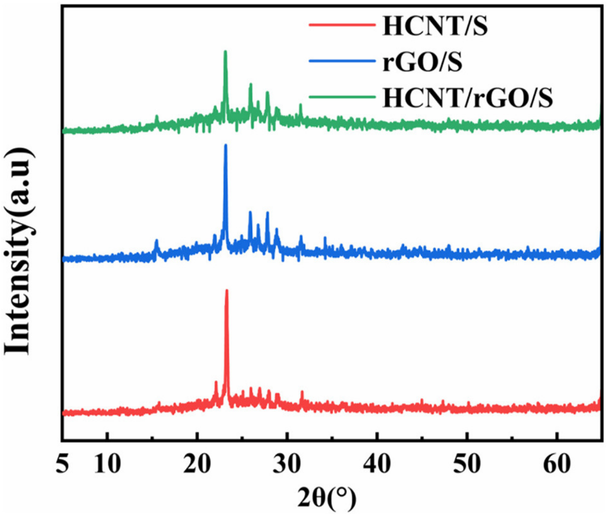

**FIGURE 2 |** XRD patterns of HCNT/S, reduced graphene oxider GO/S, HCNT/reduced graphene oxider GO/S.

**Figure 3** presents the Raman spectra of rGO/S, HCNT/S, and HCNT/rGO/S and further confirm the presence of a graphene matrix in the composites. Two Raman bands were found in the spectra of rGO/S, HCNT/S, and HCNT/rGO/S. The two broad Raman peaks observed at ∼1,351 and 1,599 $cm^{-1}$ could be attributed to the D and G bands of graphite, respectively (Hou et al., 2016). The G-band could be ascribed to $sp^2$ C vibrations, while the D-band could be ascribed to dispersive, defect-induced vibrations because of the disordered structure of graphene (Ma et al., 2017). $I_D/I_G$ results of *ca.* 1.02, 1.05, and 1.11 are obtained for HCNT/S, rGO/S, and HCNT/rGO/S, respectively. These results reflect the increasing disorder of the 1D/2D heterostructure. The positions of S in the Raman spectrum are located at 153, 218, and 474 $cm^{-1}$ (Zeng et al., 2014). The low intensity of the peaks suggests that the crystalline S clusters are homogeneously dispersed along the HCNT/rGO surface (Yang et al., 2016). After ultrasonic hydrothermal reduction, a facile and green physical coating deposition method is used to wrap S into the HCNT/rGO sheets (HCNT/rGO/S).

XPS measurement was conducted to confirm the incorporation of S into HCNT/rGO (**Figure 4**). **Figure 4A** shows the X-ray photoelectron spectrum of the HCNT/rGO/S composite. The survey spectrum confirms the coexistence of S, C, and O elements in the hybrid paper. The signal of S in the HCNT/rGO/S composite clearly shows the presence of S in the HCNT/rGO matrix. The O signals can be ascribed to residual O functional groups attached to the surface of rGO. Deconvolution of the C 1s spectrum of the HCNT/rGO/S composite shown in **Figure 4B** reveals three peaks at 286.6, 285.4, and 284.6 eV which can be designated as C–O, C–S, and C–C/C=C species, respectively (Zheng et al., 2017). As illustrated in **Figure 4C**, the binding energy of $2p_{3/2}$ and S $2p_{1/2}$ are 163.8 and 165.1 eV, respectively (Li et al., 2016). The binding energy of 163.8 eV at S $2p_{3/2}$ peak is slightly lower than that of elemental S (164.0 eV), thus suggesting the possible presence of C–S bonds (Wang Z. et al., 2014). In addition, the minor peak at ∼168.6 eV indicates the sulfate species formed by sulfur oxidation in air (Yang et al., 2016).

The weight percentage of S was characterized by thermogravimetric analysis (TGA, **Figure 5**). As shown in **Figure 5**, the weight losses of rGO/S, HCNT/S, and HCNT/rGO/S at 395°C were 87.8, 68.91, and 90.4 wt%. Acid-HCNT and rGO show a weight loss of 0.5 wt% during the process, respectively, indicating that the content of oxhydryl and carboxyl was in acid-HCNT and rGO (Wan et al., 2014). According to the weight loss of HCNT and rGO, the S content in HCNT/rGO/S is 89.5 wt%. The very high S content in HCNT/rGO/S not only allows good loading effects through the porous 3D structure but also maintains sulfur through additional active sites (Liu et al., 2017). Interestingly, the HCNT/rGO/S composite exhibited a higher sublimation temperature, indicating a strong interaction between sulfur and HCNT/rGO (Yang et al., 2018).

## Electrochemical Performance

In order to evaluate the electrochemical properties of the composites, the CR-2025 button battery with HCNT/rGO/S as cathode and the Li foil as anode were assembled for testing. On the Neware battery test system, the batteries circulate in the range of 1.5–2.8 V (relative to Li/Li$^+$), and the specific capacity is calculated based on the S content in the composites.

The Coulomb efficiency of HCNT/rGO/S at 0.1 C and the cycling stability profiles of the three cathodes at various current

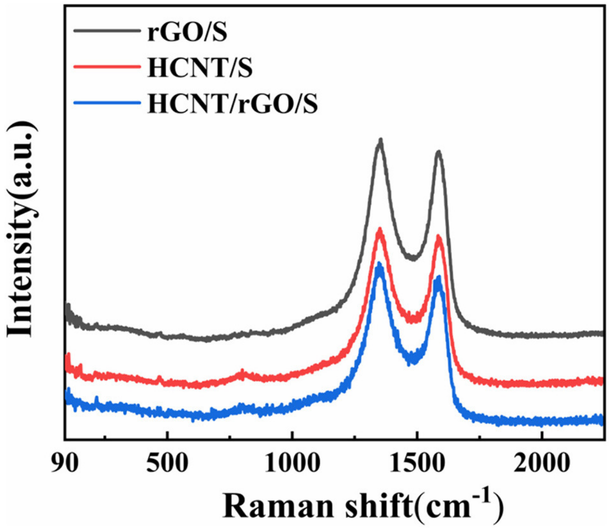

**FIGURE 3 |** Raman spectra of helical carbon nanotubes (HCNT)/sulfur (S), reduced graphene oxide (rGO)/S, and HCNT/rGO/S.

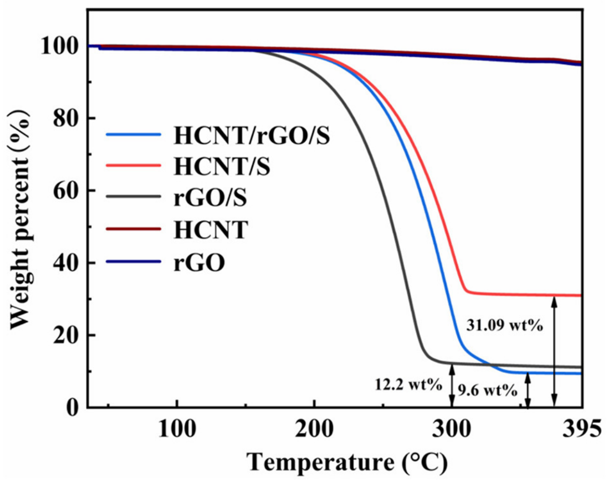

**FIGURE 5 |** Thermogravimetric (TG) curves for helical carbon nanotubes (HCNT), reduced graphene oxide (rGO), rGO/sulfur (S), HCNT/S, and HCNT/rGO/S from room temperature to 395°C at a heating rate of 10°C min$^{-1}$ under $N_2$ atmosphere.

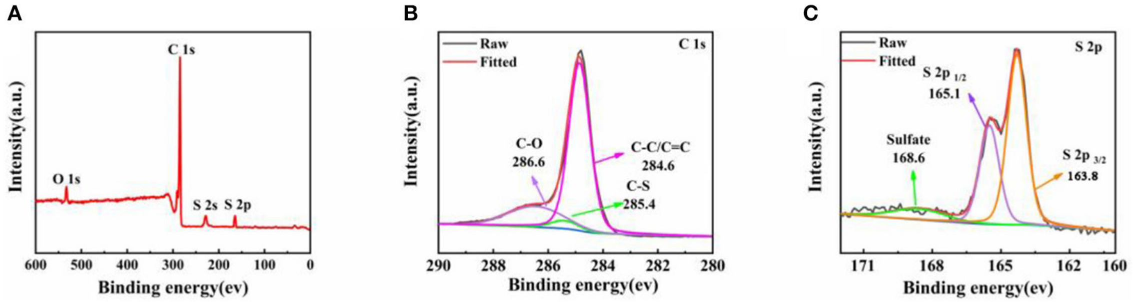

**FIGURE 4 |** X-ray photoelectron spectroscopy (XPS) survey spectrum of helical carbon nanotubes (HCNT)/reduced graphene oxide (rGO)/sulfur (S) composites **(A)**; C 1s **(B)**, and S 2p **(C)** XPS spectra of the HCNT/rGO/S composite.

densities are shown in **Figure 6**. In **Figure 6A**, the HCNT/rGO/S cathode achieves an initial specific capacity as high as 1,196 mAh $g^{-1}$ at 0.1 C with a high active-S utilization rate of 71.4% and a high initial coulomb efficiency of 96.9%. The cathode retains a high reversible specific capacity of 1,016 mAh $g^{-1}$ after 200 cycles, which corresponds to a capacity retention of 85%. For comparison, HCNT/S and rGO/S cathodes were prepared at the same conditions. The HCNT@S and rGO/S cathodes deliver initial specific discharge capacities of 1,020 and 1,107 mAh $g^{-1}$, respectively, at 0.1 C and maintain discharge specific capacities of 556 and 723 mAh $g^{-1}$ after 200 cycles, as demonstrated in **Figure 6B**. The HCNT/rGO/S cathode shows superior cycling stability. **Figures 6B–D** show the cycling performance of the HCNT/rGO/S cathode at charge/discharge rates of 0.1, 0.2 and 0.5 C, respectively. After 200 cycles, the HCNT/rGO/S cathode still exhibits a reversible specific capacity of 1,016 mAh $g^{-1}$ at 0.1 C, which corresponds to a capacity retention of 85%. When the current rate increases to 0.2 C, the initial discharge capacity (1,130 mAh $g^{-1}$) becomes lower than that at 0.1 C, but the cycle stability is significantly improved. A high reversible specific capacity of 971.8 mAh $g^{-1}$ remains after 200 cycles at 0.2 C, which corresponds to a capacity retention of 86%. This behavior is due to the high charge/discharge rate of materials, which weakens the shuttle effect of dissolved polysulfides by decreasing their retention time in the electrolyte in each cycle. Even at a high rate of 0.5 C, the HCNT/rGO/S cathode delivers an initial specific discharge capacity of 1,009 mAh $g^{-1}$. After 200 cycles, the specific capacity remains at 872 mAh $g^{-1}$, which translates to a capacity retention of 86.5%. By contrast, the HCNT/S and rGO/S cathodes deliver relatively inferior cycling stabilities of only 490 and 634 mAh $g^{-1}$, respectively, at 0.5 C after 200 cycles. The superior electrochemical performance (e.g., cycle stability and S utilization ratio) observed in HCNT/rGO/S compared with those of the HCNT/S and rGO/S electrodes could be ascribed to the unique 3D ferroconcrete-like HCNT/rGO architectures. The S particles are well-coated and confined. HCNT prompt the formation of an interconnected 3D network architecture and maintain the structural integrity of the material. The heterostructures and rGO coating, which presents numerous wrinkles, could markedly minimize direct contact between the polysulfide and the electrolyte, thereby improving the nucleation/conversion redox kinetics of the resulting material.

For further comparison, the rate capabilities of HCNT/rGO/S, HCNT/S, and rGO/S cathodes were investigated at various

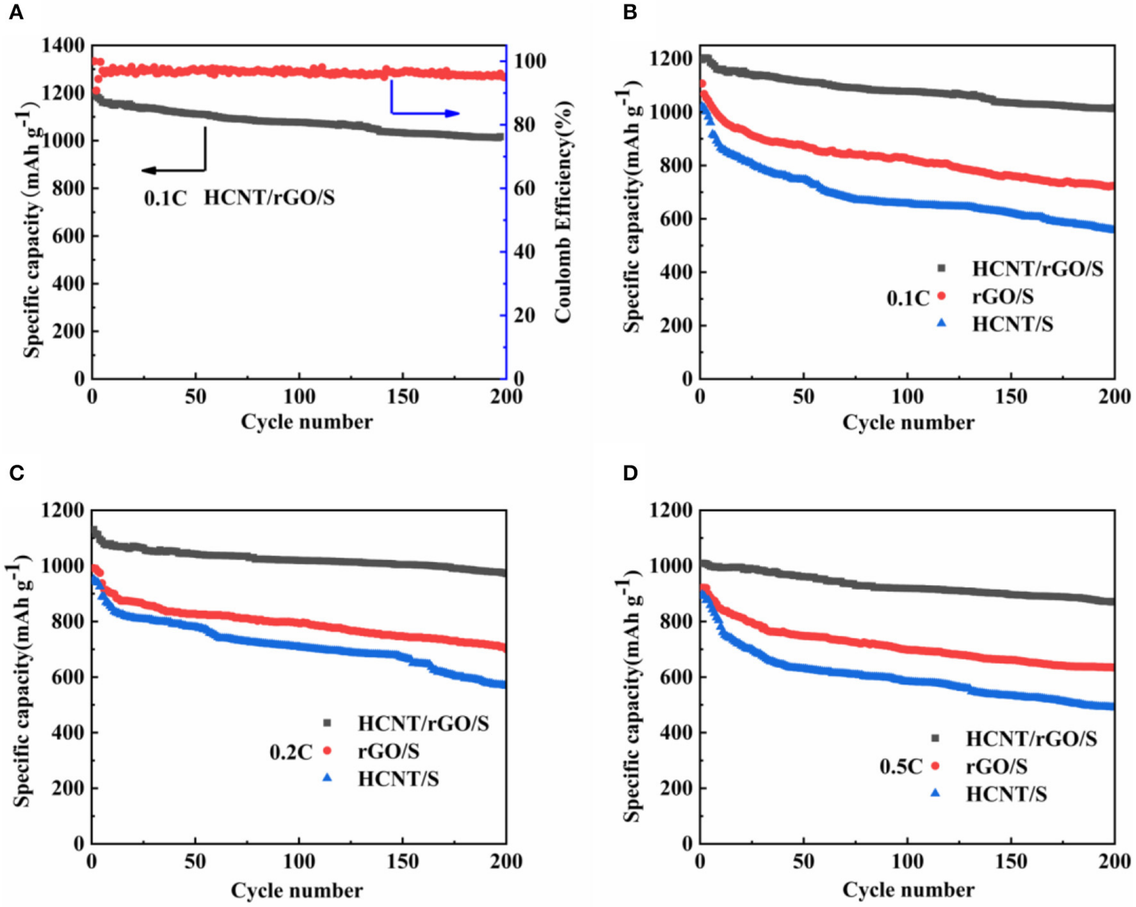

**FIGURE 6 |** Cycle performance of Li-S cells **(A)** 0.1 C, **(B)** 0.1 C, **(C)** 0.2 C, **(D)** 0.5 C.

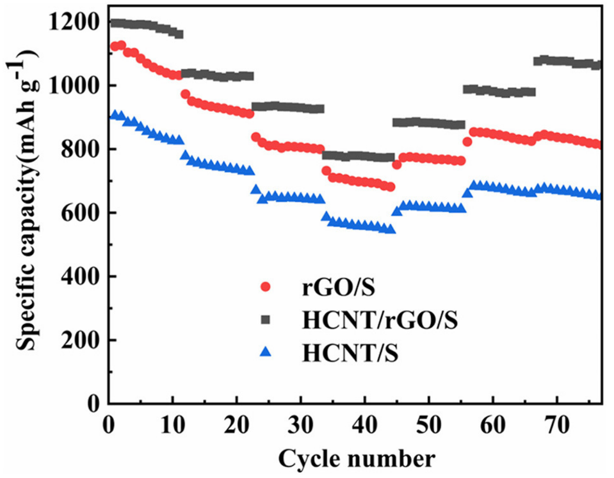

**FIGURE 7 |** Rate performance of helical carbon nanotubes (HCNT)/sulfur (S), reduced graphene oxide (rGO)/S, HCNT/rGO/S.

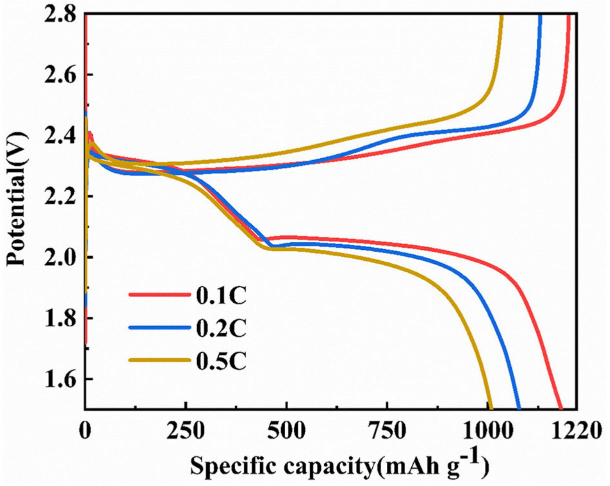

**FIGURE 8 |** The initial discharge/charge curves of the helical carbon nanotubes (HCNT)/reduced graphene oxide (rGO)/sulfur (S) cathode at various C rates from 0.1 to 0.5 C.

current rates, as depicted in **Figure 7**. The reversible discharge capacities of the cell with the HCNT/rGO/S electrode at 0.1, 0.2, 0.5, and 1 C are 1,195, 1,037, 933, and 780 mAh $g^{-1}$, respectively. When the current rate is reversed to 0.5, 0.2, and 0.1 C, the HCNT/rGO/S electrode recovers its capacities of 883, 987, and 1,075 mAh $g^{-1}$, respectively, without abrupt capacity fading. The discharge capacity gradually decreases as the current increases but maintains a considerable discharge capacity. Compared with the HCNT/rGO/S electrode, the rGO/S electrode exhibits relatively low specific capacities and discharge capacities of 1,031, 910, 799, and 681 mAh $g^{-1}$ at the end of the last cycle at rates of 0.1, 0.2, 0.5, and 1 C, respectively. By contrast, the reversible capacities of HCNT/S at current rates of 0.1, 0.2, 0.5, and 1 C are 825, 728, 639, and 545 mAh $g^{-1}$, respectively. As the current rate increases, the reversible specific capacity decreases. This phenomenon may be attributed to slow electrode kinetics on the electrode/electrolyte interface due to high S loading. The HCNT/rGO/S electrode shows better rate performance than the HCNT/S and rGO/S electrodes because the HCNT of the former are dispersed and wrapped around the GO sheets. The loose and multilevel 3D porosity heterostructure created by the HCNT and rGO helps immobilize S species and maintain the electrical conductivity and excellent polysulfide adsorption capacity of the electrode.

**Figure 8** shows the charge and discharge voltage curves of a battery in which HCNT/rGO/S was used as a cathode material. Based on the mass of S in the cathode material, the initial discharge capacities of the cathode at 0.1, 0.2, and 0.5 C are 1,196, 1,130, and 1,009 mAh $g^{-1}$, respectively, and the initial coulombic efficiency is 96.9% at 0.1 C. **Figure 8** shows that the discharge curves at the different current rates basically have two discharge platforms located at ~2.3 and 2.0 V, respectively. The platform of ~2.3 V corresponds to the reduction of $S_8$ to $Li_2S_x$ ($4 \leq x \leq 8$), and the platform of ~2.0 V corresponds to the reaction of $Li_2S_x$ ($4 \leq x \leq 8$) to $Li_2S_2/Li_2S$ (Chen et al., 2017). The discharge curves of 0.1 and 0.2 C have a higher discharge platform than the discharge curve at 0.5 C. Moreover, as the current multiplier increases, the length of the discharge platform decreases. With the increase of current rate from 0.1 to 0.5 C, a slight increase in cell polarization (voltage difference between charge platform and second discharge voltage) can be observed in the range of 0.24 to 0.32 V. This phenomenon is mainly due to fact that a large discharge current increases the polarization of the battery, and the larger the discharge current, the more obvious the polarization trend. Even at a high current rate of 0.5 C, the low discharge voltage plateau remained high at 1.95 V, which is higher and further demonstrates the great rate capability (Li et al., 2016; Zheng et al., 2017).

**Figure 9A** shows a CV curve of a battery prepared with HCNT/rGO/S at a scan rate of 0.1 mV $s^{-1}$ and a voltage range of 1.5–3 V. Two reduction peaks correspond to the formation of higher order $Li_2S_x$ ($4 \leq x \leq 8$) and insoluble $Li_2S_2/Li_2S$ (Yin et al., 2013). The oxidation peak corresponds to the oxidation of the reverse insoluble polysulfide. The small voltage shift between cathodic and anodic peaks reflects the low overvoltage of the cell and indicates the high reversibility of the cell reaction. The HCNT/rGO/S structured cell reveals a large and stable redox peak current density in the CV test. This feature explains the low polarization, good reversibility, and excellent cycle stability.

**Figure 9B** shows the charge/discharge curves for the 2nd, 10th, 50th, 100th, and 200th cycles of the HCNT/rGO/S battery at 0.1 C. The voltage profiles of the 2nd, 10th, 50th, 100th, and 200th cycles of the HCNT/S and rGO/S cathode at 0.1 C are displayed in **Figure S2**. When tested under the same C rate, two typical $Li_2S_x$ plateaus are observed at 2.25 and 1.9 V for HCNT/S and rGO/S. These values correspond to the formation of high-order and low-order polysulfides, respectively. Greater polarization and the disappearance of the first platform were watched in rGO. This phenomenon could be attributed to the lack of

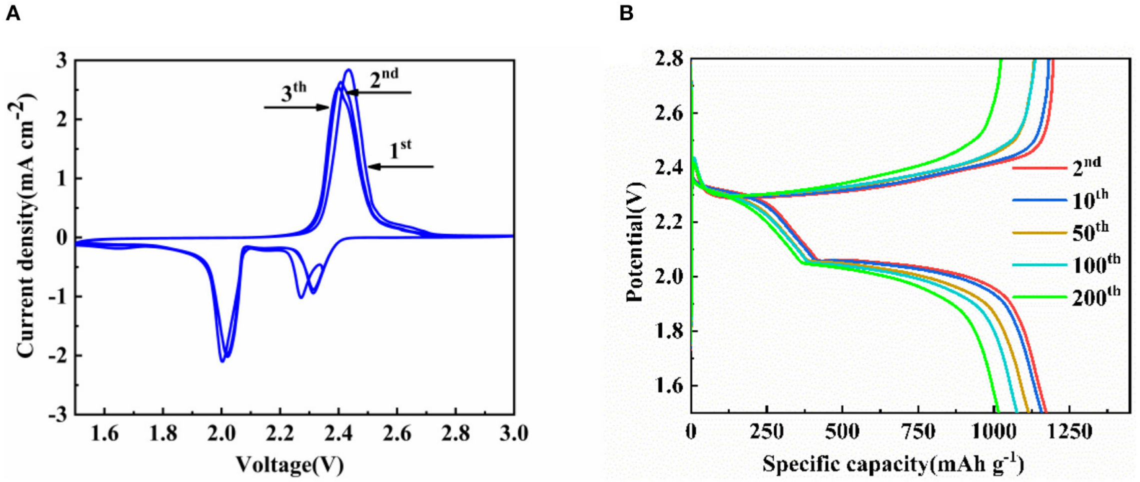

**FIGURE 9 | (A)** Cyclic voltammetry (CV) curves at the scan rate of 0.1 mV s$^{-1}$ **(B)** from 2nd to 200th discharge/charge curves of helical carbon nanotubes (HCNTs)/reduced graphene oxide (rGO)/sulfur (S) cathode at 0.1 C between 1.5 and 2.8 V.

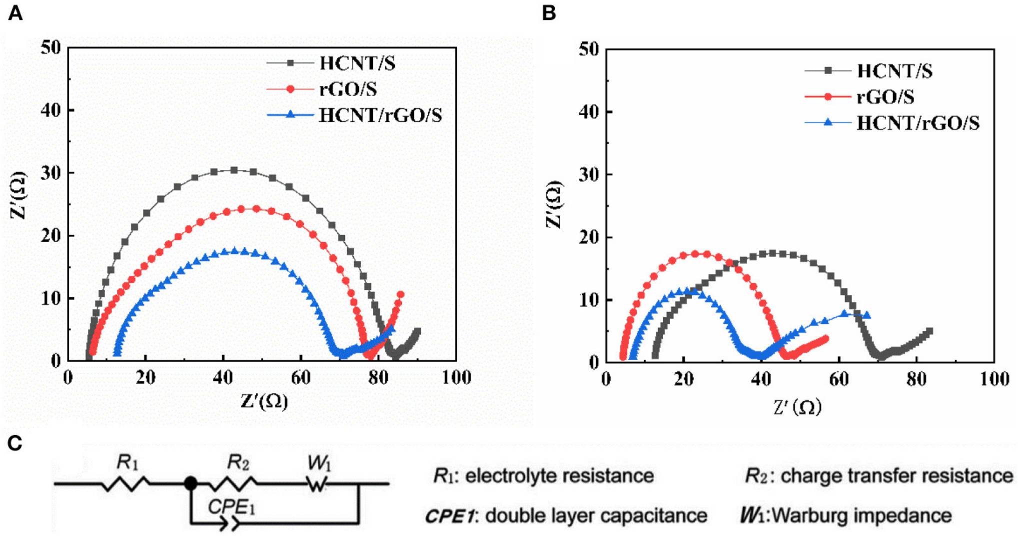

**FIGURE 10 |** Electrochemical impedance spectrum (EIS) of the cells with different cathodes **(A)** before cycling and **(B)** after cycling at 0.1 C.

conductivity of the material, which results in a markedly lower capacity compared with that of thermally reduced or HCNT-containing materials. In **Figure 9B**, the 2.3 V upper discharge platform of the HCNT/rGO/S indicates that the reduction of S leads to the formation of soluble polysulfides. Rapid S (solid)–polysulfide (liquid) reduction involves the formation, dissolution, and diffusion of polysulfides. The hysteresis between charging and discharging increases slightly as the number of cycles increases.

To investigate the effect of HCNTs on the electrochemical performance of the cell, we performed EIS after rate performance and constant-current charge/discharge testing (**Figure 10**). Impedance testing was performed in an electrochemical workstation over the frequency range of 0.01–100 kHz. In the fitted graph, $R_1$ represents the electrolyte resistance, $R_2$ represents the charge transfer resistance, $W_1$ represents the Walburg diffusion resistance, and $CPE_1$ is a constant phase. The three Nyquist diagrams of HCNT/S, rGO/S, and HCNT/rGO/S are composed of a semicircle at high intermediate frequencies, primarily because of interactions between electrolyte resistance and charge transfer resistance (Liang et al., 2016). The oblique line at low frequencies is closely related to the diffusion process of $Li^+$. The ohmic resistance is shown by the intercept of the high frequency semicircle on the coordinate axis (He et al., 2016). Comparison of the diameters of the semicircles in **Figures 10A,B** shows that the charge transfer resistance of the three samples of HCNT/S, rGO/S, and HCNT/rGO/S sequentially decreases. This result indicates that the 3D structural material has extremely excellent electrical conductivity. Comparison of the same materials shows that the charge transfer resistance after cycling is smaller than that before cycling and that the redistribution process of the active material reduces the electric resistance (Ummethala et al., 2018). Thus, the active material has a considerable utilization rate for recharging and discharging.

## CONCLUSION

In summary, we achieved the facile fabrication of a 3D HCNT/rGO/S composite bearing a ferroconcrete-like network. The unique interconnected S–HCNTs framework effectively improves electron conductivity, prevents polysulfide dissolution and minimizes the shuttle effect in the composite. Combination of HCNTs and rGO coatings reinforces electrode stability and provides pathways for rapid electron transport; the 3D structure provides effective ion diffusion channels. The rGO outer layers and heterostructures formed with HCNT confine S species and enhance the hydrophilicity of the electrolyte. These synergistic advantages endow the HCNT/rGO/S electrode with an initial discharge capacity of 1,196 mAh $g^{-1}$ and stable reversible capacity of 1,016 mAh $g^{-1}$ after 200 cycles at 0.1 C. The remarkable improvement of the electrochemical performance of the electrode indicates the importance of rationally designing the 3D structure and chemical interaction of S composite materials for Li-S batteries and other energy storage fields, such as Li-air batteries, Na-ion batteries, and supercapacitors.

## DATA AVAILABILITY STATEMENT

All datasets generated for this study are included in the article/**Supplementary Material**.

## AUTHOR CONTRIBUTIONS

All authors listed have made a substantial, direct and intellectual contribution to the work, and approved it for publication.

## FUNDING

This work was financially supported by National Natural Science Foundation of China (51662004, 11604061, 11664007, and 11764011), Natural Science Foundation of Guangxi Zhuang Autonomous Region of China (2018GXNSFAA281191 and 2018GXNSFAA050014). Supported by Foundation of Guilin University of Technology (GLUTQD2002023).

## SUPPLEMENTARY MATERIAL

The Supplementary Material for this article can be found online at: https://www.frontiersin.org/articles/10.3389/fenrg.2019.00157/full#supplementary-material

## REFERENCES

Akagi, K., Tamura, R., Tsukada, M., Itoh, S., and Ihara, S. (1995). Electronic structure of helically coiled cage of graphitic carbon. *Phys Rev Lett*. 74, 2307–2310. doi: 10.1103/PhysRevLett.74.2307

Chen, T., Cheng, B., Zhu, G., Chen, R., Hu, Y., Ma, L., et al. (2017). Highly efficient retention of polysulfides in "sea urchin"-like carbon nanotube/nanopolyhedra superstructures as cathode material for ultralong-life lithium-sulfur batteries. *Nano Lett*. 17, 437–444. doi: 10.1021/acs.nanolett.6b04433

Cherusseri, J., Sharma, R., and Kar, K. K. (2016). Helically coiled carbon nanotube electrodes for flexible supercapacitors. *Carbon N. Y.* 105, 113–125. doi: 10.1016/j.carbon.2016.04.019

Di, J., Fang, S., Moura, F. A., Galvao, D. S., Bykova, J., Aliev, A., et al. (2016). Strong, twist-stable carbon nanotube yarns and muscles by tension annealing at extreme temperatures. *Adv. Mater*. 28, 6598–6605. doi: 10.1002/adma.201600628

Ding, Y.-L., Kopold, P., Hahn, K., van Aken, P. A., Maier, J., and Yu, Y. (2016). Facile solid-state growth of 3D well-interconnected nitrogen-rich carbon nanotube-graphene hybrid architectures for lithium-sulfur batteries. *Adv. Funct. Mater*. 26, 1112–1119. doi: 10.1002/adfm.201504294

Gu, S., Sun, C., Xu, D., Lu, Y., and Wen, Z. (2018). Recent progress in liquid electrolyte-based li–s batteries: shuttle problem and solutions. *Electrochem. Energ. Rev*. 1:599. doi: 10.1007/s41918-018-0021-0

Gulzar, U., Li, T., Bai, X., Colombo, M., Ansaldo, A., Marras, S., et al. (2018). Nitrogen-doped single-walled carbon nanohorns as a cost-effective carbon host toward high-performance lithium-sulfur batteries. *ACS Appl. Mater. Interfaces* 10, 5551–5559. doi: 10.1021/acsami.7b17602

He, J., Chen, Y., Lv, W., Wen, K., Xu, C., Zhang, W., et al. (2016). Three-dimensional CNT/graphene–$Li_2S$ aerogel as freestanding cathode for high-performance Li–S batteries. *ACS Energy Lett*. 1, 820–826. doi: 10.1021/acsenergylett.6b00272

Hou, Y., Li, J., Gao, X., Wen, Z., Yuan, C., and Chen, J. (2016). 3D dual-confined sulfur encapsulated in porous carbon nanosheets and wrapped with graphene aerogels as a cathode for advanced lithium sulfur batteries. *Nanoscale* 8, 8228–8235. doi: 10.1039/C5NR09037G

Hu, G., Sun, Z., Shi, C., Fang, R., Chen, J., Hou, P., et al. (2017). A sulfur-rich copolymer@CNT hybrid cathode with dual-confinement of polysulfides for high-performance lithium-sulfur batteries. *Adv. Mater.* 29:1603835. doi: 10.1002/adma.201603835

Jin, F., Xiao, S., Lu, L., and Wang, Y. (2016). Efficient activation of high-loading sulfur by small CNTs confined inside a large CNT for high-capacity and high-rate lithium-sulfur batteries. *Nano Lett.* 16, 440–447. doi: 10.1021/acs.nanolett.5b04105

Kim, J., Lee, D.-J., Jung, H.-G., Sun, Y.-K., Hassoun, J., and Scrosati, B. (2013). An advanced lithium-sulfur battery. *Adv. Funct. Mater*. 23, 1076–1080. doi: 10.1002/adfm.201200689

Kim, K. H., Oh, Y., and Islam, M. F. (2012). Graphene coating makes carbon nanotube aerogels superelastic and resistant to fatigue. *Nat. Nanotechnol.* 7, 562–566. doi: 10.1038/nnano.2012.118

Li, G., Sun, J., Hou, W., Jiang, S., Huang, Y., and Geng, J. (2016). Three-dimensional porous carbon composites containing high sulfur nanoparticle content for high-performance lithium-sulfur batteries. *Nat. Commun.* 7:10601. doi: 10.1038/ncomms10601

Li, X., Xu, Y., Hu, G., Luo, Z., Xu, D., Tang, T., et al. (2018). Self-assembled formation of conjugated 3D reduced graphene oxide-wrapped helical CNTs nanostructure and nitrogen-doped using photochemical doping for high-performance supercapacitor electrodes. *Electrochim. Acta* 280, 33–40. doi: 10.1016/j.electacta.2018.05.106

Liang, G., Wu, J., Qin, X., Liu, M., Li, Q., He, Y., et al. (2016). Ultrafine $TiO_2$ decorated carbon nanofibers as multifunctional interlayer for high-performance lithium–sulfur battery. *ACS Appl. Mater. Interfaces* 8, 23105–23113. doi: 10.1021/acsami.6b07487

Liu, M., Qin, X., He, Y., Li, B., and Kang, F. (2017). Recent innovative configurations in high-energy lithium–sulfur batteries. *J. Mater. Chem. A* 5:5222–5234. doi: 10.1039/C7TA00290D

Ma, Z., Tao, L., Liu, D., Li, Z., Zhang, Y., Liu, Z., et al. (2017). Ultrafine nano-sulfur particles anchored on *in situ* exfoliated graphene for lithium–sulfur batteries. *J. Mater. Chem. A* 5, 9412–9417. doi: 10.1039/C7TA01981E

Manthiram, A., Fu, Y., and Su, Y. S. (2013). Challenges and prospects of lithium-sulfur batteries. *Acc. Chem. Res.* 46, 1125–1134. doi: 10.1021/ar300179v

Peng, H.-J., Huang, J.-Q., Zhao, M.-Q., Zhang, Q., Cheng, X.-B., Liu, X.-Y., et al. (2014). Nanoarchitectured graphene/CNT@porous carbon with extraordinary electrical conductivity and interconnected micro/mesopores for lithium-sulfur batteries. *Adv. Funct. Mater*. 24, 2772–2781. doi: 10.1002/adfm.201303296

Song, M. K., Cairns, E. J., and Zhang, Y. (2013). Lithium/sulfur batteries with high specific energy: old challenges and new opportunities. *Nanoscale* 5, 2186–2204. doi: 10.1039/c2nr33044j

Su, D., Cortie, M., and Wang, G. (2017). Fabrication of N-doped graphene-carbon nanotube hybrids from prussian blue for lithium-sulfur batteries. *Adv. Energy Mater*. 7:1602014. doi: 10.1002/aenm.201602014

Sun, C. L., Chang, C. T., Lee, H. H., Zhou, J., Wang, J., Sham, T. K., et al. (2011). Microwave-assisted synthesis of a core-shell MWCNT/GONR heterostructure for the electrochemical detection of ascorbic acid, dopamine, and uric acid. *ACS Nano* 5, 7788–7795. doi: 10.1021/nn2015908

Tan, L., Li, X., Wang, Z., Guo, H., and Wang, J. (2018). Lightweight reduced graphene oxide@$MoS_2$ interlayer as polysulfide barrier for high-performance lithium-sulfur batteries. *ACS Appl. Mater. Interfaces* 10, 3707–3713. doi: 10.1021/acsami.7b18645

Tang, N., Wen, J., Zhang, Y., Liu, F., Lin, K., and Du, Y. (2010). Helical carbon nanotubes: catalytic particle size-dependent growth and magnetic properties. *ACS Nano* 4, 241–250. doi: 10.1021/nn901425r

Ummethala, R., Fritzsche, M., Jaumann, T., Balach, J., Oswald, S., Nowak, R., et al. (2018). Lightweight, free-standing 3D interconnected carbon nanotube foam as a flexible sulfur host for high performance lithium-sulfur battery cathodes. *Energy Storage Mater*. 10, 206–215. doi: 10.1016/j.ensm.2017.04.004

Wan, C., Wu, W., Wu, C., Xu, J., and Guan, L. (2014). A layered porous ZrO2/RGO composite as sulfur host for lithium–sulfur batteries. *RSC Adv*. 5, 5102–5106. doi: 10.1039/C4RA12031K

Wang, B., Hu, C., and Dai, L. (2016). Functionalized carbon nanotubes and graphene-based materials for energy storage. *Chem. Commun.* 52, 14350–14360. doi: 10.1039/C6CC05581H

Wang, C., Su, K., Wan, W., Guo, H., Zhou, H., Chen, J., et al. (2014). High sulfur loading composite wrapped by 3D nitrogen-doped graphene as a cathode material for lithium–sulfur batteries. *J. Mater. Chem. A* 2, 5018–5023. doi: 10.1039/C3TA14921H

Wang, L., Liu, J., Haller, S., Wang, Y., and Xia, Y. (2015). A scalable hybrid separator for a high performance lithium-sulfur battery. *Chem. Commun.* 51, 6996–6999. doi: 10.1039/C5CC00444F

Wang, Z., Dong, Y., Li, H., Zhao, Z., Wu, H. B., Hao, C., et al. (2014). Enhancing lithium-sulphur battery performance by strongly binding the discharge products on amino-functionalized reduced graphene oxide. *Nat. Commun.* 5:5002. doi: 10.1038/ncomms6002

Xiaofei, Y., Xia, L., Keegan, A., Huamin, Z., and Xueliang, S. (2018). Structural design of lithium–sulfur batteries: from fundamental research to practical application. *Electrochem. Energ. Rev*. 1, 239–293. doi: 10.1007/s41918-018-0010-3

Xu, Y., Li, X., Hu, G., Wu, T., Luo, Y., Sun, L., et al. (2017). Graphene oxide quantum dot-derived nitrogen-enriched hybrid graphene nanosheets by simple photochemical doping for high-performance supercapacitors. *Appl. Surf. Sci.* 422, 847–855. doi: 10.1016/j.apsusc.2017.05.189

Yan, Y., Yin, Y.-X., Xin, S., Su, J., Guo, Y.-G., and Wan, L.-J. (2013). High-safety lithium-sulfur battery with prelithiated Si/C anode and ionic liquid electrolyte. *Electrochim. Acta* 91, 58–61. doi: 10.1016/j.electacta.2012.12.077

Yang, W., Yang, W., Song, A., Sun, G., and Shao, G. (2018). 3D interconnected porous carbon nanosheets/carbon nanotubes as a polysulfide reservoir for high performance lithium-sulfur batteries. *Nanoscale* 10, 816–824. doi: 10.1039/C7NR06805K

Yang, X., Zhu, W., Cao, G., and Zhao, X. (2016). Preparation of a carbon nanofibers–carbon matrix–sulfur composite as the cathode material of lithium–sulfur batteries. *RSC Adv.* 6, 7159–7171. doi: 10.1039/C5RA24129D

Yin, Y. X., Xin, S., Guo, Y. G., and Wan, L. J. (2013). Lithium-sulfur batteries: electrochemistry, materials, and prospects. *Angew. Chem. Int. Ed. Engl.* 52, 13186–13200. doi: 10.1002/anie.201304762

Yu, D., Goh, K., Wang, H., Wei, L., Jiang, W., Zhang, Q., et al. (2014). Scalable synthesis of hierarchically structured carbon nanotube-graphene fibres for capacitive energy storage. *Nat. Nanotechnol.* 9, 555–562. doi: 10.1038/nnano.2014.93

Zeng, Q., Wang, D.-W., Wu, K.-H., Li, Y., Condi de Godoi, F., and Gentle, I. R. (2014). Synergy of nanoconfinement and surface oxygen in recrystallization of sulfur melt in carbon nanocapsules and the related Li–S cathode properties. *J. Mater. Chem. A* 2:6439. doi: 10.1039/c4ta00314d

Zhang, H., Liao, X., Guan, Y., Xiang, Y., Li, M., Zhang, W., et al. (2018). Lithiophilic-lithiophobic gradient interfacial layer for a highly stable lithium metal anode. *Nat. Commun.* 9:3729. doi: 10.1038/s41467-018-06126-z

Zhang, H., Zhao, Z., Hou, Y.-N., Tang, Y., Liang, J., Liu, X., et al. (2019). Highly stable lithium–sulfur batteries based on p–n heterojunctions embedded on hollow sheath carbon propelling polysulfides conversion. *J. Mater. Chem. A* 7, 9230–9240. doi: 10.1039/C9TA00975B

Zhang, Y. Z., Liu, S., Li, G. C., Li, G. R., and Gao, X. P. (2014). Sulfur/polyacrylonitrile/carbon multi-composites as cathode materials for lithium/sulfur battery in the concentrated electrolyte. *J. Mater. Chem. A* 2, 4652–4659. doi: 10.1039/C3TA14914E

Zhang, Y. Z., Zhang, Z., Liu, S., Li, G. R., and Gao, X. P. (2018). Free-standing porous carbon nanofiber/carbon nanotube film as sulfur immobilizer with high areal capacity for lithium-sulfur battery. *ACS Appl. Mater. Interfaces* 10, 8749–8757. doi: 10.1021/acsami.8b00190

Zheng, C., Niu, S., Lv, W., Zhou, G., Li, J., Fan, S., et al. (2017). Propelling polysulfides transformation for high-rate and long-life lithium–sulfur batteries. *Nano Energy* 33, 306–312. doi: 10.1016/j.nanoen.2017.01.040

**Conflict of Interest:** The authors declare that the research was conducted in the absence of any commercial or financial relationships that could be construed as a potential conflict of interest.

frontiers in Energy Research

ORIGINAL RESEARCH
published: 24 March 2020
doi: 10.3389/fenrg.2020.00046

# Functionally Decorated Carbon Nanotube Networks for Energy Storage in Supercapacitors

*Mohamed Nawwar[1], Rakesh P. Sahu[1,2], Ishwar K. Puri[1,2] and Igor Zhitomirsky[1]**

*[1] Department of Materials Science and Engineering, McMaster University, Hamilton, ON, Canada, [2] Department of Mechanical Engineering, McMaster University, Hamilton, ON, Canada*

A novel approach has been developed for the fabrication of $Fe_3O_4$ decorated multiwalled carbon nanotubes (MWCNT) for energy storage in negative electrodes of electrochemical supercapacitors. Synthesis of $Fe_3O_4$ was performed in the presence of MWCNT, dispersed using various cationic and anionic polyaromatic dispersants. The comparison of experimental results obtained using different dispersants provided an insight into the influence of the chemical structure of the dispersant molecules on the microstructure of the $Fe_3O_4$-MWCNT materials. It was found that positively charged groups and chelating catechol ligands of the dispersants facilitated the formation of $Fe_3O_4$ decorated MWCNT with low agglomeration. The $Fe_3O_4$ -MWCNT materials, prepared using different dispersants were used for the fabrication of electrodes with mass loading of 40 mg $cm^{-2}$. The highest capacitance was obtained in 0.5 M $Na_2SO_4$ electrolyte for $Fe_3O_4$ decorated MWCNT prepared using cationic celestine blue dye as a dispersant. Improved cyclic voltammetry profile was obtained using FeOOH as an additive. Asymmetric devices were fabricated and tested based on the $Fe_3O_4$ decorated MWCNT negative electrodes and $MnO_2$-MWCNT positive electrodes.

**Keywords: carbon nanotube, iron oxide, energy, supercapacitor, dispersant**

**Edited by:**
*Kaiyuan Shi,*
*National Research Council Canada, Canada*

**Reviewed by:**
*Zhenyu Xing,*
*South China Normal University, China*
*Dan Luo,*
*University of Waterloo, Canada*

***Correspondence:**
*Igor Zhitomirsky*
*zhitom@mcmaster.ca*

**Specialty section:**
*This article was submitted to Electrochemical Energy Conversion and Storage, a section of the journal Frontiers in Energy Research*

**Received:** *19 February 2020*
**Accepted:** *05 March 2020*
**Published:** *24 March 2020*

**Citation:**
*Nawwar M, Sahu RP, Puri IK and Zhitomirsky I (2020) Functionally Decorated Carbon Nanotube Networks for Energy Storage in Supercapacitors. Front. Energy Res. 8:46. doi: 10.3389/fenrg.2020.00046*

## INTRODUCTION

Electrochemical supercapacitors are currently under intensive investigation for energy storage and capacitive water purification applications (Shi et al., 2014; Zhao and Zheng, 2015; Ding et al., 2020). Research is focused on the development of new materials and electrolytes (Brousse and Bélanger, 2003; Shi and Zhitomirsky, 2010; Li et al., 2019), fabrication of nanoparticles of active materials (Luo et al., 2016; Silva et al., 2018), design and modeling of composite electrodes and devices (Pavaskar et al., 2018; Xing et al., 2019). New strategies have been designed for the fabrication of carbon based electrodes with enhanced capacitive performance (Salinas Torres et al., 2019). Significant interest has been generated in application of carbon nanotubes (CNT) for the fabrication of composite electrode materials (Lu et al., 2019). The interest in CNT applications for supercapacitors is related to high electronic conductivity and high surface area of CNT.

It was recognized that CNT can be decorated with other functional materials (Pan et al., 2015; Hao et al., 2016). With a desire to fabricate new and advanced devices, there is growing interest in the development of new techniques for the fabrication of functionally decorated CNT, such as laser ablation (Imbrogno et al., 2017), atomic layer deposition (Ding et al., 2018), polymerization

(Zhu et al., 2014), magnetron sputtering (Wei et al., 2014), electrodeposition (Chitturi et al., 2016), and chemical precipitation (Hong et al., 2013). Decorated CNT are of particular interest for energy storage and generation devices, such as supercapacitors, batteries, and fuel cells. The use of functionally decorated CNT allowed for the fabrication of advanced batteries with enhanced capacity (Hong et al., 2013; Wei et al., 2014), good cyclic stability (Chitturi et al., 2016) and improved conductivity (Wang et al., 2010). It has been reported that CNT can be decorated with catalysts for advanced application in fuel cells (Sonkar et al., 2017). Significant advances have been achieved in applications of functionally decorated CNT for photovoltaic devices (Mathew et al., 2011; Tai et al., 2014). It has previously been shown that carbon nanotubes can be decorated with oxides (Ojha et al., 2019), polypyrrole (Su and Zhitomirsky, 2015) and activated carbon (Shi et al., 2014) for energy storage applications in supercapacitors.

Previous studies highlighted the need in the development of efficient manufacturing techniques for the fabrication of functionally decorated CNT. Such techniques need to be based on the careful selection of dispersing agents, which must be well adsorbed on the CNT surface. Good dispersion of CNT is critical for their decoration with functional materials. The use of networks of decorated CNT is promising for the fabrication of advanced supercapacitor electrodes with high active mass.

The objective of this investigation was the fabrication of $Fe_3O_4$ decorated CNT for application in negative electrodes of asymmetric supercapacitors. Following this objective we investigated anionic and cationic aromatic dispersants for the dispersion of CNT. The results presented below indicated that chemical precipitation of $Fe_3O_4$ in the presence of CNT allowed for the fabrication of $Fe_3O_4$ decorated CNT. Testing results provided an insight into the influence of electric charge and chelating groups of the dispersants on the $Fe_3O_4$ formation on the CNT surface. The fibrous networks of decorated CNT were used for the fabrication of negative electrodes with high active mass of 40 mg cm$^{-2}$. The capacitive behavior was linked to dispersant structure. Finally, we fabricated and tested an asymmetric supercapacitor device.

## EXPERIMENTAL PROCEDURES

Iron (II) chloride tetrahydrate ($FeCl_2{\cdot}4H_2O$), iron (III) chloride hexahydrate ($FeCl_3{\cdot}6H_2O$), ammonium hydroxide ($NH_4OH$), sodium hydroxide (NaOH), sodium sulfate ($Na_2SO_4$), palmetic acid (PA), celestine blue (CB), pyrocatechol violet (PV), azure A chloride (AA), m-cresol purple (CP), poly (vinyl butyral-co-vinyl-alcohol-co-vinyl-acetate) (PVB, average MW = 50,000-80,000), multiwalled carbon nanotubes (MWCNT, purity > 95 %, OD 20-30 nm, and length 1–2 μm, US Nanomaterial Inc, USA), and Ni foam (porosity of 95%, Vale Ltd., Canada) were used.

For decoration of the MWCNT by $Fe_3O_4$ nanoparticles, the synthesis of the nanoparticles was performed in the presence of dispersed MWCNT. In this procedure, 1 g L$^{-1}$ of MWCNT were dispersed in DI water by ultrasonication for 15 min and then 0.25 g L$^{-1}$ dispersant was added and suspension was ultrasonicated again for 15 min. A stoichiometric mixture of $Fe^{2+}$ and $Fe^{3+}$ salts dissolved in DI water was added to the suspension of MWCNT in order to obtain the mass ratio of $Fe_3O_4$ to MWCNT equal to 1.5. The pH was adjusted to 9 by the addition of 1 M $NH_4OH$. The obtained suspension was ultrasonicated for 40 min and then filtrated. The materials were washed with DI water and dried overnight. The magnetite decorated MWCNT, prepared using CB, PV, AA, and CP were denoted as M-CB-MWCNT, M-PV-MWCNT, M-AA-MWCNT, and M-CP-MWCNT, respectively. Non-agglomerated FeOOH nanoparticles were prepared by a chemical precipitation and liquid-liquid extraction method (Chen et al., 2019). However, in contrast to the previous investigation (Chen et al., 2019) PA was used as a new and efficient extractor. M-FH-CB-MWCNT material was prepared by mixing of M-CB-MWCNT (80%) and FeOOH (20%).

M-CB-MWCNT, M-PV-MWCNT, M-AA-MWCNT, M-CP-MWCNT, and M-FH-CB-MWCNT were dispersed in ethanol, containing dissolved PVB binder and obtained slurries were used for the impregnation of Ni foam current collectors and fabrication of negative electrodes of supercapacitors. The PVB binder content in the electrodes was 3%. The total mass of the impregnated material was 40 mg cm$^{-2}$. $MnO_2$-MWCNT material for positive electrodes was prepared by the precipitation and liquid-liquid extraction method (Chen et al., 2017). The asymmetric device was fabricated containing M-FH-CB-MWCNT negative electrodes with mass loading of 40 mg cm$^{-2}$ and $MnO_2$-MWCNT positive electrodes with mass loading of 35 mg cm$^{-2}$. At such mass loadings the capacitance of negative electrodes matched the capacitance of the positive electrodes.

Transmission electron microscopy was performed (dark field STEM) using a JEOL 2010F field emission microscope. X-ray diffraction (XRD) analysis was performed using the Bruker D8 Discover instrument comprising Davinci diffractometer and Co-Kα radiation. Particle size distribution was done using dynamic light scattering (DLS) model (DelsaMax Pro- Beckman Coulter). The analysis was carried out based on testing of 4 sets of each material with a concentration of 0.4 mg L$^{-1}$ in DI, where every set consisted of 10 acquisition.

Cyclic voltammetry (CV) and electrochemical impedance spectroscopy (EIS) studies of single electrodes and asymmetric device were performed in 0.5 L of 0.5 M $Na_2SO_4$ electrolyte as described in prior investigations (Shi and Zhitomirsky, 2013; Zhu et al., 2014; Chen et al., 2017). EIS measurements were carried out in the frequency range of 10 mHz−100 kHz with a sinusoidal signal of 10 mV. The components of complex capacitance ($C's$ and $C''s$) were calculated from the EIS data as $C's = Z'' / \omega |Z|^2 A$ and $C''s = Z' / \omega |Z|^2 A$, where $\omega = 2\pi f$ and $f$ is frequency. Galvanostatic charge–discharge of individual electrodes at different current densities was performed using Biologic VMP 300 potentiostat. The charge-discharge behavior of the asymmetric device was analyzed using battery analyzers BST8-MA and BST8-3 (MTI Corporation, USA).

## RESULTS AND DISCUSSION

**Figures 1A–D** shows chemical structures of aromatic dispersants used for dispersion of MWCNT. The polyaromatic structure of the dispersants was beneficial (Ata et al., 2018) for their adsorption on MWCNT. The adsorption mechanism involved π-π interactions. The adsorbed dispersants imparted a positive charge (CB, AA) or a negative charge (PV, CP) to MWCNT. The small size, electric charge and good adsorption of the dispersants on MWCNT facilitated MWCNT dispersion by unzipping mechanism (Ata et al., 2018; **Figure 1E**) and allowed for the fabrication of stable suspensions. **Figures 1F,G** illustrates different types of interactions of the dispersants with $Fe_3O_4$ particles. The precipitation of $Fe_3O_4$ was achieved at pH = 9, which is above the isoelectric point (pH = 6.5) (Parks, 1965) of this material. Therefore, the $Fe_3O_4$ particles were negatively charged. The negative charge of $Fe_3O_4$ resulted in electrostatic repulsion of $Fe_3O_4$ and anionic PV or CP, adsorbed on MWCNT (**Figure 1F**). In contrast, electrostatic attraction existed between $Fe_3O_4$ and cationic CB or AA molecules, adsorbed on MWCNT (**Figure 1G**). Previous investigations (Ata et al., 2014) showed that molecules, containing a catechol group, strongly adsorbed on inorganic particles, and facilitated their efficient dispersion. Therefore, CB and PV can be adsorbed on $Fe_3O_4$ particles by catecholate type bonding. **Figure 1F** shows bonding of PV to the Fe atom on the particle surface. A similar mechanism can be suggested for CB bonding. It is important to note that phenolic molecules containing single OH groups, such as CP, show poor adsorption on inorganic molecules (Ata et al., 2014). In contrast, molecules from the catechol family, such as PV, containing two adjacent OH groups, show very strong bonding to the inorganic particles (Ata et al., 2014).

X-ray diffraction studies confirmed the formation of pure $Fe_3O_4$ by precipitation from mixed $Fe^{2+}$ and $Fe^{3+}$ salt solutions (**Figure S1**). The materials prepared by precipitation from the same solutions, containing dispersed MWCNT, showed X-ray diffraction peaks of $Fe_3O_4$ and MWCNT (**Figure 2**). Peak broadening resulted from the small particle size of $Fe_3O_4$. TEM analysis revealed influence of the dispersants on the material morphologies. **Figure 3** shows TEM images of the materials at different magnifications. The TEM images of M-CB-MWCNT showed the formation of $Fe_3O_4$ decorated MWCNT. The size of the $Fe_3O_4$ particles adsorbed on the MWCNT was about 10 nm. It is suggested that electrostatic attraction of positively charged CB dispersant and negatively charged $Fe_3O_4$ as well as chelating bonding of the catechol group facilitated the formation of the decorated MWCNT. It is important to note that electrostatic repulsion of the PV dispersant, adsorbed on the MWCNT surface, and $Fe_3O_4$ nanoparticles was detrimental for the formation of the decorated MWCNT. On the other hand, the chelating bonding of the catechol groups of PV promoted $Fe_3O_4$ formation on the MWCNT surface. The chelating bonding was a dominating mechanism, which allowed for the formation of decorated MWCNT. However, the TEM studies of M-PV-MWCNT also revealed the formation of small agglomerates of the $Fe_3O_4$ particles as it is shown in **Figure 3F**. The analysis of the TEM images for M-AA-MWCNT and M-CP-MWCNT showed enhanced agglomeration of the $Fe_3O_4$ particles. The agglomeration is especially evident for M-CP-MWCNT samples. In this case the

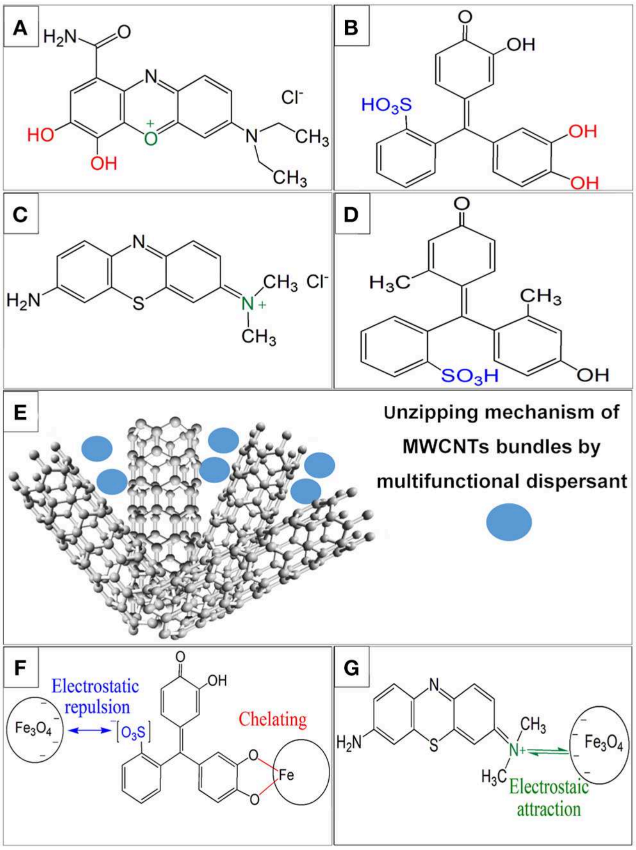

**FIGURE 1 |** Chemical structures of **(A)** CB, **(B)** PV, **(C)** AA, **(D)** CP and schematics, showing **(E)** unzipping of MWCNT bundles by dispersants, **(F)** electrostatic repulsion of PV and $Fe_3O_4$ particles and chelating bonding of PV to Fe atoms on the $Fe_3O_4$ particle surface, involving a catechol group of PV, **(G)** electrostatic attraction of AA and $Fe_3O_4$.

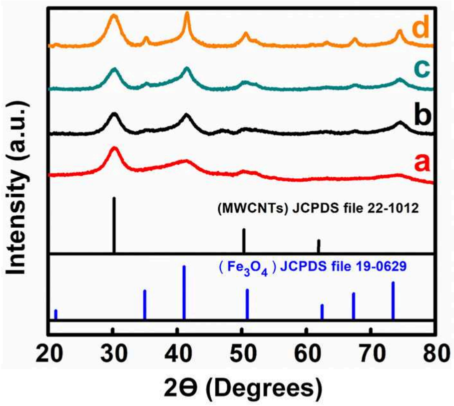

**FIGURE 2 |** X-ray diffraction patterns of (a) M-CB-MWCNT, (b) M-PV-MWCNT, (c) M-AA-MWCNT, and (d) M-CP-MWCNT.

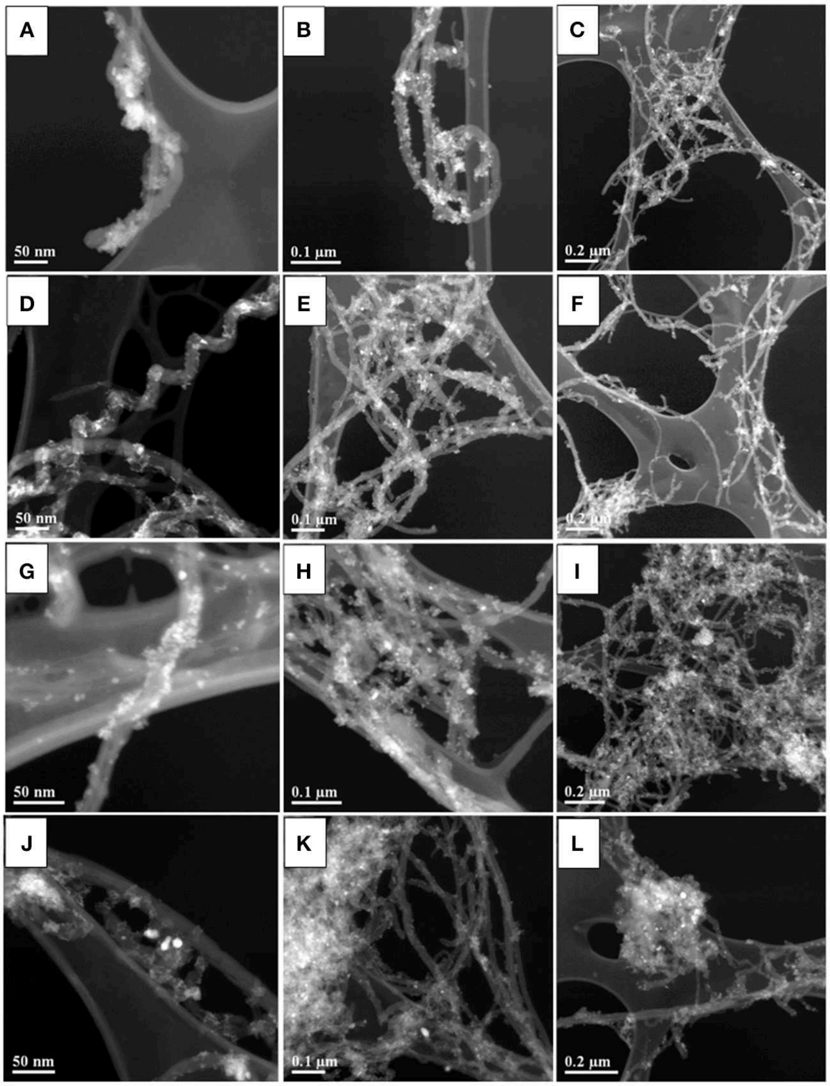

**FIGURE 3 |** TEM images at different magnifications for **(A–C)** M-CB-MWCNT, **(D–F)** M-PV-MWCNT, **(G–I)** M-AA-MWCNT, and **(J–L)** M-CP-MWCNT.

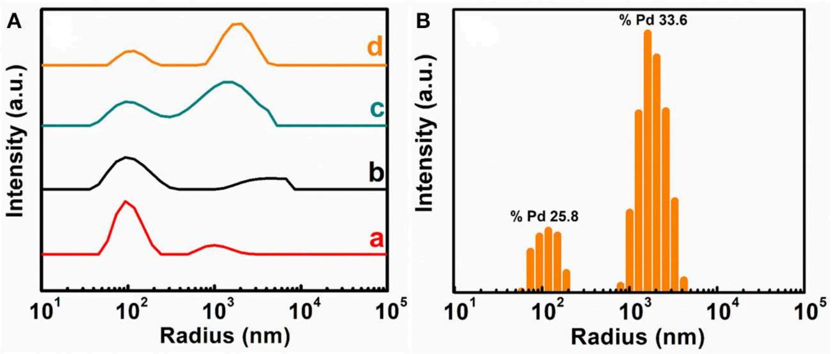

**FIGURE 4 | (A)** Average data (40 samples of each composition) for DLS analysis of (a) M-CB-MWCNT, (b) M-PV-MWCNT, (c) M-AA-MWCNT and (d) M-CP-MWCNT, **(B)** Typical spectrum for M-CP-MWCNT. The width of the peaks indicates the polydispersity of the aggregate (Pd).

poor coverage of MWCNT resulted from electrostatic repulsion of CP and $Fe_3O_4$.

The effect of different dispersing agents has also been studied using DLS analysis (**Figure 4**). The size distribution of the aggregates in all samples is bimodal with different degree of polydispersity. The first peak at ∼100 nm is present in all four dispersions with different intensities. The second peak was observed in the range of $10^3$-$10^4$ nm. The intensity and polydispersity of the second peak are smallest for M-CB-MWCNT. The polydispersity of M-PV-MWCNT is broader than that of M-CB-MWCNT. The analysis of the DLS data for M-AA-MWCNT and M-CP-MWCNT revealed significant increase in the relative intensity of the second peak, compared to the intensity of the first peak. The second peak for M-AA-MWCNT and M-CP-MWCNT shifted to larger radius numbers, compared to the second peak for M-CB-MWCNT. The increase in relative intensity of the second peak for M-AA-MWCNT and M-CP-MWCNT and peak shifts indicated an increasing number of agglomerates and increase in the agglomerate size of the particles. This is in agreement with the TEM data and indicates the beneficial effect of the catechol groups of CB and PV for the formation of decorated MWCNT and reduction of $Fe_3O_4$ agglomeration. It is important to note that the decoration of MWCNT resulted from the dispersant mediated adsorption. In this approach the changes in MWCNT structure, resulting from chemical reactions and high temperature treatment (Xing et al., 2015, 2017, 2019) can be avoided.

M-CB-MWCNT, M-PV-MWCNT, M-AA-MWCNT, M-CP-MWCNT were used for the fabrication of supercapacitor electrodes with mass loading of 40 mg $cm^{-2}$. **Figure 5** shows cyclic voltammetry data for the electrodes in the potential range of −0.9 to 0.0 V vs. SCE. M-CB-MWCNT electrodes showed a larger CV area, compared to other electrodes and higher integral capacitance in the selected potential window. The M-CP-MWCNT electrodes showed lower capacitance, compared to

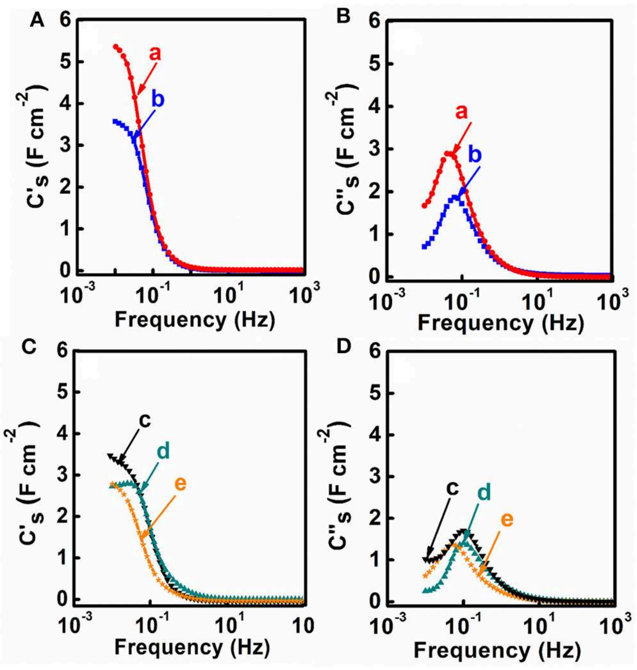

**FIGURE 6 | (A–D)** Frequency dependences of components of complex AC capacitance, calculated from impedance data for (a) M-CB-MWCNT, (b) M-FH-CB-MWCNT, (c) M-PV-MWCNT, (d) M-AA-MWCNT and (e) M-CP-MWCNT electrodes.

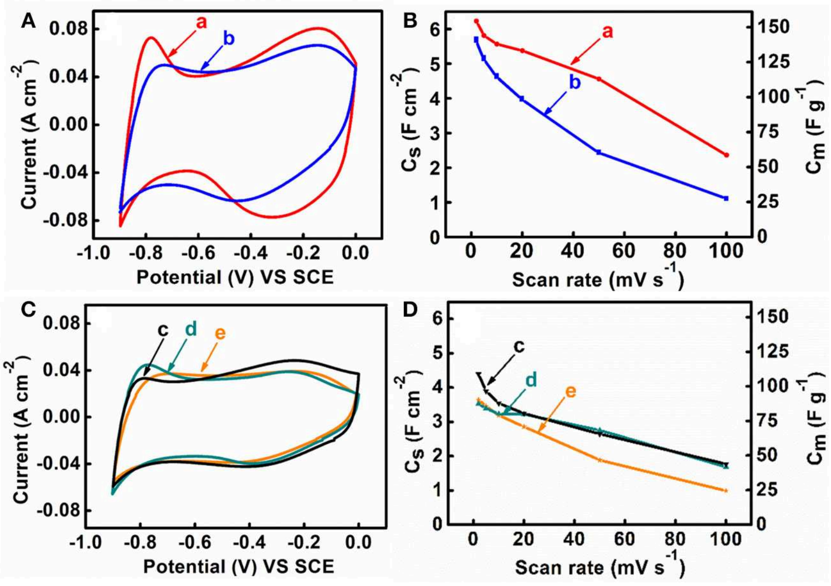

**FIGURE 5 | (A,C)** CVs and **(B,D)** capacitance vs. scan rate for (a) M-CB-MWCNT, (b) M-FH-CB-MWCNT, (c) M-PV-MWCNT, (d) M-AA-MWCNT and (e) M-CP-MWCNT electrodes.

other materials. The higher capacitance of M-CB-MWCNT can result from reduced agglomeration of the $Fe_3O_4$ particles and improved contact of $Fe_3O_4$ and MWCNT. However, the CV for M-CB-MWCNT showed redox peaks and deviated significantly from the box shape. Significant reduction of the charge and discharge currents was observed in the potential range of −0.4 to −0.7 V. The observed redox peak can result from the redox-active properties of CB (Noorbakhsh et al., 2008). Such CV shape is detrimental for the fabrication of asymmetric cells. In order to improve the CV profile, the M-CB-MWCNT was combined with FeOOH, which shows good charge storage properties in the range of −0.4 to −0.7 V (Chen et al., 2018). Therefore, M-FH-CB-MWCNT was prepared and tested. This material showed improved CV shape, compared to M-CB-MWCNT. The capacitance of 5.76 F $cm^{-2}$ (144 F $g^{-1}$) was obtained at a scan rate of 2 mV $s^{-1}$. **Figure 6** shows frequency dependences of the components of differential AC capacitance, calculated from the impedance data. M-CB-MWCNT showed the highest real part of capacitance $C'_S$ at low frequencies, compared to other materials. However, the M-FH-CB-MWCNT electrodes showed lower $C''_S$, which indicated lower energy losses. The slightly higher relaxation frequency, corresponding to maximum of $C''_S$, indicated better performance. The M-CP-MWCNT electrodes, showed lower $C'_S$ and lower relaxation frequency, compared to other materials. The capacitive behavior of the electrodes has also been analyzed by chronopotentiometry. **Figure 7** compares galvanostatic charge-discharge curves for different electrodes and capacitances, calculated from the discharge data at different current densities. The charge-discharge curves were of nearly triangular shape. The highest capacitance at 3 mA

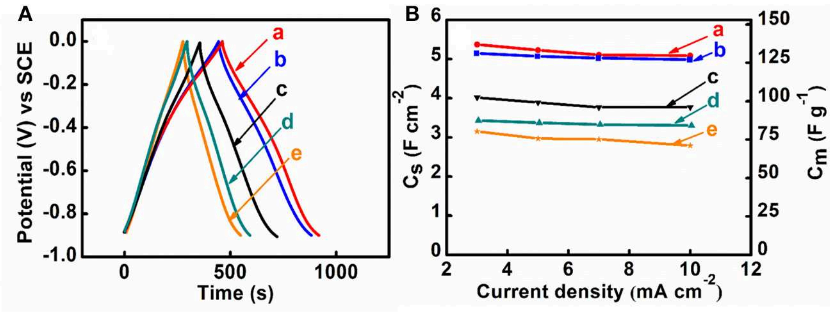

**FIGURE 7 | (A)** Charge-discharge curves at current density of 5 mA $cm^{-2}$, **(B)** capacitance, calculated from charge-discharge data, vs. current density for (a) M-CB-MWCNT, (b) M-FH-CB-MWCNT, (c) M-PV-MWCNT, (d) M-AA-MWCNT and (e) M-CP-MWCNT.

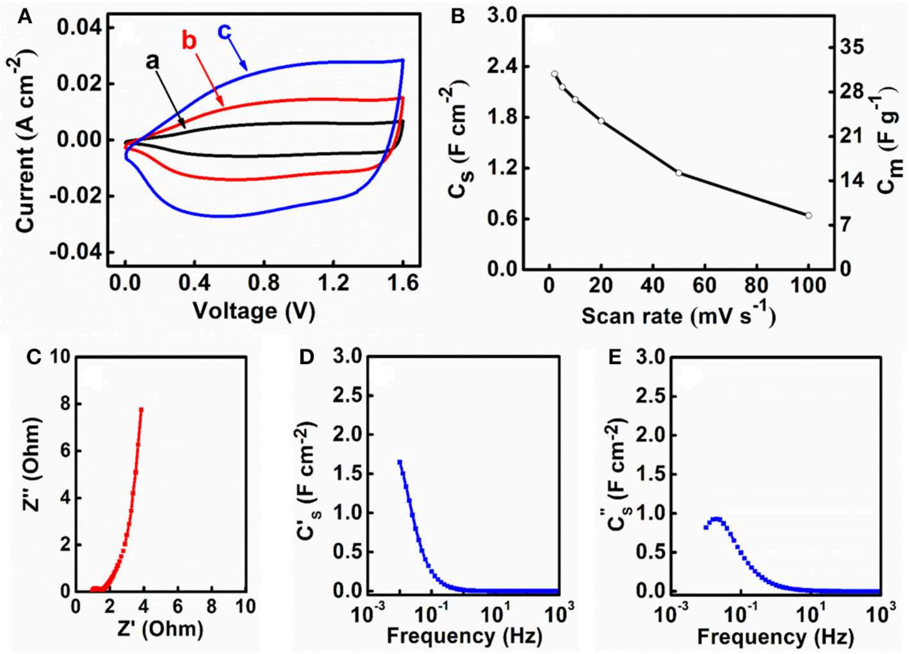

**FIGURE 8 | (A)** CVs at scan rates of (a) 2, (b) 5 and (c) 10 mV $s^{-1}$, **(B)** $C_S$ and $C_m$ calculated from the CV data vs. scan rate, **(C)** Nyquist plot of complex impedance and frequency dependences of **(D)** $C'_S$ and **(E)** $C''_S$ for an asymmetric supercapacitor cell, containing M-FH-CB-MWCNT as a negative electrode and $MnO_2$-MWCNT as a positive electrode.

cm$^{-2}$ was achieved using M-CP-MWCNT. However, M-FH-CB-MWCNT showed benefits of nearly constant capacitance in the range of 3–10 mA cm$^{-2}$. The M-CP-MWCNT and M-FH-CB-MWCNT electrodes showed practically the same capacitances at 5 and 10 mA cm$^{-2}$. The M-CP-MWCNT electrodes showed significantly lower capacitance, compared to other electrodes in agreement with CV and impedance spectroscopy data.

M-FH-CB-MWCNT electrodes were used for the fabrication of the asymmetric supercapacitor cells. One of the problems related to the fabrication of asymmetric devices with $Na_2SO_4$ electrolyte is related to lower capacitance of negative electrodes, compared to the capacitance of advanced positive electrodes, such as $MnO_2$-MWCNT (Chen et al., 2017). However, M-FH-CB-MWCNT electrodes showed relatively high capacitance and the asymmetric device was fabricated using 40 mg cm$^{-2}$ M-FH-CB-MWCNT negative electrode and 35 mg cm$^{-2}$ $MnO_2$-MWCNT positive electrode. It is known that aqueous asymmetric devices based on $Fe_3O_4$ negative electrodes and $MnO_2$ positive electrodes (Brousse and Bélanger, 2003) can operate in a voltage window of 1.8. Water decomposition can be avoided due to overpotential for oxygen evolution. **Figure 8A** shows CVs for the device in a voltage window of 1.6 V. The current increased with increasing scan rate. As expected, the capacitance $C_S$ of the device was about 50% of the capacitance of the individual electrodes (**Figure 8B**). The device showed relatively low impedance and relatively high relaxation frequency (**Figures 8C–E**). The asymmetric devices showed ideal triangular shape charge-discharge curves (**Figure 9A**, inset). The capacitance slightly decreased (**Figure 9A**) with current density in the range of 3-50 mA cm$^{-2}$. The capacitance retention after 1,000 cycles was 75% (**Figure 9B**). The Coulombic efficiency remained about 100% during cycling. The device had an energy density of about 1 mWh cm$^{-2}$ which showed relatively small variations with increasing current density in the range of 3–50 mA cm$^{-2}$ (**Figure 9C**). Two cells, connected in series, allowed for the powering of eleven 20 mA LEDs, as it is shown in **Figure 9D**.

## CONCLUSIONS

Polyaromatic CB, PV, AA, and CP molecules allowed for efficient dispersion of MWCNT. The chelating catechol groups of CB and PV as well as electrostatic attraction of cationic CB and AA with negatively charged $Fe_3O_4$ particles were beneficial for the formation of $Fe_3O_4$ decorated MWCNT. M-CB-MWCNT showed a network of $Fe_3O_4$ decorated MWCNT and low agglomeration of $Fe_3O_4$ nanoparticles. M-CB-MWCNT exhibited higher capacitance, compared to M-PV-MWCNT, M-AA-MWCNT and M-CP-MWCNT. Compared to M-CB-MWCNT, the M-FH-CB-MWCNT electrodes showed improved CV profile, reduced AC energy losses and low variation of capacitance with increasing charge-discharge current.

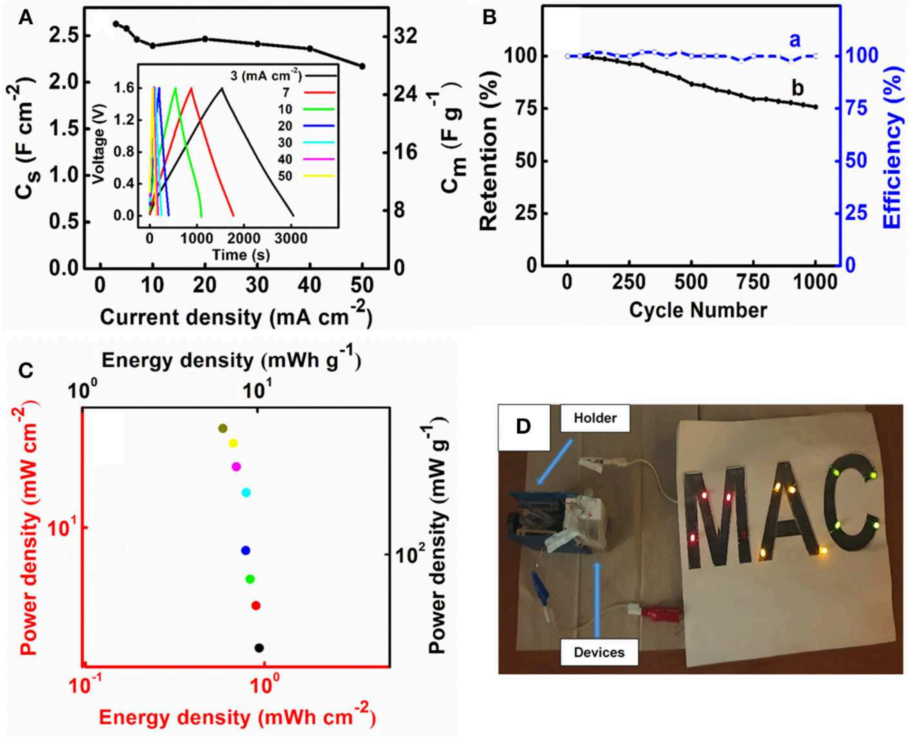

**FIGURE 9 | (A)** $C_S$ and $C_m$ vs. current density calculated from discharge data, inset shows charge-discharge curves, and different current densities, **(B)** (a) Coulombic efficiency and (b) capacitance retention and vs. cycle number, **(C)** Ragone plot for an asymmetric supercapacitor cell, containing M-FH-CB-MWCNT as a negative electrode and $MnO_2$-MWCNT as a positive electrode, **(D)** LEDs powered by two asymmetric cells.

M-FH-CB-MWCNT showed good capacitive behavior at mass loading of 40 mg $\mathrm{cm}^{-2}$. Asymmetric devices were fabricated, containing M-FH-CB-MWCNT negative electrodes and $MnO_2$-MWCNT positive electrodes, which showed promising capacitance and power-energy characteristics.

## DATA AVAILABILITY STATEMENT

The datasets generated for this study are available on request to the corresponding author.

## AUTHOR CONTRIBUTIONS

MN conducted synthesis of materials, performed materials characterization and electrochemical testing, analysis of the data and contributed to the writing of the manuscript. RS contributed to DLS and electron microscopy testing, data analysis, and writing of the manuscript. IZ contributed to the development of new dispersants, cell design. IP and IZ contributed to the data analysis and writing of the manuscript.

## FUNDING

This work was supported by the Natural Sciences and Engineering Research Council of Canada.

## ACKNOWLEDGMENTS

The authors would like to thank the Natural Sciences and Engineering Research Council of Canada for the financial support. Dr. Carmen Andrei of Canadian Centre for Electron Microscopy (CCEM), M.A.Sc. Victoria Jarvis of McMaster Analytical X-Ray Diffraction Facility for XRD for assistance with measurements, and Dr. R. Poon for fruitful discussions and technical support.

## SUPPLEMENTARY MATERIAL

The Supplementary Material for this article can be found online at: https://www.frontiersin.org/articles/10.3389/fenrg.2020.00046/full#supplementary-material

## REFERENCES

Ata, M., Liu, Y., and Zhitomirsky, I. (2014). A review of new methods of surface chemical modification, dispersion and electrophoretic deposition of metal oxide particles. *RSC Adv.* 4, 22716–22732. doi: 10.1039/c4ra02218a

Ata, M. S., Poon, R., Syed, A. M., Milne, J., and Zhitomirsky, I. (2018). New developments in non-covalent surface modification, dispersion and electrophoretic deposition of carbon nanotubes. *Carbon* 130, 584–598. doi: 10.1016/j.carbon.2018.01.066

Brousse, T., and Bélanger, D. (2003). A hybrid fe3o4-mno2 capacitor in mild aqueous electrolyte. *Electrochem Solid-State Lett.* 6, A244–A248. doi: 10.1149/1.1614451

Chen, R., Poon, R., Sahu, R. P., Puri, I. K., and Zhitomirsky, I. (2017). Mno2-carbon nanotube electrodes for supercapacitors with high active mass loadings. *J. Electrochem. Soc.* 164, A1673–A1678. doi: 10.1149/2.1491707jes

Chen, R., Puri, I., and Zhitomirsky, I. (2019). Polypyrrole-carbon nanotube-feooh composites for negative electrodes of asymmetric supercapacitors. *J. Electrochem. Soc.* 166, A935–A940. doi: 10.1149/2.0281906jes

Chen, R., Puri, I. K., and Zhitomirsky, I. (2018). High areal capacitance of feooh-carbon nanotube negative electrodes for asymmetric supercapacitors. *Ceram. Int.* 44, 18007–18015. doi: 10.1016/j.ceramint.2018.07.002

Chitturi, V. R., Ara, M., Fawaz, W., Ng, K. Y. S., and Arava, L. M. R. (2016). Enhanced lithium–oxygen battery performances with pt subnanocluster decorated n-doped single-walled carbon nanotube cathodes. *ACS Catal.* 6, 7088–7097. doi: 10.1021/acscatal.6b01016

Ding, H., Zhang, Q., Liu, Z., Wang, J., Ma, R., Fan, L., et al. (2018). Tio2 quantum dots decorated multi-walled carbon nanotubes as the multifunctional separator for highly stable lithium sulfur batteries. *Electrochim. Acta* 284, 314–320. doi: 10.1016/j.electacta.2018.07.167

Ding, Y., Wang, T., Dong, D., and Zhang, Y. (2020). Using biochar and coal as the electrode material for supercapacitor applications. *Front. Energy Res.* 7:159. doi: 10.3389/fenrg.2019.00159

Hao, M., Tang, M., Wang, W., Tian, M., Zhang, L., and Lu, Y. (2016). Silver-nanoparticle-decorated multiwalled carbon nanotubes prepared by poly (dopamine) functionalization and ultraviolet irradiation. *Compos. B. Eng.* 95, 395–403. doi: 10.1016/j.compositesb.2016.03.084

Hong, H. P., Kim, M. S., Lee, Y. H., Yu, J. S., Lee, C. J., and Min, N. K. (2013). Spray deposition of limn2o4 nanoparticle-decorated multiwalled carbon nanotube films as cathode material for lithium-ion batteries. *Thin Solid Films* 547, 68–71. doi: 10.1016/j.tsf.2013.05.002

Imbrogno, A., Pandiyan, R., Barberio, M., Macario, A., Bonanno, A., and El khakani, M. A. (2017). Pulsed-laser-ablation based nanodecoration of multi-wall-carbon nanotubes by co-ni nanoparticles for dye-sensitized solar cell counter electrode applications. *Mater. Renewable Sustainable Energy* 6:11. doi: 10.1007/s40243-017-0095-3

Li, X., Huang, Z., and Zhi, C. (2019). Environmental stability of mxenes as energy storage materials. *Front. Mater.* 6:312. doi: 10.3389/fmats.2019.00312

Lu, Z., Raad, R., Safaei, F., Xi, J., Liu, Z., and Foroughi, J. (2019). Carbon nanotube based fiber supercapacitor as wearable energy storage. *Front. Mater.* 6:138. doi: 10.3389/fmats.2019.00138

Luo, D., Wallar, C. J., Shi, K., and Zhitomirsky, I. (2016). Enhanced capacitive performance of mno2-multiwalled carbon nanotube electrodes, prepared using lauryl gallate dispersant. *Colloids Surfaces A* 509, 504–511. doi: 10.1016/j.colsurfa.2016.09.065

Mathew, A., Rao, G. M., and Munichandraiah, N. (2011). Dye sensitized solar cell based on platinum decorated multiwall carbon nanotubes as catalytic layer on the counter electrode. *Mater. Res. Bull.* 46, 2045–2049. doi: 10.1016/j.materresbull.2011.07.001

Noorbakhsh, A., Salimi, A., and Sharifi, E. (2008). Fabrication of glucose biosensor based on encapsulation of glucose-oxidase on sol-gel composite at the surface of glassy carbon electrode modified with carbon nanotubes and celestine blue. *Electroanalysis* 20, 1788–1797. doi: 10.1002/elan.200804245

Ojha, M., Le Houx, J., Mukkabla, R., Kramer, D., Andrew Wills, R. G., and Deepa, M. (2019). Lithium titanate/pyrenecarboxylic acid decorated carbon nanotubes hybrid - alginate gel supercapacitor. *Electrochim. Acta* 309, 253–263. doi: 10.1016/j.electacta.2019.03.211

Pan, Y., Hu, W., Liu, D., Liu, Y., and Liu, C. (2015). Carbon nanotubes decorated with nickel phosphide nanoparticles as efficient nanohybrid electrocatalysts for the hydrogen evolution reaction. *J. Mater. Chem. A* 3, 13087–13094. doi: 10.1039/C5TA02128F

Parks, G. A. (1965). The isoelectric points of solid oxides, solid hydroxides, and aqueous hydroxo complex systems. *Chem. Rev.* 65, 177–198. doi: 10.1021/cr60234a002

Pavaskar, G., Ramakrishnasubramanian, K., Kandagal, V. S., and Kumar, P. (2018). Modeling electric double-layer capacitors using charge variation methodology in gibbs ensemble. *Front. Energy Res.* 5:36. doi: 10.3389/fenrg.2017.00036

Salinas Torres, D., Ruiz-Rosas, R., Morallon, E., and Cazorla-Amorós, D. (2019). Strategies to enhance the performance of electrochemical capacitors based on carbon materials. *Front. Mater.* 6:115. doi: 10.3389/fmats.2019.00115

Shi, C., and Zhitomirsky, I. (2010). Electrodeposition and capacitive behavior of films for electrodes of electrochemical supercapacitors. *Nanoscale Res. Lett.* 5:518. doi: 10.1007/s11671-009-9519-z

Shi, K., Ren, M., and Zhitomirsky, I. (2014). Activated carbon-coated carbon nanotubes for energy storage in supercapacitors and capacitive water purification. *ACS Sustain. Chem. Eng.* 2, 1289–1298. doi: 10.1021/sc500118r

Shi, K., and Zhitomirsky, I. (2013). Electrophoretic nanotechnology of graphene–carbon nanotube and graphene–polypyrrole nanofiber composites for electrochemical supercapacitors. *J. Colloid Interface Sci.* 407, 474–481. doi: 10.1016/j.jcis.2013.06.058

Silva, R. M. E., Poon, R., Milne, J., Syed, A., and Zhitomirsky, I. (2018). New developments in liquid-liquid extraction, surface modification and agglomerate-free processing of inorganic particles. *Adv. Colloid Interface Sci.* 261, 15–27. doi: 10.1016/j.cis.2018.09.005

Sonkar, P. K., Prakash, K., Yadav, M., Ganesan, V., Sankar, M., Gupta, R., et al. (2017). Co(ii)-porphyrin-decorated carbon nanotubes as catalysts for oxygen reduction reactions: An approach for fuel cell improvement. *J. Mater. Chem. A* 5, 6263–6276. doi: 10.1039/C6TA10482G

Su, Y., and Zhitomirsky, I. (2015). Asymmetric electrochemical supercapacitor, based on polypyrrole coated carbon nanotube electrodes. *Appl. Energy* 153, 48–55. doi: 10.1016/j.apenergy.2014.12.010

Tai, S.-Y., Lu, M.-N., Ho, H.-P., Xiao, Y., and Lin, J.-Y. (2014). Investigation of carbon nanotubes decorated with cobalt sulfides of different phases as nanocomposite catalysts in dye-sensitized solar cells. *Electrochim. Acta* 143, 216–221. doi: 10.1016/j.electacta.2014.07.145

Wang, T., Kaempgen, M., Nopphawan, P., Wee, G., Mhaisalkar, S., and Srinivasan, M. (2010). Silver nanoparticle-decorated carbon nanotubes as bifunctional gas-diffusion electrodes for zinc-air batteries. *J. Power Sources* 195, 4350–4355. doi: 10.1016/j.jpowsour.2009.12.137

Wei, W., Ruiz, I., Ahmed, K., Bay, H. H., George, A. S., Wang, J., et al. (2014). Silicon decorated cone shaped carbon nanotube clusters for lithium ion battery anodes. *Small* 10, 3389–3396. doi: 10.1002/smll.201400088

Xing, Z., Deng, Y.-P., Sy, S., Tan, G., Li, A., Li, J., et al. (2019). Carbon-pore-sheathed cobalt nanoseeds: an exceptional and durable bifunctional catalyst for zinc-air batteries. *Nano Energy* 65, 104051. doi: 10.1016/j.nanoen.2019.104051

Xing, Z., Qi, Y., Tian, Z., Xu, J., Yuan, Y., Bommier, C., et al. (2017). Identify the removable substructure in carbon activation. *Chem. Mater.* 29, 7288–7295. doi: 10.1021/acs.chemmater.7b01937

Xing, Z., Wang, B., Halsted, J. K., Subashchandrabose, R., Stickle, W. F., and Ji, X. (2015). Direct fabrication of nanoporous graphene from graphene oxide by adding a gasification agent to a magnesiothermic reaction. *Chem. Commun.* 51, 1969–1971. doi: 10.1039/C4CC08977D

Zhao, C., and Zheng, W. (2015). A review for aqueous electrochemical supercapacitors. *Front. Energy Res.* 3:23. doi: 10.3389/fenrg.2015.00023

Zhu, Y., Shi, K., and Zhitomirsky, I. (2014). Polypyrrole coated carbon nanotubes for supercapacitor devices with enhanced electrochemical performance. *J. Power Sources* 268, 233–239. doi: 10.1016/j.jpowsour.2014.06.046

**Conflict of Interest:** The authors declare that the research was conducted in the absence of any commercial or financial relationships that could be construed as a potential conflict of interest.

The handling editor declared a past co-authorship with one of the authors IZ.

frontiers in Energy Research

BRIEF RESEARCH REPORT
published: 22 April 2020
doi: 10.3389/fenrg.2020.00060

# Rh-Decorated Three-Dimensional Graphene Aerogel Networks as Highly-Efficient Electrocatalysts for Direct Methanol Fuel Cells

*Ying Yang*[†], *Yuexin Song*[†], *Hao Sun, Danyang Xiang, Quanguo Jiang, Zhiyong Lu, Haiyan He and Huajie Huang*[*]

*College of Mechanics and Materials, Hohai University, Nanjing, China*

The exploration and development of highly-efficient Pt-alternative catalysts with acceptable costs are very essential for the large-scale commercial applications of direct methanol fuel cell (DMFC) technology. Herein, we demonstrate a facile and cost-effective self-assembly approach to the bottom-up fabrication of Rh-decorated three-dimensional graphene aerogel (Rh/3D-GA) networks as efficient DMFC anode catalysts. With the distinct textural features including large surface area, 3D porous structure, uniform Rh dispersion, and good electron conductivity, the resultant Rh/3D-GA hybrid architecture shows superior electrocatalytic properties toward methanol oxidation reaction, such as large electrochemically active surface area, low onset potential, high mass activity as well as excellent long-term stability, all of which are more competitive than those of Rh catalysts deposited on conventional carbon black, carbon nanotubes, and two-dimensional graphene supports.

**Keywords: Rhodium, graphene aerogel, three-dimensional networks, electrocatalyst, fuel cells**

***Edited by:***
*Kaiyuan Shi,*
*National Research Council*
*Canada, Canada*

***Reviewed by:***
*Xifei Li,*
*Xi'an University of Technology, China*
*Babak Shalchi Amirkhiz,*
*Department of Natural*
*Resources, Canada*

***Correspondence:***
*Huajie Huang*
*huanghuajie@hhu.edu.cn*

[†] *These authors have contributed equally to this work*

***Specialty section:***
*This article was submitted to*
*Electrochemical Energy Conversion*
*and Storage,*
*a section of the journal*
*Frontiers in Energy Research*

***Received:*** *14 February 2020*
***Accepted:*** *30 March 2020*
***Published:*** *22 April 2020*

***Citation:***
*Yang Y, Song Y, Sun H, Xiang D, Jiang Q, Lu Z, He H and Huang H (2020) Rh-Decorated Three-Dimensional Graphene Aerogel Networks as Highly-Efficient Electrocatalysts for Direct Methanol Fuel Cells. Front. Energy Res. 8:60. doi: 10.3389/fenrg.2020.00060*

## INTRODUCTION

Since the problem of energy crisis and environment pollution is becoming more and more severe, fuel cells have attracted considerable attention as advanced energy-conversion systems because of their high energy-utilization efficiency and low pollutant emission properties (Chu and Majumdar, 2012). Among different types of fuel cells, direct methanol fuel cells (DMFCs) have many distinct advantages, such as simple device construction, low working temperature, and convenient storage and transport of methanol, which have been regarded as ideal power generators for a variety of applications, including aeronautics and astronautics, electric vehicles as well as portable electronic devices (Huang and Wang, 2014). Notably, the occurrence of methanol oxidation reaction with slow kinetic rate on the anode requires highly-active electrocatalysts, which largely determine the energy density and power density of the DMFC devices (Debe, 2012).

As is well-known, platinum (Pt) is the most popular electrode catalyst for DMFCs due to its unique electrocatalytic ability for methanol oxidation reaction (Huang et al., 2014; Yang et al., 2019). However, the scarcity and poor poison tolerance of Pt-based catalysts commonly render high manufacturing costs and short lifespan of DMFCs, which remain the critical obstacles impeding their large-scale commercial applications (Chang et al., 2014; Huang et al., 2017a). Within this context, highly-active non-platinum electrocatalysts with acceptable costs have been widely studied by many researchers (Fu et al., 2018; Yang et al., 2020). Among various current Pt-alternative materials, Rhodium (Rh) nanocrystals have recently become a hot topic of interest owing to their exceptional methanol oxidation activity as well as greater resistance to byproducts (mainly CO) in alkaline medium (Han et al., 2018; Kang et al., 2018; Li F. et al., 2018). Nevertheless, similar to other noble metals, the electrocatalytic properties of Rh nanocrystals are strongly dependent on their size and morphology, thereby the rational design and controllable synthesis of small-sized and well-dispersed Rh catalysts are highly desirable.

To achieve a high utilization efficiency of noble metal nanocrystals, one effective method is to deposit them onto various carbonaceous supports, such as carbon black (Zhang et al., 2015), carbon nanotubes (Zhang et al., 2018), porous carbons (Gao et al., 2018), and graphene (Shen et al., 2018; Huang et al., 2019). In particular, graphene-supported noble metal catalysts usually possess superior electrocatalytic performance toward methanol oxidation owing to their large surface area, high electron conductivity, and good electrochemical stability (Huang et al., 2016; Zhou et al., 2016). However, two-dimensional (2D) graphene-based materials are prone to re-aggregate or re-stack due to the van der Waals forces when they are extracted from solutions, a process during which the intrinsic physicochemical properties of the separated graphene layers would disappear (Yan et al., 2018). Meanwhile, a high proportion of catalytically active regions could be covered and cannot directly engage into the eletrocatalytic reaction, leading to a large loss of electrocatalytic activity (Li M. et al., 2018). To overcome this obstacle, great efforts have been made to the construction of three-dimensional (3D) graphene aerogel networks with cross-linked porous configuration, which can well-preserve the unique structural merits of separated graphene nanosheets and simultaneously promote the transportation of external electrolytes to the interior catalytic sites (Huang et al., 2015, 2017b; Zhang et al., 2016). However, up to now, the uniform growth of small-sized Rh nanocrystals onto 3D graphene aerogel networks still remains a challenge in this area.

Herein, we present a bottom-up approach to the large-scale fabrication of ultrafine Rh nanoparticles supported on 3D interconnected graphene aerogel networks as methanol oxidation catalysts via a solvothermal self-assembly process. As illustrated in **Supplementary Figure 1**, graphene oxide (GO) nanosheets were first produced from commercial graphite powders via an improved Hummers' method and then ultrasonically dispersed in ethylene glycol solution to reach a concentration of 2 mg $mL^{-1}$. Next, $Rh(NO_3)_3$ solution was slowly added into above GO suspension under magnetic stirring for 30 min. Subsequently, the resultant mixture was moved to a Teflon-lined stainless steel autoclave and kept at 160°C for 24 h. During the solvothermal reaction, the adjacent GO nanosheets with numerous oxygen functional groups were able to interconnect with each other, and at the same time Rh nanoparticles were gradually deposited on the carbon sheets, giving birth to the Rh/3D graphene aerogel (Rh/3D-GA) architecture. Benefiting from its large surface area, 3D porous frameworks, and homogeneous Rh dispersion, the resulting Rh/3D-GA architecture exhibits superior electrocatalytic properties toward methanol oxidation, including large electrochemically active surface area, high mass activity, and reliable long-term stability, all of which are more competitive than those of Rh/carbon black (Rh/C), Rh/CNT, and Rh/reduced graphene oxide (Rh/RGO) catalysts.

# EXPERIMENTAL

## Preparation of the Rh/3D-GA Architecture

First, GO nanosheets as starting materials were produced from natural graphite powders through an improved Hummers' method (Kovtyukhova et al., 1999). Then, 40 mg of GO nanosheets were dispersed in 10 mL water and 10 mL of ethylene glycol to form a stable dark brown solution with the help of ultrasonic treatment for 1 h. Afterwards, 0.076 mL of $Rh(NO_3)_3$ solution (1.28 M) was introduced into above GO solution under magnetic stirring for 30 min. Next, the resultant mixture was moved to a Teflon-lined stainless steel autoclave and heated at 160°C for 24 h. The as-derived product was dialyzed with pure water for 3 days and then freeze-dried to preserve its 3D porous networks, leading to the formation of the Rh/3D-GA architecture. As for the preparation of Rh particles supported by conventional carbon black (Vulcan XC-72R, Cabot Corp.), multiwalled CNTs (Chengdu Organic Chemicals Co., Ltd.), and RGO materials, 20 mg of carbon materials were dispersed in 40 mL water and 40 mL of ethylene glycol solution, and then the deposition of Rh nanoparticles on these carbon supports was realized by the similar synthesis approach. For fair comparison, the Rh contents of all above catalysts were kept at 20.0 wt%.

## Characterization

The 3D porous structure and Rh dispersion of the Rh/3D-GA architecture were observed by Field-emission scanning microscopy (FE-SEM, Hitachi S-4800) and transmission electron microscopy (TEM, JEOL 2100F). The crystal structures of various samples were analyzed by Powder X-ray diffraction (XRD, Bruker D8 Advance diffractometer). The elemental composition and chemical states of Rh/3D-GA were examined by X-ray photoelectron spectroscopy (XPS, PHI Quantera X-ray photoelectron spectrometer). Nitrogen adsorption–desorption tests were conducted on a Micromeritics ASAP 2020 Plus system at 77 K.

## Electrochemical Measurements

All electrochemical measurements were conducted on a CHI 760E electrochemical workstation by using a standard three-electrode configuration, where a 3 mm glassy carbon (GC) disk with active electrocatalyst, a Pt wire, and a saturated calomel electrode (SCE) were served as the working, counter, and reference electrodes, respectively. The fabrication procedure for the working electrode is as follows: 5 mg of catalyst powder was dispersed into a mixed solution (2,375 μL of ethanol, 2,375 μL of water, and 250 μL of 5% Nafion) via ultrasonic treatment for 1 h. Subsequently, 10 μL of above catalyst dispersion was carefully pipetted onto a GC electrode surface and then directly dried in air. Therefore, the Rh loading amount on

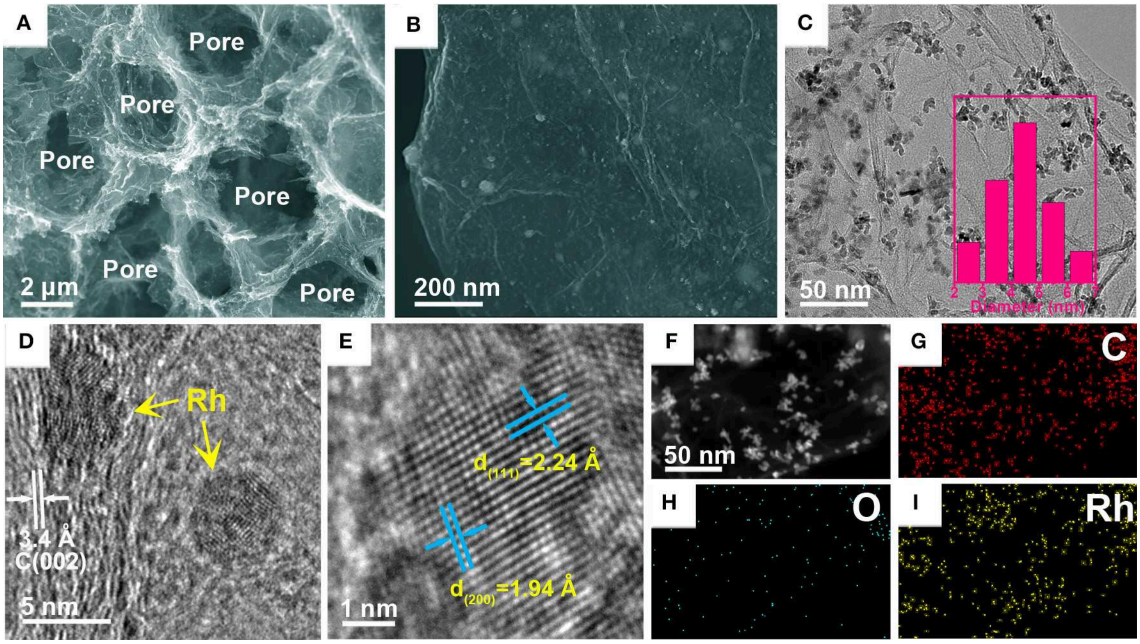

**FIGURE 1 |** Representative **(A,B)** FE-SEM, **(C)** TEM, and **(D,E)** HRTEM images of the Rh/3D-GA architecture. The inset in **(C)** is the Rh size distribution. **(F)** HAADF–STEM image and the corresponding elemental mapping analysis of **(G)** C, **(H)** O, and **(I)** Rh elements of a Rh-decorated graphene nanosheet.

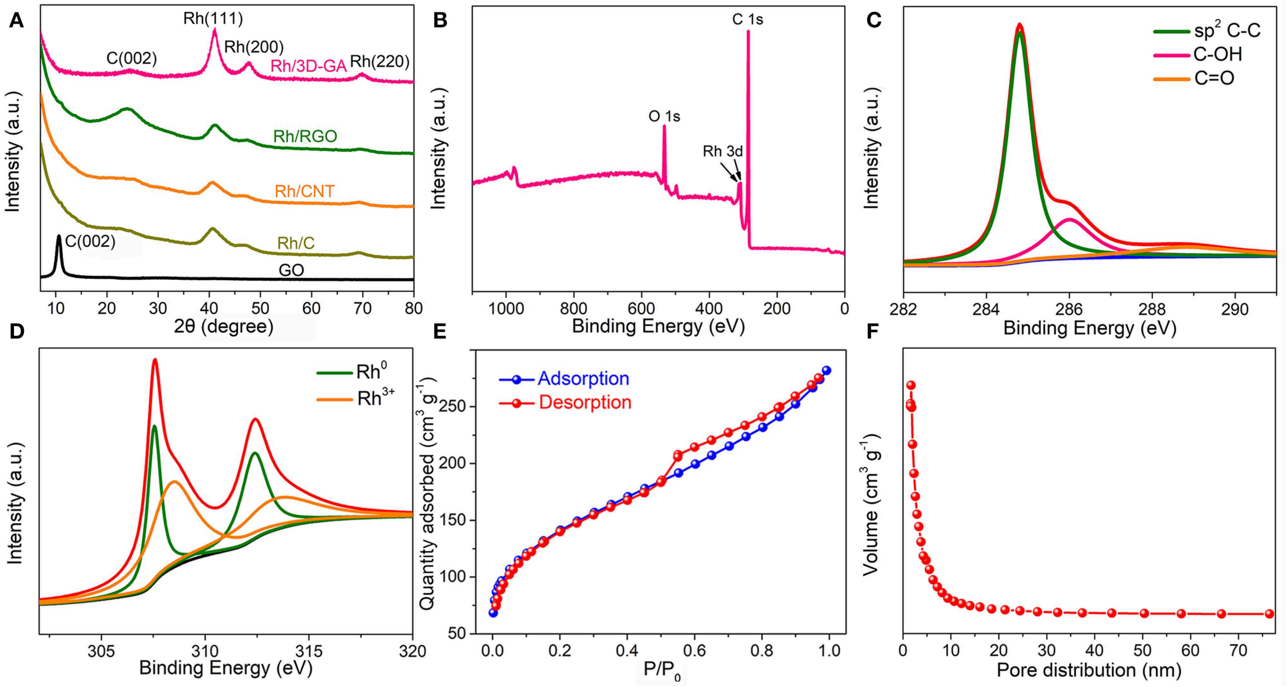

**FIGURE 2 | (A)** Typical XRD patterns of the Rh/3D-GA, Rh/RGO, Rh/CNT, Rh/C, and GO materials. **(B)** XPS survey, **(C)** C 1s, and **(D)** Rh 3d spectra of the Rh/3D-GA architecture. **(E)** Nitrogen adsorption–desorption isotherm and **(F)** pore size distribution of the Rh/3D-GA architecture.

the working electrode surface was kept at 0.028 mg cm$^{-2}$. The electrocatalytic properties of the Rh/3D-GA architecture and other reference catalysts were systematically investigated by cyclic voltammograms, chronoamperometry, and AC impedance techniques.

## RESULTS AND DISCUSSION

The 3D porous structure and morphology of the as-obtained Rh/3D-GA architecture were first observed by FE-SEM and TEM. As shown in **Figure 1A**, typical FE-SEM image

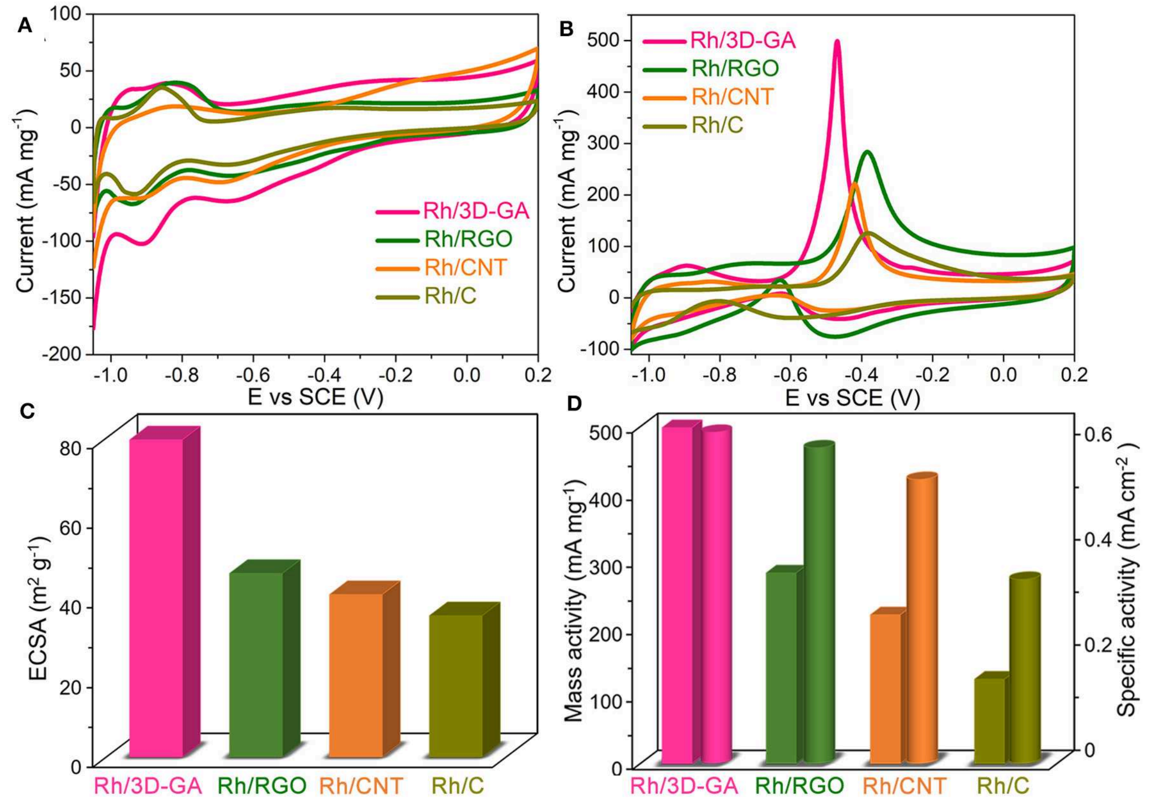

**FIGURE 3 |** CV curves of the Rh/3D-GA, Rh/RGO, Rh/CNT, and Rh/C electrodes recorded in **(A)** 1 M KOH and **(B)** 1 M KOH with 1 M $CH_3OH$ solution at 50 mV $s^{-1}$. **(C)** Specific ECSA values and **(D)** mass activity as well as specific activity (normalized by ECSA) for these four catalysts.

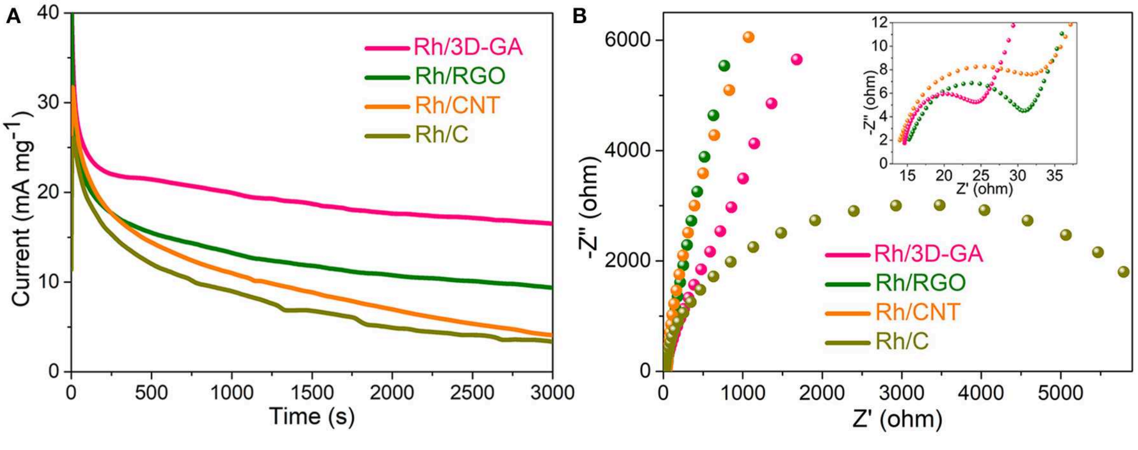

**FIGURE 4 | (A)** Chronoamperometric curves of the Rh/3D-GA, Rh/RGO, Rh/CNT, and Rh/C electrodes recorded in 1 M KOH with 1 M $CH_3OH$ solution at −0.5 V. **(B)** AC impedance spectra of the above four catalysts in 1 M KOH with 1 M $CH_3OH$ solution tested at open circuit potentials with an amplitude of 10 mV.

discloses that Rh/3D-GA possesses well-defined 3D cross-linked networks with consecutive macropores ranging from hundreds of nanometers to several micrometers. Such a 3D porous configuration can not only hamper the re-aggregation and re-stacking of graphene nanosheets, but also provides multilevel growth platforms for the deposition of Rh nanoparticles. Clearly, high-magnification FE-SEM and TEM images confirm that the ultrathin graphene sheets are decorated uniformly with a large number of Rh nanoparticles with an average diameter of about 4.3 nm (**Figures 1B,C**), which is close to that of previously reported Pt and Pd particles supported by nanocarbon matrixes (Li et al., 2012; Qian et al., 2015). Moreover, with the help of high-resolution TEM (**Figures 1D,E**), typical lattice fringes with crystal plane distance of 0.34 nm can be observed, which corresponds to the carbon (002) plane of few-layer graphene nanosheets. Meanwhile, the interplane spacings on Rh nanoparticles were determined to be 0.22 and 0.19 nm, consistent with the data for the (111) and (200) planes of cubic Rh crystals, respectively. Furthermore, high-angle annular dark-field-scanning TEM (HAADF-STEM) and element mapping analysis reveal that the Rh/3D-GA architecture consists of C, Rh, and a smaller amount of O components (**Figures 1F–I** and **Supplementary Figure 2**), which are distributed homogeneously throughout the whole sheets.

Powder XRD and XPS analysis were then carried out to study the detailed crystalline structure and elemental composition of the Rh/3D-GA architecture. As depicted in **Figure 2A**, the prominent C (002) diffraction peak of pristine GO centered at $2\theta = 10.5^\circ$ shifted to a much higher angle of $2\theta = 25.5^\circ$ in the Rh/3D-GA and Rh/RGO patterns, implying the successful transformation of GO to graphene. In addition, other four diffraction peaks located at $2\theta = 41.0^\circ$, $47.8^\circ$, $69.9^\circ$, and $84.1^\circ$ are also visible, which can be indexed to the (111), (200), (220), and (311) planes of the face centered-cubic (fcc) Rh nanocrystals. Remarkably, the above four peaks in the Rh/3D-GA pattern are more intensive than those in the Rh/RGO, Rh/CNT, and Rh/C patterns, indicating that the use of 3D graphene aerogel networks as supporting materials can promote the nucleation and crystallization of Rh nanoparticles. **Figure 2B** shows the typical XPS survey spectrum of Rh/3D-GA catalyst, where the C 1s, O 1s, and Rh 3d signals were detected, consistent with the EDX results (**Supplementary Figure 3**). Moreover, the high-resolution C 1s XPS spectrum unravels that there are three kinds of C species in the Rh/3D-GA catalyst, including $sp^2$ C–C, C-OH, and C=O groups at the binding energies of 284.8, 286.1, and 288.4 eV, respectively (**Figure 2C**). Apparently, the peak intensities for the C-OH and C=O groups in Rh/3D-GA spectrum are much lower than those in GO spectrum (**Supplementary Figure 4**), proving again the efficient reduction of GO during the solvothermal process. Besides, the deconvoluted Rh 3d spectrum in **Figure 2D** suggests two chemical states of Rh in the sample: the two intensive peaks at 307.5 and 312.4 eV are related to metal Rh, while the two weak peaks at 308.4 and 313.4 eV belong to Rh oxide. Brunauer–Emmett–Teller (BET) analysis further demonstrates that the Rh/3D-GA architecture with meso- and macroporous features has a high BET surface area of 485.0 $m^2$ $g^{-1}$ (**Figures 2E,F**), in accord with that reported for 3D graphene nanomaterials (Huang and Wang, 2014).

Inspired by the 3D porous graphene structure as well as the well-dispersive Rh nanocrystals, a series of electrochemical measurements were performed to systematically investigate the electrocatalytic properties of Rh/3D-GA architecture toward methanol oxidation reaction in alkaline medium, together with those of the Rh/RGO, Rh/CNT, and Rh/C catalysts for comparison. **Figure 3A** presents the cyclic voltammetry (CV) curves of the four electrodes recorded in 1 M KOH solution. It can be seen that all these CV curves exhibit characteristic hydrogen adsorption/desorption peaks in the potential region from −0.75 to −1.05 V (vs. SCE), which can be employed to evaluate the electrochemical active surface areas (ECSAs) for Rh-based catalysts. As calculated, the ECSA value for the Rh/3D-GA electrode is found to be 79.6 $m^2$ $g^{-1}$, which is about 1.7, 2.0, and 2.2 times larger than that of Rh/RGO (46.1 $m^2$ $g^{-1}$), Rh/CNT (40.8 $m^2$ $g^{-1}$), and Rh/C (35.5 $m^2$ $g^{-1}$) electrodes, respectively, indicating that the existence of 3D interconnected networks in Rh/3D-GA catalyst is very favorable for the exposure of catalytically active Rh sites. In the presence of 1 M KOH and 1 M $CH_3OH$ solution, the intensive current peaks appeared in the forward scans of the CV curves arise from the methanol oxidation, while the relatively weak current peaks in the reverse scan is due to the oxidative removal of the absorbed CO species (**Figure 3B**). Clearly, a very high forward peak current density (498.9 mA $mg^{-1}$) and high ECSA-normalized specific activity (0.63 mA $cm^{-2}$) are achieved on the Rh/3D-GA electrode (**Figures 3C,D**), which are higher than those on the reference electrodes (125.7–283.4 mA $mg^{-1}$ and 0.35–0.59 mA $cm^{-2}$, respectively). Furthermore, both the ECSA and mass activity of our Rh/3D-GA catalyst are superior to those of commercial 20% Pt/C catalyst (**Supplementary Figure 5**) and recent state-of-the-art Rh-based nanostructures, such as Rh nanosheets/graphene (Kang et al., 2017), Rh nanodendrites (Kang et al., 2016), and PtRh alloy (Bai et al., 2018), demonstrating that Rh/3D-GA is a highly promising anode catalyst for DMFCs.

Long-term durability of an electrocatalyst is another key performance indicator for its industrial applications. In this aspect, chronoamperometric technique was used to assess the long-term stability of Rh catalysts supported by different supports (**Figure 4A**). With a constant electrode potential, it can be clearly seen that the methanol oxidation currents on all electrodes gradually decrease as the time goes on, which should be ascribed to the accumulation of CO poisoning species on the Rh sites as well as the generation of Rh agglomerations in the architecture system. Among these investigated electrodes, the Rh/3D-GA electrode showed the slowest current decay rate and maintained the highest activity over 3,000 s, giving the best catalytic stability for methanol electrooxidation. The significantly improved durability of Rh/3D-GA catalyst should be attributed to the strong interaction between Rh and 3D-GA networks, which could prevent the Rh particles from agglomeration, dissolution, or Ostwald ripening during the catalytic process.

In order to gain more insights into the electron conductivity of various catalysts, we further conducted the AC impedance measurements to compare the charge-transfer rates. As shown in **Figure 4B**, the Nyquist plots of all these electrodes possess a depressed semiarc in the high frequency range, which is commonly employed to evaluate the catalyst's charge-transfer resistance. Based on the equivalent circuit displayed in **Supplementary Figure 6**, the charge-transfer resistance of Rh/3D-GA catalyst was estimated to be only 9.1 $\Omega$, much lower than that of Rh/RGO (18.0 $\Omega$), Rh/CNT (20.1 $\Omega$), and Rh/C (6519.0 $\Omega$) catalysts, testifying that the 3D cross-linked graphene networks could serve as efficient pathways for charge transportation. The excellent electronic conductivity of Rh/3D-GA is able to offer a large population of the triple-phase boundaries in the catalytic system, which is very conducive to boosting the electrochemical kinetics for methanol oxidation reaction.

## CONCLUSION

In summary, the bottom-up construction of Rh-decorated 3D graphene aerogel networks has been achieved through a solvothermal self-assembly approach. The resulting hybrid architecture has a series of structural advantages, such as large surface area, 3D interconnected carbon skeletons, uniform Rh dispersion, and high electron conductivity, which can not only provide a large number of catalytically active sites, but also allow a rapid transportation of ions and electrons during the electrocatalytic process. As a consequence, the Rh/3D-GA architecture shows large electrochemically active surface area, high mass activity as well as good long-term durability toward methanol oxidation reaction, superior to those of the Rh/RGO, Rh/CNT, and Rh/C catalysts synthesized by the same method. This study could provide new insights into the controllable synthesis of Pt-alternative catalysts supported by 3D porous carbon materials and facilitate their commercial applications in the electrocatalytic fields.

## DATA AVAILABILITY STATEMENT

The datasets generated for this study are available on request to the corresponding author.

## AUTHOR CONTRIBUTIONS

HHu conceived and designed the experiments. YY and YS conducted the experiments. HS, DX, QJ, ZL, and HHe recorded the structural characterization data. YY and HHu wrote the manuscript.

## FUNDING

This work was financially supported by the National Natural Science Foundation of China (51802077), the Fundamental Research Funds for the Central Universities (2019B16214), China Postdoctoral Science Foundation (Nos. 2015M580387 and 2016T90414), and Jiangsu Planned Projects for Postdoctoral Research Funds (No. 1601026A).

## SUPPLEMENTARY MATERIAL

The Supplementary Material for this article can be found online at: https://www.frontiersin.org/articles/10.3389/fenrg.2020.00060/full#supplementary-material

## REFERENCES

Bai, J., Xiao, X., Xue, Y. Y., Jiang, J. X., Zeng, J. H., Li, X. F., et al. (2018). Bimetallic Platinum-Rhodium alloy nanodendrites as highly active electrocatalyst for the ethanol oxidation reaction. *ACS Appl. Mater. Interfaces* 10, 19755–19763. doi: 10.1021/acsami.8b05422

Chang, J., Feng, L., Liu, C., Xing, W., and Hu, X. (2014). $Ni_2P$ enhances the activity and durability of the Pt anode catalyst in direct methanol fuel cells. *Energy Environ. Sci.* 7, 1628–1632. doi: 10.1039/c4ee00100a

Chu, S., and Majumdar, A. (2012). Opportunities and challenges for a sustainable energy future. *Nature* 488, 294–303. doi: 10.1038/nature11475

Debe, M. K. (2012). Electrocatalyst approaches and challenges for automotive fuel cells. *Nature* 486, 43–51. doi: 10.1038/nature11115

Fu, X., Zhao, Z., Wan, C., Wang, Y., Fan, Z., Song, F., et al. (2018). Ultrathin wavy Rh nanowires as highly effective electrocatalysts for methanol oxidation reaction with ultrahigh ECSA. *Nano Res.* 12, 211–215. doi: 10.1007/s12274-018-2204-8

Gao, Z., Li, M., Wang, J., Zhu, J., Zhao, X., Huang, H., et al. (2018). Pt nanocrystals grown on three-dimensional architectures made from graphene and $MoS_2$ nanosheets: highly efficient multifunctional electrocatalysts toward hydrogen evolution and methanol oxidation reactions. *Carbon* 139, 369–377. doi: 10.1016/j.carbon.2018.07.006

Han, S.-H., Liu, H.-M., Chen, P., Jiang, J.-X., and Chen, Y. (2018). Porous trimetallic PtRhCu cubic nanoboxes for ethanol electrooxidation. *Adv. Energy. Mater.* 8:1801326. doi: 10.1002/aenm.201801326

Huang, H., Ma, L., Tiwary, C. S., Jiang, Q., Yin, K., Zhou, W., et al. (2017a). Worm-shape Pt nanocrystals grown on nitrogen-doped low-defect graphene sheets: highly efficient electrocatalysts for methanol oxidation reaction. *Small.* 13:1603013. doi: 10.1002/smll.201603013

Huang, H., and Wang, X. (2014). Recent progress on carbon-based support materials for electrocatalysts of direct methanol fuel cells. *J. Mater. Chem. A.* 2, 6266–6291. doi: 10.1039/C3TA14754A

Huang, H., Yan, M., Yang, C., He, H., Jiang, Q., Yang, L., et al. (2019). Graphene nanoarchitectonics: recent advances in graphene-based electrocatalysts for hydrogen evolution reaction. *Adv. Mater.* 31:1903415. doi: 10.1002/adma.201903415

Huang, H., Yang, S., Vajtai, R., Wang, X., and Ajayan, P. M. (2014). Pt-decorated 3D architectures built from graphene and graphitic carbon nitride nanosheets as efficient methanol oxidation catalysts. *Adv. Mater.* 26, 5160–5165. doi: 10.1002/adma.201401877

Huang, H., Ye, G., Yang, S., Fei, H., Tiwary, C. S., Gong, Y., et al. (2015). Nanosized Pt anchored onto 3D nitrogen-doped graphene nanoribbons towards efficient methanol electrooxidation. *J. Mater. Chem. A* 3, 19696–19701. doi: 10.1039/C5TA05372B

Huang, H., Zhu, J., Li, D., Shen, C., Li, M., Zhang, X., et al. (2017b). Pt nanoparticles grown on 3D $RuO_2$-modified graphene architectures for highly efficient methanol oxidation. *J. Mater. Chem. A* 5, 4560–4567. doi: 10.1039/c6ta10548c

Huang, H., Zhu, J., Zhang, W., Tiwary, C. S., Zhang, J., Zhang, X., et al. (2016). Controllable codoping of nitrogen and sulfur in graphene for highly efficient Li-oxygen batteries and direct methanol fuel cells. *Chem. Mater.* 28, 1737–1745. doi: 10.1021/acs.chemmater.5b04654

Kang, Y., Li, F., Li, S., Ji, P., Zeng, J., Jiang, J., et al. (2016). Unexpected catalytic activity of rhodium nanodendrites with nanosheet subunits for methanol electrooxidation in an alkaline medium. *Nano Res.* 9, 3893–3902. doi: 10.1007/s12274-016-1258-8

Kang, Y., Xue, Q., Jin, P., Jiang, J., Zeng, J., and Chen, Y. (2017). Rhodium nanosheets–reduced graphene oxide hybrids: a highly active platinum-alternative electrocatalyst for the methanol oxidation reaction in alkaline media. *ACS Sustainable Chem. Eng.* 5, 10156–10162. doi: 10.1021/acssuschemeng.7b02163

Kang, Y. Q., Xue, Q., Zhao, Y., Li, X. F., Jin, P. J., and Chen, Y. (2018). Selective etching induced synthesis of hollow Rh nanospheres electrocatalyst for alcohol oxidation reactions. *Small* 14:1801239. doi: 10.1002/smll.201801239

Kovtyukhova, N. I., Ollivier, P. J., Martin, B. R., Mallouk, T. E., Chizhik, S. A., Buzaneva, E. V., et al. (1999). Layer-by-layer assembly of ultrathin composite films from micron-sized graphite oxide sheets and polycations. *Chem. Mater.* 11, 771–778. doi: 10.1021/Cm981085u

Li, F., Ding, Y., Xiao, X., Yin, S., Hu, M., Li, S., et al. (2018). From monometallic Au nanowires to trimetallic AuPtRh nanowires: interface control for the formic acid electrooxidation. *J. Mater. Chem. A* 6, 17164–17170. doi: 10.1039/c8ta05710a

Li, M., Jiang, Q., Yan, M., Wei, Y., Zong, J., Zhang, J., et al. (2018). Three-dimensional boron- and nitrogen-codoped graphene aerogel-supported Pt nanoparticles as highly active electrocatalysts for methanol oxidation reaction. *ACS Sustainable Chem. Eng.* 6, 6644–6653. doi: 10.1021/acssuschemeng.8b00425

Li, Y., Li, Y., Zhu, E., McLouth, T., Chiu, C. Y., Huang, X., et al. (2012). Stabilization of high-performance oxygen reduction reaction Pt electrocatalyst supported on reduced graphene oxide/carbon black composite. *J. Am. Chem. Soc.* 134, 12326–12329. doi: 10.1021/ja3031449

Qian, H., Huang, H., and Wang, X. (2015). Design and synthesis of palladium/graphitic carbon nitride/carbon black hybrids as high-performance catalysts for formic acid and methanol electrooxidation. *J. Power Sources* 275, 734–741. doi: 10.1016/j.jpowsour.2014.10.109

Shen, W., Ge, L., Sun, Y., Liao, F., Xu, L., Dang, Q., et al. (2018). Rhodium nanoparticles/F-doped graphene composites as multifunctional electrocatalyst superior to Pt/C for hydrogen evolution and formic acid oxidation reaction. *ACS Appl. Mater. Interfaces* 10, 33153–33161. doi: 10.1021/acsami.8b09297

Yan, M., Jiang, Q., Zhang, T., Wang, J., Yang, L., Lu, Z., et al. (2018). Three-dimensional low-defect carbon nanotube/nitrogen-doped graphene hybrid aerogel-supported Pt nanoparticles as efficient electrocatalysts toward the methanol oxidation reaction. *J. Mater. Chem. A* 6, 18165–18172. doi: 10.1039/C8TA05124K

Yang, C., Jiang, Q., Li, W., He, H., Yang, L., Lu, Z., et al. (2019). Ultrafine Pt nanoparticle-decorated 3D hybrid architectures built from reduced graphene oxide and MXene nanosheets for methanol oxidation. *Chem. Mater.* 31, 9277–9287. doi: 10.1021/acs.chemmater.9b02115

Yang, Y., Huang, H., Shen, B., Jin, L., Jiang, Q., Yang, L., et al. (2020). Anchoring nanosized Pd on three-dimensional boron- and nitrogen-codoped graphene aerogels as a highly active multifunctional electrocatalyst for formic acid and methanol oxidation reactions. *Inorg. Chem. Front.* 7, 700–708. doi: 10.1039/c9qi01448a

Zhang, F., Zhou, D., Zhang, Z., Zhou, M., and Wang, Q. (2015). Preparation of Rh/C and its high electro-catalytic activity for ethanol oxidation in alkaline media. *RSC Adv.* 5, 91829–91835. doi: 10.1039/c5ra16859g

Zhang, L. Y., Zhao, Z. L., Yuan, W. Y., and Li, C. M. (2016). Facile one-pot surfactant-free synthesis of uniform $Pd_6Co$ nanocrystals on 3D graphene as an efficient electrocatalyst toward formic acid oxidation. *Nanoscale* 8, 1905–1909. doi: 10.1039/c5nr08512h

Zhang, W., Zhang, X., Chen, L., Dai, J., Ding, Y., Ji, L., et al. (2018). Single-walled carbon nanotube induced optimized electron polarization of rhodium nanocrystals to develop an interface catalyst for highly efficient electrocatalysis. *ACS Catal.* 8, 8092–8099. doi: 10.1021/acscatal.8b02016

Zhou, Y., Hu, X.-C., Fan, Q., and Wen, H.-R. (2016). Three-dimensional crumpled graphene as an electro-catalyst support for formic acid electro-oxidation. *J. Mater. Chem. A* 4, 4587–4591. doi: 10.1039/C5TA09956K

**Conflict of Interest:** The authors declare that the research was conducted in the absence of any commercial or financial relationships that could be construed as a potential conflict of interest.

frontiers
in Energy Research

ORIGINAL RESEARCH
published: 23 April 2020
doi: 10.3389/fenrg.2020.00064

# 3D Carbon Networks Constructed $NaVPO_4F/C/rGO$ as a Cathode Material for High-Performance Sodium-Ion Batteries

**Jin-Zhi Guo [1]*, Ai-Bo Yang [2], Xin-Xin Zhao [2], Zhen-Yi Gu [1] and Xing-Long Wu [1,2]***

*[1] Key Laboratory for UV Light-Emitting Materials and Technology of Ministry of Education, Northeast Normal University, Changchun, China, [2] National & Local United Engineering Lab for Power Battery, Faculty of Chemistry, Northeast Normal University, Changchun, China*

The fluorophosphate $NaVPO_4F$ (NVPF) is a good candidate of cathode material for sodium-ion batteries (SIBs) due to its high theoretical specific capacity, high working voltage and stable structure. However, due to the low electronic conductivity of NVPF, its electrochemical properties are difficult to demonstrate. In order to address the insufficient and then enhance its electrochemical performance, a 3D carbon networks constructed $NaVPO_4F/C/rGO$ (NVPF/C/rGO) nanocomposite is prepared by freeze-drying assisted high-temperature solid-state method. When used as a cathode material for SIBs, the prepared NVPF/C/rGO can deliver a capacity of about 108.7 mA h $g^{-1}$ at 0.05 C. Moreover, NVPF/C/rGO nanocomposite also exhibits the excellent electrochemical performance, including superior rate capacities (about 65.8 mA h $g^{-1}$ specific capacity at 10 C) and outstanding cycling performance (~ 95.1% capacity retention after 200 cycles at 0.05 C), which can be attribute to the 3D carbon networks and the nanoparticles in NVPF/C/rGO nanocomposite. The preliminary results illustrate that the 3D carbon networks constructed NVPF/C/rGO could be a promising cathode material for SIBs.

**Keywords: sodium-ion batteries, cathode, $NaVPO_4F$, 3D carbon networks, nanocomposite**

OPEN ACCESS

***Edited by:***
*Tianyu Liu,*
*Virginia Tech, United States*

***Reviewed by:***
*Wei Luo,*
*Tongji University, China*
*Teng Zhai,*
*Nanjing University of Science and Technology, China*

****Correspondence:***
*Jin-Zhi Guo*
*guojz065@nenu.edu.cn*
*Xing-Long Wu*
*xinglong@nenu.edu.cn*

***Specialty section:***
*This article was submitted to Electrochemical Energy Conversion and Storage, a section of the journal Frontiers in Energy Research*

***Received:*** *26 February 2020*
***Accepted:*** *01 April 2020*
***Published:*** *23 April 2020*

***Citation:***
*Guo J-Z, Yang A-B, Zhao X-X, Gu Z-Y and Wu X-L (2020) 3D Carbon Networks Constructed $NaVPO_4F/C/rGO$ as a Cathode Material for High-Performance Sodium-Ion Batteries. Front. Energy Res. 8:64. doi: 10.3389/fenrg.2020.00064*

## INTRODUCTION

Nowadays, with the massive use of fossil energy, carbon dioxide emissions are increasing, thus aggravating the global warming (Dunn et al., 2011; Barpanda et al., 2014; Che et al., 2017). In response to this situation, it has become urgent to develop new renewable energy sources to replace the fossil energy (Kim et al., 2016; Lao et al., 2017; Yan et al., 2017). However, the renewable energy, such as wind, solar and tidal energy, is inherently intermittent and inconsecutive, and has strong regional characteristics. Therefore, advanced energy storage technology is more important for the development and application of renewable energy. Among them, electrochemical rechargeable batteries have the advantages of high energy density, long lifespans, simpler maintenance, etc., which have been paid more attention and studied by researchers (Keller et al., 2016; Kim et al., 2016). Given the fact that the lithium has lower redox potential (-3.04 V vs. SHE) and smaller atomic radius (0.76 Å), the lithium-ion batteries (LIBs) tend to be more widely studied. Nevertheless, the cost of LIBs is rise because of the limited and unevenly distributed lithium source in the Earth's crust, which leads to a boom in the study of sodium-ion batteries (SIBs) (Hwang et al., 2016; Nayak et al., 2018).

SIBs and LIBs have similar intercalation mechanism, making it possible to use the LIBs matured materials in SIBs. In addition, sodium is abundant in nature and easy to extract, so SIBs are the more cost-effective energy storage technology. Despite of numerous advantages, the development of SIBs still faces many problems, such as sodium has higher redox potential (−2.71 V vs. SHE) and larger atomic radius (1.02 Å), leading to the low energy density of SIBs (Guo et al., 2017; Pang et al., 2017). However, with the development of sustainable energy alternatives, the scientists are working to find and optimize electrode materials to create commercially viable SIBs. So far, the various types of cathodes are being reported, which includes layered oxides, polyanionic compound and so on (Barpanda et al., 2012; Jian et al., 2013; Guo S. et al., 2015). Due to the high structural stability, long-term cycling life and high ion mobility of polyanion-based cathode materials, they are even more impressive in SIBs (Barpanda et al., 2012; Fang et al., 2017). At the meantime, the fluorophosphate is even more prominent in this class, mainly because that fluorophosphate compounds have strong P-O covalent bond, which leads to greatly structural stability; furthermore, as cathode material of SIBs, the fluorophosphate materials always have higher working voltage due to strong electronegativity of $F^-$ (Park et al., 2013; Li et al., 2018).

Among them, $NaVPO_4F$ (NVPF) is a good cathode material candidate for SIBs, which possesses high theoretical capacity (143 mAh $g^{-1}$), high working voltage and stable structure (Law and Balaya, 2018; Ge et al., 2019). NVPF was originally proposed by Barker et al. (2003), it has a symmetrical tetragonal structure similar to that of $Na_3Al_2(PO_4)_2F_3$, as a cathode material, NVPF only has a discharge capacity of 82 mAh $g^{-1}$ in SIBs, and it decays to half after just 30 cycles. To improve electrochemical performance of NVPF, many strategies have been tried, including doping other metal ions, coating with some carbon materials and so on (Liu et al., 2008), which can improve the electrochemical properties of $NaVPO_4F$ to a certain extent, but their capacity is still far below its theoretical capacity, and can't meet the requirements of application (Ling et al., 2018). For the same purpose, we adopt freeze-drying assisted high-temperature solid-state method to prepare NVPF. As far as we know, for synthesis, freeze-drying is a low-cost and simple method, so that it could be a promising method for the future application (Rui et al., 2015). Meanwhile, in view of the poor electronic conductivity of NVPF, so improving electronic conductivity is the key to design high performance NVPF materials. Currently, combining with various types of carbon substrates is a universal and efficient method to enhance the conductivity of the electrode materials (Guo et al., 2015; Liu et al., 2015; Fan et al., 2017; Yin et al., 2017; Yang et al., 2020). However, a single carbon material has limited effect on the electrochemical performance of electrode materials. The conductivity of a single particle can be improved by using the carbon layer, but the effect on electron transport between particles is not significant. Moreover, the reduced graphene oxide (rGO) is regarded as one of the valued materials for improving the conductivity of materials, and has been widely used in many fields (Share et al., 2016; Liu et al., 2017).

Hence, in this work, we prepare a 3D carbon networks constructed $NaVPO_4F/C/rGO$ (abbr. NVPF/C/rGO, the C means the amorphous carbon derived from the organics) nanocomposite by freeze-drying assisted high-temperature solid-state method. In the nanocomposite, the amorphous carbon is coated on the surface of NVPF particles, and rGO layers cover on the surface of the NVPF/C particles and connect these to form a 3D conductive network. Such a modified NVPF/C/rGO nanocomposite used as a cathode material for SIBs exhibits remarkably improved electrochemical performance, especially high discharge capacity (about 108.7 mA h $g^{-1}$ specific capacity at 0.05 C), superior rate capacities (about 65.8 mA h $g^{-1}$ specific capacity at 10 C) and the long cycling performance (more than 95% of the initial capacity after 200 cycles at 0.05 C).

## EXPERIMENTAL SECTION

### Preparation of NVPF/C/rGO Nanocomposite

GO was firstly prepared by oxidation of graphite using the improved Hummers method (Hummers and Offeman, 1958; Lim et al., 2013). NVPF/C/rGO nanocomposite was prepared by a sample freeze-drying method. In a typical preparation, with the continuous stirring, the NaF, $NH_4H_2PO_4$ and $NH_4VO_3$ with the molar ratio of 1:1:1 were dissolved in the distilled water, then added the polyvinyl pyrrolidone (PVP) and citric acid, which can be used not only as the complexing agent but also as the carbon source, furthermore, the PVP also prevents the aggregation of colloidal particles and makes them more stable. Stirring the mixture at 80°C until the powder samples were completely dissolved to form a light orange-yellow aqueous solution. The above solution and the GO aqueous solution was added to a small beaker, then the sample was evenly dispersed by ultrasonic bath for 2 h. Then, the sample was rapidly frozen with liquid nitrogen, and it was dried in a freeze dryer. Finally, the sample was calcined at 750°C under the Ar atmosphere for 5 h, and the final material NVPF/C/rGO nanocomposite was formed after grinding. In this process, the GO can be reduced to the rGO at high temperature, thus playing the role of building the 3D conductive network.

### Material Characterization

The X-ray powder diffraction (XRD) on the D8 Bruker diffractometer with Cu Kα radiation ($\lambda = 1.5406$ Å) was used to detect the structure of the NVPF/C/rGO in scan range (2θ) of 10–60°. X-ray photoelectron spectroscopy (XPS) study was tested on X-ray photoelectron spectrophotometer (ESCALABMKLL) from VG. The morphology and microstructure of NVPF/C/rGO sample was characterized using the scanning electron microscope (SEM, HITACHI-SU8010, 10 kV) and transmission electron microscope (TEM, JEOL-2100 F, 200 kV).

### Electrochemical Measurement

The electrochemical properties were measured in the CR2032 coin cells. The working electrodes were made by casting a slurry of active material, acetylene black, and polyvinyl difluoride (PVDF) with a mass ratio of 8: 1: 1 in N-methylpyrrolidone (NMP) on aluminum foil and dried in vacuum. The loading mass of the active material was about 1.2–1.5 mg $cm^{-2}$. Pure sodium foil was used as both counter and reference electrodes, and the separator was glass microfiber filter (Whatman). Electrolyte was 1 mol $L^{-1}$ $NaClO_4$ dissolved in ethylene carbonate (EC) and propylene carbonate (PC) ($v_{EC}$:$v_{PC}$ =1:1) with 2 vol% fluoroethylene carbonate (FEC) as the additive. The constant current charge-discharge tests were implemented at battery testing system (LAND CT2001A) at 2.5∼4.1 V. Cyclic voltammetry (CV) curves were tested using a Princeton Applied Research (VERSASTAT 3) at 0.1 mV $s^{-1}$. For galvanostatic intermittent titration (GITT) analyses, the cells were cycled in same potential range at 0.05 C.

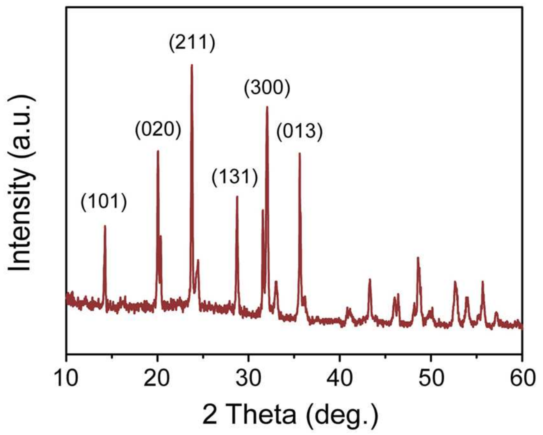

**FIGURE 1 |** The XRD pattern of NVPF/C/rGO composite.

## RESULTS AND DISCUSSION

The NVPF/C/rGO nanocomposite was prepared by freeze-drying assisted high-temperature solid-state method. As shown in **Figure 1**, the structure of NVPF/C/rGO nanocomposite was characterized according to XRD test. Consistent with the reports in the literatures (Law and Balaya, 2018; Ge et al., 2019), the diffraction pattern reveals that the peaks of NVPF/C/rGO nanocomposite are well indexed to the monoclinic crystal structure (space group *C2/c*) according to the standard card (PDF33-0804) (Liu et al., 2008). There are no obvious impurity peaks in XRD pattern, confirming that the NVPF was successfully prepared by solid-state method.

XPS test was implemented to study the elements composition and bonding configurations of NVPF/C/rGO, and **Figure 2** shows the XPS spectrum of NVPF/C/rGO nanocomposite. As shown in **Figure 2A**, there are six elements of Na, V, P, O, F, and C in the XPS full spectra of NVPF/C/rGO. From the high-resolution XPS spectra of V 2p (**Figure 2B**), the peaks at about 516.8 and 523.7 eV represent the electrons in V 2p3/2 and V 2p1/2, respectively, which are characteristic of $V^{3+}$ species and consistent well with the previous report (Zhang et al., 2018; Chen et al., 2019). **Figures 2C,D** are the high-resolution XPS

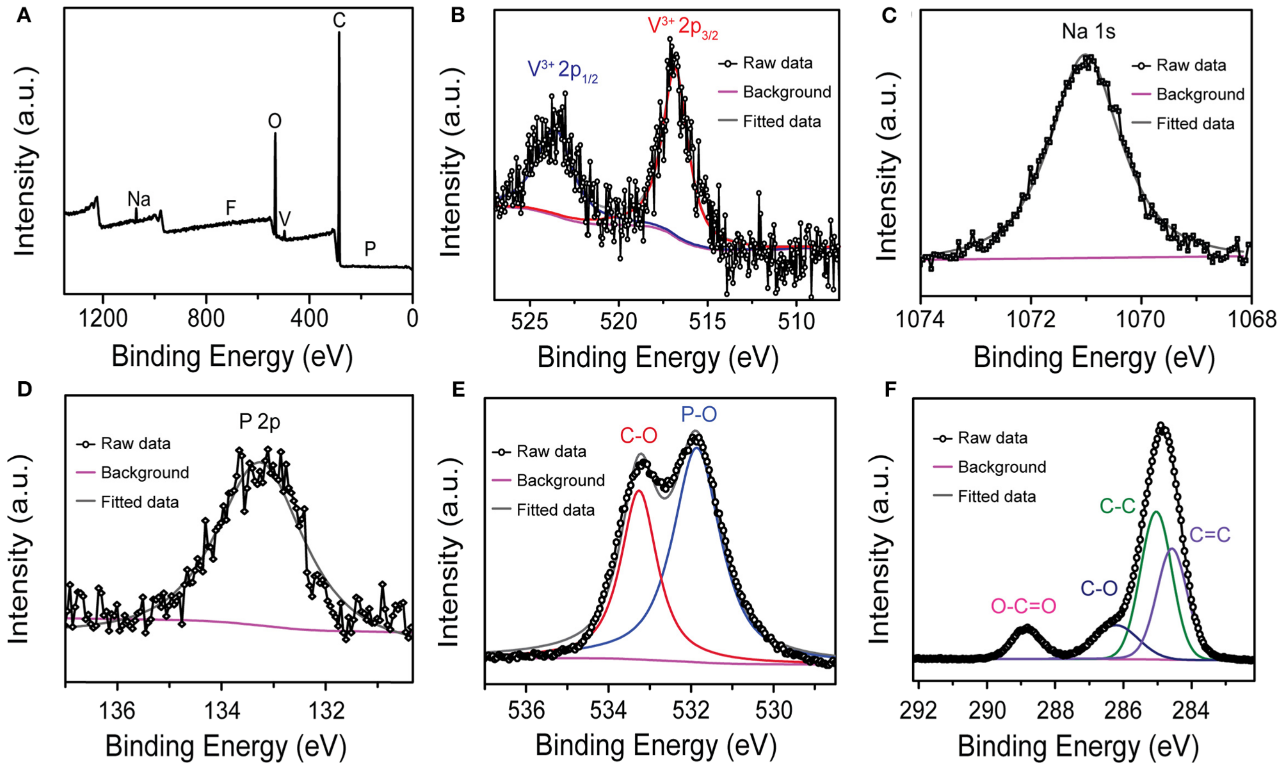

**FIGURE 2 | (A)** Full XPS spectra of the NVPF/C/rGO; high-resolution **(B)** V 2p, **(C)** Na 1s, **(D)** P 2p, **(E)** O 1s, and **(F)** C 1s spectrum of the NVPF/C/rGO.

spectrum of Na 1s and P 2p, indicating that exists Na and P elements in material. The high-resolution XPS spectra of O 1s, as shown in **Figure 2E**, the peaks at about 533.26 and 531.86 eV are assigned to C-O and P-O bonds (Gu et al., 2020). Moreover, as shown in **Figure 2F**, the C 1s peak of NVPF/C/rGO can be fitted into four peaks at 288.86, 286.21, 285.06, and 284.56 eV,

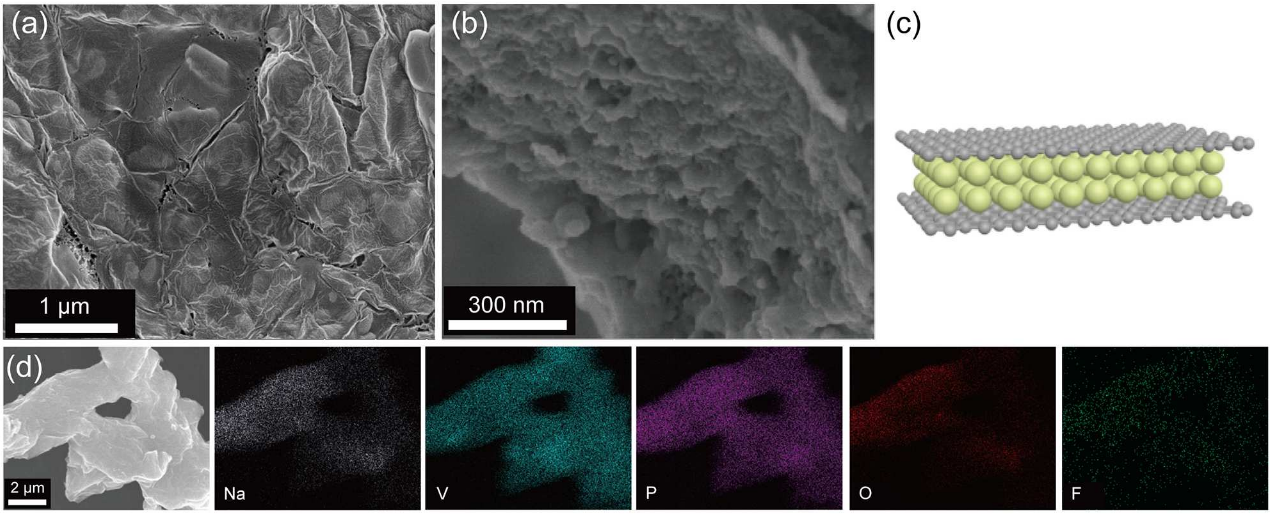

**FIGURE 3 | (a,b)** SEM images of NVPF/C/rGO under different magnifications; **(c)** the schematic illustration of NVPF/C/rGO; **(d)** the EDS mapping of NVPF/C/rGO.

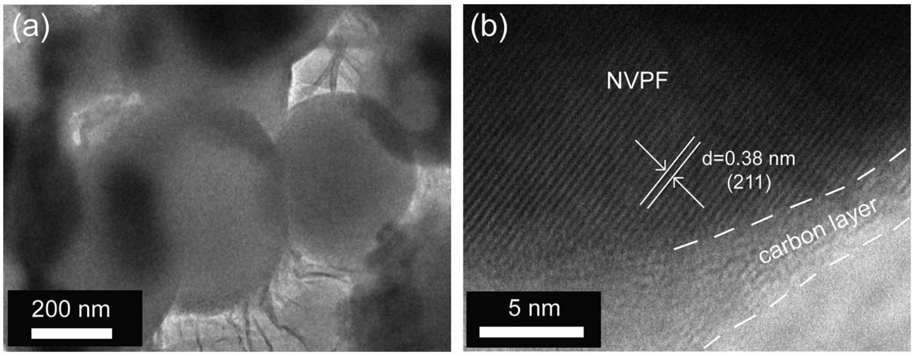

**FIGURE 4 | (a)** Low- and **(b)** high-resolution TEM images of NVPF/C/rGO.

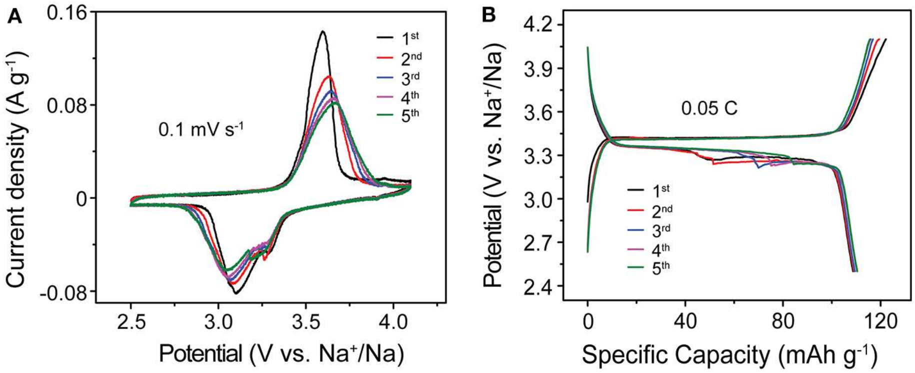

**FIGURE 5 | (A)** CV curves at the scan rate of 0.1 mV s$^{-1}$ and **(B)** galvanostatic charge–discharge profiles at 0.5C of the NVPF/C/rGO.

corresponding to O-C=O, C-O, C-C, and C=C bonds (Zhang et al., 2018).

The morphology of the NVPF/C/rGO nanocomposite was firstly characterized by SEM. In **Figures 3a,b**, the NVPF/C/rGO is mainly composed of NVPF nanoparticles and the rGO sheets, and the particle size of NVPF material is about 200-500 nm, which is benefit for the electrochemical performance. **Figure 3a** shows the rGO layers cover on the surface of the NVPF nanocomposite and connect these to form a 3D conductive network, improving the electronic conductivity of the material. And the morphology of the NVPF/C/rGO nanocomposite can be represented by schematic illustration of **Figure 3c**. Moreover, the element energy dispersive spectrometer (EDS) was implemented to explain the elements distribution of NVPF/C/rGO material, indicating the Na, V, P, O, F elements are uniformly distributed in the NVPF/C/rGO (**Figure 3d**).

The TEM was implemented to further investigate the morphology of NVPF/C/rGO, as shown in **Figure 4a**, the prepared material is granular and the particle size is nanoscale, which is consistent well with the results of the SEM. In

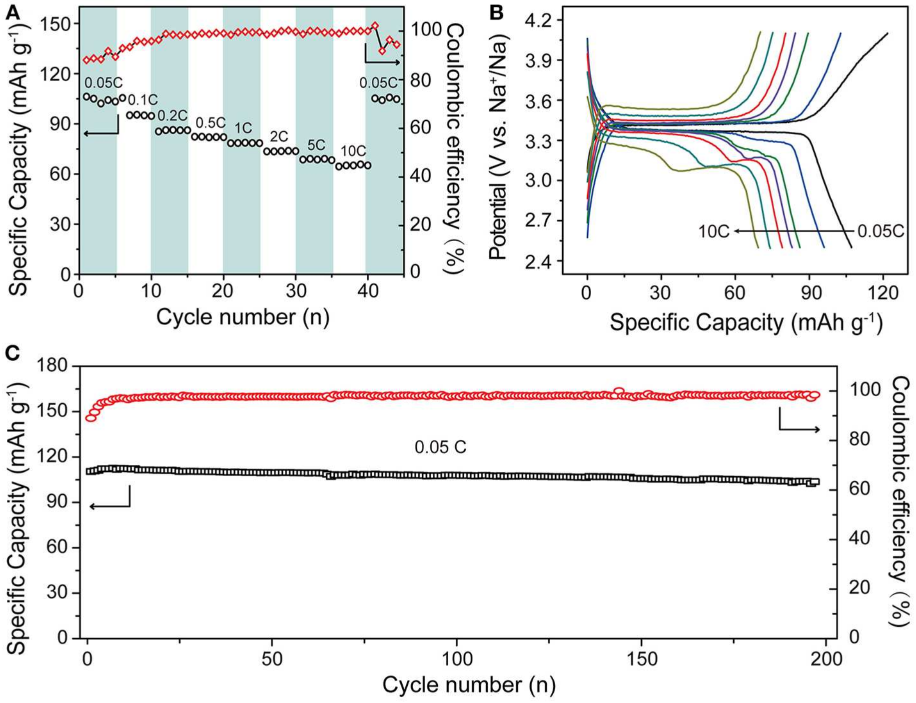

**FIGURE 6 |** Electrochemical performance of NVPF/C/rGO: **(A)** rate capability at 0.05–10 C; **(B)** the corresponding charge–discharge profiles at different rate; and **(C)** cycling performance.

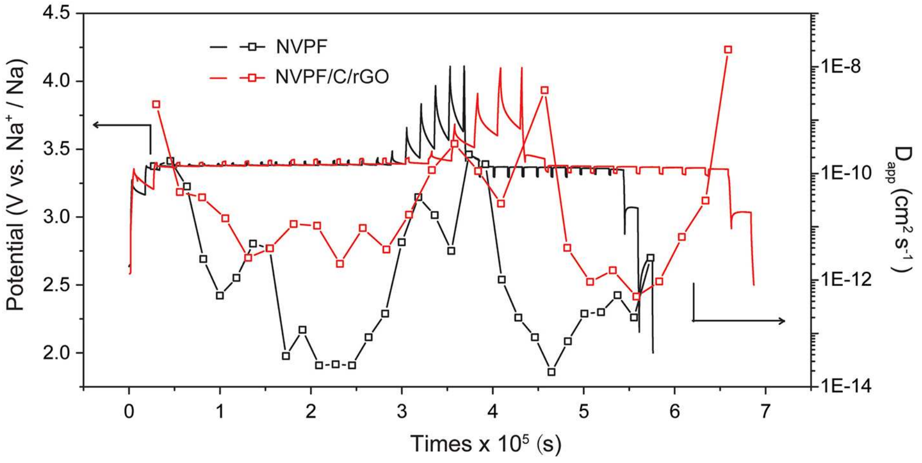

**FIGURE 7 |** GITT test results containing $D_{app}$ and variation curve along with the GCD processes of NVPF/C/rGO and NVPF.

addition, TEM image of NVPF/C/rGO demonstrates that all the NVPF particles are coated evenly by the amorphous carbon, and the rGO layers cover on the surface of particles and connect these to form a 3D conductive network. In **Figure 4b**, the high-resolution TEM (HRTEM) image shows the NVPF particle and the carbon layer. Obviously, the NVPF has high crystallinity and the lattice distance is 0.38 nm, corresponding to the (211) plane of monoclinic $NaVPO_4F$.

Used metallic Na plates as both counter and reference electrodes in the half-cells, the CV and galvanostatic charge-discharge (GCD) tests were implemented to investigate the electrochemical performance of the 3D carbon networks constructed NVPF/C/rGO. **Figure 5A** shows the CV curves, a couple of well-defined anodic/cathodic peaks at about 3.59/3.20 V vs. $Na^+/Na$, which corresponds to reversible two-phase transformation between $NaVPO_4F$ and $VPO_4F$, that is, the redox reaction of $V^{4+}/V^{3+}$ couple. However, at the sodiation process, this single peak splits as two chiseled peaks, which may be attributed to the FEC additive (Guo et al., 2015). The GCD profiles at 0.05 C in **Figure 5B** exhibit a pair of charge/discharge plateaus at about 3.42/3.34 V vs. $Na^+/Na$, which is agree with CV test results. The charge and discharge capacities at first cycle of NVPF/C/rGO are 122.1 and 108.7 mA h $g^{-1}$, respectively, and the corresponding Coulombic efficiency is only 89%, which may be caused by the side effects at first cycle due to the large specific surface area of NVPF/C/rGO nanocomposite. Moreover, the capacity of NVPF/C/rGO remains unchanged as the cycle progress, indicating the charge/discharge processes are highly reversible.

To further evaluate the electrochemical properties of the 3D carbon networks constructed NVPF/C/rGO, the rate and cycle performance of the cells were studied (**Figure 6**). **Figure 6A** exhibits the rate capabilities of NVPF/C/rGO at 0.05-10 C. At low rate of 0.05C, the NVPF/C/rGO nanocomposite delivers a capacity of 106.3 mA h $g^{-1}$, and at a very high rate of 10 C, it still has specific capacity of about 65.8 mA h $g^{-1}$, indicating the superior rate capabilities of NVPF/C/rGO nanocomposite. Moreover, when the rate returns to 0.05 C, the specific capacity of NVPF/C/rGO nanocomposite can still restore to 105.8 mA h $g^{-1}$ after the rate tests of 55 cycles. The corresponding GCD curves are further shown in **Figure 6B**, and the charge and discharge plateaus are still obvious at 10 C. Furthermore, the NVPF/C/rGO nanocomposite also demonstrates the excellent cycling performance, and shown in **Figure 6C**. After 200 cycles at 0.05 C, the NVPF/C/rGO nanocomposite still has a capacity of 104.8 mA h $g^{-1}$ with the capacity retention of above 95 %.

Combining the results of the above research to further study about the NVPF/C/rGO nanocomposite's kinetics characteristics, in **Figure 7**, GITT test was performed at a current density of 0.05 C within the potential range of 2.5–4.1 V. By applying a short enough current during the electrode is in a stable state, the voltage response curve of the system could be measured by GITT method to study the kinetics properties of the electrode material. Assuming the electrode system at steady state, $Es$ is potential and $\tau$ is duration at the moment. The total change of the cell voltage is $E_r$. $M_B$ is the electrode materials' relative molecular mass, and $m_B$ is the electrode materials' actual mass. Combining the above specific values and according to the formula (1), the apparent Na diffusion coefficient ($D_{app}$) can be calculated (Guo et al., 2014):

$$D_{app} = \frac{4}{\pi \tau}\left(\frac{m_B V_M}{M_B S}\right)^2\left(\frac{E_s}{E_\tau}\right)^2 \qquad \left(\tau \ll L^2/D\right) \qquad (1)$$

Calculated from the GITT curves, the $D_{app}$ values of the cell are in the $10^{-12}\sim10^{-8}$ $cm^2$ $s^{-1}$ order of magnitude, which is higher than those of NVPF ($10^{-14}\sim10^{-10}$ $cm^2$ $s^{-1}$) and other polyanion-type phosphate cathodes for SIBs (Liu Q. et al., 2015; Wang et al., 2015). 3D carbon networks can effectively improve the kinetics properties of NVPF material. Furthermore, the values at the plateau region are evidently low in both the charge and discharge processes, indicating that the Na intercalation/extraction process of NVPF/C/rGO nanocomposite requires more energy. The results indicate that the NVPF/C/rGO has excellent kinetics properties.

## CONCLUSION

In summary, a 3D carbon networks constructed NVPF/C/rGO nanocomposite is prepared by freeze-drying assisted high-temperature solid-state method. In NVPF/C/rGO, the amorphous carbon is coated on the surface of NVPF particles, and the rGO layers cover on the surface of the NVPF/C particles and connect these to form a 3D conductive network, effectively improving the electronic conductivity of NVPF. The NVPF/C/rGO cathode material for SIBs exhibits remarkably improved electrochemical performance, in the aspect of significantly enhanced specific capacity, great rate capability and outstanding cycling stability. Moreover, the GITT test was implemented to analyse the kinetic properties of NVPF/C/rGO electrode. Therefore, this work provides a facile synthesis method for constructing 3D conductive network modified electrode materials, promoting the development of high-performance SIBs.

## DATA AVAILABILITY STATEMENT

All datasets generated for this study are included in the article/supplementary material.

## AUTHOR CONTRIBUTIONS

All authors listed have made a substantial, direct and intellectual contribution to the work, and approved it for publication.

## FUNDING

The authors gratefully acknowledge the financial support from the National Natural Science Foundation of China (91963118), the Fundamental Research Funds for the Central Universities (2412019ZD010), the Project Funded by China Postdoctoral Science Foundation (2019M661187), and National Postdoctoral Program for Innovative Talents (BX20190064).

# REFERENCES

Barker, J., Saidi, M. Y., and Swoyer, J. L. (2003). A sodium-ion cell based on the fluorophosphate compound $NaVPO_4F$. *Electrochem. Solid State Lett.* 6:A1. doi: 10.1149/1.1523691

Barpanda, P., Nishimura, S. I., and Yamada, A. (2012). High-voltage pyrophosphate cathodes. *Adv. Energy Mater*. 2, 841–859. doi: 10.1002/aenm.201100772

Barpanda, P., Oyama, G., Nishimura, S. I., Chung, S. C., and Yamada, A. (2014). A 3.8-V earth-abundant sodium battery electrode. *Nat. Commun*. 5:4358. doi: 10.1038/ncomms5358

Che, H., Chen, S., Xie, Y., Wang, H., Amine, K., Liao, X. Z., et al. (2017). Electrolyte design strategies and research progress for room-temperature sodium-ion batteries. *Energy Environ. Sci*. 10, 1075–1101. doi: 10.1039/C7EE00524E

Chen, C., Li, T., Tian, H., Zou, Y., and Sun, J. (2019). Building highly stable and industrial $NaVPO_4F$/C as bipolar electrodes for high-rate symmetric rechargeable sodium-ion full batteries. *J. Mater. Chem. A* 7, 18451–18457. doi: 10.1039/C9TA05396D

Dunn, B., Harish, K., and Tarascon, J. M. (2011). Electrical energy storage for the grid: a battery of choices. *Science* 334, 928–935. doi: 10.1126/science.1212741

Fan, H.-H., Li, H.-H., Huang, K.-C., Fan, C.-Y., Zhang, X.-Y., Wu, X.-L., et al. (2017). Metastable Marcasite-$FeS_2$ as a new anode material for lithium ion batteries: CNFs-improved lithiation/delithiation reversibility and Li-storage properties. *ACS Appl. Mater. Interfaces* 9, 10708–10716. doi: 10.1021/acsami.7b00578

Fang, Y., Zhang, J., Xiao, L., Ai, X., Cao, Y., and Yang, H. (2017). Phosphate framework electrode materials for sodium ion batteries. *Adv. Sci*. 4:1600392. doi: 10.1002/advs.201600392

Ge, X., Li, X., Wang, Z., Guo, H., Yan, G., Wu, X., et al. (2019). Facile synthesis of $NaVPO_4F$/C cathode with enhanced interfacial conductivity towards long-cycle and high-rate sodium-ion batteries. *Chem. Eng. J*. 357, 458–462. doi: 10.1016/j.cej.2018.09.099

Gu, Z.-Y., Guo, J.-Z., Sun, Z.-H., Zhao, X.-X., Li, W.-H., Yang, X., et al. (2020). Carbon-coating-increased working voltage and energy density towards an advanced Na3V2(PO4)2F3@C cathode in sodium-ion batteries. *Sci. Bull*. 65, 702–710. doi: 10.1016/j.scib.2020.01.018

Guo, J.-Z., Wang, P.-F., Wu, X.-L., Zhang, X.-H., Yan, Q., Chen, H., et al. (2017). High-energy/power and low-temperature cathode for sodium-ion batteries: *in situ* XRD study and superior full-cell performance. *Adv. Mater*. 29:1701968. doi: 10.1002/adma.201701968

Guo, J.-Z., Wu, X.-L., Wan, F., Wang, J., Zhang, X.-H., and Wang, S. R.- (2015). A Superior $Na_3V_2(PO_4)_3$-Based nanocornposite enhanced by both N-doped coating carbon and graphene as the cathode for sodium-ion batteries. *Chem. Eur. J*. 21, 17371–17378. doi: 10.1002/chem.201502583

Guo, S., Liu, P., Yu, H., Zhu, Y., Chen, M., Ishida, M., et al. (2015). A layered P2- and O3-type composite as a high-energy cathode for rechargeable sodium-ion batteries. *Angew. Chem. Int. Ed*. 54, 5894–5899. doi: 10.1002/anie.201411788

Guo, S., Yu, H., Jian, Z., Liu, P., Zhu, Y., Guo, X., et al. (2014). A high-capacity, low-cost layered sodium manganese oxide material as cathode for sodium-ion batteries. *ChemSusChem* 7, 2115–2119. doi: 10.1002/cssc.201402138

Hummers, W. S., and Offeman, R. E. (1958). Preparation of Graphitic Oxide. *J. Am. Chem. Soc*. 80, 1339. doi: 10.1021/ja01539a017

Hwang, J.-Y., S.-,Myung, T., Yoon, C. S., Kim, S.-S., Aurbach, D., and Sun, Y.-K. (2016). Novel cathode materials for Na-Ion batteries composed of spoke-like nanorods of $Na[Ni_{0.61}Co_{0.12}Mn_{0.27}]O_2$ assembled in spherical secondary particles. *Adv. Funct. Mater*. 26, 8083–8093. doi: 10.1002/adfm.201603439

Jian, Z., Han, W., Lu, X., Yang, H., Hu, Y.-S., Zhou, J., et al. (2013). Superior electrochemical performance and storage mechanism of $Na_3V_2(PO_4)_3$ cathode for room-temperature sodium-ion batteries. *Adv. Energy Mater*. 3, 156–160. doi: 10.1002/aenm.201200558

Keller, M., Buchholz, D., and Passerini, S. (2016). Layered Na-Ion cathodes with outstanding performance resulting from the synergetic effect of mixed P- and O-type phases. *Adv. Energy Mater*. 6:1501555. doi: 10.1002/aenm.201501555

Kim, J., Park, I., Kim, H., Park, K.-Y., Park, Y.-U., and Kang, K. (2016). Tailoring a new 4V-class cathode material for Na-Ion batteries. *Adv. Energy Mater*. 6:1502147. doi: 10.1002/aenm.201502147

Lao, M., Zhang, Y., Luo, W., Yan, Q., Sun, W., Dou, S., et al. (2017). Alloy-based anode materials toward advanced sodium-ion batteries. *Adv. Mater*. 29:1700622. doi: 10.1002/adma.201700622

Law, M., and Balaya, P. (2018). $NaVPO_4F$ with high cycling stability as a promising cathode for sodium-ion battery. *Energy Storage Mater*. 10, 102–113. doi: 10.1016/j.ensm.2017.08.007

Li, C., Shen, M., Hu, B., Lou, X., Zhang, X., Tong, W., et al. (2018). High-energy nanostructured $Na_3V_2(PO_4)2O_{1.6}F_{1.4}$ cathodes for sodium-ion batteries and a new insight into their redox chemistry. *J. Mater. Chem. A* 6, 8340–8348. doi: 10.1039/C8TA00568K

Lim, C. H., Kannan, A., G., Lee, H.-W., and Kim, D., K. (2013). A high power density electrode with ultralow carbon via direct growth of particles on graphene sheets. *J. Mater. Chem. A* 1, 6183–6190. doi: 10.1039/c3ta10254h

Ling, M., Li, F., Yi, H., Li, X., Hou, G., Zheng, Q., et al. (2018). Superior Na-storage performance of molten-state-blending-synthesized monoclinic $NaVPO_4F$ nanoplates for Na-ion batteries. *J. Mater. Chem. A* 6, 24201–24209. doi: 10.1039/C8TA08842J

Liu, D.-H., Lü, H.-Y., Wu, X.-L., Hou, B.-H., Wan, F., Bao, S.-D., et al. (2015). Constructing the optimal conductive network in MnO-based nanohybrids as high-rate and long-life anode materials for lithium-ion batteries. *J. Mater. Chem. A* 3, 19738–19746. doi: 10.1039/C5TA03556B

Liu, Q., Wang, D., Yang, X., Chen, N., Wang, C., Bie, X., et al. (2015). Carbon-coated $Na_3V_2(PO_4)_2F_3$ nanoparticles embedded in a mesoporous carbon matrix as a potential cathode material for sodium-ion batteries with superior rate capability and long-term cycle life. *J. Mater. Chem. A*. 3, 21478–85. doi: 10.1039/C5TA05939A

Liu, X., Chao, D., Su, D., Liu, S., Chen, L., Chi, C., et al. (2017). Graphene nanowires anchored to 3D graphene foam via self-assembly for high performance Li and Na ion storage. *Nano Energy* 37, 108–117. doi: 10.1016/j.nanoen.2017.04.051

Liu, Z.-M., Wang, X.-Y., Wang, Y., Tang, A.-P., Yang, S.-Y., and He, L.-F. (2008). Preparation of $NaV_{1-x}Al_xPO_4F$ cathode materials for application of sodium-ion battery. *Trans. Nonferrous Metals Soc.* 18, 346–350. doi: 10.1016/S1003-6326(08)60060-6

Nayak, P. K., Yang, L., Brehm, W., and Adelhelm, P. (2018). From Lithium-ion to sodium-ion batteries: advantages, challenges, and surprises. *Angew. Chem. Int. Ed*. 57, 102–120. doi: 10.1002/anie.201703772

Pang, W.-L., Zhang, X.-H., Guo, J.-Z., Li, J.-Y., Yan, X., Hou, B. H., et al. (2017). P2-type $Na_{2/3}Mn_{1-x}Al_xO_2$ cathode material for sodium-ion batteries: Al-doped enhanced electrochemical properties and studies on the electrode kinetics. *J. Power Sources* 356, 80–88. doi: 10.1016/j.jpowsour.2017.04.076

Park, Y.-U., Seo, D.-H., Kwon, H. S., Kim, B., Kim, J., Kim, H., et al. (2013). A new high-energy cathode for a na-ion battery with ultrahigh stability. *J. Am. Chem. Soc*. 135, 13870–13878. doi: 10.1021/ja406016j

Rui, X., Sun, W., Wu, C., Yu, Y., and Yan, Q. (2015). An advanced sodium-ion battery composed of carbon coated $Na_3V_2(PO_4)_3$ in a porous graphene network. *Adv. Mater*. 27, 6670–6676. doi: 10.1002/adma.201502864

Share, K., Cohn, A. P., Carter, R., Rogers, B., and Pint, C. L. (2016). Role of nitrogen-doped graphene for improved high-capacity potassium ion battery anodes. *ACS Nano* 10, 9738–9744. doi: 10.1021/acsnano.6b05998

Wang, Q., Zhao, B., Zhang, S., Gao, X., and Deng, C. (2015). Superior sodium intercalation of honeycomb-structured hierarchical porous $Na_3V_2(PO_4)_3$/C microballs prepared by a facile one-pot synthesis. *J. Mater. Chem. A* 3, 7732–7740. doi: 10.1039/C5TA00765H

Yan, X., Ye, H., Wu, X.-L., Zheng, Y.-P., Wan, F., Liu, M., et al. (2017). Three-dimensional carbon nanotube networks enhanced sodium trimesic: a new anode material for sodium ion batteries and Na-storage mechanism revealed by ex situ studies. *J. Mater. Chem. A* 5, 16622–16629. doi: 10.1039/C7TA03484A

Yang, X., Wang, Y.-Y., Hou, B.-H., Liang, H.-J., Zhao, X.-X., Fan, H., et al. (2020). Nano-SnO2 Decorated Carbon Cloth as Flexible, Self-supporting and

Additive-Free Anode for Sodium/Lithium-Ion Batteries. *Acta Metallurgica Sinica*. doi: 10.1007/s40195-020-01001-7

Yin, Y., Xiong, F., Pei, C., Xu, Y., An, Q., Tan, S., et al. (2017). Robust three-dimensional graphene skeleton encapsulated $Na_3V_2O_2(PO_4)_2F$ nanoparticles as a high-rate and long-life cathode of sodium-ion batteries. *Nano Energy* 41, 452–459. doi: 10.1016/j.nanoen.2017.09.056

Zhang, L.-L., Ma, D., Li, T., Liu, J., Ding, X.-K., Huang, Y.-H., et al. (2018). Polydopamine-derived nitrogen-doped carbon-covered $Na_3V_2(PO_4)_2F_3$ Cathode material for high-performance na-ion batteries. *ACS Appl. Mater. Interfaces* 10, 36851–36859. doi: 10.1021/acsami.8b10299

**Conflict of Interest:** The authors declare that the research was conducted in the absence of any commercial or financial relationships that could be construed as a potential conflict of interest.

frontiers
in Energy Research

BRIEF RESEARCH REPORT
published: 30 April 2020
doi: 10.3389/fenrg.2020.00061

# Chitosan-Derived Three-Dimensional Porous Graphene for Advanced Supercapacitors

*Chao Wang*, Guobin Zhong, Wei Zhao, Shijia Wu, Wei Su*, Zengfu Wei and Kaiqi Xu*

*Electric Power Research Institute of Guangdong Power Grid Cooperation, Guangzhou, China*

Graphene for energy storage devices suffers from the preparation method and deficient quality, hindering their further widespread application. Here, we report a facile and cost-effective approach to derive three-dimensional porous graphene (3DPG) from biocompatible chitosan for massive production. Taking advantage of the large surface area, excellent electrical conductivity and high electrochemical activity of the 3DPG, an advanced symmetric supercapacitor (3DPG//3DPG SCs) is achieved by coupling two 3DPG electrodes in commercial DLC301 organic electrolyte. The device delivers a remarkable capacitance of 168.9 F g-1 at the scan rate of 10 mV s-1 and displays a superior rate capability, witnessing 81.5% capacitance retention from 10 to 100 mV s-1. Furthermore, the 3DPG//3DPG SCs exhibits prominent cyclic durability, as evidenced by its 96% capacitance after 10,000 cycles. This work might shed light on the probable application of graphene at industrial level for efficient energy storage.

**Keywords: three-Dimensional (3D), porous, graphene, chitosan, supercapacitor**

***Edited by:***
*Teng Zhai,*
*Nanjing University of Science and Technology, China*

***Reviewed by:***
*Xihong Lu,*
*Sun Yat-sen University, China*
*Tianyu Liu,*
*Virginia Tech, United States*

****Correspondence:***
*Chao Wang*
*wangchaomly@163.com*
*Wei Su*
*jxhwsu@163.com*

***Specialty section:***
*This article was submitted to Electrochemical Energy Conversion and Storage,*
*a section of the journal Frontiers in Energy Research*

***Received:*** *28 February 2020*
***Accepted:*** *31 March 2020*
***Published:*** *30 April 2020*

***Citation:***
*Wang C, Zhong G, Zhao W, Wu S, Su W, Wei Z and Xu K (2020) Chitosan-Derived Three-Dimensional Porous Graphene for Advanced Supercapacitors.*
*Front. Energy Res. 8:61.*
*doi: 10.3389/fenrg.2020.00061*

## INTRODUCTION

Environmental pollution and the increasingly severe energy crisis are stimulating intensive efforts to exploit efficient energy storage devices for conversion fulfillment and storage of renewable energy sources (Wang et al., 2018; Han et al., 2019; Lu et al., 2019). In recent decades supercapacitors (SCs) have attracted particular attention, from both industry and academy, as an emerging candidate for energy storage (Hao et al., 2015; Zhang et al., 2017). This should be attributed to their advantageous features including high power density, fast charge/discharge capability, long-term cycling stability, good safety, and low maintenance cost (Yu et al., 2013; Yan et al., 2016; Chen et al., 2018). Regrettably, the dominating factor impeding the further widespread application of SCs is their low energy density, which can hardly meet the increasing energy density demands of novel electronic devices (Wang et al., 2017; Zhang Q. et al., 2018; Zhang Z. et al., 2018). The key to solving this problem lies in the rational selection of electrode materials, which determine the electrochemical performance of SCs. Among various electrode materials, carbon materials including carbon nanotubes (Sharma et al., 2015), carbon nanosphere (Cui and Zhu, 2014), active carbon (Kołodynska et al., 2016), and graphene (Wang et al., 2017; Yang et al., 2017) have been widely utilized for high-performance SCs constructions because of their impressive merits such as large surface area, prominent electrical conductivity, admirable long-term cycling stability, good mechanical properties, low production cost, and environmental friendliness (Gnanasekaran et al., 2017; Zhao et al., 2017; Guo et al., 2018). Among them, graphene has been considered as the most attractive candidate due to its high theoretical surface area (2,630 $m^2$ $g^{-1}$), impressive electrical conductivity and unique structure (Cao et al., 2011; Shen et al., 2017; Yu et al., 2017). However, the massive production of graphene with high electrochemical performance by facile and low-cost approaches is still challenging.

Nowadays, common methods for large-scale graphene production still see visible drawbacks. For instance, the chemical vapor deposition (CVD) method allows high-quality graphene synthesis but the experimental conditions are usually harsh (Shen et al., 2017). The mechanical exfoliation method enables graphene preparation with great electrochemical properties but the product thickness of different lots is uncontrollable (Chen et al., 2012). To circumvent these issues, extensive research efforts have been devoted to the exploration of facile and reliable synthetic methods. K. Parvez et al. reported a simple electrochemical expansion approach to synthesize thin-layer graphene based on inorganic salts, and a quasi-solid-state SC with a capacitance of 18.8 F $g^{-1}$ was obtained (Shao et al., 2016). Ruoff and his co-workers designed a SC based on reduced graphene oxide by solvothermal reaction with a high capacitance of 120 F $g^{-1}$ (Ruoff et al., 2012). Despite some delightful achievements, the overall performance of the cutting-edge graphene still hardly meets the demand for practical applications, especially at industry levels. Therefore, developing highly efficient approaches is very desirable for graphene preparation with excellent electrochemical properties.

Herein, we report a highly efficient approach allowing the massive production of three-dimensional porous graphene (denoted as 3DPG) as electrode materials for high-performance SCs constructions. The raw material for 3DPG derivation, the chitosan, is biocompatible, and environmentally friendly. The 3DPG electrode is facilely obtained via a three-step process, including the crosslinking of chitosan with acetic acid, the carbonization in the $N_2$ atmosphere and the acid pickling. The porous structure and obvious graphene wrinkles of the 3DPG endow this electrode with a large surface area, which can afford a superior charge transport and adequate electrolyte diffusion into the electrode. Additionally, the nitrogen dopants in 3DPG effectively boost the reactivity and electrical conductivity by creating extrinsic defects, while the introduction of oxygen functional groups improves its electrochemical activity. As a consequence, coupling two 3DPG electrodes in commercial DLC301 organic electrolyte (denoted as 3DPG//3DPG SCs) yields an advanced symmetric SC with both a high capacitance (168.9 F $g^{-1}$ at the scan rate of 10 mV $s^{-1}$) and a superior rate capability (81.5% capacitance retention with the scan rate increase from 10 to 100 mV $s^{-1}$). Besides, the device displays extraordinary cycling durability, retaining 96% capacitance after 10,000 cycles.

# EXPERIMENTAL SECTION

## Preparation of 3DPG Sample

All the reagents utilized were of analytical grade and used directly without further purification. The 3DPG was synthesized by three steps, crosslinking, carbonization and pickling. Firstly, 3 g chitosan, 0.01 mmol $Ni(NO_3)_2$ and 1 mmol $Zn(NO_3)_2$ were dissolved in 50 mL $H_2O$ under stirring at room temperature until the solution became turbid. 1.2 mL acetic acid was then added. After crosslinking till gel, the mixed precursor was transferred to a container (∼64 mL) and dried in a freezer dryer for 36 h. The as-obtained precursor was soaked in a pure ethanol solution of 6 M KOH for 3 h and dried at 60°C for 3 h. The sample was calcined under a $N_2$ atmosphere at 500°C for 1 h and then slowly heated to 800°C for 1 h. Lastly, the carbonized sample was soaked in 3 M HCl for 3 h at room temperature and completely rinsed with deionized water, in order to fully remove the metal ions and the residual KOH solution to obtain 3DPG (1.21 mg $cm^{-1}$, BT25S, 0.01 mg).

## Electrode Preparation and Device Assembly

3DPG electrodes were prepared by mixing the 3DPG powder with polyvinylidene fluoride (PVDF) binder and carbon black at a weight ratio of 8:1:1 in N, N-dimethylformamide until a homogeneous slurry was formed. Then the slurry was uniformly painted on carbon paper and dried at 80°C overnight. A symmetric SCs was assembled into a button battery by combining two 3DPG electrodes (1.0 × 1.0 cm) and a polypropylene separator in commercial DLC301 organic electrolyte (the details can be seen in **Table S1** within the Supporting Information).

## Material Characterizations and Electrochemical Measurements

The morphology and microstructures of the 3DPG were analyzed by field-emission scanning electron microscopy (FE-SEM; JSM-6330F) and transmission electron microscope (TEM; FEI Tecnai $G^2$ F30). The chemical composition of the 3DPG was characterized by X-ray diffractometry (XRD; D8 ADVANCE), Raman spectroscopy (Renishaw in Via) and X-ray Photoelectron Spectroscopy (XPS, ESCALab250, Thermo VG). The Brunauer-Emmett-Teller (BET) surface area was measured with an ASAP2020M (Micromeritics Instrument Corp.). All the electrochemical studies of SCs in the potential range of 0–2.5 V were carried out using a button cell with a commercial DLC301 organic electrolyte. Cyclic voltammetry (CV) and galvanostatic charge/discharge measurements (GCD) were conducted on an electrochemical workstation (CHI 760E).

# RESULTS AND DISCUSSION

## Structural and Morphological Properties of Sample

The 3DPG electrode is facilely obtained via a simple three-step process, including crosslinking of chitosan with acetic acid, carbonization in the $N_2$ atmosphere, and acid pickling. **Figure 1a** presents an optical image of the freeze-dried chitosan after crosslinking with acetic acid, which swells into a sponge shape due to the formation of numerous porous channels during the crosslinking process. More significantly, in order to activate the graphene, the $Ni(NO_3)_2$ and $Zn(NO_3)_2$ were involved in a synthesis process and removed by sublimating at high temperature as well as soaking in 3 M HCl for 3 h at last, which can form a porous graphene structure with high surface area. The morphology and microstructure of the 3DPG sample was characterized by SEM and TEM. As shown in **Figure 1b**, the 3DPG sample exhibits notable graphene wrinkles with thickness <1 nm, implying the large specific surface area of the 3DPG sample. The TEM and the high-resolution transmission electron microscopy (HRTEM) images in **Figures 1c,d** reveal the ultrathin

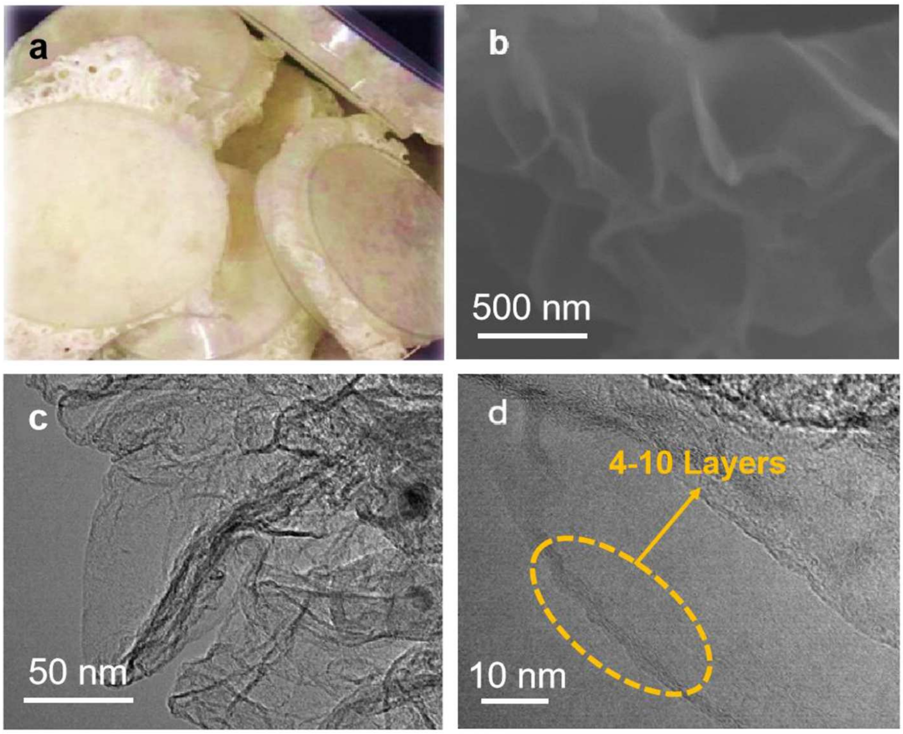

**FIGURE 1 | (a)** Optical image of freeze-dried chitosan after crosslinking, **(b)** SEM image of the 3DPG, **(c)** TEM image, and **(d)** HRTEM image of 3DPG.

wrinkles and multilayered structure of the 3DPG sample, in accordance with the SEM analysis.

The structure and crystallinity of the 3DPG sample were analyzed by conducting X-ray diffraction (XRD) measurements. As illustrated in **Figure 2A**, all of the diffraction peaks of the 3DPG sample can be perfectly indexed to hexagonal graphite (JCPDF #41-1487), which is consistent with the commercial graphene (Xiao et al., 2018). No other impurity peaks were detected, indicating that the samples are pure graphene. To evaluate the specific surface area of the 3DPG sample, nitrogen adsorption-desorption measurement was carried out in **Figure 2B**. More encouragingly, the Brunauer-Emmett-Teller (BET) specific surface area of the 3DPG sample reaches up to 330.0 $m^2$ $g^{-1}$, which exceeds that of most graphene (Yang et al., 2011, 2014, 2015). Additionally, to gain insight into the chemical composition and valence state of the 3DPG, the sample was investigated by Raman spectroscopy and X-ray photoelectron spectroscopy (XPS). The Raman spectrum in **Figure 2C** reveals that the two strong peaks at 1352.6 and 1585.2 $cm^{-1}$ correspond to the $sp^3$-type disordered carbon (D band) and $sp^2$-type ordered graphitic carbon (G band) (Teng et al., 2018). The large $I_D/I_G$ ratio of ~0.94 and the 2D band observed at 2863.5 $cm^{-1}$ imply the high defect densities as well as the few-layer nature of the 3DPG sample, which are in good agreement with the SEM and HRTEM analyses (Zhou et al., 2018). The XPS spectrum of the obtained sample is revealed in **Figure S1** (Supporting Information), which shows C, O, and N elements corresponding to atomic contents of 82.63, 9.38, and 7.99%, respectively in the 3DPG sample. To further investigate the chemical state of C in the 3DPG sample, we analyze the C 1s spectra in **Figure 2D**. The C 1s spectrum can be deconvoluted into three peaks ascribed to the $sp^2$ carbon atoms (C-C, 284.8 eV), hydroxy/epoxy groups (C-O, 286.0 eV), and carboxyl group (-COOH, 288.3 eV). The O 1s spectrum of 3DPG in **Figure 2E** can be deconvoluted into two apparent peaks assigned to C-O (398.6 eV) and -COOH groups (400.2 eV) (Zhu et al., 2015). The oxygen functional groups might endow the 3DPG with high electrochemical activity. The N 1s spectrum of 3DPG in **Figure 2F** displays two types of binding configurations, including pyridinic-N (511.2 eV) and graphitic-N (532.9 eV). The presence of N 1s and O 1s spectra indicates the successful introduction of N and O in the 3DPG sample, which is capable of boosting electrical conductivity and electrochemical activity (Zhang et al., 2016; Nandan and Nanda, 2017; Xiao et al., 2018).

## Electrochemical Characterization of SCs

The electrochemical performance of the symmetric SCs based on 3DPG electrodes was measured at a voltage of 2.5 V in a button cell with a commercial DLC301 organic electrolyte. The cyclic voltammetry (CV) curves of 3DPG//3DPG SCs presents nearly symmetric rectangular shapes at the scan rates ranging from 10 to 100 mV $s^{-1}$, suggesting the good capacitive performance of the device (**Figure 3A**). The GCD profiles of 3DPG//3DPG SCs at the different current densities of 0.25–3 mA $cm^{-2}$ were collected in **Figure 3B**. It can be clearly seen that the shape of the profiles is somewhat deviated from the linear slope of an ideal supercapacitor, again demonstrating its excellent Coulombic efficiency and capacitive performance. More interestingly, the

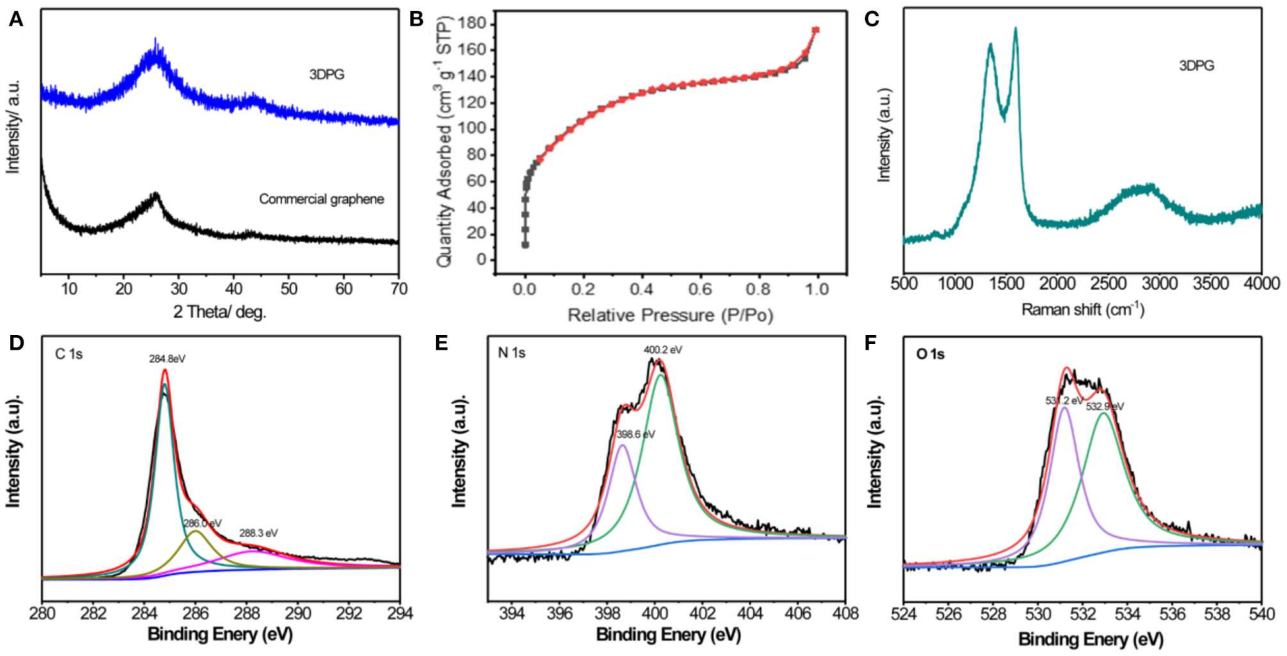

**FIGURE 2 | (A)** XRD patterns of 3DPG and commercial graphene, **(B)** Nitrogen adsorption isotherm at 77 K, **(C)** Raman spectra and **(D)** C 1s, **(E)** N 1s, **(F)** O 1s XPS spectrums of 3DPG.

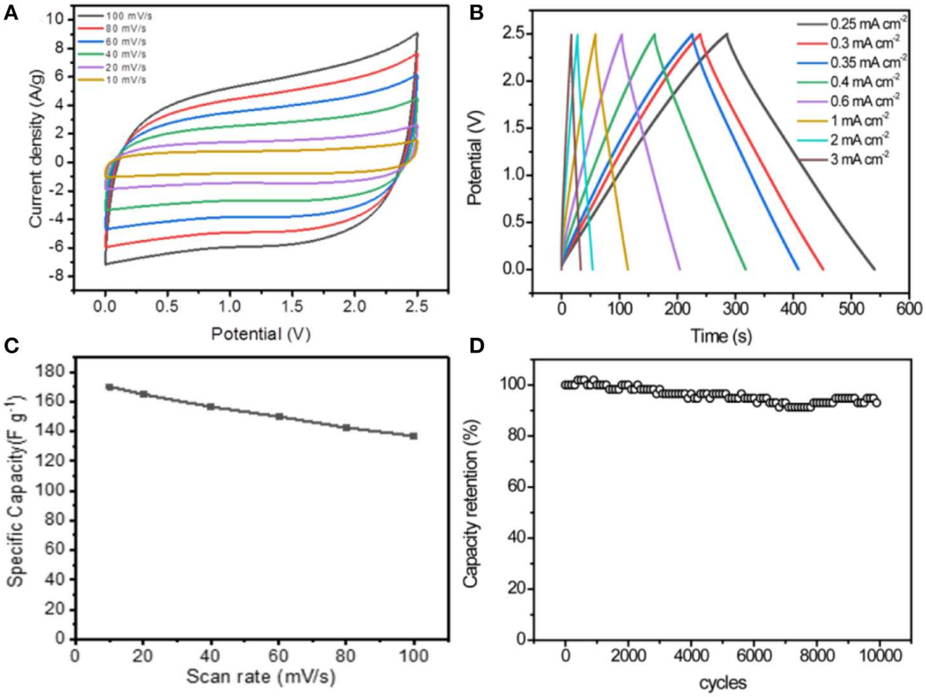

**FIGURE 3 | (A)** CV curves at different scan rates, **(B)** GCD curves at different current densities, **(C)** The rate performance, and **(D)** Cycling stability at 50 mA $s^{-1}$ of 3DPG//3DPG SCs.

3DPG//3DPG SCs delivers a maximum capacitance of 168.9 F $g^{-1}$ at the scan rate of 10 mV $s^{-1}$ and an outstanding rate capability with 81.5% retention of its initial capacitance with the current density increase to 100 mV $s^{-1}$ (**Figure 3C**). Furthermore, the cycling performance of the symmetric SC device was investigated continually by CV measurement at a

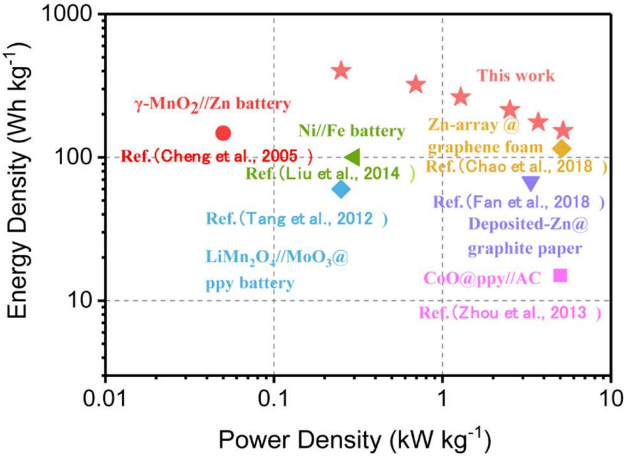

**FIGURE 4 |** Ragone plots of the 3DPG//3DPG SCs and other recently reported energy storage devices for comparison.

current density of 50 mV s$^{-1}$ in **Figure 3D**. Significantly, this 3DPG//3DPG SC exhibits excellent cyclic durability with nearly 96% capacitance retention after 10,000 cycles. Based on the discussion above, such admirable electrochemical performance of the 3DPG//3DPG SC can be ascribed to the following reasons: (1) the N-doping greatly improves the reactivity and electrical conductivity via the generation of extrinsic defects, endowing the electrode with a superior electrochemical performance, (2) the introduction of oxygen functional groups boosts its high electrochemical activity, and (3) Its specific porous structure and notable graphene wrinkles can provide massive electrochemically active sites (Zhu et al., 2016; Zhang et al., 2016; Antink et al., 2017; Chen et al., 2017).

The Ragone plot in **Figure 4** compares the energy and power densities of the symmetric 3DPG//3DPG SCs with some other recently reported energy storage devices. Impressively, our device delivers a maximum energy density of 401.2 Wh kg$^{-1}$ at a power density of 0.25 kW kg$^{-1}$. Even at a high-power density of 5.2 W kg$^{-1}$, it still achieves an exceptionally high energy density of 153.2 Wh kg$^{-1}$. Notably, the energy-power characteristic of our 3DPG//3DPG SC is superior to that of recently reported energy storage devices, such as γ-MnO$_2$//Zn battery (156.1 Wh kg$^{-1}$, 0.05 kW kg$^{-1}$) (Cheng et al., 2005), Ni//Fe battery (100 Wh kg$^{-1}$, 0.3 kW kg$^{-1}$) (Liu et al., 2014), Zn-array@graphene foam (115 Wh kg$^{-1}$, 5.1 kW kg$^{-1}$) (Chao et al., 2018), LiMn$_2$O$_4$//MoO$_3$@ppy battery (60 Wh kg$^{-1}$, 0.25 kW kg$^{-1}$) (Tang et al., 2012), Deposited-Zn@graphite paper (65.1 Wh kg$^{-1}$, 3.34 kW kg$^{-1}$) (Fan et al., 2018), CoO@ppy//AC (11.8 Wh kg$^{-1}$, 5.5 kW kg$^{-1}$) (Zhou et al., 2013).

## CONCLUSIONS

In conclusion, a facile and cost-effective approach was demonstrated to implement the large scale production of three-dimensional porous graphene derived from chitosan. The formation of a porous structure after the crosslinking process and the notable graphene wrinkles provide abundant electrochemically active sites for charge storage. Simultaneously, the introduction of oxygen functional groups and N dopants further strengthen the electrochemical activity and the electrical conductivity of the 3DPG electrode. Accordingly, an advanced symmetric SC is rationally constructed by assembling two 3DPG electrodes in commercial DLC301 organic electrolyte. The device shows an excellent capacitance of 168.9 F g$^{-1}$ at the scan rate of 10 mV s$^{-1}$ and a superior rate capability with 81.5% capacitance retention, accompanied by superior cyclic durability with 96% capacitance retention after 10,000 cycles. In consequence, such an efficient approach is of great significance in promoting the widespread application of graphene for energy storage.

## AUTHOR CONTRIBUTIONS

CW and GZ conducted the experiments. WS and WZ contributed to scientific discussions and research suggestions. KX helped with writing. CW, SW, ZW, and KX performed the characterization and data analysis. All authors involved the analysis of experimental data and manuscript preparation.

## FUNDING

This work was financially supported by the National Key Research and Development Program of China (Grant No. 2016YFB0901600).

## SUPPLEMENTARY MATERIAL

The Supplementary Material for this article can be found online at: https://www.frontiersin.org/articles/10.3389/fenrg.2020.00061/full#supplementary-material

## REFERENCES

Antink, W., Choi, Y., Seong, K., Kim, J., and Piao, Y. (2017). Recent progress in porous graphene and reduced graphene oxide-based nanomaterials for electrochemical energy storage devices. *Adv. Mater. Inter.* 5:1701212. doi: 10.1002/admi.201701212

Cao, X., Shi, Y., Shi, Y., Shi, W., Lu, G., Huang, X., et al. (2011). Preparation of novel 3D graphene networks for supercapacitor applications. *Small* 22, 3163–3168. doi: 10.1002/smll.201100990

Chao, D., Zhu, C., Song, M., Liang, P., Zhang, X., Tiep, N., et al. (2018). A high-rate and stable quasi-solid-state zinc-ion battery with novel 2D layered zinc orthovanadate array. *Adv. Mater.* 32:1803181. doi: 10.1002/adma.201803181

Chen, J., Duan, M., and Chen, G. (2012). Continuous mechanical exfoliation of graphene sheets via three-roll mill. *J. Mater. Chem.* 37:19625. doi: 10.1039/c2jm33740a

Chen, L., Lu, Y., Yu, L., and Lou, X. (2017). Designed formation of hollow particle-based nitrogen-doped carbon nanofibers for high-performance supercapacitors. *Energ. Environ. Sci.* 10, 1777–1783. doi: 10.1039/C7EE00488E

Chen, Y., Ni, D., Yang, X., Liu, C., Yin, J., and Cai, K. (2018). Microwave-assisted synthesis of honeycomblike hierarchical spherical Zn-doped Ni-MOF as a high-performance battery-type supercapacitor electrode material. *Electrochim. Acta* 278, 114–123. doi: 10.1016/j.electacta.2018.05.024

Cheng, F., Chen, J., Gou, X., and Shen, P. (2005). High-power alkaline Zn–MnO$_2$ batteries using γ-MnO$_2$ nanowires/nanotubes and electrolytic zinc powder. *Adv. Mater.* 22, 2753–2756. doi: 10.1002/adma.200500663

Cui, R., and Zhu, J. (2014). Fabrication of a novel electrochemical immunosensor based on the gold nanoparticles/colloidal carbon nanosphere hybrid material. *Electrochim. Acta* 27, 7814–7817. doi: 10.1016/j.electacta.2010.03.022

Fan, J., Xiao, Q., Fang, Y., Li, L., and Yuan, W. (2018). A rechargeable Zn/graphite dual-ion battery with an ionic liquid-based electrolyte. *Ionics* 25, 1303–1313. doi: 10.1007/s11581-018-2644-x

Gnanasekaran, K., Heijmans, T., Bennekom, S., Woldhuis, H., and Friedrich, H. (2017). 3D printing of CNT- and graphene-based conductive polymer nanocomposites by fused deposition modeling. *Appl. Mater. Today* 9, 21–28. doi: 10.1016/j.apmt.2017.04.003

Guo, Y., Xu, G., Yang, X., Ruan, K., Ma, T., Zhang, Q., et al. (2018). Significantly enhanced and precisely modeled thermal conductivity in polyimide nanocomposites with chemically modified graphene via *in situ* polymerization and electrospinning-hot press technology. *J. Mater. Chem. C* 12, 3004–3015. doi: 10.1039/C8TC00452H

Han, Y., Lu, Y., Shen, S., Zhong, Y., Liu, S., Xia, X., et al. (2019). Enhancing the capacitive storage performance of carbon fiber textile by surface and structural modulation for advanced flexible asymmetric supercapacitors. *Adv. Funct. Mater.* 29, 1806329–1806337. doi: 10.1002/adfm.201806329

Hao, P., Zhao, Z., Leng, Y., Tian, J., Sang, Y., Boughton, R., et al. (2015). Graphene-based nitrogen self-doped hierarchical porous carbon aerogels derived from chitosan for high performance supercapacitors. *Nano Energy* 15, 9–23. doi: 10.1016/j.nanoen.2015.02.035

Kołodynska, D., Krukowska, J., and Thomas, P. (2016). Comparison of sorption and desorption studies of heavy metal ions from biochar and commercial active carbon. *Chem. Eng. J.* 307, 353–363. doi: 10.1016/j.cej.2016.08.088

Liu, J., Chen, M., Zhang, L., Jiang, J., Yan, J., Huang, Y., et al. (2014). A flexible alkaline rechargeable Ni/Fe battery based on graphene foam/carbon nanotubes hybrid film. *Nano Lett.* 14, 7180–7187. doi: 10.1021/nl503852m

Lu, Y., Zeng, S., Zhou, L., Huang, X., Zeng, Y., Zheng, D., et al. (2019). Facile synthesis of porous-carbon nanoarchitectures as advanced and durable electrodes for supercapacitors. *Part. Part. Syst. Charact.* 36:1900115. doi: 10.1002/ppsc.201900115

Nandan, R., and Nanda, K. (2017). Designing N-doped carbon nanotubes and Fe–$Fe_3C$ nanostructures co-embedded in B-doped mesoporous carbon as an enduring cathode electrocatalyst for metal-air batteries. *J. Mater. Chem. A* 5, 16843–16853. doi: 10.1039/C7TA04597B

Ruoff, S., Zhang, L., Zhao, X., Stoller, D., Zhu, Y., Ji, H., et al. (2012). Highly conductive and porous activated reduced graphene oxide films for high-power supercapacitors. *Nano Lett.* 4, 1806–1812. doi: 10.1021/nl203903z

Shao, Y., Du, J., Li, H., Zhao, Y., and Xu, C. (2016). $Ni_{0.37}Co_{0.63}S_2$-reduced graphene oxide nanocomposites for highly efficient electrocatalytic oxygen evolution and photocatalytic pollutant degradation. *J. Solid State Electr.* 21, 183–192. doi: 10.1007/s10008-016-3352-y

Sharma, R., Benjwal, P., and Kar, K. (2015). *Carbon Nanotubes: Synthesis, Properties and Applications*. Kanpur: John Wiley and Sons, Inc. doi: 10.1002/9781119179108.ch4

Shen, C., Yi, J., Yan, X., Zhang, W., and Li, X. (2017). Effects of Cu contamination on system reliability for graphene synthesis by chemical vapor deposition method. *Carbon* 127, 676–680. doi: 10.1016/j.carbon.2017.11.059

Tang, W., Liu, L., Zhu, Y., Sun, H., Wu, Y., and Zhu, K. (2012). An aqueous rechargeable lithium battery of excellent rate capability based on a nanocomposite of $MoO_3$ coated with PPy and $LiMn_2O_4$. *Energ. Environ. Sci.* 5:6909. doi: 10.1039/c2ee21294c

Teng, Y., Mo, M., Yuan, L., Xue, J., and Zhao, H. (2018). Amorphous carbon-coated ZnO porous nanosheets: Facile fabrication and application in lithium- and sodium-ion batteries. *J. All. Compd.* 744, 712–720. doi: 10.1016/j.jallcom.2018.01.191

Wang, R., Lu, Y., Zhou, L., Han, Y., Ye, J., Xu, W., et al. (2018). Oxygen-deficient tungsten oxide nanorods with high crystallinity: promising stable anode for asymmetric supercapacitors. *Electrochim. Acta* 283, 639–645. doi: 10.1016/j.electacta.2018.06.188

Wang, Z., Tammela, P., Strømme, M., and Nyholm, L. (2017). Cellulose-based supercapacitors: material and performance considerations. *Adv. Energ. Mater.* 18:1700130. doi: 10.1002/aenm.201700130

Xiao, X., Zeng, Y., Feng, H., Xu, K., Zhong, G., Wu, S., et al. (2018). Three-dimensional nitrogen-doped graphene frameworks from electrochemical exfoliation of graphite as efficient supercapacitor electrodes. *Chemnanomat.* 4, 1–7. doi: 10.1002/cnma.201800452

Yan, Y., Gu, P., Zheng, S., Zheng, M., Pang, H., and Xue, H. (2016). Facile synthesis of an accordion-like Ni-MOF superstructure for high-performance flexible supercapacitors. *J. Mater. Chem. A* 4:19078. doi: 10.1039/C6TA08331E

Yang, N., Zhai, J., Wang, D., Chen, Y., and Jiang, L. (2017). Two-dimensional graphene bridges enhanced photoinduced charge transport in dye-sensitized solar cells. *ACS Nano* 2, 887–894. doi: 10.1021/nn901660v

Yang, S., Feng, X., and Mullen, K. (2011). Sandwich-like, graphene-based titania nanosheets with high surface area for fast lithium storage. *Adv Mater* 23, 3575–3579. doi: 10.1002/adma.201101599

Yang, Z., Jin, L., Lu, G., Xiao, Q., Zhang, Y., Jing, L., et al. (2014). Sponge-templated preparation of high surface area graphene with ultrahigh capacitive deionization performance. *Adv. Funct. Mater.* 24, 3917–3925. doi: 10.1002/adfm.201304091

Yang, Z., Jin, L., Lu, G., Xiao, Q., Zhang, Y., Jing, L., et al. (2015). Response to comment onsponge-templated preparation of high surface area graphene with ultrahigh capacitive deionization performance. *Adv. Funct. Mater.* 25, 182–183. doi: 10.1002/adfm.201403534

Yu, G., Xing, X., Pan, L., Bao, Z., and Yi, C. (2013). Hybrid nanostructured materials for high-performance electrochemical capacitors. *Nano Energy* 2, 213–234. doi: 10.1016/j.nanoen.2012.10.006

Yu, X., Zhang, W., Zhang, P., and Su, Z. (2017). Fabrication technologies and sensing applications of graphene-based composite films: advances and challenges. *Biosens. Bioelectron.* 89, 72–84. doi: 10.1016/j.bios.2016.01.081

Zhang Q, Han K, Li S, Li M, Li J, Ren K. Synthesis of garlic skin-derived 3D hierarchical porous carbon for high-performance supercapacitors. *Nanoscale* (2018) 10, 2427–2437. doi: 10.1039/C7NR07158B

Zhang, F., Liu, T., Li, M., Yu, M., Luo, Y., Tong, Y., et al. (2017). Multiscale pore network boosts capacitance of carbon electrodes for ultrafast charging. *Nano Lett.* 17, 3097–3104. doi: 10.1021/acs.nanolett.7b00533

Zhang, H., Qiu, W., Zhang, Y., and Han, Y. (2016). Surface engineering of carbon fiber paper for efficient capacitive energy storage. *J. Mater. Chem.* 4:18639. doi: 10.1039/C6TA08138J

Zhang, Z., Zhang, X., Feng, Y., and Sun, Q. (2018). Fabrication of porous $ZnCo_2O_4$ nanoribbon arrays on nickel foam for high-performance supercapacitors and lithium-ion batteries. *Electrochim. Acta* 260, 823–829. doi: 10.1016/j.electacta.2017.12.047

Zhao, D., Zhang, J., Fu, C., Huang, J., Xiao, D., Yuen, M., et al. (2017). Enhanced cycling stability of ring-shaped phosphorus inside multi-walled carbon nanotubes as anodes for lithium-ion batteries. *J. Mater. Chem. A* 6, 2540–2548. doi: 10.1039/C7TA07683E

Zhou, C., Zhang, Y., Li, Y., and Liu, J. (2013). Construction of high-capacitance 3D CoO@Polypyrrole nanowire array electrode for aqueous asymmetric supercapacitor. *Nano Lett.* 13, 2078–2085. doi: 10.1021/nl400378j

Zhou, F., Huang, H., Xiao, C., Zheng, S., Shi, X., Qin, J., et al. (2018). Electrochemically scalable production of fluorine-modified graphene for flexible and high-energy ionogel-based microsupercapacitors. *J. Am. Chem. Soc.* 140, 8198–8205. doi: 10.1021/jacs.8b03235

Zhu, G., Xi, C., Liu, Y., Zhua, J., and Shen, X. (2015). CN foam loaded with few-layer graphene nanosheets for high-performance supercapacitor electrodes. *J. Mater. Chem. A.* 3, 7591–7599. doi: 10.1039/C5TA00837A

Zhu, J., Childress, A., Karakaya, M., Dandeliya, S., and Podila, R. (2016). Defect-engineered graphene for high-energy and high-power density supercapacitor devices. *Adv. Mater.* 33, 7185–7192. doi: 10.1002/adma.201602028

**Conflict of Interest:** All the authors are now employed by the company Electric Power Research Institute of Guangdong Power Grid Co., Ltd. The authors declare that this study received funding from the National Key Research and Development Program of China (Grant No. 2016YFB0901600). The funder was not involved in the study design, collection, analysis, interpretation of data, the writing of this article or the decision to submit it for publication.

frontiers in Energy Research

PERSPECTIVE
published: 23 June 2020
doi: 10.3389/fenrg.2020.00125

# Overlooking Issues and Prospective Resolutions Behind the Prosperity of Three-Dimensional Porous Carbon Supercapacitor Electrodes

*Tianyu Liu**

*Department of Chemistry, Virginia Polytechnic Institute and State University, Blacksburg, VA, United States*

The past decade has witnessed the boom of porous carbon materials, especially three-dimensional (3D) ones, as supercapacitor electrode materials. Their large surface areas, tunable pore volumes, adjustable degrees of pore interconnectivity, and the potential to possess hierarchical porous networks have enabled them to achieve simultaneously high capacitance and excellent rate capability. This feature is challenging for non-3D counterparts but favorable for supercapacitors. However, behind the prosperity come the problems, and unfortunately, most of the issues are left unacknowledged and unaddressed in the literature available. This perspective aims to identify these problems, discuss the reasons for overlooking, and provide possible solutions to address these issues. The author wishes this article will draw the attention of researchers in electrochemical energy storage to tackle these roadblocks in the future development of 3D porous carbon electrodes in supercapacitors.

**Keywords: three-dimensional, pore, carbon, supercapacitor, electrodes, overlooking issue**

**Edited by:**
*Jun Yan,*
*Harbin Engineering University, China*

**Reviewed by:**
*Hao Chen,*
*Zhejiang Agriculture and Forestry University, China*
*Shulan Wang,*
*Northeastern University, China*
*Hongying Quan,*
*Nanchang Hangkong University, China*

***Correspondence:**
*Tianyu Liu*
*tliu23@vt.edu*

**Specialty section:**
*This article was submitted to Electrochemical Energy Conversion and Storage, a section of the journal Frontiers in Energy Research*

**Received:** *29 April 2020*
**Accepted:** *25 May 2020*
**Published:** *23 June 2020*

**Citation:**
*Liu T (2020) Overlooking Issues and Prospective Resolutions Behind the Prosperity of Three-Dimensional Porous Carbon Supercapacitor Electrodes. Front. Energy Res. 8:125. doi: 10.3389/fenrg.2020.00125*

## INTRODUCTION

Accompanying with the boom of electrochemical energy storage, three-dimensional (3D) porous carbon materials have emerged as rising stars of electrodes in supercapacitors. Supercapacitors, including electrical double-layer capacitors and pseudocapacitors, are electrochemical energy storage devices with power density typically about 100 times higher than those of rechargeable batteries. Their high power density bestows their applications in ultrafast charging and discharging scenarios (Miller and Simon, 2008; Salunkhe et al., 2014). As indispensable components in supercapacitors, electrodes having ultrasmall electrical resistance and ultrahigh surface areas are preferred. Therefore, a diverse array of highly conductive carbon materials with tunable morphologies have become supercapacitor electrode candidates for decades.

One of the representative conventional supercapacitor carbon electrodes is activated carbon. These carbon particles possess abundant micropores and surface areas surpassing 1,000 $m^2$ $g^{-1}$. They store charges mainly *via* the formation of electrical double layers and are used in electrical double-layer capacitors (Ji et al., 2014) or capacitive electrodes in supercapacitor-battery hybrids (Liu H. et al., 2020). Activated carbon, however, is far from ideal. Its disadvantage is two-folded. On the one hand, its powdered form demands polymer binders when being processed into electrodes, which introduces unnecessary internal resistance born from the particle-particle contact resistance as well as the low electrical conductivity of the binders (Liu T. et al., 2020). On the other hand, the micropore-dominated porous structure of activated carbon impedes ion diffusion throughout a particle, limiting the pore accessibility and, subsequently, the capacitance and energy density (Zhang et al., 2017). These two drawbacks make activated carbon unsuitable for storing large amounts of charges at elevated charge and discharge rates, the conditions under which supercapacitors are supposed to work.

The shortcomings of conventional powdered porous carbon materials have motivated the development of three-dimensional porous carbons as supercapacitor electrodes within the past decade. 3D porous carbons with high surface areas and easy ion-accessible pores allow capacitance and remarkable rate capability mutually achievable (Liu et al., 2017). Besides, the structural and morphological diversity and tunability derived from the versatility in sources and synthesis processes have generated a tremendous number of 3D carbon supercapacitor electrodes in the literature (Zhu et al., 2016; Zhang et al., 2017, 2019; Yang et al., 2019). The variety in structural parameters, including surface areas, pore interconnectivity, pore volumes, pore size distributions, and surface functionalities, is far more significant than those of non-3D carbon counterparts. These characteristics have also pushed the capacitance of carbon materials to beyond 300 F $g^{-1}$ (Liu et al., 2017), a level unattainable by conventional porous carbon materials such as activated carbon.

The thrive of 3D porous carbon materials, however, brings about issues that compromise the scientific quality and integrity of relevant works. Unfortunately, most of the problems have been left unacknowledged and unaddressed (**Figure 1**). Without exhaustively examining the literature, this perspective aims to analyze these critical issues that the author hopes to initiate discussions and cultivate consensuses among the researchers in the field of electrochemical energy storage. Corresponding solutions are given in each section below.

## COMPRESSING DAMAGES 3D STRUCTURE

Mechanical pressing or calendering, which improve the contact between carbon materials and their current collectors, are needed for manufacturing supercapacitor electrodes. These processes not only reduce the contact resistance of supercapacitor electrodes (Dsoke et al., 2013), but also increase the volumetric performance metrics such as volumetric capacitance, energy density, and power density, due to volumetric densification. As a result, most researchers mechanically compress their as-prepared 3D carbon materials onto conductive substrates, e.g., nickel foam (Zhang et al., 2017) and aluminum foil (Shah et al., 2020). In some cases, 3D porous carbon materials are ground into powders, blended with binders and carbon black (electrically conductive additive) when making electrodes (Deng et al., 2019; Nawwar et al., 2020). Inevitably, the delicate 3D architectures of the active materials are substantially altered, if not entirely demolished, after compression or grinding. Therefore, claiming that hierarchical porous structures facilitate ion diffusion or render outstanding rate capability based on morphologies before compression or grinding is inappropriate to reflect the actual working conditions of 3D porous carbon materials.

The most straightforward resolution is to avoid compressing or grinding 3D porous carbon materials. For example, Zhu et al. attached compressed Ni foam onto 3D-printed graphene aerogels using silver paste (Zhu et al., 2016), and Zhai et al. soldered copper foil onto Ni-foam-templated graphene foam (Zhai et al., 2015), both of which preserved the 3D morphologies of the active materials. However, silver or solder are prone to oxidation under positive biases, giving rise to unwanted oxidation current and redox peaks. These problems require proper sealing of the contact points (e.g., by epoxy) that complicates the fabrication, adds electrode dead mass, and leads to substantial performance deviations due to the variation in the sealant coverage. Additionally, the contact resistance might be large or small, depending on the adhesion strength between the electrodes and the current collectors. This factor makes the electrochemical performance irreproducible.

A relatively simple solution is to acknowledge the necessity of compression, but provide comprehensive characterizations to support discussions. Probing the morphologies of compressed 3D porous carbon materials is necessary. Based on the author's experience, compression only shrinks macropores. Still, it preserves mesopores and micropores, so the surface area of a 3D porous carbon material will unlikely decrease significantly compared to its uncompressed form. If macropores are partially maintained, the 3D porous network of the carbon material is still retained, though the morphology is different. Grinding, on the contrary, will most likely destroy 3D architectures entirely to broken particles and hence, is not recommended for processing 3D porous carbon materials. Top-view and cross-sectional-view scanning electron microscopy images are critical to illustrate the compressed morphologies of the active materials. Characterizing the compressed carbon materials with gas physisorption is imperative to gauge any subtle changes in the surface areas and pore size distributions. Both techniques provide foundations for discussing the structure-performance relationship of 3D porous carbon electrodes. For readers to gain comprehensive understandings of the reported materials, supplementing typical characterization results of as-prepared 3D porous carbon materials with those of compressed counterparts is encouraged.

## TO BE OR NOT TO BE SELF-STANDING?

Self-standing has emerged as a fashion term to describe the feature of 3D porous carbon electrodes. However, arbitrarily using this word without considering the characteristic of the electrodes can lead to false and misleading information.

The difference between "self-standing material" and "self-standing electrode" must be strictly distinguished. Monolithic 3D porous carbon materials should be self-standing by nature, but whether they constitute self-standing electrodes depend on the fabrication method. If binders are used to bind 3D carbon materials or their grounded granules when making electrodes, such binder-containing electrodes can no longer be called self-standing. Rigorously speaking, electrodes are not self-standing if current collectors are used; however,

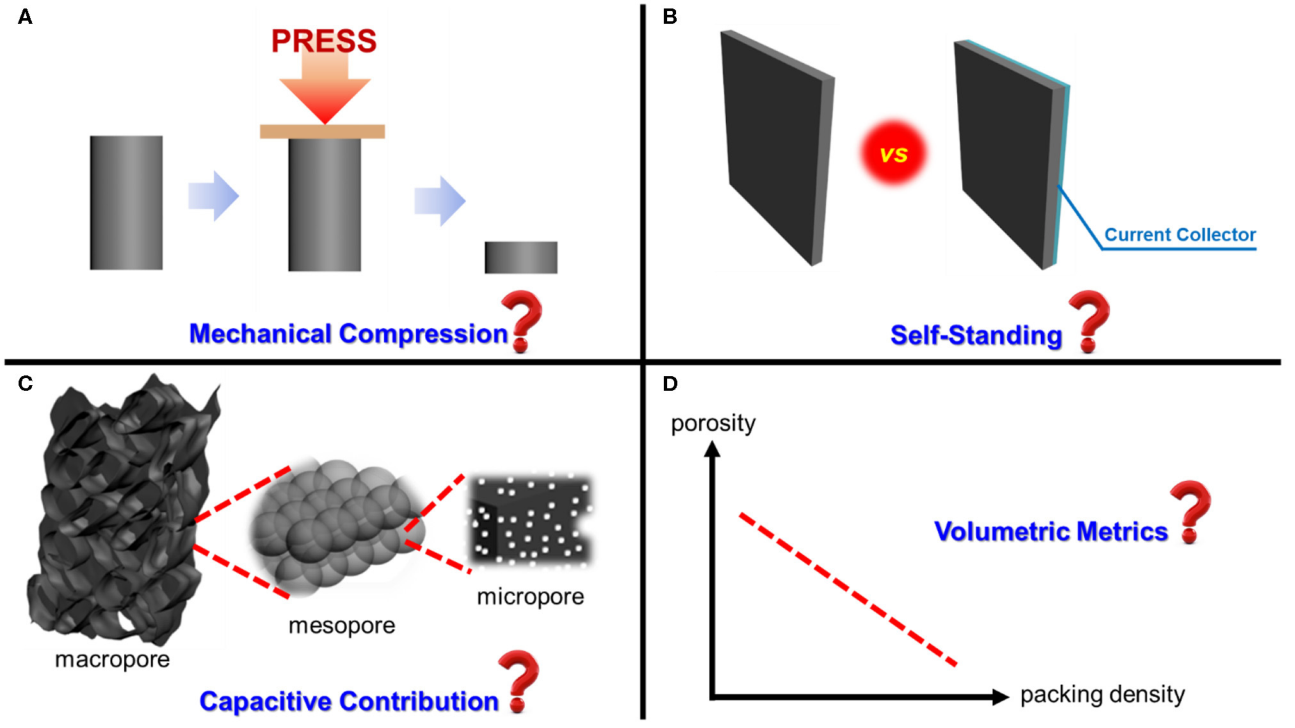

**FIGURE 1 |** Four typical overlooking issues associated with three-dimensional porous carbon supercapacitor electrodes: **(A)** Compressing damages 3D structures; **(B)** Correctly use of "self-standing;" **(C)** Explaining capacitive contributions of different pores; **(D)** Acknowledging the trade-off between porosity and packing density in terms of volumetric metrics.

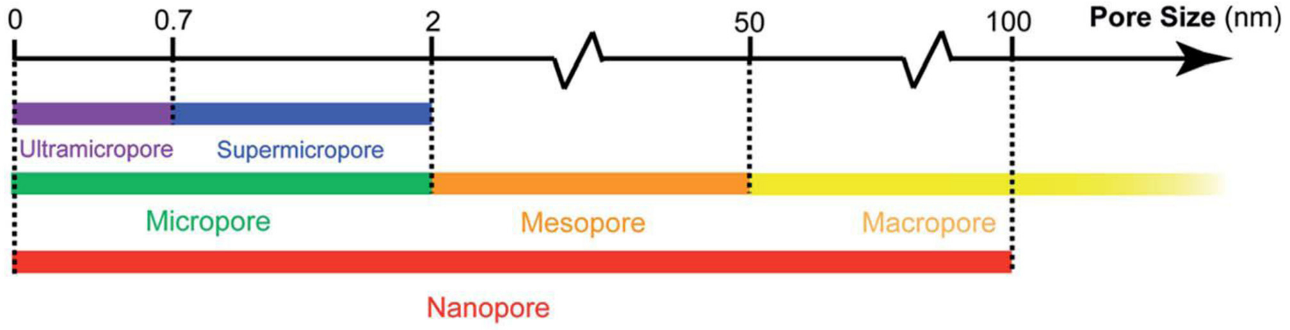

**FIGURE 2 |** Nomenclatures of pores, according to the International Union of Pure and Applied Chemistry (IUPAC) (Thommes et al., 2015). Figure reproduced with permission from Liu et al. (2017). Copyright 2017, Royal Society of Chemistry.

the author believes that removing current collectors will create unnecessary technical challenges to the evaluation of supercapacitor electrodes, so calling binder-free electrodes self-standing is acceptable.

This issue calls for the transparency of experimental conditions. Authors reporting 3D carbon electrodes in supercapacitors or electrochemical energy storage, if broadly speaking, need to present explicitly how the electrodes are made. These conditions include the use of current collectors, compositions and manufacturers of current collectors, how carbon materials are adhered to current collectors (e.g., use of binders or direct compressing), as well as the mass loadings of active materials. The bottom line is that any researchers should be able to reproduce the experiments following the provided technical details with absolutely no confusion.

## ELUCIDATING PORE CONTRIBUTIONS

One of the unique structural features of 3D porous carbon materials is their hierarchically porous structures, that is, structures with interconnecting pores of different sizes (**Figure 2**) assembled into hierarchical networks. Porous materials that contain multiscale but spatially isolated pores are not hierarchical, because their pores cannot "communicate" with each other during charge and discharge processes. Due to the diversified pore sizes and shapes, differentiating the capacitive contributions of the pores becomes increasingly critical to rationalize the design of next-generation porous carbon supercapacitor electrodes.

Despite extensive investigations, the contributions of different pores have yet reached an agreement. The general belief is that macropores and mesopores contribute little to capacitance, but they help electrolyte infiltration and facilitate ion diffusion, both of which improve the ion accessibility to micropores (Yang et al., 2017). Zhang et al. have experimentally verified that sub-micron macropores and mesopores in a chitosan-derived carbon aerogel are indispensable for maintaining its excellent rate capability (Zhang et al., 2017). Micropores are mainly responsible for high surface areas and ion storage, resulting in capacitance. The general belief, however, is challenged by simulation works that show macropores and mesopores are unnecessary, as they facilitate electrolyte infiltration but not ion diffusion (Borchardt et al., 2018). Others have revealed that micropores of pore openings less than 1 nm can accelerate ion diffusion due to the ion packing patterns in ionophobic pores (Mo et al., 2020). Although the author is puzzled about the exact causes of the discrepancy between the simulation results and experimental observations, a possible reason is the different experimental setups. Most simulations choose ionic liquids as study objects because of their simplicity (no solvent molecules and ion solvation) to reduce calculation costs. In contrast, the majority of laboratory supercapacitors adopt aqueous electrolytes because of their safety, ease of fabrication, and intrinsically rapid ion diffusion.

Besides simulations, some experimental observations also contradict the general belief. For example, depending on the source, commercial activated carbon can contain mesopores slightly bigger than 2 nm, according to $N_2$-physisorption (Liu T. et al., 2020), but their capacitance still decreases dramatically at elevated discharging rates. Carbide-derived carbons, though possessing large numbers of mesopores and macropores, still exhibit satisfactory rate capability in aqueous electrolytes (Huang et al., 2016).

These outliers in the literature highlight the complex roles of various pores. Perhaps the pore geometry, surface functionality, and graphitization degrees of 3D porous carbon electrodes all profoundly alter the electrochemical responses. For example, Dyatkin et al. simulated that the oxygen functional groups inside pores attracted planar anions in ionic liquids. This attraction aligned the anions in parallel to the pore surface and provided relatively clear transport channels to enhance rate capability (Dyatkin et al., 2016). The alliance between experimentalists and theorists, as well as alignment between experimental conditions and computational inputs, are undoubtedly indispensable to drive future investigations on the charge-storage mechanisms of 3D porous carbon electrodes. Additionally, the progress of advanced characterization methods, including quasi-elastic neutron scattering (Osti and Mamontov, 2020), quartz crystal microbalance (Levi et al., 2016), *in-situ* nuclear magnetic resonance spectroscopy (Forse et al., 2017), are vital tools for future investigations. Supporting experimental findings with simulation results in a research article is strongly encouraged if condition permits. This practice may become a new norm for publishing manuscripts in top-tier journals and can reward interdisciplinary researches with crystal-clear mutual communications among all the practitioners involved. The author believes that the role-determination of pores in versatile 3D porous carbon materials will remain as frontiers in electrochemical energy storage.

## PACKING DENSITY *VS.* POROSITY

Perhaps the most common criticism of 3D porous carbon electrodes is their large porosity that declines the packing density of an electrode. Small packing density leads to low volumetric performance metrics, such as volumetric capacitance.

While the author fully agrees that volumetric metrics are crucial for rechargeable batteries whose working space is tight (Choi and Aurbach, 2016), the working environments of supercapacitors are far more diversified than those of batteries. 3D porous carbon materials with large porosity have the advantage of low volumetric density or lightweight. This characteristic makes them especially suitable for portable electronics needing high power density, such as drills and drones (Lin et al., 2018). In such cases, the volume of an energy-storage device is less considerable than its weight. Therefore, the author believes that it is unfair to criticize 3D porous carbon electrodes based on their low packing density. Comprehensive evaluations of a 3D porous carbon electrode and reporting a full set of gravimetric, areal, and volumetric performance metrics are highly recommended.

Another issue calling attention is the report of the gravimetric capacitance of 3D porous carbon materials. The relationship between the total capacitance ($C_T$) and gravimetric capacitance, or specific capacitance ($C_m$), of an electrode, is:

$$C_T = C_m \times m$$

where $m$ is the mass of active materials. Based on this equation, achieving ultrahigh numbers of gravimetric capacitance becomes diminishingly meaningful if the mass loading of the active material is limited, as the total capacity is insignificant. Therefore, it is always a good practice to report gravimetric performance in the context of mass loading. For commercial viability, the mass loading of an electrode material must be 10 mg $\text{cm}^{-2}$ or above (Chen et al., 2020). Still, this standard should not be rigid to restrict the development of laboratory-scale supercapacitors, which usually involve mass loadings of active materials between 1 and 10 mg $\text{cm}^{-2}$. Nevertheless, explicitly reporting mass loading and accurately characterizing the influence of mass loading on electrochemical performance are always welcome and practically meaningful (Lin et al., 2015). Additionally, as areal capacitance depends on mass loading, reporting both gravimetric capacitance and areal capacitance for single electrodes is beneficial to avoid deceitfully excellent charge-storage performance.

## CONCLUSIONS AND OUTLOOKS

This perspective highlights four main issues behind the prosperity of 3D porous carbon materials as supercapacitor electrodes. They are mostly overlooked in the existing literature, and if continually left unaddressed, are harmful to the healthy development of supercapacitors. Hence, the article presents the current understanding, points out the existing challenges, and discusses the possible resolutions of each issue. The author hopes this perspective will draw the attention of the practitioners in the electrochemical energy storage community to address the issues by intimate collaboration, protocol unification, and frequent idea exchange in the ensuing years.

## AUTHOR CONTRIBUTIONS

The author confirms being the sole contributor of this work and has approved it for publication.

## ACKNOWLEDGMENTS

We acknowledges Dr. Francesco Coneri for his assistance in arranging the submission of this article.

## REFERENCES

Borchardt, L., Leistenschneider, D., Haase, J., and Dvoyashkin, M. (2018). Revising the concept of pore hierarchy for ionic transport in carbon materials for supercapacitors. *Adv. Energy Mater.* 8:1800892. doi: 10.1002/aenm.201800892

Chen, R., Yu, M., Sahu, R. P., Puri, I. K., and Zhitomirsky, I. (2020). The development of pseudocapacitor electrodes and devices with high active mass loading. *Adv. Energy Mater.* 10:1903848. doi: 10.1002/aenm.201903848

Choi, J. W., and Aurbach, D. (2016). Promise and reality of post-lithium-ion batteries with high energy densities. *Nat. Rev. Mater.* 1:16013. doi: 10.1038/natrevmats.2016.13

Deng, X., Zhua, S., Li, J., He, F., Liu, E., He, C., et al. (2019). Bio-inspired three-dimensional carbon network with enhanced mass-transfer ability for supercapacitors. *Carbon* 143, 728–735. doi: 10.1016/j.carbon.2018.11.055

Dsoke, S., Tian, X., Täubert, C., Schlüter, S., and Wohlfahrt-Mehrens, M. (2013). Strategies to reduce the resistance sources on electrochemical double layer capacitor electrodes. *J. Power Sources* 238, 422–429. doi: 10.1016/j.jpowsour.2013.04.031

Dyatkin, B., Zhang, Y., Mamontov, E., Kolesnikov, A. I., Cheng, Y., Meyer, H. M., et al. (2016). Influence of surface oxidation onion dynamics and capacitance in porous and nonporous carbon electrodes. *J. Phys. Chem. C* 120, 8730–8741. doi: 10.1021/acs.jpcc.6b01204

Forse, A. C., Griffin, J. M., Merlet, C., Carretero-Gonzalez, J., Raji, A.-R. O., Trease, N. M., et al. (2017). Direct observation of ion dynamics in supercapacitor electrodes using *in situ* diffusion NMR spectroscopy. *Nat Energy* 2:16216. doi: 10.1038/nenergy.2016.216

Huang, P., Lethien, C., Pinaud, S., Brousse, K., Laloo, R., Turq, V., et al. (2016). On-chip and freestanding elastic carbon films for micro-supercapacitors. *Science* 351, 691–695. doi: 10.1126/science.aad3345

Ji, H., Zhao, X., Qiao, Z., Jung, J., Zhu, Y., Lu, Y., et al. (2014). Capacitance of carbon-based electrical double-layer capacitors. *Nat. Commun.* 5:3317. doi: 10.1038/ncomms4317

Levi, M. D., Daikhin, L., Aurbach, D., and Presser, V. (2016). Quartz crystal microbalance with dissipation monitoring (EQCM-D) for in-situ studies of electrodes for supercapacitors and batteries: a mini-review. *Electrochem. Commun.* 67, 16–21. doi: 10.1016/j.elecom.2016.03.006

Lin, T., Chen, I. W., Liu, F., Yang, C., Bi, H., Xu, F., et al. (2015). Nitrogen-doped mesoporous carbon of extraordinary capacitance for electrochemical energy storage. *Science* 350, 1508–1513. doi: 10.1126/science.aab3798

Lin, Z., Goikolea, E., Balducci, A., Naoi, K., Taberna, P. L., Salanne, M. G., et al. (2018). Materials for supercapacitors: When Li-ion battery power is not enough. *Mater. Today* 21, 419–436. doi: 10.1016/j.mattod.2018.01.035

Liu, H., Liu, X., Wang, S., Liu, H.-K., and Li, L. (2020). Transition metal based battery-type electrodes in hybrid supercapacitors: a review. *Energy Stor. Mater.* 28, 122–145. doi: 10.1016/j.ensm.2020.03.003

Liu, T., Serrano, J., Elliott, J., Yang, X., Cathcart, W., Wang, Z., et al. (2020). Exceptional capacitive deionization rate and capacity by block copolymer–based porous carbon fibers. *Sci. Adv.* 6:eaaz0906. doi: 10.1126/sciadv.aaz0906

Liu, T., Zhang, F., Song, Y., and Li, Y. (2017). Revitalizing carbon supercapacitor electrodes with hierarchical porous structures. *J. Mater. Chem. A* 5, 17151–17173. doi: 10.1039/c7ta05646j

Miller, J. R., and Simon, P. (2008). Materials science. Electrochemical capacitors for energy management. *Science* 321, 651–652. doi: 10.1126/science.1158736

Mo, T., Bi, S., Zhang, Y., Presser, V., Wang, X., Gogotsi, Y., et al. (2020). Ion structure transition enhances charging dynamics in subnanometer pores. *ACS Nano* 14, 2395–2403. doi: 10.1021/acsnano.9b09648

Nawwar, M., Sahu, R. P., Puri, I. K., and Zhitomirsky, I. (2020). Functionally decorated carbon nanotube networks for energy storage in supercapacitors. *Front. Energy Res.* 8:46. doi: 10.3389/fenrg.2020.00046

Osti, N. C., and Mamontov, E. (2020). Microscopic dynamics in room-temperature ionic liquids confined in materials for supercapacitor applications *Sust. Energy Fuels* 4, 1554–1575. doi: 10.1039/C9SE00829B

Salunkhe, R. R., Lee, Y. H., Chang, K. H., Li, J. M., Simon, P., Tang, J., et al. (2014). Nanoarchitectured graphene-based supercapacitors for next-generation energy-storage applications. *Chemistry* 20, 13838–13852. doi: 10.1002/chem.201403649

Shah, S. A., Kulhanek, D., Sun, W., Zhao, X., Yu, S., Parviz, D., et al. (2020). Aramid nanofiber-reinforced three-dimensional graphene hydrogels for supercapacitor electrodes. *J. Colloid Interface Sci.* 560, 581–588. doi: 10.1016/j.jcis.2019.10.066

Thommes, M., Kaneko, K., Neimark, A. V., Olivier, J. P., Rodriguez-Reinoso, F., Rouquerol, J., et al. (2015). Physisorption of gases, with special reference to the evaluation of surface area and pore size distribution (IUPAC Technical Report). *Pure Appl. Chem.* 87, 1051–1069. doi: 10.1515/pac-2014-1117

Yang, J., Wu, H., Zhu, M., Ren, W., Lin, Y., Chen, H., et al. (2017). Optimized mesopores enabling enhanced rate performance in novel ultrahigh surface area meso-/microporous carbon for supercapacitors. *Nano Energy* 33, 453–461. doi: 10.1016/j.nanoen.2017.02.007

Yang, S., Wang, S., Liu, X., and Li, L. (2019). Biomass derived interconnected hierarchical micro-meso-macro- porous carbon with ultrahigh capacitance for supercapacitors. *Carbon* 147, 540–549. doi: 10.1016/j.carbon.2019.03.023

Zhai, T., Lu, X., Wang, H., Wang, G., Mathis, T., Liu, T., et al. (2015). An electrochemical capacitor with applicable energy density of 7.4 Wh/kg at average power density of 3000 W/kg. *Nano Lett.* 15, 3189–3194. doi: 10.1021/acs.nanolett.5b00321

Zhang, F., Liu, T., Li, M., Yu, M., Luo, Y., Tong, Y., et al. (2017). Multiscale pore network boosts capacitance of carbon electrodes for ultrafast charging. *Nano Lett.* 17, 3097–3104. doi: 10.1021/acs.nanolett.7b00533

Zhang, Y., Yang, S., Wang, S., Liu, X., and Li, L. (2019). Microwave/freeze casting assisted fabrication of carbon frameworks derived from embedded upholder in tremella for superior performance supercapacitors. *Energy Storage Mater.* 18, 447–455. doi: 10.1016/j.ensm.2018.08.006

Zhu, C., Liu, T., Qian, F., Han, Y.-J., Duoss, E. B., Kuntz, J. D., et al. (2016). Supercapacitors based on three-dimensional hierarchical graphene aerogels with periodic macropores. *Nano Lett.* 16, 3448–3456. doi: 10.1021/acs.nanolett.5b04965

**Conflict of Interest:** The author declares that the research was conducted in the absence of any commercial or financial relationships that could be construed as a potential conflict of interest.

frontiers in Energy Research

BRIEF RESEARCH REPORT
published: 24 June 2020
doi: 10.3389/fenrg.2020.00109

# Three-Dimensional Carbon-Supported $MoS_2$ With Sulfur Defects as Oxygen Electrodes for Li-$O_2$ Batteries

**Yun Liu[1], Yipeng Zang[1], Xinmiao Liu[1], Jinyan Cai[1], Zheng Lu[1], Shuwen Niu[1], Zhibin Pei[2]*, Teng Zhai[3] and Gongming Wang[1]***

[1] Hefei National Laboratory for Physical Sciences at the Microscale, Department of Chemistry, University of Science & Technology of China, Hefei, China, [2] School of Environment and Energy, South China University of Technology, Guangzhou, China, [3] School of Materials Science and Engineering, Nanjing University of Science and Technology, Nanjing, China

Recently, Li-$O_2$ batteries have been considered to be promising next-generation energy storage devices owing to their high theoretical specific energy. However, due to the sluggish reaction kinetics of oxygen conversion, practical applications cannot achieve the desired results. By introducing vacancies in the $MoS_2$ basal plane and using an *in-situ* synthesis method, we demonstrated the excellent catalysis of $MoS_{2-x}$ for oxygen redox kinetics, which can improve Li-$O_2$ battery performance. The prepared $MoS_{2-x}$ displays little polarization, with a potential gap of 0.59 V and a high discharge capacity of 8,851 mA h $g^{-1}$ at a current density of 500 mA $g^{-1}$. The improved performance is mainly attributable to abundant S defects and plentiful diffusion channels in the $MoS_{2-x}$/carbon 3D structural cathodes, which enable the adsorption of gaseous oxygen, reaction intermediates, and discharge products. To the best of our knowledge, these structures fabricated through 3D network design and surface modulation are among the best oxygen conversion catalysts developed so far, offering a new vista for the design of Li-$O_2$ catalysts and beyond.

**Keywords: $MoS_{2-x}$, defects, catalytic sites, cathode, Li-$O_2$ battery**

***Edited by:***
*Jun Yan,*
*Harbin Engineering University, China*

***Reviewed by:***
*Liang Huang,*
*Huazhong University of Science and Technology, China*
*Xu Xiao,*
*Drexel University, United States*

****Correspondence:***
*Zhibin Pei*
*peizb@scut.edu.cn*
*Gongming Wang*
*wanggm@ustc.edu.cn*

***Specialty section:***
*This article was submitted to Electrochemical Energy Conversion and Storage,*
*a section of the journal Frontiers in Energy Research*

***Received:*** *21 April 2020*
***Accepted:*** *11 May 2020*
***Published:*** *24 June 2020*

***Citation:***
*Liu Y, Zang Y, Liu X, Cai J, Lu Z, Niu S, Pei Z, Zhai T and Wang G (2020) Three-Dimensional Carbon-Supported $MoS_2$ With Sulfur Defects as Oxygen Electrodes for Li-$O_2$ Batteries. Front. Energy Res. 8:109. doi: 10.3389/fenrg.2020.00109*

## INTRODUCTION

Rechargeable non-aqueous Li-$O_2$ batteries, which have an ultra-high theoretical energy density (>3,450 Wh $Kg^{-1}$), have been widely studied as a promising alternative energy storage system for the next generation of long-range electric vehicles and other high-energy devices (Cheng and Chen, 2012; Zhang P. et al., 2018; Zhang X. et al., 2018). Although the operation of Li-$O_2$ batteries is based on a simple electrochemical reaction ($2Li^+ + O_2 + 2e^- > Li_2O_2$, $E_0 = 2.96$ V), on the cathode, where there is a triple-phase contact interface, much more complicated *in-situ* reactions occur consisting of an oxygen reduction reaction (ORR) and an oxygen evolution reaction (OER) (Xu et al., 2016; Lyu et al., 2017). During discharge, ORR has been generally accepted to occur in two major steps. Firstly, $O_2$ is reduced to $O_2^-$, followed by combination with $Li^+$ to form $LiO_2$. Then, these superoxide intermediates undergo further electrochemical reduction or chemical disproportionation to form $Li_2O_2$, which is deposited on the cathode (Aurbach et al., 2016; Dong et al., 2018; Chaozhu et al., 2019). The charge process (OER) is far more complicated since the mechanism is indistinct and there are multiple charging intermediates, such as $Li_{2-x}O_2$, $LiO_2$, and

$O_2^-$ (Li and Chen, 2017; Lim et al., 2017). Many researchers have demonstrated that the bonding ability of the reaction intermediates to the solid ($Li_2O_2$)-solid (catalyst) interface is a key factor governing OER activity in the presence of a catalyst (Lu et al., 2013; Zhu et al., 2015; Lai et al., 2018). In general, a series of reactions starting from the adsorption of gaseous oxygen place great demands on the active sites on the cathode surface, while simultaneously, the deposition of a large amount of insulating $Li_2O_2$ also requires that the cathode structure provide sufficient accommodation space (Liu et al., 2015; Feng et al., 2016). These sluggish and unsustainable reactions on the triple-phase contact interface of the cathode always result in poor round-trip efficiency, limited rate capacity, and weak durability, which are critical defects for Li-$O_2$ batteries, severely hindering their practical application. Thus, designing catalysts with high activity and a porous structure to promote kinetics reaction is a prerequisite for further advancement of Li-$O_2$ technology (Chang et al., 2017; Hu X. et al., 2017; Wu et al., 2017).

Until now, numerous studies have been devoted to exploring alternative electrocatalysts and designing a good cathode architecture as the main strategies for improving the kinetics of oxygen conversion. Among them, molybdenum disulfide ($MoS_2$) has outstanding performance and low cost as a star catalyst (Asadi et al., 2016, 2018; Behranginia et al., 2016). However, as a typical layered transition metal dichalcogenide, its reactivity is mainly attributable to the low-coordinated unsaturated fringe zone of the layered structure, and yet the predominantly highly exposed basal plane atoms have not yet exerted their unique structural advantages (Jaramillo et al., 2007). In the field of electrochemical catalysis and Li-S batteries, a lot of research has focused on increasing the number of edge active sites and modifying the basal plane to further optimize its activity (Li et al., 2011; Kibsgaard et al., 2012; Xie et al., 2013; Yin et al., 2016; Hu J. et al., 2017). For instance, through introducing edge defect sites and doping oxygen to increase chaos, Xie et al. promoted the transfer of plane electrons to the edge to enhance their electrochemical reactivity (Xie et al., 2013; Xie J. et al., 2013). Lin et al. found that $MoS_{2-x}$/rGO with defective sites can effectively catalyze the conversion of lithium polysulfide and accelerate its oxidation-reduction reaction kinetics. Defects such as $MoS_2$ edge sites and terrace surfaces have exhibited great electrochemical activity for the deposition of discharge products (Lin et al., 2017). Thus, surface regulation of $MoS_2$ to improve intrinsic conductivity and the number of active sites exposed on the basal plane could greatly improve catalysis activity, especially in Li-$O_2$ systems that have high requirements on the adsorption of active sites.

To essentially manipulate the intrinsic properties of $MoS_2$ to further enhance its application value for cathode catalysis, as well as to study the effect of S defects on $MoS_2$ activity in Li-$O_2$ batteries, we prepared sulfur-deficient $MoS_2$ nanoflakes ($MoS_{2-x}$) growing *in-situ* on macroporous carbon paper as the binder-free Li-$O_2$ battery cathode. The 3D hierarchical porous cathode structure not only provides excellent electrical conductivity but also facilitates efficient gas transportation and lithium-ion diffusion and accommodates a large number of discharge products to increase battery capacity. Impressively, in the presence of the S defects in $MoS_{2-x}$ on porous carbon paper, the cathode exhibits excellent oxygen redox catalytic performance, with an overall potential gap of 0.59 V and a discharge capacity of 8,851 mA h $g^{-1}$. Scanning electron microscopy (SEM) images obtained after discharge also show the different $Li_2O_2$ morphologies formed on $MoS_2$ and $MoS_{2-x}$, which relate to the adsorption of intermediates onto their surface. To the best of knowledge, this performance makes $MoS_{2-x}$ as one of the best oxygen conversion catalysts, and these methods of surface modulation could offer a new vista for the design of Li-$O_2$ catalysts and beyond.

## EXPERIMENTAL DETAILS

### Material Synthesis

In a typical procedure, 0.196 g ammonium molybdate [$(NH_4)_6Mo_7O_{24}\cdot 4H_2O$] and 3.92 g sodium thiosulfate ($Na_2S_2O_3$) were dissolved in 18 mL deionized water with ultrasonic assistance. Then, the solution was transferred into a 20-mL Teflon-lined stainless-steel autoclave with punched carbon paper with a diameter of 11 mm as the growth substrate. After keeping the hydrothermal reaction temperature at 200°C for 20 h, the carbon paper was taken out, cleaned with deionized water and ethanol, and dried in a vacuum oven at 60°C for 10 h. $MoS_2$ growing on carbon paper was obtained at a loading of 0.8–1.0 mg. The $MoS_{2-x}$ sample was formed by heating the prepared $MoS_2$ in a 10% $H_2$/Ar atmosphere at 500°C for 3 h.

### Structural Characterization

The morphologies were characterized by scanning electron microscopy (SEM, JEOL-JSM-6700F), transmission electron microscopy (TEM, Hitachi H7650), and high-angle annular dark-field scanning TEM (HAADF-STEM, JEOL JEM-ARF200F TEM/STEM). X-ray diffraction (XRD) measurement was conducted on a Philips X'pert Super diffractometer with Cu Kα, $\lambda$ =1.54178 Å, and Raman spectra were recorded on a Renishaw RM 3000 Micro-Raman system. X-ray photoelectron spectroscopy (XPS, ESCALAB 250 spectrometer, Perkin-Elmer) was collected at the BL10B of the National Synchrotron Radiation Laboratory (NSRL). The surface area and pore distribution plots were collected by Brunauer–Emmett–Teller (BET, Micromeritics ASAP 2020).

### Electrochemical Measurements

The Li-$O_2$ electrochemical performance was measured in 2,032 cells with 19 pores on the steel cathode shells. All of the cells are assembled in an Ar-filled glove box ($O_2$, $H_2O < 1$ ppm) by using a lithium metal foil as the anode, a glass fiber separator as the separator, the prepared electrode as the gas cathode, and 75 vol% dimethyl sulfoxide (DMSO) and 25 vol% 1-ethyl-3-methylimidazolium tetrafluoroborate (EMIM-BF4) with 0.1 M lithium bis(trifluoromethanesulfonyl)imide (LiTFSI) (>99.0%) as the electrolyte. The cathode prepared by the coating method was made from a powder slurry of the corresponding material. The powdered samples were mixed with acetylene black and poly (vinylidene difluoride) (PVDF) in an 8:1:1 ratio, and commercial CNT samples were mixed with PVDF at 9:1 in

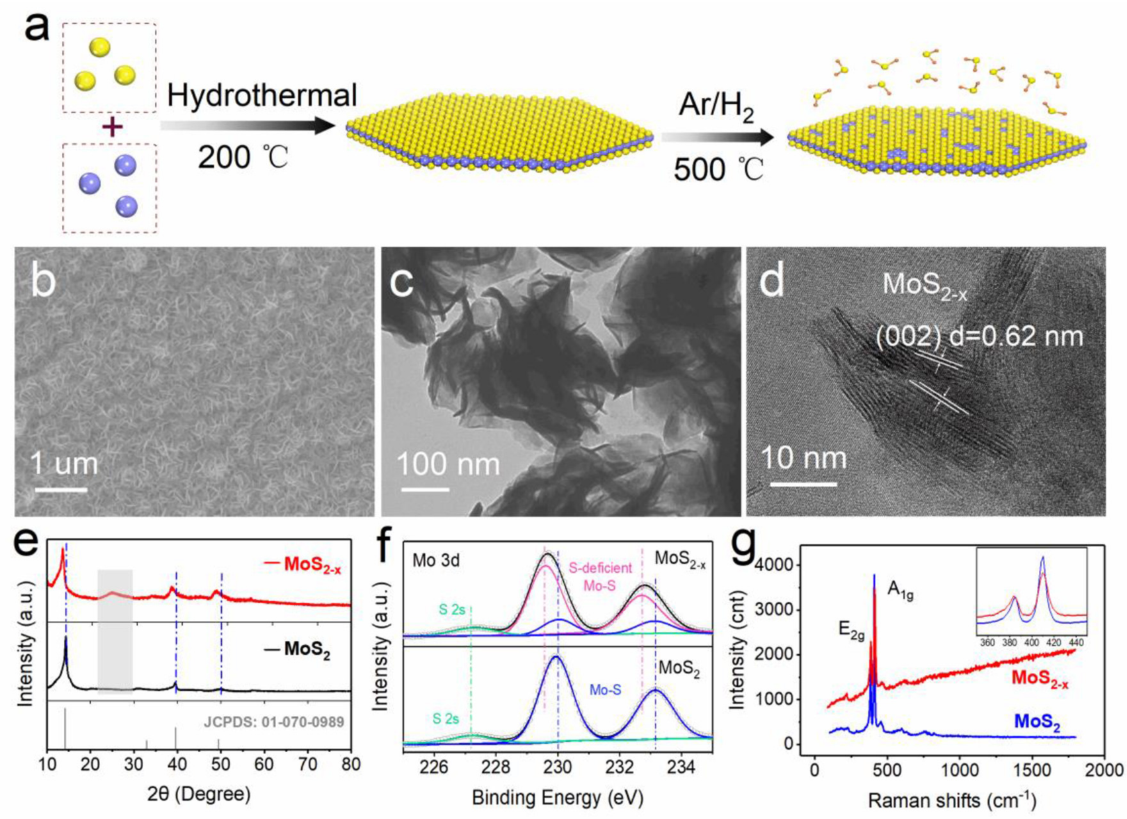

**FIGURE 1 |** Material synthesis and characterization. **(a)** Schematic of the synthesis. **(b)** SEM image of $MoS_{2-x}$ on carbon paper. **(c)** TEM image of $MoS_{2-x}$. **(d)** High-resolution TEM of $MoS_{2-x}$. **(e)** XRD patterns of $MoS_{2-x}$ and $MoS_2$. **(f)** XPS core-level Mo 3d spectra from $MoS_{2-x}$ and $MoS_2$. **(g)** Raman spectra of $MoS_{2-x}$ and $MoS_2$.

N-methyl-2-pyrrolidone (NMP). The coating slurry was then applied to the carbon paper with a loading of 0.7 mg. The electrochemical performances of the cathodes were tested using a specific capacity-controlled mode at various current densities in pure $O_2$. Electrochemical impedance spectroscopy (EIS) were performed under open-circuit voltage with the frequency ranging from 1 Hz to 100 kHz.

# RESULTS AND DISCUSSION

## Material and Structural Characterization

As shown schematically in **Figure 1a**, molybdenum source and sulfur source will nucleate and grow into flake-like $MoS_2$ crystals through hydrothermal reaction under high temperature and high pressure. When treated in an $H_2$/Ar atmosphere at high temperature, part of the sulfur will be taken away by the reducing atmosphere to form $H_2S$, leaving a lot of S defects on the $MoS_2$ basal plane. $MoS_{2-x}$ with S defects shows more layers than do pristine $MoS_2$ nanoflakes and has larger surface area, as the SEM images in **Figure S1** show. It can also be seen from the TEM images in **Figure S2** that $MoS_{2-x}$ has thinner nanoflakes at the edges, which may attribute to non-stoichiometric $MoS_{2-x}$ with increased disorder of the atomic arrangement. It is these disordered S defects that endow the inert basal plane with a large amount of active sites at which to adsorb oxygen and discharge/charge intermediates and discretely induce the deposition of discharge products, promoting a series of oxygen redox catalytic processes. The SEM image in **Figure 1b** shows $MoS_{2-x}$ nanoflakes uniformly and densely growing on carbon paper; this is enlarged in **Figure S3**. The TEM image and its enlarged view in **Figure 1c** and **Figure S4**, respectively, display the super-thin layer-like structure of $MoS_{2-x}$ nanoflakes, which are about several nanometers thick. The high-resolution (HRTEM) image in **Figure 1d** reveals well-resolved lattice fringes with an interplanar spacing of 0.62 nm, which are assigned to the (002) plane of hexagonal $MoS_2$. We also performed HRTEM to characterize the defects of the $MoS_{2-x}$ basal plane, as shown in **Figure S5**. The red regular hexagon indicates that the shooting angle is focused on the basal surface of hexagonal $MoS_{2-x}$. Many defects can be seen on the basal plane, as marked by the brown circle.

The effects of S defects on the structure of $MoS_{2-x}$ were analyzed by XRD, and the results are seen in **Figure 1e**. The diffraction peaks of the $MoS_2$ nanoflakes can be well converted to No. 01-070-0989. For $MoS_{2-x}$, there was a slight shift to a lower degree, indicating an increase in the lattice spacing,

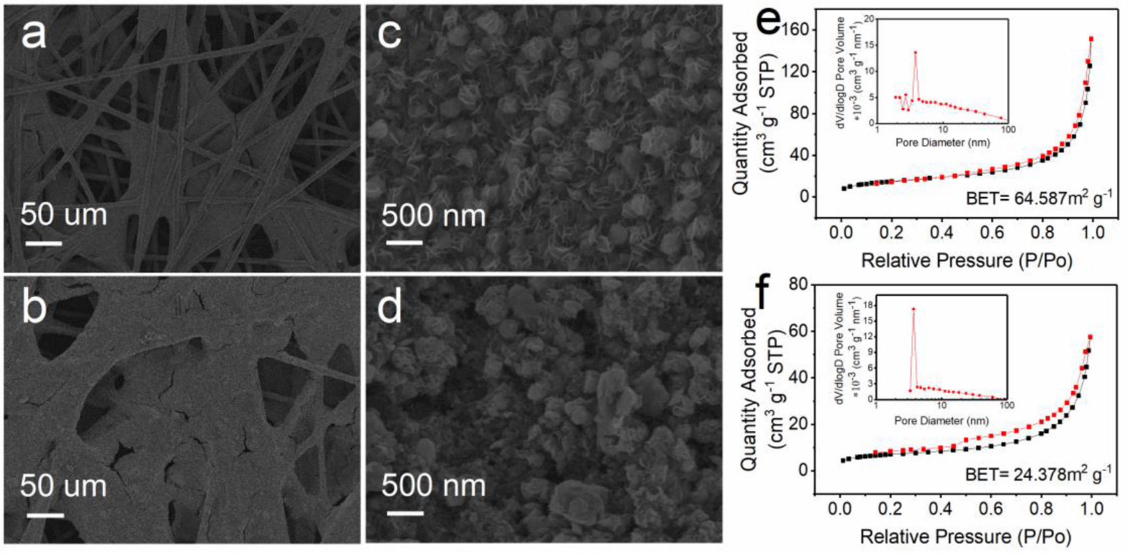

**FIGURE 2 |** Structural characterization of $MoS_{2-x}$ growing on or coating carbon paper. **(a,b)** SEM images. **(c,d)** Enlarged SEM view of **(a,b)**. **(e,f)** Nitrogen adsorption and desorption isotherms and pore-size distribution.

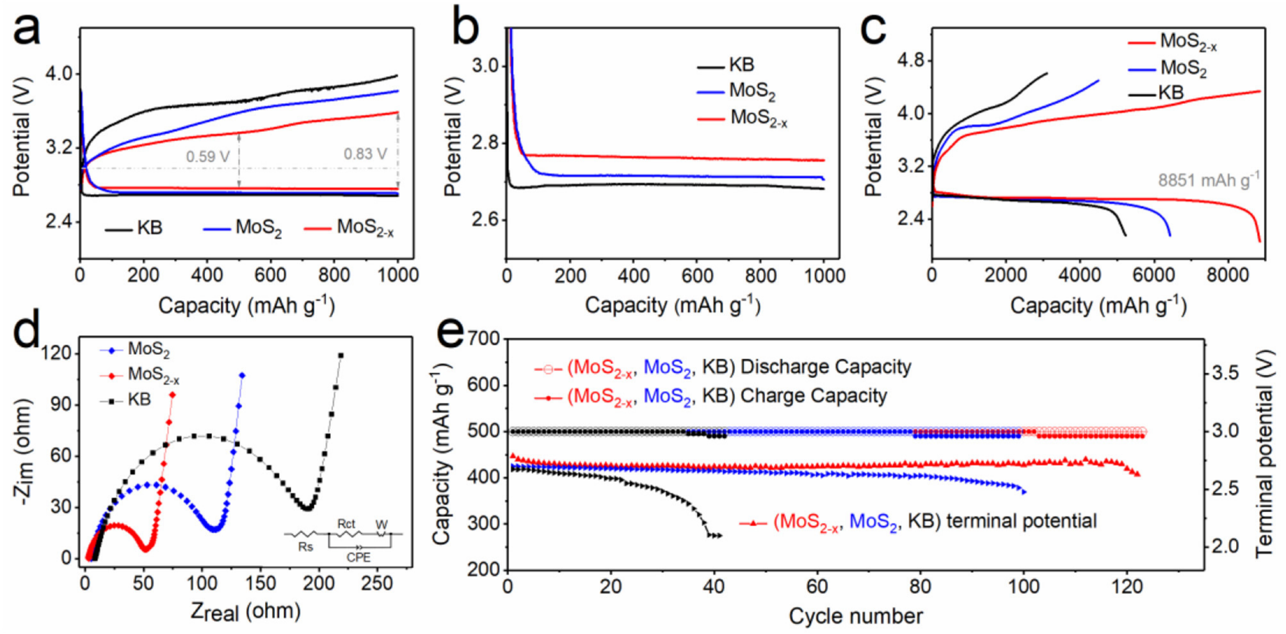

**FIGURE 3 |** Electrochemical properties. **(a)** First cycling galvanostatic discharge and recharge profiles of $MoS_{2-x}$, $MoS_2$, and Kejen Black. **(b)** Enlarged image of the discharge curves in **(a)**. **(c)** Full discharge and recharge curves of Li–$O_2$ batteries with $MoS_{2-x}$ and $MoS_2$ cathodes. **(d)** EIS spectra of $MoS_{2-x}$, $MoS_2$, and Kejen Black at open-circuit voltages. The inset is the equivalent circuit. **(e)** Cycling stability and the terminal discharge potential of $MoS_{2-x}$ and $MoS_2$ cathodes.

caused most likely by the removal of sulfur atoms. The resultant reduction of Mo, moving it to a lower oxidation state with a larger atomic radius, led to the increase in the lattice spacing. In addition, newly emerging diffraction peaks between 20 and 30 degrees represent the increase in the degree of disorder of the $MoS_2$ lattice. XPS analysis was conducted to obtain insights into the chemical composition and electronic states of $MoS_{2-x}$ and $MoS_2$. **Figure 1f** displays the deconvoluted XPS Mo 3d spectra, in which $MoS_{2-x}$ exhibits the characteristic peaks of both stoichiometric $MoS_2$ (blue) and sulfur-deficient $MoS_2$

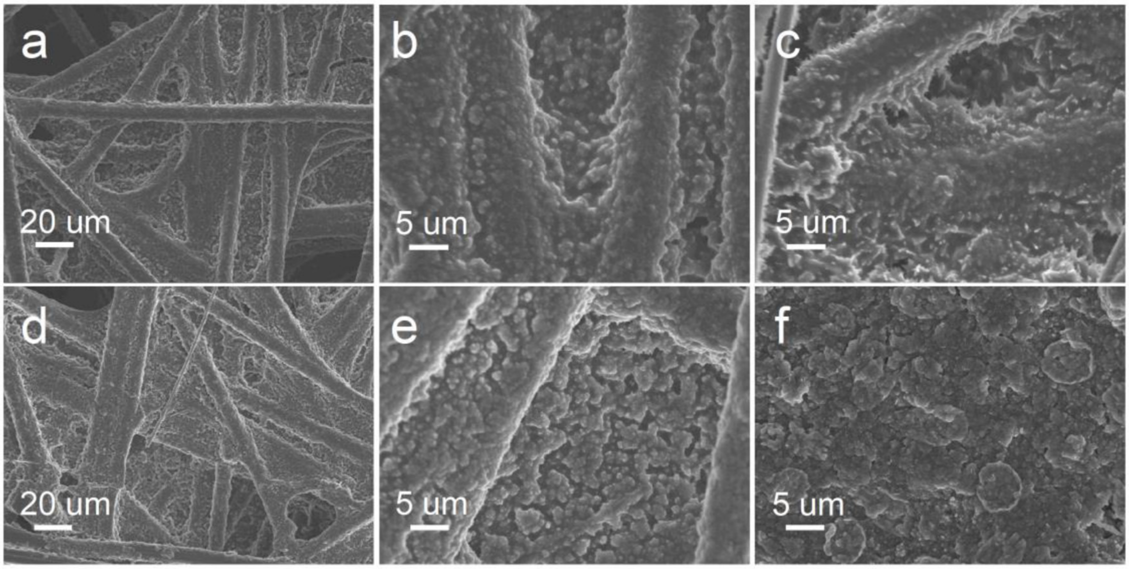

**FIGURE 4 |** Morphological evolution of the discharge products. **(a)** SEM image of $MoS_{2-x}$ after discharge to 500 mA h $g^{-1}$. **(b)** Enlarged view of **(a)**. **(C)** SEM image of $MoS_{2-x}$ after discharge to 1,000 mA h $g^{-1}$. **(d)** SEM image of $MoS_2$ after discharge to 500 mA h $g^{-1}$. **(e)** Enlarged view of **(d)**. **(f)** SEM image of $MoS_2$ after discharge to 1,000 mA h $g^{-1}$. Galvanostatic discharge with current at 500 mA $g^{-1}$.

(red). Specifically, the sulfur-deficient $MoS_2$ possesses lower binding energy than stoichiometric $MoS_2$ in Mo $3d_{5/2}$ (229.6 eV compared with 230.02 eV) and $3d_{3/2}$ (232.71 eV compared with 233.11 eV) doublets, illustrating the decrease in the valence state of Mo. Besides, the peak at 227.3 eV is attributed to S 2s, and the XPS total survey spectra and S 2p spectra are also displayed in **Figure S6**. In addition, the structural differences can also be detected by Raman spectroscopy. In **Figure 1g**, the fingerprint bands of $MoS_2$ are located at 376 and 402 $cm^{-1}$, caused by the in-plane ($E_{2g}$) and out-plane ($A_{1g}$) Mo-S phonon mode vibration of $MoS_2$, respectively. Obviously, the weakening of Raman peak intensity can be explained by the decrease in the content of vibration groups. The Raman peak is a statistical result, and the same peak broadening is due to lower structural uniformity of the vibrating molecules, which is caused by inducing S defects.

Considering the huge influence of the electrode structure on the performance of the battery, the loading methods of the catalyst $MoS_{2-X}$ on porous carbon paper are also studied here. We compare a cathode of catalyst grown *in-situ* on carbon paper with a cathode coated with catalyst powder and find that the coated slurry easily blocked the original pores of the carbon paper and blocked the gas channel, as shown in **Figures 2a,b**; this can be compared with the pure carbon paper framework in **Figure S7**. Besides, the slurry used in the coating method will destroy the uniform arrangement of the catalyst on the conductive carbon paper, and the micron-level insulating binder used therein will also greatly affect the conductivity of the electrode, as shown in **Figures 2c,d**. $N_2$ adsorption–desorption techniques were employed to characterize the surface structural features. $MoS_{2-x}$ (growing on carbon paper) exhibits a surface area of 64.587 $m^2$ $g^{-1}$, which is superior to the $MoS_{2-x}$ coating on carbon paper (24.378 $m^2$ $g^{-1}$) and pure carbon paper (9.093 $m^2$ $g^{-1}$), as shown in **Figures 2e,f** and **Figure S8**. The isotherm profile in **Figure 2c** is categorized as type IV with a hysteresis loop (H3), and the pore-size distribution determined by the BJH shows pore diameters centered at a range of 4–30 nm (mainly mesopores). This meaningful 3D hierarchical porous structure not only acts as ion and gas transmission channels but also contributes to increasing the specific surface area to deliver more active sites and sufficient room to accommodate solid discharge products to achieve satisfying specific capacity performance.

## Electrochemical Performance of Li-$O_2$ Batteries

To examine the electrochemical properties of the prepared $MoS_{2-x}$ and $MoS_2$ cathodes, Kejen Black (denoted as KB) was employed as a comparison, and Li-$O_2$ 2032 coin cells were assembled. At a current of 500 mA $g^{-1}$ and a cutoff capacity of 1,000 mA h $g^{-1}$, the discharge and charge potential gap of $MoS_{2-x}$ is 0.59 V, much lower than that of $MoS_2$ (0.87 V) and Kejen Black (1.03 V) at half capacity, as shown in **Figure 3a**. During the charge process, the charge potential platform of $MoS_{2-x}$ is 3.55 V and the overpotential is 0.57 V, which is significantly lower than for $MoS_2$ (3.79, 0.81 V) and Kejen Black (3.96, 0.98 V), indicating excellent OER catalytic activity. For the discharge (ORR) process, as is enlarged in **Figure 3b**, $MoS_{2-x}$ displayed a discharge platform at 2.75 V, higher than $MoS_2$ (2.71 V) and Kejen Black (2.68 V). Compared with the cathode constructed by the coating method, both $MoS_{2-x}$ and $MoS_2$ have far superior performance in reducing overpotential, demonstrating the structural advantages of a self-growing cathode for Li-$O_2$ batteries, as shown in **Figure S9**. The corresponding round-trip efficiency based on calculus is 85.56% for $MoS_{2-x}$, much higher than the values of 76.46, 76.61, 74.85, and 71.9% obtained for $MoS_2$ growing on carbon paper, $MoS_{2-x}$, $MoS_2$, and Kejen Black coating on carbon paper, respectively, as shown in **Figure S10**. Furthermore, to gain an insight into the full specific capacity of the $MoS_{2-x}$ cathode, the $MoS_{2-x}$ and $MoS_2$-based Li-$O_2$ batteries were tested under deep discharge/charge and limited capacity conditions. The $MoS_2$ cathode could deliver a high discharge capacity of about 6,312 mA h $g^{-1}$ during the discharge process, while the charge process showed quite serious polarization and poor reversibility (**Figure 3c**). On the contrary, the $MoS_{2-x}$ cathode could not only obtain a discharge capacity as high as 8,851 mA h $g^{-1}$ but also exhibited better reversibility with lower charging energy. This improved performance can be attributed to it being a monolithic cathode with a hierarchical porous structure and extensive active deposition sites provided by S defects, which is vital for an $O_2$-based electrode in an energy storage device. We also performed extended galvanostatic discharge and charge tests with the current density varying from 200 to 2,000 mA $g^{-1}$ to further assess the rate performance. The results are shown in **Figure S11**. The $MoS_{2-x}$ cathode exhibits a small polarization with clear voltage plateaus and superior reversibility, demonstrating resistance to large currents and accelerated electrochemical reactions.

In addition, we conducted an EIS test at open-circuit voltage to study the interfacial kinetics in Li-$O_2$ batteries (**Figure 3d**), with the Nyquist plots fitted by an equivalent electrical circuit (**Figure 3d**, inset). $MoS_{2-x}$ exhibits a lower charge-transfer resistance (Rct) of 50.8 $\Omega$ compared with $MoS_2$ (108.4 $\Omega$) and Kejen Black (188.94 $\Omega$), indicating that it has ultrafast charge transfer behavior. $MoS_{2-x}$ achieves a lower energy barrier to trigger and support robust oxygen conversion and charge transfer, demonstrating a significant promotion of ORR and OER catalytic activity in Li-$O_2$ batteries. As shown in **Figure 3e**, the long cycling stability was tested at 500 mA $g^{-1}$ with a cutoff capacity of 1,000 mA h $g^{-1}$. The terminal discharge potential of the $MoS_2$ cathode obviously decreases to 2.5 V after 99 cycles, while the battery with a $MoS_{2-x}$ cathode can achieve more than 123 cycles before the terminal discharge potential reaches 2.6 V, displaying that it has superior reversibility and cycling stability. Based on the above results, we can conclude that the introduction of S defects greatly improves the cathode catalytic activity and capacity for Li-$O_2$ batteries.

### Morphological Evolution of the Discharge Products

The morphologies of discharge products are accepted to be significant factors affecting the subsequent electrochemical reaction. Thus, SEM investigations were carried out to characterize the evolution of discharge products. After discharging to 500 mA $g^{-1}$ for 1 h, the pores of the cathode were partially covered with film-like discharge products, as shown in **Figures 4a,b**. After continued discharge to 1,000 mA h $g^{-1}$, thicker aggregates were present on the $MoS_{2-x}$ cathode (**Figure 4c**), indicating the continuous reduction of oxygen into discharge products and deposition on the cathode. For direct comparison, the typical morphologies of the $MoS_2$ cathode after discharging were also tested, as shown in **Figures 4d–f**. After discharging to 1,000 mA h $g^{-1}$, the cathode can be seen to be uniformly covered with patelloid products in **Figure 4c** and **Figure S12**, suggesting that the $MoS_2$ cathode behaves quite differences from the $MoS_{2-x}$ cathode. During the discharging process, the exertion of a strong adsorption force on the intermediate discharge products always led the superoxide intermediate products to experience further electrochemical reduction, thus forming a film-like discharge product, while weak adsorption often led to large-sized crystal discharge products, which need higher energy for oxidative decomposition. On the surface of the $MoS_{2-x}$ cathode, strong adsorption to discharge intermediates can be attributed to S defects, which enhance the adsorption activity and the number of adsorption sites and provide an excellent prerequisite for the subsequent charging process.

## CONCLUSIONS

In summary, we have demonstrated that $MoS_2$ with S defects can intrinsically promote the corresponding thermodynamic and kinetic processes in Li-$O_2$ batteries. XRD and XPS are used to characterize the defects of the $MoS_2$ materials, which can act as active centers for the adsorption and conversion of superoxide intermediate products. SEM and BET tests demonstrate that *in-situ* growth on carbon paper can be used to successfully fabricate a multilayer hierarchical 3D structure that can provide abundant channels for ion and gas molecule diffusion. Due to these advantages, a $MoS_{2-x}$ electrode exhibits an overpotential of 0.59 V and a discharge capacity of 8,851 mA h $g^{-1}$ at a current density of 500 mA $g^{-1}$, showing the best performance. Moreover, the large number and film-like distribution of discharge products on the $MoS_{2-x}$ surface means a stronger adsorption effect on intermediate products. Therefore, this study, in designing the 3D host materials and tuning the electronic structure of the $MoS_2$ surface, paves a new way to the high-energy application of Li-$O_2$ batteries.

## DATA AVAILABILITY STATEMENT

The original contributions presented in the study are included in the article/**Supplementary Material**, further inquiries can be directed to the corresponding author/s.

## AUTHOR CONTRIBUTIONS

GW and TZ designed and supervised the project. GW, ZP, and YL conducted the project and wrote and revised the manuscript. YZ conducted XPS measurements. XL helped to disassemble the batteries. ZL and SN performed SEM characterization and provided valuable help in the data analysis. All of the authors discussed the results and commented on the manuscript.

## FUNDING

This work was supported by the National Key Research and Development Program of China (2017YFA0206703), the Natural Science Fund of China (Nos. 21771169, 11722543, and 11505187), the Fundamental Research Funds for the Central Universities (WK2060190074, WK2060190081, and WK2310000066), USTC start-up funding, and the Recruitment Program of Global Experts.

## ACKNOWLEDGMENTS

We thank the Photoemission End stations at BL10B, the National Synchrotron Radiation Laboratory, for XPS characterizations.

## SUPPLEMENTARY MATERIAL

The Supplementary Material for this article can be found online at: https://www.frontiersin.org/articles/10.3389/fenrg.2020.00109/full#supplementary-material

## REFERENCES

Asadi, M., Kumar, B., Liu, C., Phillips, P., Yasaei, P., Behranginia, A., et al. (2016). Cathode based on molybdenum disulfide nanoflakes for lithium-oxygen batteries. *ACS Nano* 10, 2167–2175. doi: 10.1021/acsnano.5b06672

Asadi, M., Sayahpour, B., Abbasi, P., Ngo, A. T., Karis, K., Jokisaari, J. R., et al. (2018). A lithium-oxygen battery with a long cycle life in an air-like atmosphere. *Nature* 555, 502–507. doi: 10.1038/nature25984

Aurbach, D., McCloskey, B. D., Nazar, L. F., and Bruce, P. G. (2016). Advances in understanding mechanisms underpinning lithium-air batteries. *Nat. Energy* 1, 1–11. doi: 10.1038/nenergy.2016.128

Behranginia, A., Asadi, M., Liu, C., Yasaei, P., Kumar, B., Phillips, P., et al. (2016). Highly efficient hydrogen evolution reaction using crystalline layered three-dimensional molybdenum disulfides grown on graphene film. *Chem. Mater.* 28, 549–555. doi: 10.1021/acs.chemmater.5b03997

Chang, Z., Xu, J., and Zhang, X. (2017). Recent progress in electrocatalyst for Li-$O_2$ batteries. *Adv. Energy Mater.* 7:1700875. doi: 10.1002/aenm.201700875

Chaozhu, S., Jiazhao, W., Jianping, L., Hua-Kun, L., and Shi-Xue, D. (2019). Understanding the reaction chemistry during charging in aprotic lithium–oxygen batteries: existing problems and solutions. *Adv. Mater.* 31:1804587. doi: 10.1002/adma.201804587

Cheng, F., and Chen, J. (2012). Metal-air batteries: from oxygen reduction electrochemistry to cathode catalysts. *Chem. Soc. Rev.* 41, 2172–2192. doi: 10.1039/c1cs15228a

Dong, J.-C., Zhang, X.-G., Briega-Martos, V., Jin, X., Yang, J., Chen, S., et al. (2018). *In situ* Raman spectroscopic evidence for oxygen reduction reaction intermediates at platinum single-crystal surfaces. *Nat. Energy* 4, 60–67. doi: 10.1038/s41560-018-0292-z

Feng, N., He, P., and Zhou, H. (2016). Critical challenges in rechargeable aprotic Li-$O_2$ batteries. *Adv. Energy Mater.* 6:1502303. doi: 10.1002/aenm.201502303

Hu, J., Zhang, C., Jiang, L., Lin, H., An, Y., Zhou, D., et al. (2017). Nanohybridization of MoS2 with layered double hydroxides efficiently synergizes the hydrogen evolution in alkaline media. *Joule* 1, 383–393. doi: 10.1016/j.joule.2017.07.011

Hu, X., Wang, J., Li, Z., Wang, J., Gregory, D. H., and Chen, J. (2017). MCNTs@$MnO_2$ nanocomposite cathode integrated with soluble $O_2$-carrier co-salen in electrolyte for high-performance Li-air batteries. *Nano Lett.* 17, 2073–2078. doi: 10.1021/acs.nanolett.7b00203

Jaramillo, T. F., Jorgensen, K. P., Bonde, J., Nielsen, J. H., Horch, S., and Chorkendorff, I. (2007). Identification of active edge sites for electrochemical $H_2$ evolution from MoS2 nanocatalysts. *Science* 317, 100–102. doi: 10.1126/science.1141483

Kibsgaard, J., Chen, Z., Reinecke, B. N., and Jaramillo, T. F. (2012). Engineering the surface structure of $MoS_2$ to preferentially expose active edge sites for electrocatalysis. *Nat. Mater.* 11, 963–969. doi: 10.1038/nmat3439

Lai, N. C., Cong, G., Liang, Z., and Lu, Y. C. (2018). A highly active oxygen evolution catalyst for lithium-oxygen batteries enabled by high-surface-energy facets. *Joule* 2, 1511–1521. doi: 10.1016/j.joule.2018.04.009

Li, F., and Chen, J. (2017). Mechanistic evolution of aprotic lithium-oxygen batteries. *Adv. Energy Mater.* 7:1602934. doi: 10.1002/aenm.201602934

Li, Y., Wang, H., Xie, L., Liang, Y., Hong, G., and Dai, H. (2011). MoS2 nanoparticles grown on graphene: an advanced catalyst for the hydrogen evolution reaction. *J. Am. Chem. Soc.* 133, 7296–7299. doi: 10.1021/ja201269b

Lim, H. D., Lee, B., Bae, Y., Park, H., Ko, Y., Kim, H., et al. (2017). Reaction chemistry in rechargeable Li-$O_2$ batteries. *Chem. Soc. Rev.* 46, 2873–2888. doi: 10.1039/c6cs00929h

Lin, H., Yang, L., Jiang, X., Li, G., Zhang, T., Yao, Q., et al. (2017). Electrocatalysis of polysulfide conversion by sulfur-deficient $MoS_2$ nanoflakes for lithium–sulfur batteries. *Energy Environ. Sci.* 10, 1476–1486. doi: 10.1039/c7ee01047h

Liu, Q. C., Xu, J. J., Xu, D., and Zhang, X. B. (2015). Flexible lithium-oxygen battery based on a recoverable cathode. *Nat. Commun.* 6, 1–8. doi: 10.1038/ncomms8892

Lu, Y.-C., Gallant, B. M., Kwabi, D. G., Harding, J. R., Mitchell, R. R., Whittingham, M. S., et al. (2013). Lithium–oxygen batteries: bridging mechanistic understanding and battery performance. *Energy Environ. Sci.* 6, 750. doi: 10.1039/c3ee23966g

Lyu, Z., Zhou, Y., Dai, W., Cui, X., Lai, M., Wang, L., et al. (2017). Recent advances in understanding of the mechanism and control of $Li_2O_2$ formation in aprotic Li-$O_2$ batteries. *Chem. Soc. Rev.* 46, 6046–6072. doi: 10.1039/c7cs00255f

Wu, S., Qiao, Y., Yang, S., Ishida, M., He, P., and Zhou, H. (2017). Organic hydrogen peroxide-driven low charge potentials for high-performance lithium-oxygen batteries with carbon cathodes. *Nat. Commun.* 8, 1–9. doi: 10.1038/ncomms15607

Xie, J., Zhang, H., Li, S., Wang, R., Sun, X., Zhou, M., et al. (2013). Defect-rich $MoS_2$ ultrathin nanosheets with additional active edge sites for enhanced electrocatalytic hydrogen evolution. *Adv. Mater.* 25, 5807–5813. doi: 10.1002/adma.201302685

Xie, J. F., Zhang, J. J., Li, S., Grote, F., Zhang, X. D., Zhang, H., et al. (2013). Controllable disorder engineering in oxygen-incorporated $MoS_2$ ultrathin nanosheets for efficient hydrogen evolution. *J. Am. Chem. Soc.* 135, 17881–17888. doi: 10.1021/ja408329q

Xu, J. J., Chang, Z. W., Wang, Y., Liu, D. P., Zhang, Y., and Zhang, X. B. (2016). Cathode surface-induced, solvation-mediated, micrometer-sized $Li_2$ $O_2$ cycling for Li-$O_2$ batteries. *Adv. Mater.* 28, 9620–9628. doi: 10.1002/adma.201603454

Yin, Y., Han, J., Zhang, Y., Zhang, X., Xu, P., Yuan, Q., et al. (2016). Contributions of phase, sulfur vacancies, and edges to the hydrogen evolution reaction catalytic activity of porous molybdenum disulfide nanosheets. *J. Am. Chem. Soc.* 138, 7965–7972. doi: 10.1021/jacs.6b03714

Zhang, P., Zhao, Y., and Zhang, X. (2018). Functional and stability orientation synthesis of materials and structures in aprotic Li-O$_2$ batteries. *Chem. Soc. Rev.* 47, 2921–3004. doi: 10.1039/c8cs00009c

Zhang, X., Mu, X., Yang, S., Wang, P., Guo, S., Han, M., et al. (2018). Research progress for the development of Li-air batteries: addressing parasitic reactions arising from air composition. *Energy Environ. Mater.* 1, 61–74. doi: 10.1002/eem2.12008

Zhu, J., Wang, F., Wang, B., Wang, Y., Liu, J., Zhang, W., et al. (2015). Surface acidity as descriptor of catalytic activity for oxygen evolution reaction in Li-O$_2$ Battery. *J. Am. Chem. Soc.* 137, 13572–13579. doi: 10.1021/jacs.5b07792

**Conflict of Interest:** The authors declare that the research was conducted in the absence of any commercial or financial relationships that could be construed as a potential conflict of interest.

frontiers in Energy Research

MINI REVIEW
published: 27 August 2020
doi: 10.3389/fenrg.2020.00210

# Three-Dimensional Ordered Porous Carbon for Energy Conversion and Storage Applications

*Jinxiu Feng[1], Dong Zheng[1], Xinlong Gao[1], Wenbin Que[1], Wenhui Shi[2]*, Wenxian Liu[1], Fangfang Wu[1] and Xiehong Cao[1]**

*[1] College of Materials Science and Engineering, Zhejiang University of Technology, Hangzhou, China, [2] Center for Membrane Separation and Water Science & Technology, Zhejiang University of Technology, Hangzhou, China*

The performance of energy storage devices is highly related to the properties of electrode materials, such as components, morphology, configurations and so on. As a typical hierarchical carbon material, three-dimensional ordered porous carbon (3D-OPC) has unique characteristics of low cost, large specific surface area, highly ordered channels, and high electronic and ionic conductivity, which shows great potential in energy storage and conversion applications. In this mini review, we summarize various template-assisted preparation methods for 3D-OPC, including hard-, ice- and self-templated approaches, and their applications in electrocatalysis, batteries and supercapacitors. Additionally, the critical roles of vertical channels in 3D-OPC when used as electrodes are also discussed. Finally, the current challenges and future research outlook of 3D-OPC are proposed.

**Keywords: 3D ordered porous carbon, energy storage and conversion, vertical channels, template-assisted methods, low tortuosity**

OPEN ACCESS

***Edited by:***
*Teng Zhai,*
*Nanjing University of Science and Technology, China*

***Reviewed by:***
*Xihong Lu,*
*Sun Yat-sen University, China*
*Xinhui Xia,*
*Zhejiang University, China*

****Correspondence:***
*Wenhui Shi*
*shiwh@zjut.edu.cn*
*Xiehong Cao*
*gcscaoxh@zjut.edu.cn;*
*caoxiehong@gmail.com*

***Specialty section:***
*This article was submitted to Electrochemical Energy Conversion and Storage, a section of the journal Frontiers in Energy Research*

***Received:*** *29 June 2020*
***Accepted:*** *05 August 2020*
***Published:*** *27 August 2020*

***Citation:***
*Feng J, Zheng D, Gao X, Que W, Shi W, Liu W, Wu F and Cao X (2020) Three-Dimensional Ordered Porous Carbon for Energy Conversion and Storage Applications. Front. Energy Res. 8:210. doi: 10.3389/fenrg.2020.00210*

## INTRODUCTION

Developing safe, low-cost and efficient energy storage and conversion devices has become an urgent need, owing to the growing demands of sustainable resources, such as solar and wind power (Cao et al., 2017; Li et al., 2020; Wu M. et al., 2020). Carbon materials exhibit numerous advantages, such as high electrical conductivity, low cost and high specific surface area (Cao et al., 2014; Li et al., 2019; Wu Q. et al., 2020). Carbon materials can be categorized into four types, i.e., zero-dimensional (0D, e.g., $C_{60}$), one-dimensional (1D, e.g., carbon nanofibers and carbon nanotubes), two-dimensional (2D, e.g., graphene and carbon sheets), and three-dimensional structures (3D, e.g., 3D porous carbon and graphene foam) (Zhang F. et al., 2017). In recent years, 3D carbon materials have demonstrated excellent electrochemical performance in a wide range of applications including energy storage and conversion (Ullah et al., 2019; Ni and Li, 2020).

In a conventional route for preparation of a certain electrode, a slurry composed of active material, conductive agent and binder is normally casted onto a current collector. With increase of the loading mass of active material and the thickness of electrode, its electrical conductivity decreases. Besides, thick electrode leads to high tortuosity, which hinders the penetration of electrolyte and ion transport and results in limited utilization of active materials (Wang et al., 2019; Shi et al., 2020a). It is an effective way to promote the transportation of ions and electrons by fabricating low-tortuosity electrode.

The three-dimensional ordered porous carbon (3D-OPC) possesses low tortuosity and open pores (Qiao et al., 2019; Zhou et al., 2019). When used as an electrode material, it can not only provide fast electron transport path, but also significantly shorten ion diffusion length to achieve fast kinetic performance (**Figure 1a**). In addition, 3D-OPC effectively suppresses the agglomeration of nanoparticles and maintains a large specific surface area (Zhao et al., 2015). However, the controllable preparation of 3D-OPC is still a challenge. In this review, we summarize the controllable preparation methods for 3D-OPC, and the latest research progress of 3D-OPC in energy storage and conversion applications.

## PREPARATION METHODS

The methods to prepare 3D-OPC can be divided into template-assisted methods and non-template approaches. Based on the different types of templates, the template-assisted methods include hard-templating method (Masuda and Fukuda, 1995; Li X. et al., 2018), ice-templating method (Roberts et al., 2014; Zhai et al., 2017), soft-templating method (Peng et al., 2019), and self-templating method (Feng and Yin, 2018). However, the soft-templating method normally lack of controllability, which is difficult to form a stable structure with vertical channels. Herein, we focus on the research progress of the other three template-assisted preparation methods for 3D-OPC.

### Ice-Templating Synthesis

The ice-templating method is based on the solid phase produced in the process of phase separation, followed by removing solidified solvent with the solid phase frame retained (Shao et al., 2020). The structures produced by ice-templating method can be easily regulated. Moreover, this method is applicable to a wide range of materials, such as polymers, carbon aerogels and so on. According to different precursors, carbon aerogels can be divided into graphene aerogels, carbon nanotube-based aerogels, biomass-derived aerogels and so on (Shahbazi et al., 2020). Graphene oxide (GO) aerogels with good physical and chemistry properties is one of the most widely studied carbon-based aerogels. Wang et al. first proposed a freeze-drying method followed by a reduction process to prepare the reduced graphene oxide (rGO) aerogels (Wang and Ellsworth, 2009). Since then, the graphene aerogels prepared by the ice-templating method have been extensively studied. As a typical example, Zhang et al. added ethanol to the GO suspension, which was then transferred to a polytetrafluoroethylene (PTFE) mold for the subsequent rapid-freeze process in liquid nitrogen (Zhang P. et al., 2017). Finally, a long vertical graphene film was produced by freeze-drying and annealing. Ethanol is used as anti-freeze agent to reduce the freezing point, which has a significant influence on the crystallization behavior of ice. In addition, Wang et al. prepared a GO aerogel with a radially aligned structure by bidirectional freeze-casting method (Wang C. et al., 2018). During the freezing process, ordered porous GO aerogel was formed with a continuous 3D network. To study freezing/assembling mechanism, the authors added different additives, such as ethanol, chitosan or cellulose nanofibers to the aqueous solution of GO. It is revealed that different additives affected the interaction between ice crystals and GO nanosheets, resulting in the ice crystals with different shapes. Furthermore, Mochizuki et al. reported vertical aligned rGO electrodes through electrodeposition of GO to form rGO and subsequent freeze-drying process (**Figure 1b**; Mochizuki et al., 2019). This method can control the film thickness and pore size to achieve fast charge storage and low resistance. In addition, the pore size can be controlled in the range of 10–100 $\mu$m by adjusting the freezing rate.

### Hard-Templating Synthesis

The hard template not only has high stability, but also can control morphology and increase specific surface area of catalysts. There are numerous hard templates, such as salt (Zhang et al., 2020), metal (Cao et al., 2011), and silica (Byeon et al., 2020), available to prepare carbon materials. For example, Kim et al. used various-sized silica nanoparticles as template which was subsequently removed by 1M NaOH to obtain mesoporous nitrogen (N)-doped carbon (Byeon et al., 2020). Kyotani et al. (1988) first proposed that carbon materials can be synthesized via hard-templating method in 1988. Further, the next breakthrough was achieved by Kyotani et al. (1995), who synthesized carbon nanotubes with a uniform length and diameter by using anodic aluminum oxide (AAO) as a hard template in 1995. The porous AAO template is a typical hard template with low cost and highly ordered nano-scale array channels. Since then, the preparation of various 3D-OPCs through AAO template had become a research hotspot. Typically, Wang et al. used AAO as a hard template to prepare CNT-coated Sn nanoparticles with almost 100% particle encapsulation and high filling uniformity by a chemical vapor deposition (CVD) process (Wang et al., 2009). Similarly, Zhou et al. prepared a sulfur-doped carbon nanotube cathode (S-CNTs) by using sulfate-containing AAO templates (**Figure 1c**; Zhou et al., 2012). The specific surface area of S-CNTs with mesoporous structure reached 613 $m^2 g^{-1}$. The authors claimed that the mesoporous structures of S-CNTs can reduce cathode polarization, and promote ion transportation. Moreover, sulfur is confined in the walls of the nanotubes which can restrict the dissolution of formed polysulfides when used as cathode for Li-S battery.

### Self-Templated Synthesis

Direct synthesis without additional template can significantly reduce cost in practical applications. Wood is a natural composite material composing vertical channels. After carbonization, its original features of low tortuous, open micro-channels and 3D layered porous structure can be maintained, which is suitable as building block for constructing ultra-thick electrodes. The wood-derived carbon material was first reported as electrode materials for supercapacitors in 2004 (Wu et al., 2004). Since then, the application of wood-derived materials have been further extended to batteries, electrocatalysis and so on. For example, Li et al. pre-carbonized wood slices at 260°C for 6 h in air atmosphere, then carbonized them at 1000°C for 6 h in Ar atmosphere, and finally activated the carbonized slices in $CO_2$ atmosphere at 800°C (Li et al., 2017). During the process, $CO_2$ reacted with the amorphous carbon in carbonized wood to produce porous structure. The activated wood has an anisotropic

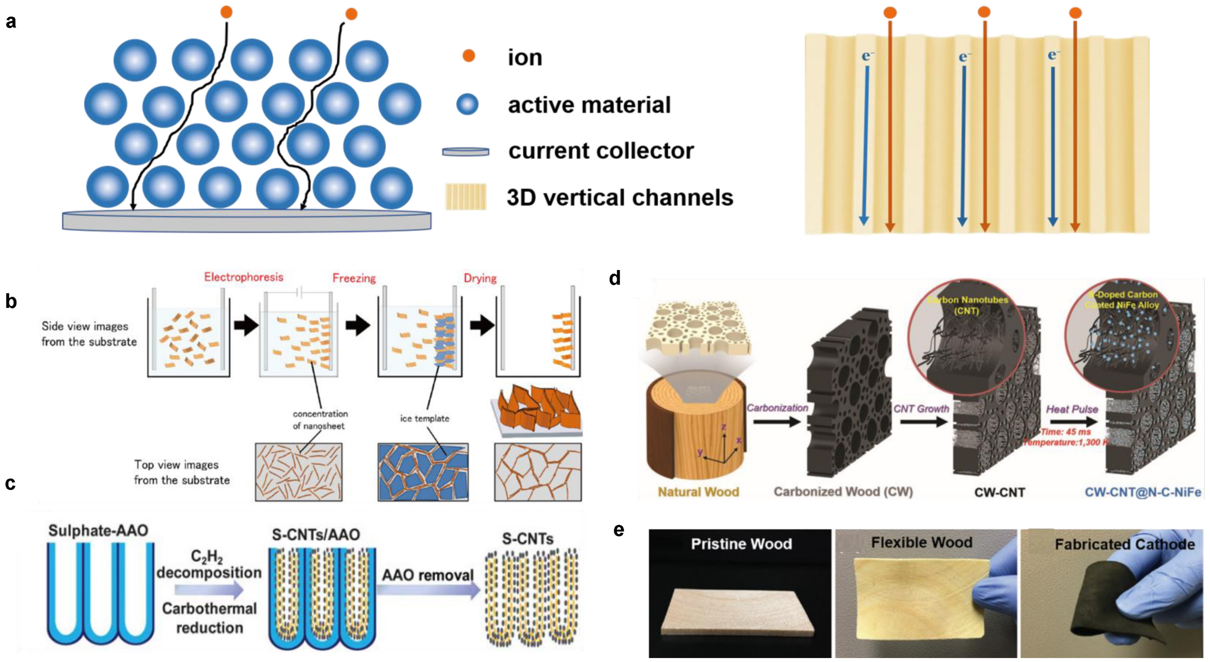

**FIGURE 1 | (a)** Schematic illustration of the different configurations of electrode materials: fabricate electrodes by slurry-casting process (left) and 3D-OPC electrodes (right). **(b)** Formation mechanism of the vertically aligned film by electrophoresis and freeze-drying (source: Mochizuki et al., 2019). Reproduced by permission of American Chemical Society https://doi.org/10.1021/acsaem.8b01478. **(c)** Thermal decomposition of $C_2H_2$ in a sulfate-containing AAO template and the formation of S-CNTs after AAO removal (source: Zhou et al., 2012). Reproduced by permission of Royal Society of Chemistry https://doi.org/10.1039/C2EE22294A. **(d)** The fabrication process of the CW-CNT@N-C-NiFe electrode (source: Li Y. et al., 2018). Reproduced by permission of WILEY-VCH Verlag GmbH & Co. KGaA, Weinheim https://doi.org/10.1002/aenm.201801289. **(e)** Photos of the pristine wood, the flexible wood, and the flexible cathode with the CNT coating and Ru (source: Xu et al., 2018). Reproduced by permission of Royal Society of Chemistry https://doi.org/10.1039/C8EE01468J.

structure and excellent deformation resistance. After that, rGO and S were filled into the microchannels of the carbonized wood to achieve a high sulfur mass load. Furthermore, Wu et al. used $H_2$ as the reducing gas, ethylene as the carbon source and Ar gas as the carrying gas to *in situ* grow CNTs in carbonized wood channels by CVD method (**Figure 1d**; Wu et al., 2019). The specific surface area of the electrode was increased to 537.9 $m^2$ $g^{-1}$ because of the introduction of CNTs. Then, the authors improved the hydrophilicity of the material after treating them using a mixed solution containing $HNO_3$ and $H_2SO_4$, achieving the reduction of contact angle from 144 to 27.1°. Lignin, cellulose and hemicellulose are important components of wood. Xu et al. used sulfites to remove lignin which makes wood rigidity (Xu et al., 2019). Meanwhile, hemicellulose and cellulose could be dissolved by soaking in a basic solution containing sulfites, which made the treated wood more flexible (**Figure 1e**). Later, the surface of the flexible carbonized wood was coated with ruthenium-decorated CNT network (CNT/Ru) by vacuum-assisted method. Based on the Xu's research, Chen et al. reported a carbonized sponge with a high compressibility of $\sim$ 80% and high fatigue resistance (10,000 cycles at 50% strain), which was prepared by a wood template (Chen et al., 2018). In this work, more lignin and hemicellulose inside wood were removed by a treatment of $H_2O_2$. A subsequent carbonization leads to a sponge with unique lamellar structure.

# APPLICATIONS OF ENERGY STORAGE AND CONVERSION

## Electrocatalysis

Noble metal-based catalysts (e.g., Pt and Ir) are efficient electrocatalysts for oxygen evolution reaction (OER), oxygen reduction reaction (ORR) and hydrogen evolution reaction (HER). However, scarcity and valuableness greatly restrict their commercial applications (Deng et al., 2019; Liu et al., 2019, 2020). Therefore, it is desirable to develop inexpensive and efficient alternatives. Ordered porous carbon with vertical channels is a promising candidate, which has advantages of fast ion diffusion and electron transport.

Recently, 3D wood-based materials have aroused numerous researchers' interest. Li et al. demonstrated the core-shell nitrogen doped, few-graphene-layer-encapsulated nickel iron alloy nanoparticles (N-C-NiFe) in the carbonized wood with CNTs (N-C-NiFe@CW-CNT) by thermal-pulse method (Li Y. et al., 2018). The N-C-NiFe was anchored on CNTs uniformly (**Figures 2a–d**). Low-tortuosity microchannels were favor to hydrogen release and electrolyte penetration, therefore, N-C-NiFe@CW-CNT showed good electrochemical performance of HER with a small Tafel slop (52.8 mV $dec^{-1}$), low overpotential (179 mV, at 10 mA $cm^{-2}$) and good cycling stability (**Figure 2e**). Inspired by this, Yang et al. designed a $CoFeP_x$ nano-catalyst with thin iron shells in wood wall ($CoFeP_x$/c-wood) by making

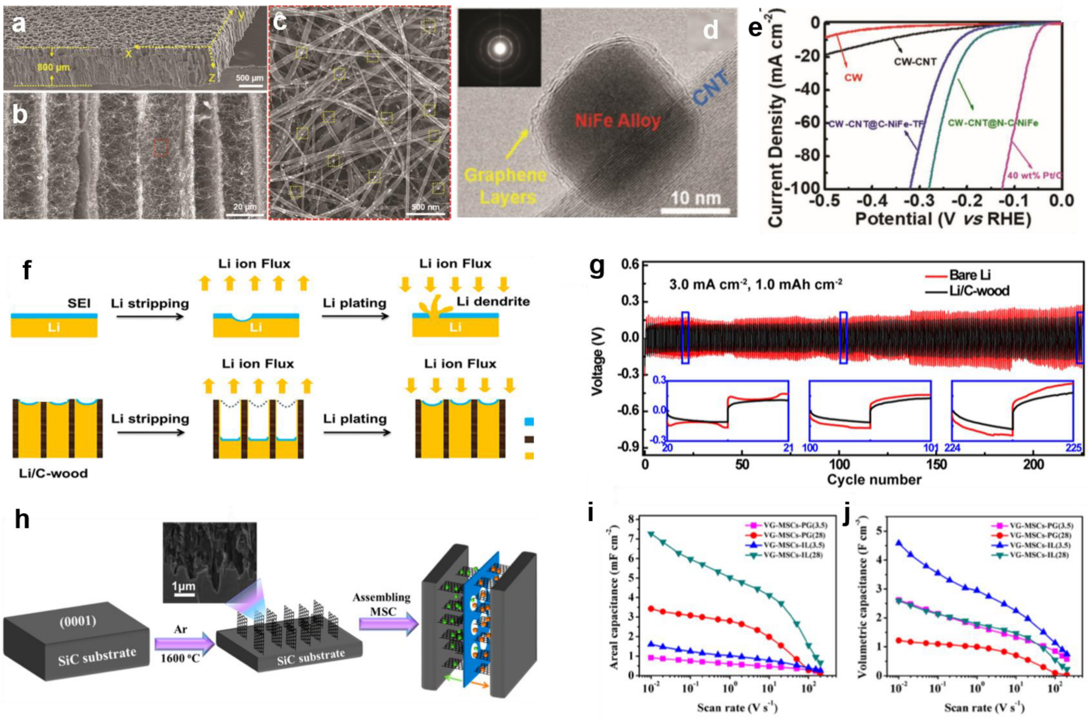

**FIGURE 2 | (a–d)** Morphology of the CW-CNT@N-C-NiFe. **(a–c)**: SEM images of CW-CNTs@N-C-NiFe **(d)**TEM image of CW-CNTs@N-C-NiFe, it shows the NiFe alloy nanoparticle which is inset in CNT and encapsulated by the few graphene layers) **(e)** LSV curves of the CW, CW-CNTs, CW-CNTs@C-NiFe-NF, CW-CNTs@N-C-NiFe, and commercial 40 wt% Pt/C electrodes (source: Li Y. et al., 2018). Reproduced by permission of WILEY-VCH Verlag GmbH & Co. KGaA, Weinheim https://doi.org/10.1002/aenm.201801289. **(f)** Li stripping/plating of bare Li metal electrodes and Li/c-wood electrodes. **(g)** Voltage profiles of bare Li metal and Li/c-wood cell at 3 mA·cm$^{-2}$, Li/c-wood cells exhibited smaller voltage and long-term cycling stability (source: Zhang Y. et al., 2017). Reproduced by permission of American Chemical Society https://doi.org/10.1073/pnas.1618871114. **(h)** VG films derived from the *SiC* substrates to form VG-MSCs. **(i,j)** Areal/volumetric capacitance of different VG-MSCs (PG means using $H_2SO_4$/PVA as gel electrolyte, IL means using $EMIMBF_4$ as liquid electrolyte) (source: Zheng et al., 2017). Reproduced by permission of American Chemical Society https://doi.org/10.1021/acsnano.7b00553.

use of the steam pressure difference between Fe and Co at high temperature (Yang et al., 2019). The thin iron shell (∼2 nm) as the protective layer of $CoFeP_x$ greatly improved the durability of catalyst without sacrificing the activity of the catalyst due to geometric effects of the thin coating layer. Compared to $CoP_x$ and $FeP_x$, $CoFeP_x$ showed a better OER electrochemical performance with lowest overpotential (323 mV at 10 mA cm$^{-2}$) and Tafel slope (58 mV dec$^{-1}$). Besides, $CoFeP_x$/c-wood possessed excellent cycling stability of 50 h.

## Batteries

Rechargeable batteries, such as lithium-ion batteries (Zhang et al., 2018; Deng et al., 2020a,b; Huang et al., 2020), sodium-ion batteries (Gao et al., 2020; Jin et al., 2020; Shi et al., 2020b,c; Wang et al., 2020) and metal-air batteries (Shi et al., 2019; Wu F. et al., 2020), have been intensively investigated recently. Due to the long cycling life, high voltage and energy density, lithium-ion batteries are widely used in electronic devices and other fields (Yan et al., 2019; Deng et al., 2020b).

Li metal anode undergoes large volume change during Li ion intercalation/deintercalation, which destroys the solid electrolyte interphase (SEI), making fresh Li metal exposed to electrolyte and leads to excessive growth of SEI. Zhang Y. et al. (2017) injected the molten lithium metal into the channels of carbonized wood to form a Li metal/carbonized wood (lithium/c-wood) electrode, in which the ZnO coating made the interface between c-wood and Li more wettable. Moreover, c-wood with 3D porous conductive frame structure is an ideal host for lithium metal, which can adapt to the volume change of lithium metal during the long cycle (**Figure 2f**). In addition, compared to bare Li metal, Li/c-wood electrodes in symmetrical batteries had a lower overpotential (90 mV at 3 mA cm$^{-2}$), better cycling performance (150 h at 3 mA cm$^{-2}$) and more stable stripping/plating profiles. Even at a high current density of 3 mA cm$^{-2}$, the Li/c-wood electrodes in the commercial electrolyte achieved long-term cyclic stability (**Figure 2g**). Similarly, Xue et al. (2018) assembled continuous silver nanowires onto an interconnected 3D graphene network (3D Ag-GN) by ice-templating method, and designed a layered 3D porous structure as a host for the lithium metal composite anode. The hierarchical networks not only provided ultrafast electron transport channels and non-nucleation barrier sites to limit lithium deposition, but also had excellent mechanical strength to support lithium deposition. Moreover, 3D Ag-GN could work over 1000 plating/stripping cycles with low overpotential (at 40 mA cm$^{-2}$) in a symmetric cell. As the thickness of the electrode increased, the dynamics of ion transport were hindered, and the rate performance of the lithium-ion batteries decreased. Zhang et al. (2019) used magnetite ($Fe_3O_4$) with high theoretical capacity to produce aligned $Fe_3O_4$/GO electrodes with fast ion transmission channels by ice-templating method. Besides, they proved that $Fe_3O_4$/GO had a fast ion transfer kinetics by galvanostatic intermittent titration technique (GITT), electrochemical impedance spectroscopy (EIS), and cyclic voltammetry (CV).

### Supercapacitors

Supercapacitors is one of the most promising energy storage devices due to long lifetime, high power density, and fast charge/discharge rates (Xu et al., 2017, 2018). However, traditional supercapacitor electrode materials (e.g., activated carbon, carbonized derived carbon, and carbon nanotubes) normally have a long ion-diffusion path. Moreover, the presence of binder in powder-based electrode materials covers a part of the active sites, which reduces energy density. Electrode with vertical channels can provide fast mass transportation. Zheng et al. (2017) designed vertically aligned graphene (VG) nanocrystals by decomposing *SiC* matrix at high temperature, which used as electrode materials for micro-supercapacitors (MSCs) (**Figure 2h**). The VG nanocrystals micro-supercapacitors (VG-MSCs) had high areal and volumetric capacitance, and fast frequency response. More importantly, it showed high power density in gel electrolyte ($\sim$15 W $cm^{-3}$) and ionic liquid ($\sim$61 W $cm^{-3}$) (**Figures 2i,j**). In addition, Chen et al. designed an all-wood-structured asymmetric supercapacitor (ASC) using a $MnO_2$/wood carbon as cathode, an activated wood carbon as anode, and a wood membrane as separator (Chen et al., 2017). Remarkably, a high mass load of active material can be achieved by increasing electrode thickness or extending electrodeposition time of $MnO_2$. The prepared electrode materials maintained the unique anisotropy structure of the wood and highly exposure active sites, allowing the electrolyte ions to pass directly through the channels, showing high ionic conductivity. The ASC retained $\sim$0.6 mW h $cm^{-2}$ (5.7 W h $kg^{-1}$) at a power density of 24440 mW $cm^{-2}$ (107.7 W $kg^{-1}$), which can light up a light-emitting diode (LED) after pre-charging to 1.8 V. Furthermore, Wang Y. et al. (2018) applied $Co(OH)_2$@CW as cathode of an all-solid-state asymmetric supercapacitors, which possessed high energy/power density, and maintained 85% capacitance retention after 10000 charge/discharge cycles.

## CONCLUSION

The versatility and availability of the 3D-OPC with high specific surface area, highly ordered channels, low tortuosity and open pores have been demonstrated in various applications in energy storage and conversion. In this review, we outlined the latest development on the rational design and controllable preparation of 3D-OPC and their composites for applications of electrocatalysis, batteries and supercapacitors. The strategies to achieve controllable synthesis of 3D-OPC can be classified as follows. Firstly, a hard template with appropriate size and morphology can be selected to synthesize electrode materials. Secondly, in ice-templated approach, the electrode thickness and pore size can be controlled through modulating the crystallization behavior of ice by adding various additives (e.g., ethanol, chitosan, or cellulose nanofibers), and adjusting the freezing rate, which achieve high conductivity, shorten ion diffusion length and large specific surface area. Thirdly, carbonization temperature and calcination atmosphere control the shrinkage rate as well as the consequent aperture changes of carbonized wood, which play an essential role in the formation of internal pores and surface morphology of samples.

Although the 3D-OPC or their composites with ultrafast electron/ion transport path, abundant active sites, and fast reaction kinetics showed superior electrochemical performance when applied in energy storage devices, it still has several challenges. First, the methods based on hard templates inevitably involve the corrosive solution in post-processing step, which largely increases the cost and is not suitable to industrialization. Second, the controllable growth of active materials on the 3D-OPC is still a challenge, since uneven distribution of reactants in channels normally results in asymmetrical nucleation and growth of active materials. Third, the relation between morphology, pore size, structure of the 3D-OPC and electrochemical performance is vague and imprecise.

In spite of the vast research and progress that were discussed, there are still many opportunities for further advancement of 3D-OPC. First, the influence of the penetrability of vertical channels (the diffusion of adjacent channels) on electrochemical performance could be further studied. Second, the other active materials, such as perovskite, single atom, can be loaded on the 3D-OPC to improve the performance for photocatalysis, electrocatalysis, and so on. Third, it is significant to proceed the computational simulation about the relation between pore size of vertical channels and electrochemical performance. Moreover, there are still some other methods may be explored for preparing 3D-OPC, such as template-free method, biomass-derived method, the assembly of $sp^2$-hybridized carbon. It is also promising to explore the applications of 3D-OPC in gas separation, dye degradation, water purification, and capacitive deionization (CDI). Therefore, tremendous explorations and optimizations of the 3D-OPC and their composites are indispensable in the future work.

## AUTHOR CONTRIBUTIONS

JF, DZ, XG, WQ, WS, WL, FW, and XC contributed to the discussion and writing in this work. All authors listed have made a substantial, direct and intellectual contribution to the work, and approved it for publication.

## FUNDING

This work was supported by National Natural Science Foundation of China (Grant Nos. 51702286, 51972286, and 21905246) and Zhejiang Provincial Natural Science Foundation of China (LR19E020003 and LQ20B010011), and the China Postdoctoral Science Foundation Funded Project (2019M660144 and 2020T130596).

## REFERENCES

Byeon, A., Cho, J., Kim, J., Chae, K., Park, H., Hong, S., et al. (2020). High-yield electrochemical hydrogen peroxide production from an enhanced two-electron oxygen reduction pathway by mesoporous nitrogen-doped carbon and manganese hybrid electrocatalysts. *Nanoscale Horiz.* 5, 832–838. doi: 10.1039/c9nh00783k

Cao, X., Shi, Y., Shi, W., Lu, G., Huang, X., Yan, Q., et al. (2011). Preparation of novel 3D graphene networks for supercapacitor applications. *Small* 7, 3163–3168. doi: 10.1002/smll.201100990

Cao, X., Tan, C., Sindoro, M., and Zhang, H. (2017). Hybrid micro-/nano-structures derived from metal-organic frameworks: preparation and applications in energy storage and conversion. *Chem. Soc. Rev.* 46, 2660–2677. doi: 10.1039/c6cs00426a

Cao, X., Yin, Z., and Zhang, H. (2014). Three-dimensional graphene materials: preparation, structures and application in supercapacitors. *Energy Environ. Sci.* 7, 1850–1865. doi: 10.1039/c4ee00050a

Chen, C., Song, J., Zhu, S., Li, Y., Kuang, Y., Wan, J., et al. (2018). Scalable and sustainable approach toward highly compressible, anisotropic, lamellar carbon sponge. *Chem* 4, 544–554. doi: 10.1016/j.chempr.2017.12.028

Chen, C., Zhang, Y., Li, Y., Dai, J., Song, J., Yao, Y., et al. (2017). All-wood, low tortuosity, aqueous, biodegradable supercapacitors with ultra-high capacitance. *Energy Environ. Sci.* 10, 538–545. doi: 10.1039/c6ee03716j

Deng, S., He, Z., Liu, B., Yang, L., Wang, X., Shen, S., et al. (2020a). Synergy of ion doping and spiral array architecture on Ti2Nb10O29: a new way to achieve high-power electrodes. *Adv. Funct. Mater.* 30:2002665. doi: 10.1002/adfm.202002665

Deng, S., Zhu, H., Wang, G., Luo, M., Shen, S., Ai, C., et al. (2020b). Boosting fast energy storage by synergistic engineering of carbon and deficiency. *Nat. Commun.* 11:132. doi: 10.1038/s41467-019-13945-1

Deng, S., Luo, M., Ai, C., Zhang, Y., Liu, B., Huang, L., et al. (2019). Synergistic doping and intercalation: realizing deep phase modulation on MoS2 arrays for high-efficiency hydrogen evolution reaction. *Angew. Chem. Int. Ed.* 58, 16289–16296. doi: 10.1002/anie.201909698

Feng, J., and Yin, Y. (2018). Self-templating approaches to hollow nanostructures. *Adv. Mater.* 31:1802349. doi: 10.1002/adma.201802349

Gao, X., Shi, W., Ruan, P., Feng, J., Zheng, D., Yu, L., et al. (2020). Ultrathin carbon boosted sodium storage performance in aqueous electrolyte. *Funct. Mater. Lett.* 13, 2030002–2030010. doi: 10.1142/s1793604720300029

Huang, L., Li, J., Liu, B., Li, Y., Shen, S., Deng, S., et al. (2020). Electrode design for lithium-sulfur batteries: problems and solutions. *Adv. Funct. Mater.* 30:1910375. doi: 10.1002/adfm.201910375

Jin, T., Han, Q., and Jiao, L. (2020). Binder-free electrodes for advanced sodium-ion batteries. *Adv. Mater.* 32:e1806304. doi: 10.1002/adma.201806304

Kyotani, T., Sonobe, N., and Tomita, A. (1988). Formation of highly orientated graphite from polyacrylonitrile by using a two-dimensional space between montmorillonite lamellae. *Nature* 331, 331–333. doi: 10.1038/331331a0

Kyotani, T., Tsai, L.-F., and Tomita, A. (1995). Formation of ultrafine carbon tubes by using an anodic aluminum oxide film as a template. *Chem. Mater.* 7, 1427–1428. doi: 10.1021/cm00056a001

Li, C., Li, Q., Kaneti, Y., Hou, D., Yamauchi, Y., and Mai, Y. (2020). Self-assembly of block copolymers towards mesoporous materials for energy storage and conversion systems. *Chem. Soc. Rev.* 49, 4681–4736. doi: 10.1039/d0cs00021c

Li, W., Fang, R., Xia, Y., Zhang, W., Wang, X., Xia, X., et al. (2019). Multiscale porous carbon nanomaterials for applications in advanced rechargeable batteries. *Batter. Supercaps* 2, 9–36. doi: 10.1002/batt.201800067

Li, X., Guan, B., Gao, S., and Lou, X. (2018). A general dual-templating approach to biomass-derived hierarchically porous heteroatom-doped carbon materials for enhanced electrocatalytic oxygen reduction. *Environ. Sci. Technol.* 12:648. doi: 10.1039/C8EE02779J

Li, Y., Gao, T., Yao, Y., Liu, Z., Kuang, Y., Chen, C., et al. (2018). In situ "chainmail catalyst" assembly in low-tortuosity, hierarchical carbon frameworks for efficient and stable hydrogen generation. *Adv. Energy Mater.* 8:1801289. doi: 10.1002/aenm.201801289

Li, Y., Fu, K., Chen, C., Luo, W., Gao, T., Xu, S., et al. (2017). Enabling high-areal-capacity lithium-sulfur batteries: designing anisotropic and low-tortuosity porous architectures. *ACS Nano* 11, 4801–4807. doi: 10.1021/acsnano.7b01172

Liu, W., Yin, R., Xu, X., Zhang, L., Shi, W., and Cao, X. (2019). Structural engineering of low-dimensional metal-organic frameworks: synthesis, properties, and applications. *Adv. Sci.* 6:1802373. doi: 10.1002/advs.201802373

Liu, W., Yu, L., Yin, R., Xu, X., Feng, J., Jiang, X., et al. (2020). Non-3d metal modulation of a 2D Ni-Co heterostructure array as multifunctional electrocatalyst for portable overall water splitting. *Small* 16:1906775. doi: 10.1002/smll.201906775

Masuda, H., and Fukuda, K. (1995). Ordered metal nanohole arrays made by a two-step replication of honeycomb structures of anodic alumina. *Science* 268, 1466–1468. doi: 10.1126/science.268.5216.1466

Mochizuki, D., Tanaka, R., Makino, S., Ayato, Y., and Sugimoto, W. (2019). Vertically aligned reduced graphite oxide nanosheet film and its application in a high-speed charge/discharge electrochemical capacitor. *ACS Appl. Energy Mater.* 2, 1033–1039. doi: 10.1021/acsaem.8b01478

Ni, J., and Li, L. (2020). Cathode architectures for rechargeable ion batteries: progress and perspectives. *Adv. Mater.* 32:2000288. doi: 10.1002/adma.202000288

Peng, H., Yao, B., Wei, X., Liu, T., Kou, T., Xiao, P., et al. (2019). Pore and heteroatom engineered carbon foams for supercapacitors. *Adv. Energy Mater.* 9:1803665. doi: 10.1002/aenm.201803665

Qiao, Y., Han, R., Pang, Y., Lu, Z., Zhao, J., Cheng, X., et al. (2019). 3D well-ordered porous phosphorus doped carbon as an anode for sodium storage: structure design, experimental and computational insights. *J. Mater. Chem. A* 7, 11400–11407. doi: 10.1039/c9ta02268f

Roberts, A., Li, X., and Zhang, H. (2014). Porous carbon spheres and monoliths: morphology control, pore size tuning and their applications as Li-ion battery anode materials. *Chem. Soc. Rev.* 43, 4341–4356. doi: 10.1039/c4cs00071d

Shahbazi, M.-A., Ghalkhani, M., and Maleki, H. (2020). Directional freeze-casting: a bioinspired method to assemble multifunctional aligned porous structures for advanced applications. *Adv. Eng. Mater.* 22:2000033. doi: 10.1002/adem.202000033

Shao, G., Hanaor, D., Shen, X., and Gurlo, A. (2020). Freeze casting: from low-dimensional building blocks to aligned porous structures-A review of novel materials, methods, and applications. *Adv. Mater.* 32:1907176. doi: 10.1002/adma.201907176

Shi, B., Shang, Y., Pei, Y., Pei, S., Wang, L., Heider, D., et al. (2020a). Low tortuous, highly conductive, and high-areal-capacity battery electrodes enabled by through-thickness aligned carbon fiber framework. *Nano Lett.* 20, 5504–5512. doi: 10.1021/acs.nanolett.0c02053

Shi, W., Gao, X., Mao, J., Qian, X., Liu, W., Wu, F., et al. (2020b). Exploration of energy storage materials for water desalination via next-generation capacitive deionization. *Front. Chem.* 8:415. doi: 10.3389/fchem.2020.00415

Shi, W., Liu, X., Deng, T., Huang, S., Ding, M., Miao, X., et al. (2020c). Enabling superior sodium capture for efficient water desalination by a tubular polyaniline decorated with prussian blue nanocrystals. *Adv. Mater.* 2020:1907404. doi: 10.1002/adma.201907404

Shi, W., Mao, J., Xu, X., Liu, W., Zhang, L., Cao, X., et al. (2019). An ultra-dense NiS2/reduced graphene oxide composite cathode for high-volumetric/gravimetric energy density nickel-zinc batteries. *J. Mater. Chem. A* 7, 15654–15661. doi: 10.1039/c9ta04900b

Ullah, S., Hasan, M., Ta, H., Zhao, L., Shi, Q., Fu, L., et al. (2019). Synthesis of doped porous 3D graphene structures by chemical vapor deposition and its applications. *Adv. Funct. Mater.* 29:1904457. doi: 10.1002/adfm.201904457

Wang, B., Cheng, Y., Su, H., Cheng, M., Li, Y., Geng, H., et al. (2020). Boosting transport kinetics of cobalt sulfides yolk-shell spheres by anion doping for advanced lithium and sodium storage. *ChemSusChem* 13, 1–9. doi: 10.1002/cssc.202001261

Wang, C., Chen, X., Wang, B., Huang, M., Wang, B., Jiang, Y., et al. (2018). Freeze-casting produces a graphene oxide aerogel with a radial and centrosymmetric structure. *ACS Nano* 12, 5816–5825. doi: 10.1021/acsnano.8b01747

Wang, Y., Lin, X., Liu, T., Chen, H., Chen, S., Jiang, Z., et al. (2018). Wood-derived hierarchically porous electrodes for high-performance all-solid-state supercapacitors. *Adv. Funct. Mater.* 28:1806207. doi: 10.1002/adfm.201806207

Wang, J., and Ellsworth, M. (2009). Graphene aerogels. *ECS Trans.* 19, 241–247. doi: 10.1149/1.3119548

Wang, X., Wang, T., Borovilas, J., He, X., Du, S., and Yang, Y. (2019). Vertically-aligned nanostructures for electrochemical energy storage. *Nano Res.* 12, 2002–2017. doi: 10.1007/s12274-019-2392-x

Wang, Y., Wu, M., Jiao, Z., and Lee, J. (2009). Sn@CNT and Sn@C@CNT nanostructures for superior reversible lithium ion storage. *Chem. Mater.* 21, 3210–3215. doi: 10.1021/cm900702d

Wu, C., Zhang, S., Wu, W., Xi, Z., Zhou, C., Wang, X., et al. (2019). Carbon nanotubes grown on the inner wall of carbonized wood tracheids for high-performance supercapacitors. *Carbon* 150, 311–318. doi: 10.1016/j.carbon.2019.05.032

Wu, F.-C., Tseng, R.-L., Hu, C.-C., and Wang, C.-C. (2004). Physical and electrochemical characterization of activated carbons prepared from firwoods for supercapacitors. *J. Power Sources* 138, 351–359. doi: 10.1016/j.jpowsour.2004.06.023

Wu, F., Gao, X., Xu, X., Jiang, Y., Gao, X., Yin, R., et al. (2020). MnO2 nanosheet-assembled hollow polyhedron grown on carbon cloth for flexible aqueous zinc-ion batteries. *ChemSusChem* 13, 1537–1545. doi: 10.1002/cssc.201903006

Wu, M., Liao, J., Yu, L., Lv, R., Li, P., Sun, W., et al. (2020). 2020 roadmap on carbon materials for energy storage and conversion. *Chem. Asian J.* 15, 995–1013. doi: 10.1002/asia.201901802

Wu, Q., Yang, L., Wang, X., and Hu, Z. (2020). Mesostructured carbon-based nanocages: an advanced platform for energy chemistry. *Sci. China Chem.* 63, 665–681. doi: 10.1007/s11426-020-9748-0

Xu, S., Chen, C., Kuang, Y., Song, J., Gan, W., Liu, B., et al. (2019). Flexible lithium-CO2 battery with ultrahigh capacity and stable cycling. *Environ. Sci. Technol.* 11, 3231–3237. doi: 10.1039/C8EE01468J

Xu, X., Shi, W., Li, P., Ye, S., Ye, C., Ye, H., et al. (2017). Facile fabrication of three-dimensional graphene and metal-organic framework composites and their derivatives for flexible all-solid-state supercapacitors. *Chem. Mater.* 29, 6058–6065. doi: 10.1021/acs.chemmater.7b01947

Xu, X., Shi, W., Liu, W., Ye, S., Yin, R., Zhang, L., et al. (2018). Preparation of two-dimensional assembled Ni-Mn-C ternary composites for high-performance all-solid-state flexible supercapacitors. *J. Mater. Chem. A* 6, 24086–24091. doi: 10.1039/c8ta06412a

Xue, P., Liu, S., Shi, X., Sun, C., Lai, C., Zhou, Y., et al. (2018). A hierarchical silver-nanowire-graphene host enabling ultrahigh rates and superior long-term cycling of lithium-metal composite anodes. *Adv. Mater.* 30:1804165. doi: 10.1002/adma.201804165

Yan, Z., Jin, H., and Guo, J. (2019). Low-temperature synthesis of graphitic carbon-coated silicon anode materials. *Carbon Energy* 1, 246–252. doi: 10.1002/cey2.8

Yang, C., Cui, M., Li, N., Liu, Z., Hwang, S., Xie, H., et al. (2019). In situ iron coating on nanocatalysts for efficient and durable oxygen evolution reaction. *Nano Energy* 63:103855. doi: 10.1016/j.nanoen.2019.103855

Zhai, H., Xu, P., Ning, M., Cheng, Q., Mandal, J., and Yang, Y. (2017). A flexible solid composite electrolyte with vertically aligned and connected ion-conducting nanoparticles for lithium batteries. *Nano Lett.* 17, 3182–3187. doi: 10.1021/acs.nanolett.7b00715

Zhang, F., Wei, M., Viswanathan, V., Swart, B., Shao, Y., Wu, G., et al. (2017). 3D printing technologies for electrochemical energy storage. *Nano Energy* 40, 418–431. doi: 10.1016/j.nanoen.2017.08.037

Zhang, P., Li, J., Lv, L., Zhao, Y., and Qu, L. (2017). Vertically aligned graphene sheets membrane for highly efficient solar thermal generation of clean water. *ACS Nano* 11, 5087–5093. doi: 10.1021/acsnano.7b01965

Zhang, Y., Luo, W., Wang, C., Li, Y., Chen, C., Song, J., et al. (2017). High-capacity, low-tortuosity, and channel-guided lithium metal anode. *Proc. Natl. Acad. Sci. U.S.A.* 114, 3584–3589. doi: 10.1073/pnas.1618871114

Zhang, L., Liu, W., Shi, W., Xu, X., Mao, J., Li, P., et al. (2018). Boosting lithium storage properties of MOF derivatives through a wet-spinning assembled fiber strategy. *Chemistry* 24, 13792–13799. doi: 10.1002/chem.201802826

Zhang, X., Ju, Z., Housel, L., Wang, L., Zhu, Y., Singh, G., et al. (2019). Promoting transport kinetics in Li-ion battery with aligned porous electrode architectures. *Nano Lett.* 19, 8255–8261. doi: 10.1021/acs.nanolett.9b03824

Zhang, X., Zhang, S., Yang, Y., Wang, L., Mu, Z., Zhu, H., et al. (2020). A general method for transition metal single atoms anchored on honeycomb-like nitrogen-doped carbon nanosheets. *Adv. Mater.* 32:1906905. doi: 10.1002/adma.201906905

Zhao, Q., Wang, X., Liu, J., Wang, H., Zhang, Y., Gao, J., et al. (2015). Design and synthesis of three-dimensional hierarchical ordered porous carbons for supercapacitors. *Electrochim. Acta* 154, 110–118. doi: 10.1016/j.electacta.2014.12.052

Zheng, S., Li, Z., Wu, Z., Dong, Y., Zhou, F., Wang, S., et al. (2017). High packing density unidirectional arrays of vertically aligned graphene with enhanced areal capacitance for high-power micro-supercapacitors. *ACS Nano* 11, 4009–4016. doi: 10.1021/acsnano.7b00553

Zhou, G., Wang, D.-W., Li, F., Hou, P.-X., Yin, L., Liu, C., et al. (2012). A flexible nanostructured sulphur-carbon nanotube cathode with high rate performance for Li-S batteries. *Energy Environ. Sci.* 5, 8901–8906. doi: 10.1039/c2ee22294a

Zhou, X., Chen, L., Zhang, W., Wang, J., Liu, Z., Zeng, S., et al. (2019). Three-dimensional ordered macroporous metal-organic framework single crystal-derived nitrogen-doped hierarchical porous carbon for high-performance potassium-ion Batteries. *Nano Lett.* 19, 4965–4973. doi: 10.1021/acs.nanolett.9b01127

**Conflict of Interest:** The authors declare that the research was conducted in the absence of any commercial or financial relationships that could be construed as a potential conflict of interest.

frontiers
in Energy Research

REVIEW
published: 03 September 2020
doi: 10.3389/fenrg.2020.00139

# Three-Dimensional Architectures in Electrochemical Capacitor Applications – Insights, Opinions, and Perspectives

*Przemyslaw Galek, Adam Mackowiak, Paulina Bujewska and Krzysztof Fic**

*Institute of Chemistry and Technical Electrochemistry, Poznań, Poland*

This review focuses on describing the current state-of-the-art research in the synthesis of 3D architectures for electrochemical capacitor applications. The selection is based on both template and non-template strategies. Particular attention has been paid to carbon materials because of their structural interconnection, as they create not only the desired hierarchical porous channels but also ensure high conductivity and mechanical stability. A comprehensive overview of electrode materials is presented here with a detailed discussion of composite solutions, including their advantages and disadvantages. Numerous examples from the literature are presented for individual solutions. The future challenges posed for this type of material are finally summarized.

**Keywords: electrochemical energy storage, porous carbon materials, supercapacitors, supercapacitor (SC), activated-carbon, 3D carbon materials**

**Edited by:**
*Tianyu Liu,*
*Virginia Tech, United States*

**Reviewed by:**
*Yu Song,*
*Northeastern University, China*
*Bin Yao,*
*University of California, Santa Cruz, United States*

***Correspondence:**
*Krzysztof Fic*
*krzysztof.fic@put.poznan.pl*

**Specialty section:**
*This article was submitted to Electrochemical Energy Conversion and Storage, a section of the journal Frontiers in Energy Research*

**Received:** *01 April 2020*
**Accepted:** *05 June 2020*
**Published:** *03 September 2020*

**Citation:**
*Galek P, Mackowiak A, Bujewska P and Fic K (2020) Three-Dimensional Architectures in Electrochemical Capacitor Applications – Insights, Opinions, and Perspectives. Front. Energy Res. 8:139. doi: 10.3389/fenrg.2020.00139*

## INTRODUCTION

This review follows a slightly different manner than other papers that appear in the field. The great variety of the materials that might be successfully described and compared makes honest comparison and comprehensive description almost impossible in the frame of one paper. Undoubtedly, there are several reasons for such a situation, with a subjective point of view as the first one. The primary goal of this paper is instead to provide some insights and opinions on the methods and materials that have recently attracted scientific interest and might be considered as promising candidates for further development. Throughout the text, there are almost no values presented, compared, and discussed, essentially in the "better/worse" context; this kind of approach is followed for a specific purpose. Namely, a broad spectrum of the methods applied for the materials testing does not allow for reliable comparisons and evaluation, as the specific capacitance depends on many factors. Of course, taking into account the formula for energy stored in the system, one might expect some kind of contest in this field. But this way might quickly lead to . . . nowhere. For instance, such a competition in numbers generated the large amount of papers that have reported enormous capacitance values, reaching hundreds or thousands of Farads per gram. Still, they are (in a great majority of cases) battery-like materials, having nothing in common with capacitive or pseudocapacitive properties. Thus, the primary "take-home message" from this paper is that reasonable development does not mean that there should be a race or competition in specific capacitance values, cycle numbers, or Volts presented as operating voltage. Rational development and promising material must be sourced from multivariant analyses that also take into consideration the application of the device, user safety, and the broad spectrum of the final system demands. Without such a discussion and consideration, each new material will be just a small piece of a big cake, that might be (of course!) very tasty but must still contribute to the final effect. In other words, we do not pretend to be able to judge whether an apple pie is better than a brownie, but we instead describe and discuss how to prepare them if there is a wish to enjoy some treat.

## ENERGY STORAGE DEVICES

The energy storage devices market has been growing over the last decades, and it is a big challenge to satisfy the requirements of modern society. Additionally, an increase in energy consumption and, consequently, fossil fuel depletion has led scientists from all over the world to try to use renewable energy sources and find new materials for advanced technologies (Wang X. et al., 2014; Yu et al., 2015c; Alola et al., 2019). Moreover, it is essential to store energy safely and use it efficiently when needed. Batteries and electrochemical capacitors (ECs) seem to be adequate devices for these purposes (Bernardo et al., 2011; Xu et al., 2013). A comparison between different devices based on specific power and energy values that can be reached by these systems is presented in the Ragone plot (**Figure 1**).

Lithium-ion batteries are one of the most popular devices, applied when required power is rather low, e.g., portable electronics such as cell phones and laptops, but also in electric vehicles. Batteries are also characterized by high energy density values – significantly higher if compared with ECs (Etacheri et al., 2011; Scrosati, 2011; Schipper et al., 2017). On the other hand, when moderate energy has to be delivered in a short time, ECs can be successfully used. ECs are used as a memory back-up in small electrical equipment, such as photo and video cameras or coffee machines. In the automotive industry, ECs can be coupled with batteries and used in hybrid cars, but also in city transportation where "stop-and-go" technology is implemented (Nomoto et al., 2001; Shukla et al., 2012; Miller et al., 2014). Hence, the utility of batteries and ECs strongly depends on the needed properties.

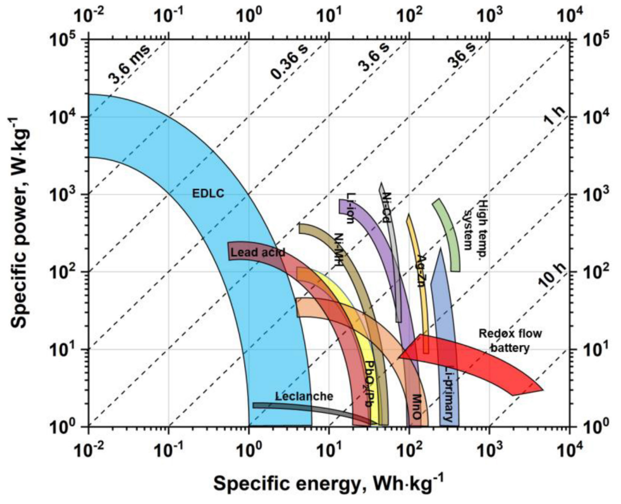

**FIGURE 1 |** The Ragone plot presenting specific power and energy values reached by different energy storage devices. Based on data sourced from Simon and Gogotsi (2010), Béguin and Frąckowiak (2013), Budde-Meiwes et al. (2013).

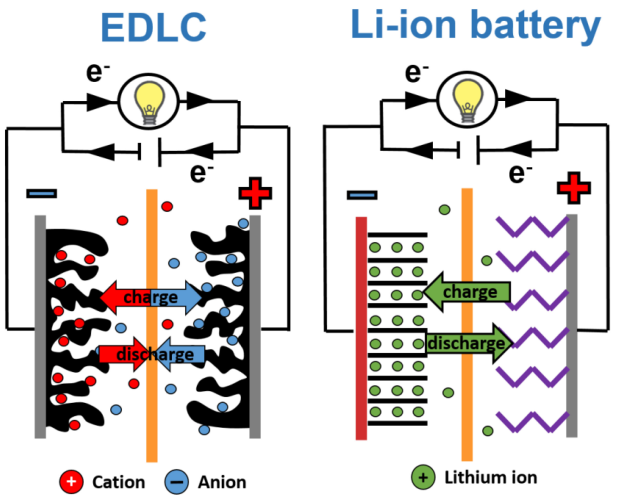

**FIGURE 2 |** Electrochemical capacitor and lithium-ion cell construction. Adapted from Béguin and Frąckowiak (2009) and Béguin and Frąckowiak (2013) with permission from Wiley-VCH Verlag GmbH & Co. KGaA.

All the mentioned differences between batteries and ECs' performance come from their different constructions and principles of operation, presented in **Figure 2**.

A Li-ion battery is composed of one or more cells where chemical reactions occur at a positive and a negative electrode during the charging and discharging processes. The positive electrode (cathode), as a source of lithium cations, can be made of lithium-metal oxides (e.g., $LiMn_2O_4$, $LiCoO_2$), olivine $LiFePO_4$, $LiNiPO_4$ or $LiCoPO_4$ and others containing nickel ($LiMnNiCoO_3$, $LiNi_{0.8}Co_{0.15}Al_{0.005}O_2$). The negative electrode (anode) is usually a layered carbon material where lithium ions can be stored (during charge) and released from layers (during discharge). The most popular material is graphite because of its low cost, ready availability and relatively stable structure (Daniel, 2008; Nitta et al., 2015; Kim et al., 2019). There is also a separator between the electrodes that allows ions to flow from one electrode to another, but which prevents electrons from moving through it, to avoid a short circuit. In batteries, different types of electrolytes can be used. Still, liquid organic electrolytes with lithium salts like $LiPF_6$ or $LiBF_4$, or more complex compounds such as $LiBC_4O_8$ or $Li[PF_3(C_2F_5)_3]$ in organic solvents (e.g., dimethyl carbonate DMC, ethyl methyl carbonate EMC, acetonitrile ACN, and propylene carbonate PC) are used (Younesi et al., 2015).

When the battery is being charged, electrons are moved from the positive electrode to the negative one through an external circuit (the positive electrode is being oxidized, the negative electrode is being reduced) and the positive electrode "releases" some of its lithium ions, which move *via* the electrolyte to the negative electrode. Energy is taken in and stored in the cell.

During discharge, the opposite process takes place – the electrons move back to the positive electrode (reduction of electrode occurs) and lithium ions reach this electrode as well. Chemical energy is thus converted in this process into electricity, and the external device can be powered (Barai et al., 2015; Yu et al., 2019).

ECs' construction is rather simple – two electrodes made of a highly porous carbon material (with a specific surface area around 2000 $m^2 \cdot g^{-1}$) are immersed in an electrolyte solution (which is a source of ions) and, like in batteries, separated by a separator (quite often made of glassy fiber) (Pandolfo and Hollenkamp, 2006; Béguin et al., 2014; Zhong et al., 2015; Fic et al., 2018). The principle of operation is based on electrostatic interaction between ions and an electrode surface. During this process, the so-called electrical double-layer is formed. Because of this phenomenon, ECs are also called electric double-layer capacitors (EDLCs). Ions' attraction to the electrode surface is a very fast and reversible process. The specific power of these devices is higher if compared to batteries.

Electrolytes used for ECs can be aqueous (Khomenko et al., 2006; Ruiz et al., 2009; Fic et al., 2012a,b; Gao et al., 2012; Ratajczak et al., 2014), organic, or ionic liquids (Ruch et al., 2010; Krause and Balducci, 2011; Wang et al., 2012a; Weingarth et al., 2013; Mirzaeian et al., 2017; Hirota et al., 2018). Each of them have different advantages and disadvantages. An operating voltage strongly depends on the kind of medium used and, consequently, the specific energy depends on it as well (Frackowiak et al., 2005; Pandolfo and Hollenkamp, 2006; Béguin et al., 2014).

It seems to be evident that the same electrode materials cannot be used in both device types, because of asymmetric construction of batteries, symmetric construction of EDLCs, and different energy storage/conversion mechanisms. Moreover, the behavior of the electrodes during device operation is supposed to be different. Because of the intercalation process onto negative electrode occurring in Li-ion batteries, the graphite structure can be changed/destroyed when cycled, so it can (and does) expand. It is one of the factors that limits the battery lifetime. Theoretically, for EC's electrodes, dimensional changes are not expected. However, investigations performed for organic electrolytes mostly show quite significant changes in electrode volume, especially when the electrode is polarized negatively (Hahn et al., 2006; Hantel et al., 2014; Prehal et al., 2015).

The capacity of batteries originates directly from redox reactions, hence its value is relatively high. Capacity is here understood as the amount of charge that can be stored in the cell. It is calculated for active material in the battery. This value is given in Ah and strongly depends on battery "state-of-health" – batteries lose their capacity over time. Moreover, the energy stored in batteries can reach much higher values than in the case of ECs.

To express ECs' performance, a capacitance value should be calculated ($C_{device}$). The full device is considered as two capacitors connected in series and the capacitance can be calculated as follows:

$$\frac{1}{C_{device}} = \frac{1}{C_{electrode(+)}} + \frac{1}{C_{electrode(-)}} \tag{1}$$

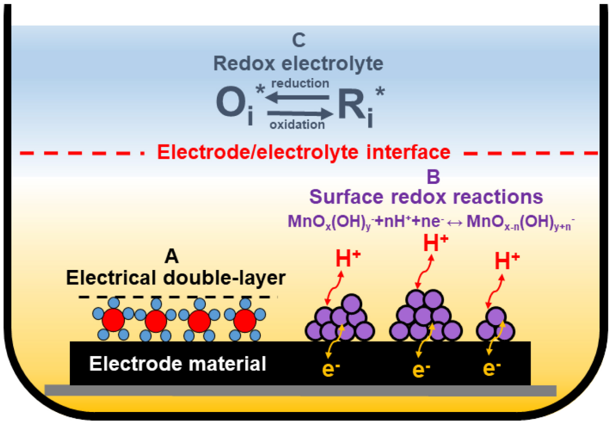

**FIGURE 3 |** Various charge storage mechanisms in ECs: electrical double-layer formation **(A)** and surface redox reactions **(B)** at the electrode/electrolyte interface; redox reactions from the redox-active electrolyte **(C)**.

In the case of the symmetric cell, both electrodes [$C_{electrode(+)}$ and $C_{electrode(-)}$] have the same capacitance values, hence:

$$\frac{1}{C_{device}} = \frac{2}{C_{electrode}} \tag{2}$$

$$C_{device} = \frac{C_{electrode}}{2}. \tag{3}$$

Because of different carbon materials utilization, various constructions, and electrode masses, one should recalculate capacitance given from Eq. 3 to gravimetric capacitance, based on the mass of active material ($m_{act}$) (Eq. 5) or to normalized capacitance (based on the electrode area) (Eq. 5):

$$C_{electrode} = \frac{2 \cdot C_{device}}{0.5 \cdot m_{act}}, \text{ hence} \tag{4}$$

$$C_{electrode} = \frac{4 \cdot C_{device}}{m_{act}} \left[F \cdot g^{-1}\right] \tag{5}$$

$$C = \frac{C_{electrode}\left[F \cdot g^{-1}\right]}{SSA\left[m^2 \cdot g^{-1}\right]} \cdot 10^2 \left[\mu F \cdot cm^{-2}\right] \tag{6}$$

The specific energy value of ECs strongly depends on capacitance, and it can be calculated as follows:

$$E = \frac{1}{2} \cdot C_{device} \cdot U^2 \tag{7}$$

Scientists all over the world have been working on ECs' performance and energy improvement to reach values competitive to batteries. Hence, modifications of conventional EDLCs were invented (**Figure 3**).

Except for typical electrical double-layer formations (**Figure 3A**), redox reactions can be implemented in ECs. These reactions may have a different origin. One possibility is a modification of the electrode material by introducing transition metal oxides (TMOs) (like manganese oxide) (Khomenko et al., 2006; Yang X.-H. et al., 2007; Malak et al., 2010), or intrinsically

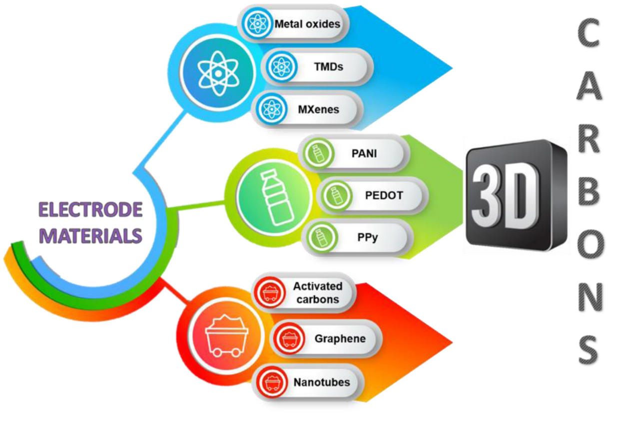

**FIGURE 4 |** Division of EDLC electrode materials.

conducting polymers (ICPs) (Peng et al., 2008; Li et al., 2009; Fang et al., 2010) or heteroatoms-enriched carbons (Figueiredo et al., 1999; Frackowiak et al., 2006; Raymundo-Piñero et al., 2006; Lota et al., 2007; **Figure 3B**). This "additional capacitance" from redox reactions occurring at the electrode/electrolyte interface is called pseudocapacitance. Materials that could be used for this purpose are discussed in detail in the next section of this review. Redox-active electrolytes can also be used in ECs as a redox-active species source (**Figure 3C**). The most popular ones in the aqueous medium are halides (bromide and iodide anions) (Frackowiak et al., 2012; Chen et al., 2015; Menzel et al., 2015; Sathyamoorthi et al., 2016). However, recently, a different group has also been implemented as a redox-active electrolyte – pseudohalides (thiocyanates and selenocyanates) (Gorska et al., 2017; Bujewska et al., 2019).

## ELECTRODE MATERIALS USED IN ELECTROCHEMICAL CAPACITORS

The key components of the EC are the electrode materials presented in **Figure 4**, and the electrolyte (Frackowiak et al., 2013). The role of charging the ion-sensitive interface between electrode and electrolyte is here fundamental (Béguin et al., 2014). It seems that higher values of capacitance are obtained when the larger surface area of the electrode is used. However, it has been demonstrated that the pore volume corresponds more substantially with specific capacitance than the surface area does (Frackowiak et al., 2006). Advancement of the specific surface area typically makes the pore walls thinner and the pore diameter a bit wider, but so-called screening effects begin to influence the capacitance properties severely. Therefore, the electrode pore size arrangement cannot be neglected (Pandolfo and Hollenkamp, 2006). Recently, the production of electrode materials has been geared toward achieving sufficient pore size (in correlation with selected electrolyte) with effective pore distribution during long-term cycling for enhanced charge propagation and chemical stability (Alexandru and Andrea, 2017).

### Carbon Materials

Activated carbon (AC) is the material most widely used as an electrode component. Activated carbon has attracted significant attention due to its large surface area, great electrochemical properties, and moderate cost (Pineiro-Prado et al., 2016). Activated carbons can be produced from various types of carbonaceous materials, which are well abundant, *via* either physical or chemical activation. Physical activation requires the treatment of carbon precursors in the presence of gases such as air, $CO_2$, or steam at high temperatures from 700 to 1200°C. With regards to chemical activation, the activating agents such as sodium hydroxide, potassium hydroxide, zinc chloride, and phosphoric acid are used at lower temperatures from 400 to 700°C (Pandolfo and Hollenkamp, 2006). Activated carbons' porous structure is obtained using activation processes that have a wide distribution of the pore size consisting of macro-, meso-, and micropores (<2 nm). Overactivation results in large volumes of pores, which in turn leads to drawbacks such as poor conductivity and material density, resulting in low energy density and power loss (Heimbckel et al., 2019). Development and further efforts in carbonization procedures seem to be necessary to consider them as industrially reasonable and feasible.

Activated carbons made of biomass have attracted the attention of scientists around the world as they use abundant and renewable resources. Besides that, they have intriguing properties that derive from the relatively high content of various elements which can provide higher electron density and pseudocapacitive contribution (Yang et al., 2019). An essential feature of the synthesis of ACs from biomass is the low production price. Activated carbons could be produced from different materials like shells, leaves, flowers, bamboo, banana peels, seaweeds, olive stones, and coffee grounds (Fic et al., 2018). Coconut shell is an abundant material with a proper compact structure that is most commonly used in research (Ghosh et al., 2019). Usually, biomass carbonization yield is highly dependent on the type of precursor, preliminary drying, and purification processes, and the yield has a wide range from 30 to 50%. Quite often, the authors are picking biomass without considering a yield of carbonization, elemental composition, quality, price, etc. (Herou et al., 2018). For example, the carbonization of certain flowers is highly doubtful and meaningless due to the scarcity and minor content of carbon, which affects the yield of carbonization (Zhao and Zheng, 2015).

Graphene has recently enjoyed tremendous attention (Marcano et al., 2010). One atom-thick 2D structure has emerged as a unique carbon material with potential for use in energy storage devices due to its outstanding characteristics of high electrical conductivity, chemical stability, and large surface area (Miller et al., 2018; Najib and Erdem, 2019). Recently, it has been suggested that graphene could be used in ECs because it does not rely on the distribution of solid-state pores compared to other carbon materials such as ACs or carbon nanotubes (CNTs; Kim et al., 2013). When the entire specific surface area is fully used, graphene could achieve a capacitance up to 550 $F{\cdot}g^{-1}$ (Qingqing and John, 2016). The leading quality is that both of the main graphene sheet surfaces could be exterior and easily accessible by an electrolyte. In the area of high-power applications, it is necessary to produce capacitors with high specific capacitance and quick charging times at high current density. It could be possible by synthesizing graphene from the modified Hummer's method and tip sonication, for use in electric vehicles (Vivekchand et al., 2008). The major drawback of graphene is the process of agglomeration which can lead to restacking back to graphite. This downside could be reduced by thermal reduction of graphite oxide at high temperatures and later rapid cooling using liquid nitrogen.

Carbon nanotubes caught a lot of attention in electrochemistry because of their specific pore structure, good mechanical and thermal stability, and excellent electrical properties (Winkless, 2014). Carbon nanotubes are usually formed by catalytic decomposition of certain hydrocarbons. It is possible to create nanostructures in different frameworks by manipulating different parameters (Zhou Y. et al., 2013). The CNT, unlike other carbon-based electrodes, has mesopores that are intertwined, enabling a continuous charge delivery that uses almost all of the available surface area. Nanotubes are distinguished by their lower electrical resistance values due to the high content of mesopores, which promote the diffusion of ions (Jian et al., 2012). Carbon nanotubes can be used as high-power electrode materials because of their great conductivity and accessible surface area. CNTs could also be a support for other active materials because of their elasticity and mechanical resistance. Unfortunately, nanotubes have a small specific surface area ($<500\ m^2\cdot g^{-1}$) which in turn leads to a low energy density relative to ACs. However, it is possible to improve specific capacitance of CNTs using chemical activation with potassium hydroxide (Simon and Gogotsi, 2008).

Moreover, carbon materials can be easily modified to improve energy storage devices' performance. In the case of ECs, surface modifications are the most important due to the surface-related mechanism of charge storage. However, most of the changes also concern the bulk of the material. A comprehensive discussion on this topic can be found in the literature (Liu et al., 2010; Wang G. et al., 2014; Wang et al., 2015; Slesinski et al., 2018; Yao et al., 2020). In many cases, this kind of modification allows an operating voltage to be increased, most likely by changing the pH at the electrode/electrolyte interface (in the case of aqueous electrolytes). It can be done through the self-adjusting mechanism of the pH gradient generation and by creating a protective layer on the electrodes responsible for higher solvent decomposition overpotentials. The introduction of functional groups on the electrode surface may also lead to the redox activity, which directly affects the obtained high capacity value of the device. Nevertheless, one should be aware that oxygen groups present at the surface can diminish the material conductivity; hence, the power and lifetime of the device operating with modified electrodes can be aggravated.

## Intrinsically Conducting Polymers

Intrinsically conducting polymers (ICPs) have obtained significant interest as electrode materials for ECs. That is because of their simple manufacturing process and low cost (Kang et al., 2016). Also, in comparison with carbon materials, conductive polymers have a relatively high conductivity and equivalent series resistance. ICPs use reduction-oxidation processes to store and release charge. During the oxidation process (doping), ions are transferred from solution to the polymer chain, but during the reduction process (de-doping) ions are released back to the solution (Thanh-Hai et al., 2017). The reduction-oxidation process creates mechanical stress which, in effect, restricts the stability of the electrode material through many cycles of charge-discharge (Mastragostino et al., 2002).

One of the most popular intrinsically conducting polymer is polyaniline (PANI) due to its high conductivity, simple method of synthesis, and low cost (Zhu H. et al., 2013). Nevertheless, PANI is susceptible to rapid deterioration of performance due to swelling and shrinking during repeated charge-discharge cycles. To avoid this restriction, the combination of PANI with carbon materials has been shown to improve PANI's stability as well as increase the capacitance value (Chen and Elabd, 2017; Simotwo and Kalra, 2018). Other conductive polymers are polypyrrole (PPy) and poly(3, 4-ethylenedioxythiophene) (PEDOT). They have many advantages, including low cost, flexibility and good electrical conductivity and pseudocapacitance (Tong et al., 2015; Kashani et al., 2016). However, the major drawback remains the same as in the case of PANI: poor stability implying a noticeable decrease in efficiency after a certain number of charge-discharge cycles (Sen and De, 2010; Huang et al., 2016). Another factor that restrains the use of PEDOT and PPy in the ECs industry is limited capacitance. There are several solutions to solve these problems, including the application of conducting nanofillers to improve conductivity and the mixing or depositing of metal oxide to increase capacitance (Zhao et al., 2016).

## Miscellaneous Materials

Transition metal oxides can be listed as materials of interest for use in ECs applications, but caution should be taken when reporting their electrochemical metrics. Some of them provide enough high conductivity, high specific capacity, and low equivalent series resistance, thus making the construction of ECs with high energy and reasonable power appear to be easy (Ullah et al., 2015; Crosnier et al., 2018). $RuO_2$ is among the most highly studied TMOs (Nguyen and Rochefort, 2014). $RuO_2$ has been met with considerable interest due to its long cycle life, wide potential window and highly reversible reduction-oxidation reaction (Amir et al., 2016). However, $RuO_2$ has lost the attention of the industry because of the high production price (Augustyn et al., 2014). Other TMOs commonly used in energy storage devices are NiO (in hybrid systems) and $MnO_2$ (for pseudocapacitive storage) (Zhao et al., 2017; Sadayappan and Kwang-Sun, 2019). Their advantages include their low production cost and environmental friendliness. Nevertheless, they cause cracking of electrodes which results in short-term stability, as their pores cannot be designed or altered in any form (Julien and Mauger, 2017). This is a significant disadvantage that limits their use in electrochemistry.

Metal sulfides, metal selenides, or polyanionic compounds have also received considerable attention. Nickel cobalt sulfide electrodes in asymmetric EDLCs might achieve high values of capacitance and power density with a short charging time (Chen W. et al., 2014). Metal selenides, like cobalt selenides, also exhibit high specific capacitance values and they are distinguished by the great flexibility of final electrodes that might be interesting for use in personal electronic application (Zhang et al., 2019). Polyanionic molybdenophosphate anodes could largely extend the cathodic stability of water and allow the assembly of 2.7 V aqueous ECs (Song et al., 2019). However, all of these materials suffer from low conductivity, which restricts the fast electron transport required for high rate capability, which can even work as an insulator. This kind of problem has been overcome by incorporating highly conductive carbon materials in pseudocapacitive electrodes – it allows the hybrid system to be constructed (Theerthagiri et al., 2018).

Recently, transition metal dichalcogenides (TMDs) have enjoyed widespread interest as electrode materials for ECs. The TMDs are inorganic structured materials composed of transition metals (M) and chalcogens (X: S, Se, Te) which form with a chemical composition of $MX_2$, that provides a rich range of physicochemical properties (Manish et al., 2013). Many two-dimensional (2D) TMDs are used in ECs such as: $MoS_2$, $MoSe_2$, $WS_2$, $WTe_2$, etc. The most commonly used and studied among these TMDs is $MoS_2$. However, $MoSe_2$ presents better electrochemical properties than $MoS_2$, because transition metal selenides demonstrate higher electrical conductivity than their sulfide counterparts (Eftekhari, 2017). The existence of several oxidation states and the large surface area allows 2D TMDs to store charge by Faradic mechanism as well as electric double-layer (EDL) mechanism, ensuring a high specific capacitance and energy density (Nam et al., 2016; Choi et al., 2017). With some interesting features of 2D TMDs, their low inner electrical conductivity hampers their potential to be great electrode materials for ECs (Pumera et al., 2014; Yang et al., 2014).

MXenes are a group of two-dimensional materials that consist of very thin layers of transition metal carbides, nitrides, or carbonitrides (Lukatskaya et al., 2013; Dall'agnese et al., 2014; Ghidiu et al., 2014). The suffix "ene" was added to MAX phases to emphasize their similarity to graphene (Naguib and Gogotsi, 2015). The best known and first discovered MXene is $Ti_3C_2$. This material shows capacitance values up to 100 $F \cdot g^{-1}$ for insertion of $Li^+$, $Mg^{2+}$, or $Al^{3+}$ in aqueous solutions (Dall'agnese et al., 2016). MXene efficiency can be dramatically improved by adjusting the specific surface groups, or by delaminating or incorporating carbon nanoparticles (Liu Y. et al., 2015; Zhao et al., 2015). However, MXene has been studied primarily in aqueous electrolytes, which have a limited potential window due to water electrolysis. Furthermore, oxidation of $Ti_3C_2$ in aqueous electrolytes under strong anodic potentials also restricts its use mostly to asymmetric systems. As both the energy and the power density increase with the square of the voltage, it is crucial to expand the potential window which will improve the performance of ECs.

## Nanocomposites (for Hybrid Systems)

Composite electrodes combine carbon-based materials with either metal oxide, intrinsically conducting polymer materials, or different carbon materials, which in turn provides both physical and chemical charging storage mechanisms in one single electrode (Vangari et al., 2013).

Carbon materials have a high specific surface area which leads to high capacitance values. By enriching with other carbonaceous material, it is possible to increase the active surface area and thus obtain carbon–carbon ECs with higher energy and power. This would also solve some of the material's drawbacks. For example, the chemical reduction of graphene oxide may lead to its aggregation and restacking through van der Waals interactions back to graphite, thereby making less area for the electrolyte. However, the use of single-walled CNTs as their spacers is sufficient to prevent the restacking. Furthermore, by injecting CNTs, the intra-pores for the electrolyte are generated (Zhang et al., 2013b). However, from an industrial point of view, such a sophisticated approach might be too expensive.

Another way of obtaining a good composite is by adding a conducting polymer to the carbon material. It has been confirmed that mixing PANI with AC (Wang et al., 2019) or PEDOT and CNTs (Dettlaff et al., 2018) results in a higher specific capacitance of carbon-conductive polymer materials than individual components separately. Also, mixing metal oxides with carbonaceous materials develops a specific capacitance. Synthesis of CNTs and an $MnO_2$ hybrid (Dan et al., 2020) or graphene and $MnO_2$ (Cheng et al., 2011) results in improved conductivity, which affects the electrochemical properties of the capacitor. Creating hybrid materials has many advantages. However, they do not significantly improve the properties of electrode materials and, unfortunately, it increases production price (Borenstein et al., 2017).

# 3D MATERIALS

## Definition

Nanostructured materials can be divided into four general groups: (1) 0D zero-dimensional nanomaterials (nanoparticles, nanospheres); (2) 1D one-dimensional nanomaterials (nanorods, nanowires); (3) 2D two-dimensional nanomaterials (nanoplates); and (4) 3D three-dimensional nanomaterials. Nanosized particles that have their length and width within the nanometer range (<100 nm) belong to 0D (1). All dimensions (length, width, and height) are presented by one parameter, e.g., radius. In 1D nanomaterials (2), one dimension is outside the nanoscale, in 2D nanomaterials (3) two dimensions are outside the nanoscale. 3D nanomaterials (4) are materials that are not confined to the nanoscale in any dimension.

Currently, three-dimensional (3D) carbon materials are becoming a promising alternative to AC for ECs application. They can be used both as an active material and as supporting scaffolds for other pseudocapacitive materials with relatively limited electrical conductivity (Wang et al., 2013a; Cao et al., 2014a; Zhang et al., 2014). 3D materials, if used in ECs as electrodes, should have strictly designed porosity, surface, density, wettability, flexibility, etc. Such structures are intended to provide primarily high conductivity and to control the distribution of heteroatoms. The unique pore network (e.g., hierarchical porous structures) reduces dead volume (the volume of the electrode that the ions cannot access). Such solutions ensure the rapid diffusion of ions from the electrolyte bulk to

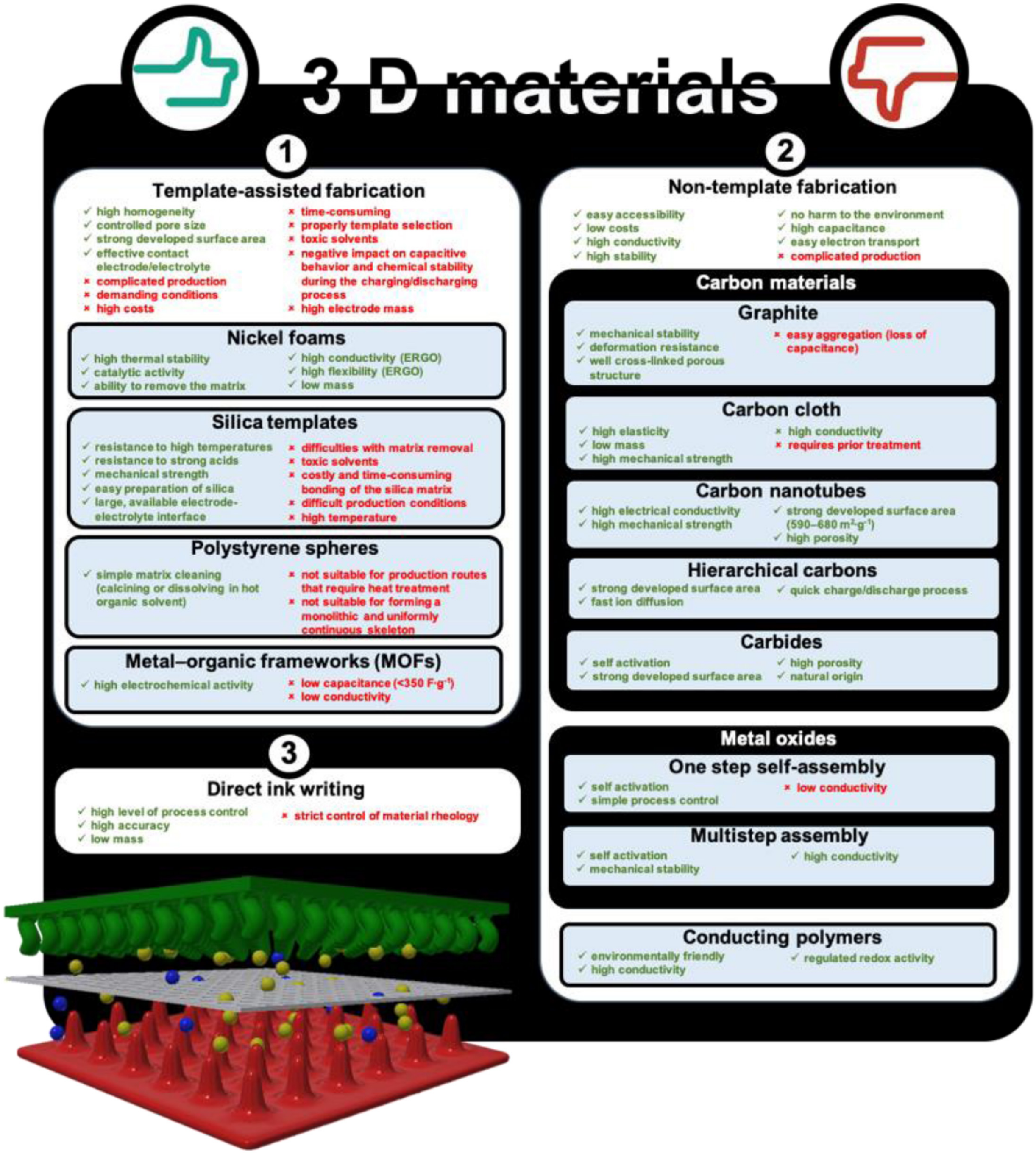

**SCHEME 1 |** Advantages and disadvantages of 3D architectures.

the electrode surface and efficient charge accumulation (Suss et al., 2013; Song et al., 2018). Quite often, electrodes based on 3D materials do not require any additives or binders to prepare the electrodes, while maintaining high flexibility. However, one should be aware that these architectures are not suitable for every type of energy storage/conversion device.

It is accepted that 3D materials construction should perfectly match the device parameters and their work conditions (like the device dimensions, type of electrolyte, temperature, pressure, or susceptibility to disruptions) to ensure good performance. Some advantages and disadvantages of different 3D structures are presented in **Scheme 1**.

It has to be pointed out that there are some incorrect definitions of 3D materials in the literature. For instance, ACs should not be bracketed within 3D materials. Activated carbons have, indeed, a highly developed porosity and surface, however, their structure is disordered – there are no repetitive elements. Furthermore, ACs are not ideal for a new generation of ECs because of three major disadvantages:

1. Quite often, during electrode preparation, electrically insulating binders need to be added; that increases the total weight of the device (so-called dead mass) and hinders the transport of ions.
2. Micropores in ACs make up about 90% of its porosity (Simon and Gogotsi, 2013; Fic et al., 2018). Such a large number of micropores hinders ion diffusion in pores and limits the capacitance at ultra-fast charging conditions (especially for pores with a diameter smaller than ion size) (He et al., 2016).
3. Disordered pore distribution leads to a tortuous and stochastic porous network, which also reduces the rate of ion diffusion (Zhu et al., 2016).

# Family of 3D Materials

## Template-Based Methods

Synthesis of materials based on the template method appears to be the easiest way to create 3D architectures. The matrix can be a permanent scaffold for a 3D electrode, and it participates in the creation of the electrode. There are also methods where the matrix acts only in a transitional stage (schematic illustration presented in **Figure 5**).

After applying the proper electrode material and its anastomosis with the active material, the matrix is removed, and the created 3D electrode material resembles its shape. Removing the matrix allows the highly developed surface area electrode to be formed. However, in many cases, the presence of the matrix ensures the entire structure stability. Examples of active materials include metal oxides and hydroxides, which provide high gravimetric/volumetric capacity in hybrid storage systems. The matrix method uses such processes as: (1) a chemical vapor deposition (CVD), (2) a hydrothermal reaction, or (3) electrodeposition. There are three main types of templates: (1) nickel foams, (2) silica matrixes, or (3) polystyrene (PS) spheres.

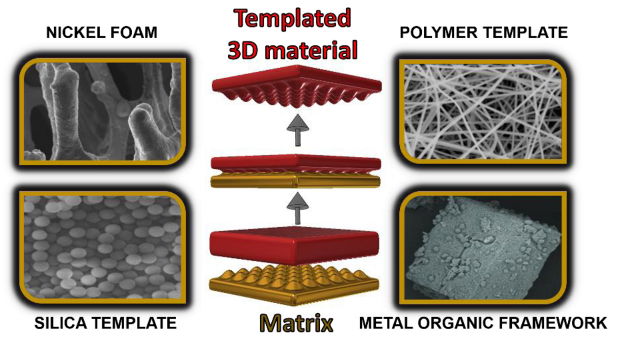

**FIGURE 5 |** Schematic illustration of template-based 3D materials. SEM pictures adapted from Ahn et al. (2019), Ussia et al. (2019), Zhou (2019), and Wang et al. (2020) under the Creative Commons CC BY license.

### *Nickel foams*

Nickel foam (NF) is made of a conductive, connected framework of pure nickel. The pore density of such a skeleton varies between 50 and 90%, and the conductivity ~350 $S \cdot cm^{-1}$. Electrodes manufactured based on a continuous NF network usually adopt a monolithic structure. Popular active materials include: metal oxides (Yan D. et al., 2012; Chen et al., 2013; Zhou C. et al., 2013; Xu et al., 2014; Zhai et al., 2015), sulfurs (Pu et al., 2013; Wei et al., 2014), hydroxides (Guan et al., 2011; Yuan et al., 2014; Qu et al., 2015), and their composites (Guan et al., 2011; Tang et al., 2013; Cai D. et al., 2014). Incorporation of metal oxides to the nickel skeleton can be realized by electrochemical reduction and electrosorption (Zhang et al., 2014). Besides, the nickel susceptibility makes the improvement of nickel oxides or hydroxides deposition possible (Cai S. et al., 2014; Xiong et al., 2015). It is worth mentioning that intermediate elements are also used as the additive to the matrix and active compounds. The most common additives are graphene coatings applied to NF. In turn, the active material is applied to the graphene layer. Graphene growth is realized by chemical vapor deposition (CVD; Zongping et al., 2011; Ji et al., 2012; Chen M. et al., 2014; Liu et al., 2014; Patil et al., 2014; Zhang et al., 2014) or by an electrochemical method of dissolving and reducing graphene oxide (product – ERGO material). In the CVD technique, the graphene layer is deposited in the atmosphere $CH_4/H_2/Ar$ (~ 1000°C) (Zhang et al., 2014) on NF, and then impregnated by, for example, poly(methyl methacrylate) (PMMA). The use of PMMA protects the graphene layer from damage when the NF is removed. Poly(methyl methacrylate) dissolves, and poly(dimethylsiloxane) (PDSM) is introduced into the graphene framework. There is an increase in strength and flexibility of such a network (Zongping et al., 2011). Finally, the templates are selectively removed (e.g., by $FeCl_3$-HCl or 6 $mol \cdot L^{-1}$ HCl) to create a 3D graphene architecture. There are also hybrid solutions using CNTs, which serve as a conductive carrier but also increase the surface area of the metal oxides/hydroxides used. The alternative is the hydrothermal reduction of graphene oxide suspension (Luan et al., 2013). This technique does not require the use of PMMA impregnation (Zhai et al., 2015). Nickel and cobalt-based particles are then deposited on graphene foam to catalyze CNT growth. Then a dense CNT layer is grown on both the outer and inner spaces of each empty graphene wall (Liu et al., 2014).

### *Silica templates*

Silica templates have different morphologies: (1) nanoparticles (Pan et al., 2012), (2) nanosheets (Nakanishi et al., 2013), and (3) ordered mesoporous/macroporous structures (Huang et al., 2012). This method is usually accompanied by high-temperature treatment or a strongly acidic environment (Lei et al., 2011). The use of these templates is mainly limited to carbonization of organic precursors to produce porous carbon networks (e.g., ordered mesoporous carbon) or for the preparation of materials that are stable against strong alkalis (Lee et al., 2000; Ryoo et al., 2001; Lee et al., 2004). Silica particles, used as templates, are firstly dispersed in the reaction solution. Then the material growth process takes place on the dispersed silica template. The general preparation route may consist of three stages: (1) impregnation of the template with the active material, (2) use of pyrolysis/crystallization/sublimation to obtain the desired product with the desired crystallinity, and (3) removal of the silica matrix (HF etching or hot etching with, e.g., LiOH, KOH) (Lu et al., 2014a; Zhang et al., 2017). The material is activated by KOH treatment. The produced porous electrode material is applied onto the foil (e.g., Cu, Al) and used as a current collector. The separated nature of the material hinders the capacitive performance of the EC without the use of a foil. Despite the monodisperse features of silica particles, this technique is also known for obtaining a continuous 3D structure by combining silica particles into a colloidal 3D crystal (Kuai et al., 2003; Wong et al., 2003). This technique involves matrix colloid precipitation under external forces (gravity, capillary forces, electrostatic forces, and hydrophobic interactions on the oil–water interface) (Liu Y. et al., 2013). After creating the connections between the particles, a 3D network is obtained, and the active material can be placed in the porous space. However, the scale of grain connection is still smaller than in the case of NF, due to the small size of the silica grains. This method is still expensive; therefore it is used as an auxiliary tool for integrating mesopores into a macroporous backbone (e.g., graphene foam or aerogel) for the construction of bimodal or tri-modal porous 3D frames (Lu et al., 2011; Huang et al., 2012). Composite-based 3D electrode templates (e.g., a combination of GA graphene aerogel and a $SiO_2$ mesoporous silica layer) are obtained with this approach. It is also possible to insert silica into a macroporous structure to increase its strength and to ensure the hierarchical structure. An example of such a material is highly conductive graphite. Between graphene layers, mesoporous carbon spheres are located, which are obtained as a result of the deposition of carbonaceous material in silica spheres. In the next stage, the carbon spheres are removed (leaving an ordered mesoporous carbon structure). In this case, graphene provides high conductivity, while incorporated carbon spheres play the role of conductive spacers (Lu et al., 2011).

### *Polymer templates*

3D structures obtained with polymer templates include two manufacturing strategies: (1) converting colloids into 3D colloidal crystals before forming a matrix (Zhou M. et al., 2013), and (2) self-assembly of such templates with other materials (e.g., graphene) to generate additional porosity (Liu et al., 2009). Transfer methods to a conductive substrate include:

(1) dropping polymer colloids on the lateral surface of the substrate along with further evaporation (Müller et al., 2000),
(2) deposition of the polymer on a vertically suspended colloidal polymer substrate by solvent evaporation (Bartlett et al., 2000; Karuturi et al., 2012),
(3) a dipping method in which the substrate is withdrawn from a colloidal polymer solution at a constant speed and angle (Xia et al., 2010; Elias et al., 2013; Hsia et al., 2014),
(4) electrophoretic deposition of polymer spheres on a conductive substrate (Yamaguchi et al., 2009).

Colloidal 3D crystals preparation usually takes more time compared to procedures that directly integrate polymer spheres into macroporous matrices. The most popular matrix is PS template, but polyurethane sponges (PU) might be considered as well.

### *Metal–organic frameworks*

Metal–organic frameworks (MOFs) or skeletons enable much greater flexibility in the design of 3D electrodes. In the case of the previously mentioned templates, a higher-order structure was used to produce a lower-order structure. On the contrary, the MOF structure is made up of microscopic particles with geometric symmetry and places that coordinate metal ions, thus making the 3D structure design more flexible (Li and Xu, 2013). Until now, their usage was limited to fulfilling the function of precursors/matrices for carbons (Salunkhe et al., 2015; Wang et al., 2016) or as composites with conductive additives such as graphene (Choi et al., 2014). Recent research results propose solutions for using MOF as pure active substances without the use of a binding agent (Sheberla et al., 2016). The ECs' capacitance based on MOFs quite often exceeds the capacitance of devices operating with carbon electrodes. This might originate from the well-developed specific surface area; however, one should pay special attention to the absolute values reported from the nitrogen adsorption technique (Farha et al., 2012). The conductivity of such materials reaches similar values as graphene ($5000\ S{\cdot}m^{-1}$), significantly exceeding the conductivity of AC and graphite (Yuxi et al., 2014). The conditions for producing MOFs are much milder than those used in the preparation of graphite carbons (John et al., 2015).

### *Other materials*

Other materials used as templates include macroscopic skeletons (Lang et al., 2011, 2012; Liu N. et al., 2013; He et al., 2014) and molecular templates (Meng et al., 2013) combined with self-organizing graphene. Among them, there are structures with an active layer embedded on them in graphene, which in turn is an electron-conducting path (Liu N. et al., 2013). Hybrid 3D electrodes are another type (Lang et al., 2011). Molecular templates (e.g., $CaCO_3$) are used as supports in the self-assembly of graphene or as forms for the design of hollow structures (similar to silica and polymer templates) (Meng et al., 2013).

## Non-templated Methods

The unconventional methods for obtaining electrodes are an alternative to the template methods that allow many of the disadvantages (associated with the first production method) to be eliminated (**Figure 6**). Obtaining 3D architectures involves:

(1) self-organization of low-dimensional monomers,
(2) multi-stage assembly of hierarchical structures, and
(3) processing of natural 3D precursors.

### *Carbon materials*

Thanks to their irreplaceable properties, carbon materials are commonly used for electrode preparation in ECs application.

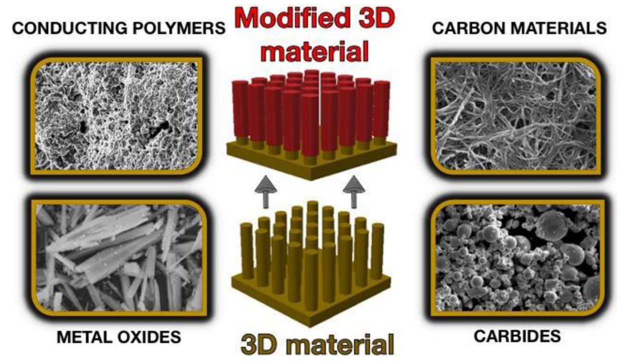

**FIGURE 6 |** Schematic illustration of non-template-based 3D materials. SEM pictures adapted from Hayashi and Hakuta (2010), Deng et al. (2015), Tomczykowa and Plonska-Brzezinska (2019), and He et al. (2020) under the Creative Commons CC BY license.

Thus, this type of material is also very often considered for 3D electrodes production.

Graphene has a unique lamellar structure. Graphene is a type of single-layer carbon with $sp^2$ hybridization that allows the electron mobility to be high. Moreover, it is characterized by its high mechanical strength and large available surface area (2600 $m^2 \cdot g^{-1}$). Graphene is a component of graphite, where many units of graphene are arranged in parallel. Graphite was initially considered as a potential component of capacitor electrodes due to the distance between the graphene layers, which is 0.354 nm. Such a distance ensures the free movement of ions in the material. This also enables the formation of ionic or covalent intercalated graphite compounds (GICs; Liu J. et al., 2013; Abdelkader et al., 2015) as a result of the exfoliation process. The most critical stages of material exfoliation are GIC formation and volumetric expansion (Wang G. et al., 2011; Wang J. et al., 2011; Wei et al., 2012; Parvez et al., 2014). GIC formation can be performed with chemical exfoliation – by oxidation of natural graphite powder with strong oxidants or by electrochemical exfoliation. The most cost-effective technique of exfoliation is the second one, because of its low equipment requirements and the lack of strong acids and oxidants. Moreover, it has a limited impact on the environment that can be an additional advantage (Yenny et al., 2008; Abdelkader et al., 2015; Yang et al., 2016). However, the degree of exfoliation should be carefully monitored. Too high a degree breaks the graphite into small pieces of graphene, which reduces time efficiency and increases production costs but also worsens the internal continuity and conductivity of the 3D graphite network. To meet those requirements, different strategies for partial electrochemical exfoliation, without damaging the structural integrity of graphite, were developed (Song et al., 2014; Song et al., 2015b). Such exfoliation consists of intense gas evolution followed by ion intercalation. The upper graphite layers are exfoliated in aqueous solution by the evolution of gas. Then the ions (e.g., nitrate ions) are intercalated through the upper layers under positive voltage to further exfoliate the graphite layers underneath (Song et al., 2016). Bent graphene layers can also be obtained from graphene oxide (GO) dispersion by direct drying or spray drying (Wen et al., 2012; Yan J. et al., 2012; Yoon et al., 2013). Under these conditions, graphene sheets tend to create a strongly crumpled surface with a large pore volume, which prevents their agglomeration. Stabilization of GO sheets is carried out in an aqueous environment (hydrothermal method), which is associated with a balance of van der Waals forces between GO sheets and electrostatic repulsion of hydrophilic oxygen groups on the edges of these sheets. The self-organization of sheets is possible when the balance of forces is broken. Chemical doping with effective atoms is performed to improve charge density and electrical conductivity. Moreover, this solution introduces additional pseudocapacitance in the system. The most common additives are nitrogen (Wu et al., 2012), sulfur (Zhang et al., 2013a), phosphorus (Some et al., 2012; Zhang et al., 2013a), boron (Martins et al., 2007; Wu et al., 2012), double Ni-Co hydroxide (Song et al., 2015a), PANI (Geng et al., 2017; Ye et al., 2017), and tungsten trioxide (Yu et al., 2015b).

Filtration is another common method for constructing 3D graphene from GO dispersion. In this situation, graphene appears macroscopically as thin paper (Dmitriy et al., 2007; Chen et al., 2008; Yang et al., 2011). The main problem in these processes is easy aggregation and re-arranging of graphene sheets into a graphite structure. The reason for this phenomenon is the interaction between p–p stacks and van der Waals attraction between their underlying planes. Aggregation hinders the diffusion of ions into the space of densely packed graphene sheets. To solve this problem, spacers in the form of CNTs (Fan et al., 2010; Du et al., 2011; You et al., 2013), metal oxides (Shao et al., 2010; Xie et al., 2013; Cao et al., 2014b), polymers (Meng et al., 2013; Zhang et al., 2013d), and others (Gong et al., 2014) can be implemented. Another solution is the use of intercalation ions in the graphite (e.g., $Li^+$). Graphene layers fold under the influence of these ions. After that, ions, e.g., $ClO_{4,-}$ are introduced. After immersion of such an electrode in water, hydroxylate and carbonyl groups are integrated on the corrugated surface of graphene.

### *3D carbon cloths*

Carbon cloth (CC; also called tissue or textile) can play a dual function. In some cases, it plays the role of a matrix material for other structures, but it can also exist as an individual electrode material. However, it requires previous processing due to its low capacitance (∼ 1 $F \cdot g^{-1}$) and surface area (∼ 5 $m^2 \cdot g^{-1}$) (Wang et al., 2015) at the initial production step. Activation involves chemical oxidation and a two-stage reduction with hydrazine and ammonia vapors (Liu T. et al., 2015). This leads to increased fiber roughness and reduced resistance. The capacitance of such a material increases significantly. Electrochemical peeling can also be used for CC activation (Song et al., 2018). Carbon cloth is treated with $H_2SO_4$-$HNO_3$ mixture with a positive bias of 3.0 V (Liu T. et al., 2015). There is also an acid-free method that includes peeling, oxidation, and reduction steps (Song et al., 2017). In the first stage, the material is exfoliated by $NO_3^-$ ions. Then CC is oxidized by $NO_3$–GIC hydrolysis. Reductions of oxygen content are carried out in 0.1% aqueous hydrate solution. The material after this process has a higher conductivity. Such a structure can also buffer the volumetric deformation of the electrode during charge/discharge processes, thereby increasing the life of the device. The combination of matrix fabric with several compounds results in promising pseudocapacitive composite electrodes. The applied compounds include PPy (Huang et al., 2015), $MnO_2$ (Feng et al., 2016), TiN (Lu et al., 2012; Lu et al., 2014a), VN (Lu et al., 2013), $V_6O_{13-x}$ (Zhai et al., 2014), $V_6O_{13}$ (Wang et al., 2012b), and $Fe_2O_3$ (Liu T. et al., 2015).

### *Carbon nanotubes*

The CNTs are porous tubular structures. There are mainly two strategies for producing 3D CNT based electrodes: using CNT as "wires" for weaving into 3D architecture (Niu et al., 2012), and direct deposition of active substances on the CNT surface (e.g., manganese oxide and PANI) (Kohlmeyer et al., 2011). Intrinsically existing CNT structures are not a promising material; however, their combination with pseudocapacitive materials allows the unique properties of the composite material to be obtained (Chen et al., 2009, 2011; Zhang et al., 2011; Chen et al., 2012). Twisted graphene sheets (in the form of a horn) can also be seen as structures belonging to the CNT group. These structures are also characterized by high self-assembly into three-dimensional balls with diameters below 100 nm (Yang C.-M. et al., 2007; Azami et al., 2008; Izadi-Najafabadi et al., 2011; Zhang et al., 2011; Deshmukh and Shelke, 2013; Jung et al., 2013). Modifications of these materials (in the form of open cones) demonstrate higher capacitance in the double-layer compared to classic CNTs (Yang C.-M. et al., 2007). Nanocorns, in combination with pseudocapacitive materials, also show high capacitance.

### *Hierarchical carbons*

Hierarchical carbon materials are described as materials with well-developed micro-, meso-, and macro-porous structure. Micropores have a significant contribution to energy storage. Mesopores and macropores are channels that distribute ions to the micropores in the electrode. This group of materials includes porous graphite carbons (HPGC) (Wang et al., 2008) and carbon aerogels (CA; Miller and Dunn, 1999; Li et al., 2006a,b; Hwang and Hyun, 2007; An et al., 2010; Chien et al., 2012) obtained from the pyrolysis of polymeric materials. Also, in the case of these materials, there are examples of composites with pseudocapacitive materials, such as nitrogen atoms (Li et al., 2012; Dhawale et al., 2013; Hou et al., 2015; Wei et al., 2016), $MnO_2$ (Li et al., 2006a; Chien et al., 2012), $NiCo_2O_4$ (Chien et al., 2012), $SnO_2$ (Hwang and Hyun, 2007), and PPy (An et al., 2010). The synthesis process consists of three main stages (Zhang et al., 2016): (1) mixing the carbon precursor (e.g., chitosan) and the blowing agent (e.g., $K_2CO_3$), (2) gelation (e.g., with glutaraldehyde), (3) lyophilization, and (4) annealing ($\sim 600°C$). Processes (2) and (3) enhance carbon sheets into a porous structure. Step (4), in turn, generates a meso- and microporous structure.

### *Carbide carbons*

Organic carbide (biocarbon) is also a key material for the production of 3D architecture (Kalpana et al., 2009; Lv et al., 2012; Biswal et al., 2013; He et al., 2013; Yun et al., 2013; Jin et al., 2014; Genovese et al., 2015). This type of material is usually obtained by pyrolysis. Activation is ensured by natural compounds found in the precursor itself (Biswal et al., 2013). The pyrolysis process and exfoliation through thermal rinsing allows the amorphous environment to be removed, and, as a result, the material takes the form of thin sheets of carbon. Exfoliated biocarbon is also functionalized by oxygen groups that enables a high capacitance. Generating 3D structures from natural materials and waste is one of the most desirable solutions.

### *Metal oxides*

Metal oxides such as $MnO_2$ (Yu et al., 2013; Jin et al., 2014), NiO (Liang et al., 2012; Xia et al., 2012), $Co_3O_4$ (Zhang et al., 2013c; Guan et al., 2014; Xia et al., 2014a), $VO_x$ (Wang et al., 2012b; Zhai et al., 2014), and $Fe_2O_3$ (Lu et al., 2014b) are materials that might be claimed as promising for hybrid storage mechanisms. They provide higher specific capacity values than carbon materials, which further increases the EC energy density (Lu et al., 2014b). The reason for that is their ability to store energy *via* the electrical double-layer formation and charge accumulation, but also through reversible Faradaic reactions. The methods of constructing 3D metal oxide electrodes can be briefly divided into one-stage and multi-stage assembly.

*One-stage assembly.* The self-organization of three-dimensional metal oxides is based on crystal growth. Popular methods of synthesis of metal oxide crystals include:

1. electrochemical deposition,
2. the hydrothermal method, and
3. the solvothermal method (Liang et al., 2012; Xie et al., 2013; Zhu J. et al., 2013).

The controlled production of 3D architectures is accomplished by selecting conditions during the growth of metal oxide crystals. The hydrothermal method allows for adjusting the synthesis of nanocrystalline oxides by choosing the reaction time, precursors, temperature, and additives.

*Multi-stage assembly.* The multi-stage assembly of 3D material production is based on the production of low-dimensional skeletal material, followed by the embedding of branched material. Often ZnO is used as the basis (Sun et al., 2013) because of the well-known synthesis of this material. In addition, there are also $Co_3O_4$ (Liu et al., 2011), $SnO_2$ (Yan et al., 2011), CuO (Yu and Thomas, 2014), and $MnMoO_4$ (Mai et al., 2011) skeletons. In the next stage, a thin layer of branched $MnO_2$ (Liu et al., 2011; Sun et al., 2013), NiO (Xia et al., 2012), $V_2O_5$ (Yan et al., 2011), NiOH (Guan et al., 2011), $Fe_2O_3$ (Wu et al., 2013), and $CoMnO_4$ (Mai et al., 2011) is deposited on the skeleton while maintaining skeletal morphology (Liu et al., 2012; Xia et al., 2012). Through the use of synergistic effects from capacitance, the 3D structure usually provides favorable electrochemical parameters.

*Other materials.* This group of materials also belongs to conductive polymers like PANI (Fan et al., 2007; Meng et al., 2014; Yu et al., 2014), PPy, PEDOT, and poly (styrene sulfonate) PEDOT-PSS (Cuentas Gallegos and Rincón, 2006).

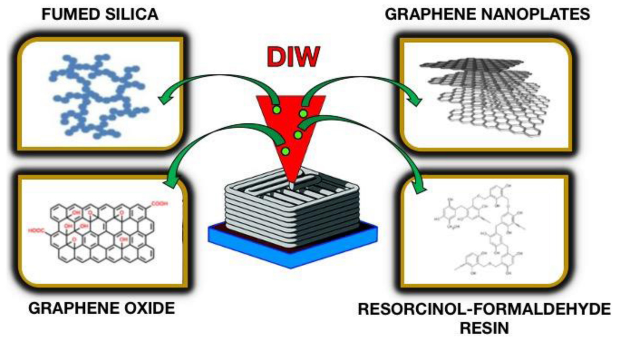

**FIGURE 7 |** Direct ink writing method.

The 3D material is produced by the self-assembly of small-sized nanostructures (Cuentas Gallegos and Rincón, 2006; Yu et al., 2014). Typical preparation methods are mainly divided into electrochemical polymerization (Fan et al., 2007; Meng et al., 2014; Yu et al., 2014) and direct chemical polymerization (Cuentas Gallegos and Rincón, 2006; Antiohos et al., 2011). Polymer electrodes are characterized by their high extensibility and very low capacitance decrease in repeated bending, and there are also premises on the materials based on nitrides (Lu et al., 2012; Balogun et al., 2015; Yu et al., 2015a), sulfides (Xia et al., 2014b; Xiao et al., 2014), and metal selenides (Wang et al., 2013b).

#### Direct Ink Writing

This method allows the highest degree of control of the porous structure to be formed. 3D printing techniques, such as direct ink writing (DIW), are becoming powerful material engineering tools (Ambrosi and Pumera, 2016). In this case, the moving nozzle forming the material is regulated by computer software based on a previously planned computer-generated project (Lewis, 2006). The extruded material, in the form of a liquid or semi-liquid, creates 3D architecture layer by layer. Requirements for DIW inks are their continuity and resistance to collapse, expansion, and sagging. To meet these requirements, the printing materials must be shear thinned fluids: the viscosity of the fluid should drastically decrease under shear and recover quickly after removing the force. The surface area, electrical conductivity, and capacitance are controlled by the proportion of individual components of such an ink. An example of DIW is a material based on graphene aerogel (Zhu et al., 2016). The ink contains graphene oxide [a graphene aerogel precursor (Worsley et al., 2010)], graphene nanoplates (electrically conductive additive), resorcinol-formaldehyde resin (gelation catalyst), and fumed silica (they serve as both a porogen and a viscosity enhancer) (**Figure 7**). The print consists of alternately applied aerogel gird structures.

## FUTURE PERSPECTIVES

Thousands of solutions have still not allowed us to construct the perfect energy storage device that provides both high power and energy density. Looking ahead, there are still challenges to be solved. In particular, 3D carbons and their composites have great application potential. These structures can be successfully implemented in energy storage devices as a new generation of high-power electrodes at high mass loading, breaking the energy and power limits of recent systems. However, these technologies are not versatile, and, above all, they suffer from complicated manufacturing processes and quite often very high prices. Further work is needed to understand their chemistry and charge storage mechanisms.

It is also necessary to improve the electrical conductivity of these materials. Separating ion transport and accumulation from electrons in different phases of the composite could offer a unique interfacial storage mechanism, which would dominate the internal limitations of traditional electrode materials. For electrode materials – their flexibility plays a significant role. This property not only allows for using these materials in devices subjected to bending but also extends their lifetime. Repeated charge and discharge processes result in volumetric changes of the electrodes. In the case of traditional electrode materials, the performance of such a device decreases over time as a result of micro-cracks arising and an increase in the resistance to charge transfer at the electrode/electrolyte interface. 3D structures significantly limit this adverse effect. Porous 3D conductive scaffoldings offer interpenetrating electron and ion transport paths that ensure very efficient charge delivery to and from electrodes. These transport routes are necessary to translate the extraordinary performance achieved through nanoscale materials into macroscopic electrodes. The ability to increase the mass loading of active materials, without compromising charge (energy) storage efficiency, is required not only to capture the benefits of a new generation of high-performance electrode materials in practice but also contributes to crossing the border of traditional electrode materials by reducing the dead volume of the electrode or the number of passive materials. These improvements can increase the overall energy and power density.

### Materials Morphology

Template methods allow us to control the morphology of the pores in the final structure because the electrodes inherit the macroscopic shape of the template. However, these techniques might be ineffective at generating large scale and well-ordered micro- and mesoporous structures that have a much more pronounced effect on capacitive performance than macropores. The solutions proposed to solve this problem relate to the combination of chemical activation on hard matrices. Micro- and meso-structures generated by activation, together with macropores formation by removing the matrix, create hierarchical porous structures that can increase the surface area available for ions, while facilitating fast ions diffusion. Another more straightforward solution is to use templates with pore sizes in the range of mesopores and micropores. Besides, the use of interactions (e.g., electrostatic attraction, complexation) between the matrix and the deposited material would be crucial in the implementation of a uniform meso- and microporous dispersion. However, the thickness of the carbon film on the matrix should be taken into account. If the coated carbon material is too thin, structural integrity may not be maintained during the matrix removal process.

Like the matrix technique, the DIW technique works in the engineering of size and distribution of macropores but shows little efficiency in the case of meso- and micropores. Improving print resolution through the joint efforts of industry and the academic community is desirable to transform DIW into a more efficient electrode production tool. Besides, the ink must be varied by incorporating more electrochemically active materials. For example, converting biomass precursors used in the template-free method into print inks could be a promising direction for future research.

## Production Conditions

In addition to the morphology itself, controlling the conditions of these materials' production plays an important role. For example, the degree of exfoliation should be strictly controlled because it is an essential parameter for structural integrity as well as for electrochemical performance. Currently, the control of the degree of exfoliation is still insufficient. There is no effective approach to the controlled conversion of entire loose structures into porous, connected 3D networks. Potential in this area is derived from two-stage exfoliation, which is a combination of severe and then mild exfoliation. The first stage is designed to reveal the internal space through deep exfoliation and the second stage, in turn, can further fine-tune the degree of exfoliation without destroying the monolithic 3D network. However, this technology is not fully understood and requires further research. It has to be mentioned here that 3D architectures usually demonstrate high (or at least satisfactory) gravimetric capacitance values. However, their porosity makes the volumetric capacitance rather moderate. This might be another aspect that requires further development, as for portable electronics the volume required for an energy storage system is quite often very limited. It also raises the question of the right performance metrics to be reported that allows for fair comparison between materials (Balducci et al., 2017). In our opinion, both characteristics should be presented – or at least the data that allows to calculate it should be provided.

Moreover, very sophisticated 3D structures might be destroyed during electrode material preparation; hence, the future of this group is foreseen for self-assembled structures and techniques that produce the electrodes "ready-to-use," similar to carbon monoliths or CCs. This seems to be the only way to save the 3D architecture in the final electrode material.

Nowadays, organic materials have become a fashionable trend. In addition to the limited or complete absence of negative effects on the environment, electrode materials based on them are characterized by a simple production scheme. However, the unpredictable behavior of structural evolution during pyrolysis under various conditions (time, temperature, heating speed, etc.) justifies the difficulty of controlling the size of the pores, their distribution, and capacitance. That is why it is so important to know the mechanistic evolution of the structure during pyrolysis under given annealing conditions, to improve the controllability of this method. An indispensable element is also the repeatability of obtaining 3D material. The composition of the biomass precursors of subsequent batches will always vary, which is related to their origin, time, and processing technique. It imposes the need to modify the conditions of biomass processing into the final electrode product.

## Research Techniques

To ensure the continuous development of electrode materials, it is also necessary to provide various research techniques, including primarily high-resolution TEM *in situ*, atomic force microscopy *in situ*, X-ray spectroscopy *in situ*, NMR *in situ* spectroscopy and cryo-electron and transmission microscopy. Consequently, it will make it possible to visualize electrochemical processes in real-time and will finally allow for the electrochemical mechanisms to be described in detail. This can help to formulate guiding principles for material development and electrode design.

## Safety

Every year, energy-related devices are increasingly subjected to safety regulations. When the energy is released accidentally, in an uncontrolled and cascading way, it results in temperature rises and disastrous consequences. Interest should be focused on developing compatible electrolytes and separators with high thermal stability, fully compatible with the proposed structures and compounds, which can further prevent overheating, internal short circuits, fires or explosions. In the research world, the cell and case design are very often neglected. However, when one thinks about system commercialization, it is necessary to develop new solutions strictly designed for the "heart" of the device (electrodes, electrolyte). When designing commercial, poorly understood 3D electrode structures, all inconveniences should be taken into account from the very beginning, to prevent them from hampering cell construction and from being hazardous both to the user and the environment.

# THEORETICAL CONSIDERATIONS

The theoretical considerations supported by molecular simulations are also an indispensable element. They play an irreplaceable role in understanding the mechanisms of charge storage and the synthesis-structure-property relationship associated with 3D electrodes. The theory can support experiments and create a basis for further studies. An optimally planned experimental route reduces both research time and costs.

# SUMMARY

In this article, recent progress in the use of 3D carbon nanostructures as electrode materials for advanced capacitor devices has been compiled. The review begins with a comprehensive discussion of common electrode materials used in energy storage devices and ends with an updated review and division of carbon-based 3D architectures. Particular attention was paid to clarifying the definition of 3D materials and errors in the use of this definition in the literature. The basic division of these structures has been done based on the technology of their manufacture. This review summarizes three basic groups: materials created based on matrices, matrix-less materials, and materials produced using 3D printing. Due to the structural interconnection of carbon-based 3D nanostructures, they not only create hierarchical porous channels but also have a higher electrical conductivity and mechanical stability than commonly used materials. A rational combination of connected meso- and micropores in electrode materials significantly improves electrochemical parameters. Significant progress has been made so far, but a full understanding of the relationship between 3D carbon nanostructures and improved electrochemical performance is still unclear. There is great potential in the design and synthesis of new 3D materials for advanced ECs with high energy and power density as well as a long life. The road for creating the ideal energy storage device is still very long, but the reasonable development of the proposed structures could bring the goal a bit closer.

## AUTHOR CONTRIBUTIONS

All authors listed have made a substantial, direct and intellectual contribution to the work, and approved it for publication.

## FUNDING

The European Commission, in the form of The European Research Council, is acknowledged for its financial support within the Starting Grant Project (GA 759603) under the European Union's Horizon 2020 Research and Innovation Programme.

## REFERENCES

Abdelkader, A. M., Cooper, A. J., Dryfe, R. A. W., and Kinloch, I. A. (2015). How to get between the sheets: a review of recent works on the electrochemical exfoliation of graphene materials from bulk graphite. *Nanoscale* 7, 6944–6956. doi: 10.1039/C4NR06942K

Ahn, J., Ahn, C., Jeon, S., and Park, J. (2019). Atomic layer deposition of inorganic thin films on 3D polymer nanonetworks. *Appl. Sci.* 9:1990. doi: 10.3390/app9101990

Alexandru, V., and Andrea, B. (2017). Supercapacitors: porous materials get energized. *Nat. Mater.* 16:161. doi: 10.1038/nmat4851

Alola, A. A., Bekun, F. V., and Sarkodie, S. A. (2019). Dynamic impact of trade policy, economic growth, fertility rate, renewable and non-renewable energy consumption on ecological footprint in Europe. *Sci. Total Environ.* 685, 702–709. doi: 10.1016/j.scitotenv.2019.05.139

Ambrosi, A., and Pumera, M. (2016). 3D-printing technologies for electrochemical applications. *Chem. Soc. Rev.* 45, 2740–2755. doi: 10.1039/C5CS00714C

Amir, F. Z., Pham, V. H., Mullinax, D. W., and Dickerson, J. H. (2016). Enhanced performance of HRGO-RuO2 solid state flexible supercapacitors fabricated by electrophoretic deposition. *Carbon* 107, 338–343. doi: 10.1016/j.carbon.2016.06.013

An, H., Wang, Y., Wang, X., Zheng, L., Wang, X., Yi, L., et al. (2010). Polypyrrole/carbon aerogel composite materials for supercapacitor. *J. Power Sources* 195, 6964–6969. doi: 10.1016/j.jpowsour.2010.04.074

Antiohos, D., Folkes, G., Sherrell, P., Ashraf, S., Wallace, G. G., Aitchison, P., et al. (2011). Compositional effects of PEDOT-PSS/single walled carbon nanotube films on supercapacitor device performance. *J. Mater. Chem.* 21:15987. doi: 10.1039/c1jm12986d

Augustyn, V., Simon, P., and Dunn, B. (2014). Pseudocapacitive oxide materials for high-rate electrochemical energy storage. *Energy Environ. Sci.* 7, 1597–1614. doi: 10.1039/c3ee44164d

Azami, T., Kasuya, D., Yuge, R., Yudasaka, M., Iijima, S., Yoshitake, T., et al. (2008). Large-Scale Production of Single-Wall Carbon Nanohorns with High Purity. *J. Phys. Chem. C* 112, 1330–1334. doi: 10.1021/jp076365o

Balducci, A., Belanger, D., Brousse, T., Long, J. W., and Sugimoto, W. (2017). A Guideline for Reporting Performance Metrics with Electrochemical Capacitors: From Electrode Materials to Full Devices. *J. Electrochem. Soc.* 164, A1487–A1488. doi: 10.1149/2.0851707jes

Balogun, M.-S., Qiu, W., Wang, W., Fang, P., Lu, X., and Tong, Y. (2015). Recent advances in metal nitrides as high-performance electrode materials for energy storage devices. *J. Mater. Chem. A* 3, 1364–1387. doi: 10.1039/C4TA05565A

Barai, A., Chouchelamane, G. H., Guo, Y., Mcgordon, A., and Jennings, P. (2015). A study on the impact of lithium-ion cell relaxation on electrochemical impedance spectroscopy. *J. Power Sources* 280, 74–80. doi: 10.1016/j.jpowsour.2015.01.097

Bartlett, P. N., Birkin, P. R., and Ghanem, M. A. (2000). Electrochemical deposition of macroporous platinum, palladium and cobalt films using polystyrene latex sphere templates. *Chem. Commun.* 17, 1671–1672. doi: 10.1039/b004398m

Béguin, F., and Frąckowiak, E. (2009). *Carbons for Electrochemical Energy Storage and Conversion Systems*. New York, NY: CRC Press. doi: 10.1201/9781420055405

Béguin, F., and Frąckowiak, E. (2013). *Supercapacitors*. Weinheim: Wiley-VCH Verlag GmbH & Co. KGaA. doi: 10.1002/9783527646661

Béguin, F., Presser, V., Balducci, A., and Frackowiak, E. (2014). Carbons and electrolytes for advanced supercapacitors. *Adv. Mater.* 26, 2219–2251. doi: 10.1002/adma.201304137

Bernardo, P., Dentzer, J., Gadiou, R., Märkle, W., Goers, D., Novák, P., et al. (2011). Influence of graphite surface properties on the first electrochemical lithium intercalation. *Carbon* 49, 4867–4876. doi: 10.1016/j.carbon.2011.07.007

Biswal, M., Banerjee, A., Deo, M., and Ogale, S. (2013). From dead leaves to high energy density supercapacitors. *Energy Environ. Sci.* 6, 1249–1259. doi: 10.1039/c3ee22325f

Borenstein, A., Hanna, O., Attias, R., Luski, S., Brousse, T., and Aurbach, D. (2017). Carbon-based composite materials for supercapacitor electrodes: a review. *J. Mater. Chem. A* 5, 12653–12672. doi: 10.1039/C7TA00863E

Budde-Meiwes, H., Drillkens, J., Lunz, B., Muennix, J., Lehner, S., Kowal, J., et al. (2013). A review of current automotive battery technology and future prospects. *Proc. Inst. Mech. Eng. Part D* 227, 761–776. doi: 10.1177/0954407013485567

Bujewska, P., Gorska, B., and Fic, K. (2019). Redox activity of selenocyanate anion in electrochemical capacitor application. *Synthetic Metals* 253, 62–72. doi: 10.1016/j.synthmet.2019.04.024

Cai, D., Huang, H., Wang, D., Liu, B., Wang, L., Liu, Y., et al. (2014). High-Performance Supercapacitor Electrode Based on the Unique ZnO@Co 3 O 4 Core/Shell Heterostructures on Nickel Foam. *ACS Appl. Mater. Interf.* 6, 15905–15912. doi: 10.1021/am5035494

Cai, S., Zhang, D., Shi, L., Xu, J., Zhang, L., Huang, L., et al. (2014). Porous NiMn oxide nanosheets in situ formed on nickel foam as 3D hierarchical monolith de-NO x catalysts. *Nanoscale* 6, 7346–7353. doi: 10.1039/C4NR00475B

Cao, X., Yin, Z., and Zhang, H. (2014a). Three-dimensional graphene materials: preparation, structures and application in supercapacitors. *Energy Environ. Sci.* 7, 1850–1865. doi: 10.1039/C4EE00050A

Cao, X., Zheng, B., Rui, X., Shi, W., Yan, Q., and Zhang, H. (2014b). Metal Oxide-Coated Three-Dimensional Graphene Prepared by the Use of Metal–Organic Frameworks as Precursors. *Angewandte Chem. Int. Edn.* 53, 1404–1409. doi: 10.1002/anie.201308013

Chen, H., Müller, M. B., Gilmore, K. J., Wallace, G. G., and Li, D. (2008). Mechanically Strong, Electrically Conductive, and Biocompatible Graphene Paper. *Adv. Mater.* 20, 3557–3561. doi: 10.1002/adma.200800757

Chen, M., Liu, J., Chao, D., Wang, J., Yin, J., Lin, J., et al. (2014). Porous α-Fe2O3 nanorods supported on carbon nanotubes-graphene foam as superior anode for lithium ion batteries. *Nano Energy* 9, 364–372. doi: 10.1016/j.nanoen.2014.08.011

Chen, W., Xia, C., and Alshareef, H. N. (2014). One-step electrodeposited nickel cobalt sulfide nanosheet arrays for high-performance asymmetric supercapacitors. *ACS Nano* 8:9531. doi: 10.1021/nn503814y

Chen, S.-E., Evanko, B., Wang, X., Vonlanthen, D., Ji, X., Stucky, G. D., et al. (2015). Design of aqueous redox-enhanced electrochemical capacitors with high specific energies and slow self-discharge. *Nat. Commun.* 6, 1–10. doi: 10.1038/ncomms8818

Chen, T.-L., and Elabd, Y. A. (2017). Hybrid-Capacitors with Polyaniline/Carbon Electrodes Fabricated via Simultaneous Electrospinning/Electrospraying. *Electrochim. Acta* 229, 65–72. doi: 10.1016/j.electacta.2017.01.140

Chen, Y., Qu, B., Hu, L., Xu, Z., Li, Q., and Wang, T. (2013). High-performance supercapacitor and lithium-ion battery based on 3D hierarchical NH 4 F-induced nickel cobaltate nanosheetnanowire cluster arrays as self-supported electrodes. *Nanoscale* 5, 9812–9820. doi: 10.1039/c3nr02972g

Chen, Z., Augustyn, V., Jia, X., Xiao, Q., Dunn, B., and Lu, Y. (2012). High-performance sodium-ion pseudocapacitors based on hierarchically porous nanowire composites. *ACS Nano* 6, 4319–4327. doi: 10.1021/nn300920e

Chen, Z., Augustyn, V., Wen, J., Zhang, Y., Shen, M., Dunn, B., et al. (2011). High-Performance Supercapacitors Based on Intertwined CNT/V2O5 Nanowire Nanocomposites. *Adv. Mater.Adv. Mater.* 23, 791–795. doi: 10.1002/adma.201003658

Chen, Z., Qin, Y., Weng, D., Xiao, Q., Peng, Y., Wang, X., et al. (2009). Design and Synthesis of Hierarchical Nanowire Composites for Electrochemical Energy Storage. *Adv. Funct. Mater.* 19, 3420–3426. doi: 10.1002/adfm.200900971

Cheng, Q., Tang, J., Ma, J., Zhang, H., Shinya, N., and Qin, L.-C. (2011). Graphene and nanostructured MnO 2 composite electrodes for supercapacitors. *Carbon* 49, 2917–2925. doi: 10.1016/j.carbon.2011.02.068

Chien, H. C., Cheng, W. Y., Wang, Y. H., and Lu, S. Y. (2012). Ultrahigh Specific Capacitances for Supercapacitors Achieved by Nickel Cobaltite/Carbon Aerogel Composites. *Adv. Funct. Mater.* 22, 5038–5043. doi: 10.1002/adfm.201201176

Choi, K. M., Jeong, H. M., Park, J. H., Zhang, Y.-B., and Kang, J. K. (2014). Supercapacitors of Nanocrystalline Metal À Organic Frameworks. *ACS Nano* 8, 7451–7457. doi: 10.1021/nn5027092

Choi, W., Choudhary, N., Han, G. H., Park, J., Akinwande, D., and Lee, Y. H. (2017). Recent development of two-dimensional transition metal dichalcogenides and their applications. *Mater. Today* 20, 116–130. doi: 10.1016/j.mattod.2016.10.002

Crosnier, O., Goubard-Bretesché, N., Buvat, G., Athouël, L., Douard, C., Lannelongue, P., et al. (2018). Polycationic oxides as potential electrode materials for aqueous-based electrochemical capacitors. *Curr. Opin. Electrochem.* 9, 87–94. doi: 10.1016/j.coelec.2018.05.005

Cuentas Gallegos, A. K., and Rincón, M. E. (2006). Carbon nanofiber and PEDOT-PSS bilayer systems as electrodes for symmetric and asymmetric electrochemical capacitor cells. *J. Power Sour.* 162, 743–747. doi: 10.1016/j.jpowsour.2006.06.085

Dall'agnese, Y., Lukatskaya, M. R., Cook, K. M., Taberna, P.-L., Gogotsi, Y., and Simon, P. (2014). High capacitance of surface-modified 2D titanium carbide in acidic electrolyte. *Electrochem. Commun.* 48, 118–122. doi: 10.1016/j.elecom.2014.09.002

Dall'agnese, Y., Rozier, P., Taberna, P.-L., Gogotsi, Y., and Simon, P. (2016). Capacitance of two-dimensional titanium carbide (MXene) and MXene/carbon nanotube composites in organic electrolytes. *J. Power Sour.* 306, 510–515. doi: 10.1016/j.jpowsour.2015.12.036

Dan, W., Xiubo, X., Yuping, Z., Dongmei, Z., Wei, D., Xiaoyu, Z., et al. (2020). MnO2/carbon composites for supercapacitor: synthesis and electrochemical performance. *Front. Mater.* 7:2. doi: 10.3389/fmats.2020.00002

Daniel, C. (2008). Materials and processing for lithium-ion batteries. *JOM* 60, 43–48. doi: 10.1007/s11837-008-0116-x

Deng, D., Zhang, L., Niu, T., Liu, H., and Zhang, H. (2015). Microstructures and Wear Performance of PTAW Deposited Ni-Based Coatings with Spherical Tungsten Carbide. *Metals* 5, 1984–1996. doi: 10.3390/met5041984

Deshmukh, A. B., and Shelke, M. V. (2013). Synthesis and electrochemical performance of a single walled carbon nanohornFe 3 O 4 nanocomposite supercapacitor electrode. *RSC Adv.* 3, 21390–21393. doi: 10.1039/C3RA43079K

Dettlaff, A., Das, P. R., Komsiyska, L., Osters, O., Łuczak, J., and Wilamowska-Zawłocka, M. (2018). Electrode materials for electrochemical capacitors based on poly(3,4 ethylenedioxythiophene) and functionalized multi-walled carbon nanotubes characterized in aqueous and aprotic electrolytes. *Synthetic Metals* 244, 80–91. doi: 10.1016/j.synthmet.2018.07.006

Dhawale, D. S., Mane, G. P., Joseph, S., Anand, C., Ariga, K., and Vinu, A. (2013). Enhanced Supercapacitor Performance of N-Doped Mesoporous Carbons Prepared from a Gelatin Biomolecule. *ChemPhysChem* 14, 1563–1569. doi: 10.1002/cphc.201300132

Dmitriy, A. D., Sasha, S., Eric, J. Z., Richard, D. P., Geoffrey, H. B. D., Guennadi, E., et al. (2007). Preparation and characterization of graphene oxide paper. *Nature* 448:457. doi: 10.1038/nature06016

Du, F., Yu, D., Dai, L., Ganguli, S., Varshney, V., and Roy, A. K. (2011). Preparation of Tunable 3D Pillared Carbon Nanotube–Graphene Networks for High-Performance Capacitance. *Chem. Mater.* 23, 4810–4816. doi: 10.1021/cm2021214

Eftekhari, A. (2017). Molybdenum diselenide (MoSe 2) for energy storage, catalysis, and optoelectronics. *Appl. Mater. Today* 8, 1–17. doi: 10.1016/j.apmt.2017.01.006

Elias, J., Utke, I., Yoon, S., Bechelany, M., Weidenkaff, A., Michler, J., et al. (2013). Electrochemical growth of ZnO nanowires on atomic layer deposition coated polystyrene sphere templates. *Electrochim. Acta* 110, 387–392. doi: 10.1016/j.electacta.2013.04.168

Etacheri, V., Marom, R., Elazari, R., Salitra, G., and Aurbach, D. (2011). Challenges in the development of advanced Li-ion batteries: a review. *Energy Environ. Sci.* 4, 3243–3262. doi: 10.1039/c1ee01598b

Fan, L. Z., Hu, Y. S., Maier, J., Adelhelm, P., Smarsly, B., and Antonietti, M. (2007). High Electroactivity of Polyaniline in Supercapacitors by Using a Hierarchically Porous Carbon Monolith as a Support. *Adv. Funct. Mater.* 17, 3083–3087. doi: 10.1002/adfm.200700518

Fan, Z., Yan, J., Zhi, L., Zhang, Q., Wei, T., Feng, J., et al. (2010). A Three-Dimensional Carbon Nanotube/Graphene Sandwich and Its Application as Electrode in Supercapacitors. *Adv. Mater.* 22, 3723–3728. doi: 10.1002/adma.201001029

Fang, Y., Liu, J., Yu, D. J., Wicksted, J. P., Kalkan, K., Topal, C. O., et al. (2010). Self-supported supercapacitor membranes: Polypyrrole-coated carbon nanotube networks enabled by pulsed electrodeposition. *J. Power Sour.* 195, 674–679. doi: 10.1016/j.jpowsour.2009.07.033

Farha, O. K., Eryazici, I., Jeong, N. C., Hauser, B. G., Wilmer, C. E., Sarjeant, A. A., et al. (2012). Metal-organic framework materials with ultrahigh surface areas: is the sky the limit? *J. Am. Chem. Soc.* 134:15016. doi: 10.1021/ja3055639

Feng, D.-Y., Song, Y., Huang, Z.-H., Xu, X.-X., and Liu, X.-X. (2016). Rate capability improvement of polypyrrole via integration with functionalized commercial carbon cloth for pseudocapacitor. *J. Power Sour.* 324, 788–797. doi: 10.1016/j.jpowsour.2016.05.112

Fic, K., Frackowiak, E., and Béguin, F. (2012a). Unusual energy enhancement in carbon-based electrochemical capacitors. *J. Mater. Chem.* 22:24213. doi: 10.1039/c2jm35711a

Fic, K., Lota, G., Meller, M., and Frackowiak, E. (2012b). Novel insight into neutral medium as electrolyte for high-voltage supercapacitors. *Energy Environ. Sci.* 5, 5842–5850. doi: 10.1039/C1EE02262H

Fic, K., Platek, A., Piwek, J., and Frackowiak, E. (2018). Sustainable materials for electrochemical capacitors. *Mater. Today* 21, 437–454. doi: 10.1016/j.mattod.2018.03.005

Figueiredo, J. L., Pereira, M. F. R., Freitas, M. M. A., and Órfão, J. J. M. (1999). Modification of the surface chemistry of activated carbons. *Carbon* 37, 1379–1389. doi: 10.1016/S0008-6223(98)00333-9

Frackowiak, E., Abbas, Q., and Béguin, F. (2013). Carbon/carbon supercapacitors. *J. Energy Chem.* 22, 226–240. doi: 10.1016/S2095-4956(13)60028-5

Frackowiak, E., Fic, K., Meller, M., and Lota, G. (2012). Electrochemistry serving people and nature: high-energy ecocapacitors based on redox-active electrolytes. *ChemSusChem* 5, 1181–1185. doi: 10.1002/cssc.201200227

Frackowiak, E., Lota, G., Machnikowski, J., Vix-Guterl, C., and Beguin, F. (2006). Optimisation of supercapacitors using carbons with controlled nanotexture and nitrogen content. *Electrochim. Acta* 51, 2209–2214. doi: 10.1016/j.electacta.2005.04.080

Frackowiak, E., Lota, G., and Pernak, J. (2005). Room-temperature phosphonium ionic liquids for supercapacitor application. *Appl. Phys. Lett.* 86, 1–3. doi: 10.1063/1.1906320

Gao, Q., Demarconnay, L., Raymundo-Piero, E., and Bguin, F. (2012). Exploring the large voltage range of carbon/carbon supercapacitors in aqueous lithium sulfate electrolyte. *Energy Environ. Sci.* 5, 9611–9617. doi: 10.1039/c2ee22284a

Geng, J.-W., Ye, Y.-J., Guo, D., and Liu, X.-X. (2017). Concurrent electropolymerization of aniline and electrochemical deposition of tungsten oxide for supercapacitor. *J. Power Sour.* 342, 980–989. doi: 10.1016/j.jpowsour.2017.01.029

Genovese, M., Jiang, J., Lian, K., and Holm, N. (2015). High capacitive performance of exfoliated biochar nanosheets from biomass waste corn cob. *J. Mater. Chem. A* 3, 2903–2913. doi: 10.1039/C4TA06110A

Ghidiu, M., Lukatskaya, M. R., Zhao, M.-Q., Gogotsi, Y., and Barsoum, M. W. (2014). Conductive two-dimensional titanium carbide 'clay' with high volumetric capacitance. *Nature* 516:78. doi: 10.1038/nature13970

Ghosh, S., Santhosh, R., Jeniffer, S., Raghavan, V., Jacob, G., Nanaji, K., et al. (2019). Natural biomass derived hard carbon and activated carbons as electrochemical supercapacitor electrodes. *Sci. Rep.* 9:16315. doi: 10.1038/s41598-019-52006-x

Gong, Y., Yang, S., Zhan, L., Ma, L., Vajtai, R., and Ajayan, P. M. (2014). A Bottom-Up Approach to Build 3D Architectures from Nanosheets for Superior Lithium Storage. *Adv. Funct. Mater.* 24, 125–130. doi: 10.1002/adfm.201300844

Gorska, B., Bujewska, P., and Fic, K. (2017). Thiocyanates as attractive redox-active electrolytes for high-energy and environmentally-friendly electrochemical capacitors. *Phys. Chem. Chem. Phys.* 19, 7923–7935. doi: 10.1039/C7CP00722A

Guan, C., Liu, J., Cheng, C., Li, H., Li, X., Zhou, W., et al. (2011). Hybrid structure of cobalt monoxide nanowire @ nickel hydroxidenitrate nanoflake aligned on nickel foam for high-rate supercapacitor. *Energy Environ. Sci.* 4, 4496–4499. doi: 10.1039/c1ee01685g

Guan, C., Zeng, Z., Li, X., Cao, X., Fan, Y., Xia, X., et al. (2014). Atomic-Layer-Deposition-Assisted Formation of Carbon Nanoflakes on Metal Oxides and Energy Storage Application. *Small* 10, 300–307. doi: 10.1002/smll.201301009

Hahn, M., Barbieri, O., Gallay, R., and Kotz, R. (2006). A dilatometric study of the voltage limitation of carbonaceous electrodes in aprotic EDLC type electrolytes by charge-induced strain. *Carbon* 44, 2523–2533. doi: 10.1016/j.carbon.2006.05.002

Hantel, M. M., Weingarth, D., and Kotz, R. (2014). Parameters determining dimensional changes of porous carbons during capacitive charging. *Carbon* 69, 275–286. doi: 10.1016/j.carbon.2013.12.026

Hayashi, H., and Hakuta, Y. (2010). Hydrothermal Synthesis of Metal Oxide Nanoparticles in Supercritical Water. *Materials* 3, 3794–3817. doi: 10.3390/ma3073794

He, W., Jiang, C., Wang, J., and Lu, L. (2014). High-Rate Oxygen Electroreduction over Graphitic-N Species Exposed on 3D Hierarchically Porous Nitrogen-Doped Carbons. *Angewandte Chem. Int. Edn.* 53, 9503–9507. doi: 10.1002/anie.201404333

He, X., Ling, P., Yu, M., Wang, X., Zhang, X., and Zheng, M. (2013). Rice husk-derived porous carbons with high capacitance by ZnCl2 activation for supercapacitors. *Electrochim. Acta* 105, 635–641. doi: 10.1016/j.electacta.2013.05.050

He, X., Wang, X., Sun, B., Wan, J., Wang, Y., He, D., et al. (2020). Synthesis of three-dimensional hierarchical furball-like tungsten trioxide microspheres for high performance supercapacitor electrodes. *RSC Adv.* 10, 13437–13441. doi: 10.1039/C9RA10995A

He, Y., Qiao, R., Vatamanu, J., Borodin, O., Bedrov, D., Huang, J., et al. (2016). Importance of Ion Packing on the Dynamics of Ionic Liquids during Micropore Charging. *J. Phys. Chem. Lett.* 7:36. doi: 10.1021/acs.jpclett.5b02378

Heimbckel, R., Hoffmann, F., and Frba, M. (2019). Insights into the influence of the pore size and surface area of activated carbons on the energy storage of electric double layer capacitors with a new potentially universally applicable capacitor model. *Phys. Chemi. Chem. Phys.* 21, 3122–3133. doi: 10.1039/C8CP06443A

Herou, S., Schlee, P., Jorge, A. B., and Titirici, M. (2018). Biomass-derived electrodes for flexible supercapacitors. *Curr. Opin. Green Sustain. Chem.* 9, 18–24. doi: 10.1016/j.cogsc.2017.10.005

Hirota, N., Okuno, K., Majima, M., Hosoe, A., Uchida, S., and Ishikawa, M. (2018). High-performance lithium-ion capacitor composed of electrodes with porous three-dimensional current collector and bis(fluorosulfonyl)imide-based ionic liquid electrolyte. *Electrochim. Acta* 276, 125–133. doi: 10.1016/j.electacta.2018.04.148

Hou, J., Cao, C., Idrees, F., and Ma, X. (2015). Hierarchical porous nitrogen-doped carbon nanosheets derived from silk for ultrahigh-capacity battery anodes and supercapacitors. *ACS Nano* 9:2556. doi: 10.1021/nn506394r

Hsia, B., Kim, M. S., Luna, L. E., Mair, N. R., Kim, Y., Carraro, C., et al. (2014). Templated 3D Ultrathin CVD graphite networks with controllable geometry: synthesis and application as supercapacitor electrodes. *ACS Appl. Mater. Interf.* 6, 18413–18417. doi: 10.1021/am504695t

Huang, X., Qian, K., Yang, J., Zhang, J., Li, L., Yu, C., et al. (2012). Functional Nanoporous Graphene Foams with Controlled Pore Sizes. *Adv. Mater.* 24, 4419–4423. doi: 10.1002/adma.201201680

Huang, Y., Li, H., Wang, Z., Zhu, M., Pei, Z., Xue, Q., et al. (2016). Nanostructured Polypyrrole as a flexible electrode material of supercapacitor. *Nano Energy* 22, 422–438. doi: 10.1016/j.nanoen.2016.02.047

Huang, Z.-H., Song, Y., Xu, X.-X., and Liu, X.-X. (2015). Ordered Polypyrrole Nanowire Arrays Grown on a Carbon Cloth Substrate for a High-Performance Pseudocapacitor Electrode. *ACS Appl. Mater. Interf.* 7:25506. doi: 10.1021/acsami.5b08830

Hwang, S.-W., and Hyun, S.-H. (2007). Synthesis and characterization of tin oxide/carbon aerogel composite electrodes for electrochemical supercapacitors. *J. Power Sour.* 172, 451–459. doi: 10.1016/j.jpowsour.2007.07.061

Izadi-Najafabadi, A., Yamada, T., Futaba, D. N., Yudasaka, M., Takagi, H., Hatori, H., et al. (2011). High-power supercapacitor electrodes from single-walled carbon nanohorn/nanotube composite. *ACS Nano* 5:811. doi: 10.1021/nn1017457

Ji, H., Zhang, L., Pettes, M., Li, H., Chen, S. S., Shi, L., et al. (2012). Ultrathin graphite foam: a three-dimensional conductive network for battery electrodes. *Nano Lett.* 12, 2446–2451. doi: 10.1021/nl300528p

Jian, L., Xiaoqian, C., Alexey, S., and Michael, K. (2012). Review of Electrochemical Capacitors Based on Carbon Nanotubes and Graphene. *Graphene* 1, 1–13. doi: 10.4236/graphene.2012.11001

Jin, H., Wang, X., Shen, Y., and Gu, Z. (2014). A high-performance carbon derived from corn stover via microwave and slow pyrolysis for supercapacitors. *J. Anal. Appl. Pyrol.* 110, 18–23. doi: 10.1016/j.jaap.2014.07.010

John, W. F. T., Zheng, C., Hongbin, Y., Jiajun, H., Kwanpyo, K., Ho-Hsiu, C., et al. (2015). Ultrahigh Surface Area Three-Dimensional Porous Graphitic Carbon from Conjugated Polymeric Molecular Framework. *ACS Central Sci.* 1, 68–76. doi: 10.1021/acscentsci.5b00149

Julien, C. M., and Mauger, A. (2017). Nanostructured MnO 2 as Electrode Materials for Energy Storage. *Nanomaterials* 7:396. doi: 10.3390/nano7110396

Jung, H. J., Kim, Y.-J., Han, J. H., Yudasaka, M., Iijima, S., Kanoh, H., et al. (2013). Thermal-Treatment-Induced Enhancement in Effective Surface Area of Single-Walled Carbon Nanohorns for Supercapacitor Application. *J. Phys. Chem. C* 117, 25877–25883. doi: 10.1021/jp405839z

Kalpana, D., Cho, S. H., Lee, S. B., Lee, Y. S., Misra, R., and Renganathan, N. G. (2009). Recycled waste paper—A new source of raw material for electric double-layer capacitors. *J. Power Sour.* 190, 587–591. doi: 10.1016/j.jpowsour.2009.01.058

Kang, M., Lee, J. E., Shim, H. W., Jeong, M. S., Im, W. B., and Yoon, H. (2016). Correction: intrinsically conductive polymer binders for electrochemical capacitor application. *RSC Adv.* 6, 23658–23658. doi: 10.1039/C6RA90020H

Karuturi, S. K., Luo, J., Cheng, C., Liu, L., Su, L. T., Tok, A. I. Y., et al. (2012). A Novel Photoanode with Three-Dimensionally, Hierarchically Ordered Nanobushes for Highly Efficient Photoelectrochemical Cells. *Adv. Mater.* 24, 4157–4162. doi: 10.1002/adma.201104428

Kashani, H., Chen, L., Ito, Y., Han, J., Hirata, A., and Chen, M. (2016). Bicontinuous nanotubular graphene–polypyrrole hybrid for high performance flexible supercapacitors. *Nano Energy* 19, 391–400. doi: 10.1016/j.nanoen.2015.11.029

Khomenko, V., Raymundo-Piñero, E., Frackowiak, E., and Béguin, F. (2006). High-voltage asymmetric supercapacitors operating in aqueous electrolyte. *Appl. Phys. A* 82, 567–573. doi: 10.1007/s00339-005-3397-8

Kim, T., Jung, G., Yoo, S., Suh, K. S., and Ruoff, R. S. (2013). Activated graphene-based carbons as supercapacitor electrodes with macro- and mesopores. *ACS Nano* 7:6899. doi: 10.1021/nn402077v

Kim, T., Song, W., Son, D.-Y., Ono, L. K., and Qi, Y. (2019). Lithium-ion batteries: outlook on present, future, and hybridized technologies. *J. Mater. Chem. A* 7, 2942–2964. doi: 10.1039/C8TA10513H

Kohlmeyer, R. R., Lor, M., Deng, J., Liu, H., and Chen, J. (2011). Preparation of stable carbon nanotube aerogels with high electrical conductivity and porosity. *Carbon* 49, 2352–2361. doi: 10.1016/j.carbon.2011.02.001

Krause, A., and Balducci, A. (2011). High voltage electrochemical double layer capacitor containing mixtures of ionic liquids and organic carbonate as electrolytes. *Electrochem. Commun.* 13, 814–817. doi: 10.1016/j.elecom.2011.05.010

Kuai, S., Badilescu, S., Bader, G., Brüning, R., Hu, X., and Truong, V. V. (2003). Preparation of Large-Area 3D Ordered Macroporous Titania Films by Silica Colloidal Crystal Templating. *Adv. Mater.* 15, 73–75. doi: 10.1002/adma.200390015

Lang, X., Hirata, A., Fujita, T., and Chen, M. (2011). Nanoporous metal/oxide hybrid electrodes for electrochemical supercapacitors. *Nat. Nanotechnol.* 6, 232–236. doi: 10.1038/nnano.2011.13

Lang, X., Zhang, L., Fujita, T., Ding, Y., and Chen, M. (2012). Three-dimensional bicontinuous nanoporous Au/polyaniline hybrid films for high-performance electrochemical supercapacitors. *J. Power Sour.* 197, 325–329. doi: 10.1016/j.jpowsour.2011.09.006

Lee, J., Han, S., and Hyeon, T. (2004). Synthesis of new nanoporous carbon materials using nanostructured silica materials as templates. *J. Mater. Chem.* 14:478. doi: 10.1039/b311541k

Lee, J., Yoon, S., Oh, S. M., Shin, C. H., and Hyeon, T. (2000). Development of a New Mesoporous Carbon Using an HMS Aluminosilicate Template. *Adv. Mater.* 12, 359–362. doi: 10.1002/(SICI)1521-4095(200003)12:5<359::AID-ADMA359>3.0.CO;2-1

Lei, Z., Zhang, J., and Zhao, X. S. (2011). Ultrathin MnO2 nanofibers grown on graphitic carbon spheres as high-performance asymmetric supercapacitor electrodes. *J. Mater. Chem.* 22, 153. doi: 10.1039/C1JM13872C

Lewis, J. A. (2006). Direct Ink Writing of 3D Functional Materials. *Adv. Funct. Mater.* 16, 2193–2204. doi: 10.1002/adfm.200600434

Li, H., Wang, J., Chu, Q., Wang, Z., Zhang, F., and Wang, S. (2009). Theoretical and experimental specific capacitance of polyaniline in sulfuric acid. *J. Power Sour.* 190, 578–586. doi: 10.1016/j.jpowsour.2009.01.052

Li, J., Wang, X., Huang, Q., Gamboa, S., and Sebastian, P. J. (2006a). A new type of MnO.sub.2[middle dot]xH.sub.2O/CRF composite electrode for supercapacitors.(Report). *J. Power Sour.* 160:1501. doi: 10.1016/j.jpowsour.2006.02.045

Li, J., Wang, X., Huang, Q., Gamboa, S., and Sebastian, P. J. (2006b). Studies on preparation and performances of carbon aerogel electrodes for the application of supercapacitor. *J. Power Sour.* 158, 784–788. doi: 10.1016/j.jpowsour.2005.09.045

Li, S.-L., and Xu, Q. (2013). Metalorganic frameworks as platforms for clean energy. *Energy Environ. Sci.* 6, 1656–1683. doi: 10.1039/c3ee40507a

Li, Z., Zhang, L., Amirkhiz, B. S., Tan, X., Xu, Z., Wang, H., et al. (2012). Carbonized Chicken Eggshell Membranes with 3D Architectures as High-Performance Electrode Materials for Supercapacitors (Adv. Energy Mater. 4/2012). *Adv. Energy Mater.* 2, 430–430. doi: 10.1002/aenm.201290018

Liang, K., Tang, X., and Hu, W. (2012). High-performance three-dimensional nanoporous NiO film as a supercapacitor electrode. *J. Mater. Chem.* 22:11062. doi: 10.1039/c2jm31526b

Liu, C., Li, F., Ma, L. P., and Cheng, H. M. (2010). Advanced Materials for Energy Storage. *Adv. Mater.* 22:E28. doi: 10.1002/adma.200903328

Liu, H.-J., Cui, W.-J., Jin, L.-H., Wang, C.-X., and Xia, Y.-Y. (2009). Preparation of three-dimensional ordered mesoporous carbon sphere arrays by a two-step templating route and their application for supercapacitors. *J. Mater. Chem.* 19:3661. doi: 10.1039/b819820a

Liu, J., Jiang, J., Bosman, M., and Fan, H. J. (2012). Three-dimensional tubular arrays of MnO 2 –NiO nanoflakes with high areal pseudocapacitance. *J. Mater. Chem.* 22, 2419–2426. doi: 10.1039/C1JM14804D

Liu, J., Jiang, J., Cheng, C., Li, H., Zhang, J., Gong, H., et al. (2011). Energy Storage: Co3O4 Nanowire@MnO2 Ultrathin Nanosheet Core/Shell Arrays: a new class of high-performance pseudocapacitive materials (Adv. Mater. 18/2011. *Adv. Mater.* 23, 2075–2075. doi: 10.1002/adma.201190066

Liu, J., Poh, C. K., Zhan, D., Lai, L., Lim, S. H., Wang, L., et al. (2013). Improved synthesis of graphene flakes from the multiple electrochemical exfoliation of graphite rod. *Nano Energy* 2, 377–386. doi: 10.1016/j.nanoen.2012.11.003

Liu, N., Ma, W., Tao, J., Zhang, X., Su, J., Li, L., et al. (2013). Cable-Type Supercapacitors of Three-Dimensional Cotton Thread Based Multi-Grade Nanostructures for Wearable Energy Storage. *Adv. Mater.* 25, 4925–4931. doi: 10.1002/adma.201301311

Liu, Y., Goebl, J., and Yin, Y. (2013). Templated synthesis of nanostructured materials. *Chem. Soc. Rev.* 42, 2610–2653. doi: 10.1039/C2CS35369E

Liu, J., Zhang, L., Wu, H. B., Lin, J., Shen, Z., and Lou, X. W. (2014). High-performance flexible asymmetric supercapacitors based on a new graphene foam/carbon nanotube hybrid film. *Energy Environ. Sci.* 7, 3709–3719. doi: 10.1039/C4EE01475H

Liu, T., Ling, Y., Yang, Y., Finn, L., Collazo, E., Zhai, T., et al. (2015). Investigation of hematite nanorod-nanoflake morphological transformation and the application of ultrathin nanoflakes for electrochemical devices. *Nano Energy* 10:169. doi: 10.1016/j.nanoen.2014.12.023

Liu, Y., Wang, W., Ying, Y., Wang, Y., and Peng, X. (2015). Binder-free layered Ti 3 C 2/CNTs nanocomposite anodes with enhanced capacity and long-cycle life for lithium-ion batteries. *Dalton Trans.* 44, 7123–7126. doi: 10.1039/C4DT02058H

Lota, G., Lota, K., and Frackowiak, E. (2007). Nanotubes based composites rich in nitrogen for supercapacitor application. *Electrochem. Commun.* 9, 1828–1832. doi: 10.1016/j.elecom.2007.04.015

Lu, X., Liu, T., Zhai, T., Wang, G., Yu, M., Xie, S., et al. (2014a). Improving the cycling stability of metal–nitride supercapacitor electrodes with a thin carbon shell. *Adv. Energy Mater.* 4:1300994. doi: 10.1002/aenm.201300994

Lu, X., Zeng, Y., Yu, M., Zhai, T., Liang, C., Xie, S., et al. (2014b). Oxygen-Deficient Hematite Nanorods as High-Performance and Novel Negative Electrodes for Flexible Asymmetric Supercapacitors. *Adv. Mater.* 26, 3148–3155. doi: 10.1002/adma.201305851

Lu, X., Wang, G., Zhai, T., Yu, M., Xie, S., Ling, Y., et al. (2012). Stabilized TiN Nanowire Arrays for High-Performance and Flexible Supercapacitors. *Nano Lett.* 12, 5376–5381. doi: 10.1021/nl302761z

Lu, X., Yu, M., Zhai, T., Wang, G., Xie, S., Liu, T., et al. (2013). High energy density asymmetric quasi-solid-state supercapacitor based on porous vanadium nitride nanowire anode. *Nano Lett.* 13:2628. doi: 10.1021/nl400760a

Lu, X., Zheng, D., Zhai, T., Liu, Z., Huang, Y., Xie, S., et al. (2011). Facile synthesis of large-area manganese oxide nanorod arrays as a high-performance electrochemical supercapacitor. *Energy Environ. Sci.* 4, 2915–2921. doi: 10.1039/c1ee01338f

Luan, F., Wang, G., Ling, Y., Lu, X., Wang, H., Tong, Y., et al. (2013). High energy density asymmetric supercapacitors with a nickel oxide nanoflake cathode and a 3D reduced graphene oxide anode. *Nanoscale* 5, 7984–7990. doi: 10.1039/c3nr02710d

Lukatskaya, M. R., Mashtalir, O., Ren, C. E., Dall'agnese, Y., Rozier, P., Taberna, P. L., et al. (2013). Cation intercalation and high volumetric capacitance of two-dimensional titanium carbide.(REPORTS)(Author abstract). *Science* 341:1502. doi: 10.1126/science.1241488

Lv, Y., Gan, L., Liu, M., Xiong, W., Xu, Z., Zhu, D., et al. (2012). A self-template synthesis of hierarchical porous carbon foams based on banana peel for supercapacitor electrodes. *J. Power Sour.* 209, 152–157. doi: 10.1016/j.jpowsour.2012.02.089

Mai, L.-Q., Yang, F., Zhao, Y.-L., Xu, X., Xu, L., and Luo, Y.-Z. (2011). Hierarchical MnMoO4/CoMoO4 heterostructured nanowires with enhanced supercapacitor performance. *Nat. Commun.* 2:381. doi: 10.1038/ncomms1387

Malak, A., Fic, K., Lota, G., Vix-Guterl, C., and Frackowiak, E. (2010). Hybrid materials for supercapacitor application. *J. Solid State Electrochem.* 14, 811–816. doi: 10.1007/s10008-009-0856-8

Manish, C., Hyeon Suk, S., Goki, E., Lain-Jong, L., Kian Ping, L., and Hua, Z. (2013). The chemistry of two-dimensional layered transition metal dichalcogenide nanosheets. *Nat. Chem.* 5:263. doi: 10.1038/nchem.1589

Marcano, D. C., Kosynkin, D. V., Berlin, J. M., Sinitskii, A., Sun, Z., Slesarev, A., et al. (2010). Improved synthesis of graphene oxide. *ACS Nano* 4:4806. doi: 10.1021/nn1006368

Martins, T. B., Miwa, R. H., Da Silva, A. J. R., and Fazzio, A. (2007). Electronic and transport properties of boron-doped graphene nanoribbons. *Phys. Rev. Lett.* 98:196803. doi: 10.1103/PhysRevLett.98.196803

Mastragostino, M., Arbizzani, C., and Soavi, F. (2002). Conducting polymers as electrode materials in supercapacitors. *Solid State Ionics* 148, 493–498. doi: 10.1016/S0167-2738(02)00093-0

Meng, C., Maeng, J., John, S. W. M., and Irazoqui, P. P. (2014). Ultrasmall Integrated 3D micro-supercapacitors solve energy storage for miniature devices. *Adv. Energy Mater.* 4:1301269. doi: 10.1002/aenm.201301269

Meng, Y., Wang, K., Zhang, Y., and Wei, Z. (2013). Hierarchical Porous Graphene/Polyaniline Composite Film with Superior Rate Performance for Flexible Supercapacitors. *Adv. Mater.* 25, 6985–6990. doi: 10.1002/adma.201303529

Menzel, J., Fic, K., and Frackowiak, E. (2015). Hybrid aqueous capacitors with improved energy/power performance. *Progr. Nat. Sci.* 25, 642–649. doi: 10.1016/j.pnsc.2015.12.001

Miller, E. E., Hua, Y., and Tezel, F. H. (2018). Materials for energy storage: review of electrode materials and methods of increasing capacitance for supercapacitors. *Jo. Energy Stor.* 20, 30–40. doi: 10.1016/j.est.2018.08.009

Miller, J. M., and Dunn, B. (1999). Morphology and electrochemistry of ruthenium/carbon aerogel nanostructures. *Langmuir* 15, 799–806. doi: 10.1021/la980799g

Miller, J. M., Onar, O. C., White, C., Campbell, S., Coomer, C., Seiber, L., et al. (2014). Demonstrating dynamic wireless charging of an electric vehicle: the benefit of electrochemical capacitor smoothing. *IEEE Power Electr. Magn.* 1, 12–24. doi: 10.1109/MPEL.2014.2300978

Mirzaeian, M., Abbas, Q., Ogwu, A., Hall, P., Goldin, M., Mirzaeian, M., et al. (2017). Electrode and electrolyte materials for electrochemical capacitors. *Int. J. Hydrog. Energy* 42, 25565–25587. doi: 10.1016/j.ijhydene.2017.04.241

Müller, M., Zentel, R., Maka, T., Romanov, S. G., and Sotomayor Torres, C. M. (2000). Photonic Crystal Films with High Refractive Index Contrast. *Adv. Mater.* 12, 1499–1503. doi: 10.1002/1521-4095(200010)12:20<1499::AID-ADMA1499>3.0.CO;2-M

Naguib, M., and Gogotsi, Y. (2015). Synthesis of two-dimensional materials by selective extraction. *Acc Chem. Res.* 48, 128–135. doi: 10.1021/ar500346b

Najib, S., and Erdem, E. (2019). Current progress achieved in novel materials for supercapacitor electrodes: mini review. *Nanoscale Adv.* 1, 2817–2827. doi: 10.1039/C9NA00345B

Nakanishi, K., Tomita, M., and Kato, K. (2013). Improvement in the catalytic activity of cytochrome c by immobilisation on a novel mesoporous silica sheet. *RSC Adv.* 4, 4732–4735. doi: 10.1039/C3RA45861J

Nam, M. S., Patil, U., Park, B., Sim, H. B., and Jun, S. C. (2016). A binder free synthesis of 1D PANI and 2D MoS 2 nanostructured hybrid composite electrodes by the electrophoretic deposition (EPD) method for supercapacitor application. *RSC Adv.* 6, 101592–101601. doi: 10.1039/C6RA16078F

Nguyen, N. L., and Rochefort, D. (2014). Electrochemistry of ruthenium dioxide composite electrodes in diethylmethylammonium-triflate protic ionic liquid and its mixtures with acetonitrile. *Electrochim. Acta* 147, 96–103. doi: 10.1016/j.electacta.2014.08.143

Nitta, N., Wu, F., Lee, J. T., and Yushin, G. (2015). Li-ion battery materials: present and future. *Mater. Today* 18, 252–264. doi: 10.1016/j.mattod.2014.10.040

Niu, Z., Chen, J., Hng, H. H., Ma, J., and Chen, X. (2012). A Leavening Strategy to Prepare Reduced Graphene Oxide Foams. *Adv. Mater.* 24, 4144–4150. doi: 10.1002/adma.201200197

Nomoto, S., Nakata, H., Yoshioka, K., Yoshida, A., and Yoneda, H. (2001). Advanced capacitors and their application. *J. Power Sour.* 9, 807–811. doi: 10.1016/S0378-7753(01)00612-7

Pan, L., He, Q., Liu, J., Chen, Y., Ma, M., Zhang, L., et al. (2012). Nuclear-Targeted Drug Delivery of TAT Peptide-Conjugated Monodisperse Mesoporous Silica Nanoparticles. *J. Am. Chem. Soc.* 134, 5722–5725. doi: 10.1021/ja211035w

Pandolfo, A. G., and Hollenkamp, A. F. (2006). Carbon properties and their role in supercapacitors. *J. Power Sour.* 157, 11–27. doi: 10.1016/j.jpowsour.2006.02.065

Parvez, K., Wu, Z.-S., Li, R., Liu, X., Graf, R., Feng, X., et al. (2014). Exfoliation of graphite into graphene in aqueous solutions of inorganic salts. *J. Am. Chem. Soc.* 136:6083. doi: 10.1021/ja5017156

Patil, U. M., Sohn, J. S., Kulkarni, S. B., Lee, S. C., Park, H. G., Gurav, K. V., et al. (2014). Enhanced supercapacitive performance of chemically grown cobalt-nickel hydroxides on three-dimensional graphene foam electrodes. *ACS Appl. Mater. Interf.* 6:2450. doi: 10.1021/am404863z

Peng, C., Zhang, S., Jewell, D., and Chen, G. Z. (2008). Carbon nanotube and conducting polymer composites for supercapacitors. *Progr. Nat. Sci.* 18, 777–788. doi: 10.1016/j.pnsc.2008.03.002

Pineiro-Prado, I., Salinas-Torres, D., Ruiz-Rosas, R., Morallon, E., and Cazorla-Amoros, D. (2016). Design of Activated Carbon/Activated Carbon Asymmetric Capacitors. *(Report)(Author abstract)* 3:16. doi: 10.3389/fmats.2016.00016

Prehal, C., Weingarth, D., Perre, E., Lechner, R. T., Amenitsch, H., Paris, O., et al. (2015). Tracking the structural arrangement of ions in carbon supercapacitor nanopores using in situ small-angle X-ray scattering. *Energy Environ. Sci.* 8, 1725–1735. doi: 10.1039/C5EE00488H

Pu, J., Wang, Z., Wu, K., Yu, N., and Sheng, E. (2013). Co 9 S 8 nanotube arrays supported on nickel foam for high-performance supercapacitors. *Phys. Chemi. Chem. Phys.* 16, 785–791. doi: 10.1039/C3CP54192D

Pumera, M., Sofer, Z., and Ambrosi, A. (2014). Layered transition metal dichalcogenides for electrochemical energy generation and storage. *J. Mater. Chem. A* 2, 8981–8987. doi: 10.1039/C4TA00652F

Qingqing, K., and John, W. (2016). Graphene-based materials for supercapacitor electrodes – A review. *J. Materiom.* 2, 37–54. doi: 10.1016/j.jmat.2016.01.001

Qu, L., Zhao, Y., Khan, A. M., Han, C., Hercule, K. M., Yan, M., et al. (2015). Interwoven Three-Dimensional Architecture of Cobalt Oxide Nanobrush-Graphene@Ni x Co 2 x (OH) 6 x for High-Performance Supercapacitors. *Nano Lett.* 15, 2037–2044. doi: 10.1021/nl504901p

Ratajczak, P., Jurewicz, K., Skowron, P., Abbas, Q., and Béguin, F. (2014). Effect of accelerated ageing on the performance of high voltage carbon/carbon electrochemical capacitors in salt aqueous electrolyte. *Electrochim. Acta* 130, 344–350. doi: 10.1016/j.electacta.2014.02.140

Raymundo-Piñero, E., Leroux, F., and Béguin, F. (2006). A high-performance carbon for supercapacitors obtained by carbonization of a seaweed biopolymer. *Adv. Mater.* 18, 1877–1882. doi: 10.1002/adma.200501905

Ruch, P. W., Cericola, D., Foelske, A., Kötz, R., and Wokaun, A. (2010). A comparison of the aging of electrochemical double layer capacitors with acetonitrile and propylene carbonate-based electrolytes at elevated voltages. *Electrochim. Acta* 55, 2352–2357. doi: 10.1016/j.electacta.2009.11.098

Ruiz, V., Santamaria, R., Granda, M., and Blanco, C. (2009). Long-term cycling of carbon-based supercapacitors in aqueous media. *Electrochim. Acta* 54, 4481–4486. doi: 10.1016/j.electacta.2009.03.024

Ryoo, R., Joo, S. H., Kruk, M., and Jaroniec, M. (2001). Ordered Mesoporous Carbons. *Adv. Mater.* 13, 677–681. doi: 10.1002/1521-4095(200105)13:9<677::AID-ADMA677>3.0.CO;2-C

Sadayappan, N., and Kwang-Sun, R. (2019). Synthesis of Ag/NiO Honeycomb Structured Nanoarrays as the Electrode Material for High Performance Asymmetric Supercapacitor Devices. *Sci. Rep.* 9, 1–11. doi: 10.1038/s41598-019-41446-0

Salunkhe, R. R., Tang, J., Kamachi, Y., Nakato, T., Kim, J. H., and Yamauchi, Y. (2015). Asymmetric Supercapacitors Using 3D Nanoporous Carbon and Cobalt Oxide Electrodes Synthesized from a Single Metal-Organic Framework. *ACS Nano* 9:6288. doi: 10.1021/acsnano.5b01790

Sathyamoorthi, S., Kanagaraj, M., Kathiresan, M., Suryanarayanan, V., and Velayutham, D. (2016). Ethyl viologen dibromide as a novel dual redox shuttle for supercapacitors. *J. Mater. Chem. A* 4, 4562–4569. doi: 10.1039/C6TA00858E

Schipper, F., Erickson, E. M., Erk, C., Shin, J.-Y., Chesneau, F. F., and Aurbach, D. (2017). Review—Recent advances and remaining challenges for lithium ion battery cathodes: I. Nickel-Rich, LiNiCoMnO. *J. Electrochem. Soc.* 164, A6220–A6228. doi: 10.1149/2.0351701jes

Scrosati, B. (2011). History of lithium batteries. *J. Solid State Electrochem.* 15, 1623–1630. doi: 10.1007/s10008-011-1386-8

Sen, P., and De, A. (2010). Electrochemical performances of poly(3,4-ethylenedioxythiophene)–NiFe 2O 4 nanocomposite as electrode for supercapacitor. *Electrochim. Acta* 55, 4677–4684. doi: 10.1016/j.electacta.2010.03.077

Shao, P., Zhang, Q., Li, Y., and Wang, H. (2010). Aqueous synthesis of color-tunable and stable Mn2+-doped ZnSe quantum dots. *J. Mater. Chem.* 21:151. doi: 10.1039/C0JM01878C

Sheberla, D., Bachman, J. C., Elias, J. S., Sun, C.-J., Shao-Horn, Y., and Dincă, M. (2016). Conductive MOF electrodes for stable supercapacitors with high areal capacitance. *Nat. Mater.* 16, 220–224. doi: 10.1038/nmat4766

Shukla, A. K., Banerjee, A., Ravikumar, M. K., and Jalajakshi, A. (2012). Electrochemical capacitors: technical challenges and prognosis for future markets. *Electrochim. Acta* 84, 165–173. doi: 10.1016/j.electacta.2012.03.059

Simon, P., and Gogotsi, Y. (2008). Materials for electrochemical capacitors. *Nat. Mater.* 7, 845–854. doi: 10.1038/nmat2297

Simon, P., and Gogotsi, Y. (2010). Charge storage mechanism in nanoporous carbons and its consequence for electrical double layer capacitors. *Philos. Trans. A Math. Phys. Eng. Sci.* 368, 3457–3467. doi: 10.1098/rsta.2010.0109

Simon, P., and Gogotsi, Y. (2013). Capacitive Energy Storage in Nanostructured Carbon-Electrolyte Systems. *ACC. Chem. Res.* 46, 1094–1103. doi: 10.1021/ar200306b

Simotwo, S. K., and Kalra, V. (2018). Polyaniline-carbon based binder-free asymmetric supercapacitor in neutral aqueous electrolyte. *Electrochim. Acta* 268, 131–138. doi: 10.1016/j.electacta.2018.01.157

Slesinski, A., Matei-Ghimbeu, C., Fic, K., Béguin, F., and Frackowiak, E. (2018). Self-buffered pH at carbon surfaces in aqueous supercapacitors. *Carbon* 129, 758–765. doi: 10.1016/j.carbon.2017.12.101

Some, S., Kim, J., Lee, K., Kulkarni, A., Yoon, Y., Lee, S., et al. (2012). Highly Air-Stable Phosphorus-Doped n-Type Graphene Field-Effect Transistors. *Adv. Mater.* 24, 5481–5486. doi: 10.1002/adma.201202255

Song, Y., Cai, X., Xu, X., and Liu, X.-X. (2015a). Integration of nickelcobalt double hydroxide nanosheets and polypyrrole films with functionalized partially exfoliated graphite for asymmetric supercapacitors with improved rate capability. *J. Mater. Chem. A* 3, 14712–14720. doi: 10.1039/C5TA02810H

Song, Y., Feng, D.-Y., Liu, T.-Y., Li, Y., and Liu, X.-X. (2015b). Controlled partial-exfoliation of graphite foil and integration with MnO 2 nanosheets for electrochemical capacitors. *Nanoscale* 7, 3581–3587. doi: 10.1039/C4NR06559J

Song, Y., Deng, P., Qin, Z., Feng, D., Guo, D., Sun, X., et al. (2019). A polyanionic molybdenophosphate anode for a 2.7 V aqueous pseudocapacitor. *Nano Energy* 65:104010. doi: 10.1016/j.nanoen.2019.104010

Song, Y., Liu, T., Qian, F., Zhu, C., Yao, B., Duoss, E., et al. (2018). Three-dimensional carbon architectures for electrochemical capacitors. *J. Colloid Interface Sci.* 509, 529–545. doi: 10.1016/j.jcis.2017.07.081

Song, Y., Liu, T.-Y., Xu, G.-L., Feng, D.-Y., Yao, B., Kou, T.-Y., et al. (2016). Tri-layered graphite foil for electrochemical capacitors. *J. Mater. Chem. A* 4, 7683–7688. doi: 10.1039/C6TA02075E

Song, Y., Liu, T. Y., Yao, B., Kou, T. Y., Feng, D. Y., Liu, X. X., et al. (2017). Amorphous mixed-valence vanadium oxide/exfoliated carbon cloth structure shows a record high cycling stability. *Small* 13:1700067. doi: 10.1002/smll.201700067

Song, Y., Xu, J.-L., and Liu, X.-X. (2014). Electrochemical anchoring of dual doping polypyrrole on graphene sheets partially exfoliated from graphite foil for high-performance supercapacitor electrode.(Report). *J. Power Sour.* 249:48. doi: 10.1016/j.jpowsour.2013.10.102

Sun, X., Li, Q., Lü, Y., and Mao, Y. (2013). Three-dimensional ZnO@MnO2 core@shell nanostructures for electrochemical energy storage. *Chem. Commun.* 49:4456. doi: 10.1039/c3cc41048j

Suss, M. E., Baumann, T. F., Worsley, M. A., Rose, K. A., Jaramillo, T. F., Stadermann, M., et al. (2013). Impedance-based study of capacitive porous carbon electrodes with hierarchical and bimodal porosity. *J. Power Sour.* 241, 266–273. doi: 10.1016/j.jpowsour.2013.03.178

Tang, C.-H., Yin, X., and Gong, H. (2013). Superior Performance Asymmetric Supercapacitors Based on a Directly Grown Commercial Mass 3D Co 3 O 4 @Ni(OH) 2 Core–Shell Electrode. *ACS Appl. Mater. Interf.* 5, 10574–10582. doi: 10.1021/am402436q

Thanh-Hai, L., Yukyung, K., and Hyeonseok, Y. (2017). Electrical and Electrochemical Properties of Conducting Polymers. *Polymers* 9:150. doi: 10.3390/polym9040150

Theerthagiri, J., Karuppasamy, K., Durai, G., Rana, A. U. H. S., Arunachalam, P., Sangeetha, K., et al. (2018). Recent Advances in Metal Chalcogenides (MX; =) nanostructures for electrochemical supercapacitor applications: a brief review. *Nanomaterials* 8:256. doi: 10.3390/nano8040256

Tomczykowa, M., and Plonska-Brzezinska, M. E. (2019). Conducting polymers. hydrogels and their composites: preparation, properties and bioapplications. *Polymers* 11:350. doi: 10.3390/polym11020350

Tong, L., Skorenko, K. H., Faucett, A. C., Boyer, S. M., Liu, J., Mativetsky, J. M., et al. (2015). Vapor-phase polymerization of poly(3,4-ethylenedioxythiophene) (PEDOT) on commercial carbon coated aluminum foil as enhanced electrodes for supercapacitors. *J. Power Sour.* 297, 195–201. doi: 10.1016/j.jpowsour.2015.06.128

Ullah, N., Mcarthur, M. A., and Omanovic, S. (2015). Iridium-ruthenium-oxide coatings for supercapacitors. *Can. J. Chem. Eng.,* 93, 1941–1948. doi: 10.1002/cjce.22318

Ussia, M., Urso, M., Miritello, M., Bruno, E., Curcuruto, G., Vitalini, D., et al. (2019). Hybrid nickel-free graphene/porphyrin rings for photodegradation of emerging pollutants in water. *RSC Adv.* 9, 30182–30194. doi: 10.1039/C9RA06328E

Vangari, M., Pryor, T., and Jiang, L. (2013). Supercapacitors: review of materials and fabrication methods. *J. Energy Eng.* 139, 72–79. doi: 10.1061/(ASCE)EY.1943-7897.0000102

Vivekchand, S., Rout, C., Subrahmanyam, K., Govindaraj, A., and Rao, C. (2008). Graphene-based electrochemical supercapacitors. *J. Chem. Sci.* 120, 9–13. doi: 10.1007/s12039-008-0002-7

Wang, D. W., Li, F., Liu, M., Lu, G. Q., and Cheng, H. M. (2008). 3D aperiodic hierarchical porous graphitic carbon material for high-rate electrochemical capacitive energy storage. *Angewandte Chem. Int. Edn.* 47, 373–376. doi: 10.1002/anie.200702721

Wang, G., Lei, Z., and Jiujun, Z. (2012a). A review of electrode materials for electrochemical supercapacitors. *ChemsucChem* 5:797. doi: 10.1039/C1CS15060J

Wang, G., Lu, X., Ling, Y., Zhai, T., Wang, H., Tong, Y., et al. (2012b). LiCl/PVA gel electrolyte stabilizes vanadium oxide nanowire electrodes for pseudocapacitors. *ACS Nano* 6:10296. doi: 10.1021/nn304178b

Wang, G., Ling, Y., Qian, F., Yang, X., Liu, X.-X., and Li, Y. (2011). Enhanced capacitance in partially exfoliated multi-walled carbon nanotubes. *J. Power Sour.* 196, 5209–5214. doi: 10.1016/j.jpowsour.2011.02.019

Wang, J., Manga, K. K., Bao, Q., and Loh, K. P. (2011). High-yield synthesis of few-layer graphene flakes through electrochemical expansion of graphite in propylene carbonate electrolyte. *J. Am. Chem. Soc.* 133, 8888. doi: 10.1021/ja203725d

Wang, G., Wang, H., Lu, X., Ling, Y., Yu, M., Zhai, T., et al. (2014). Solid-State Supercapacitor Based on Activated Carbon Cloths Exhibits Excellent Rate Capability. *Adv. Mater.* 26, 2676–2682. doi: 10.1002/adma.201304756

Wang, X., Lu, X., Liu, B., Chen, D., Tong, Y., and Shen, G. (2014). Flexible Energy-Storage Devices: Design Consideration and Recent Progress. *Adv. Mater.* 26, 4763–4782. doi: 10.1002/adma.201400910

Wang, L., Han, Y., Feng, X., Zhou, J., Qi, P., and Wang, B. (2016). Metal-organic frameworks for energy storage: batteries and supercapacitors. *Coordinat. Chem. Rev.* 307, 361–381. doi: 10.1016/j.ccr.2015.09.002

Wang, W., Guo, S., Penchev, M., Ruiz, I., Bozhilov, K. N., Yan, D., et al. (2013a). Three dimensional few layer graphene and carbon nanotube foam architectures for high fidelity supercapacitors. *Nano Energy* 2, 294–303. doi: 10.1016/j.nanoen.2012.10.001

Wang, X., Liu, B., Wang, Q., Song, W., Hou, X., Chen, D., et al. (2013b). Three-Dimensional Hierarchical GeSe 2 Nanostructures for High Performance Flexible All-Solid-State Supercapacitors. *Adv. Mater.* 25, 1479–1486. doi: 10.1002/adma.201370061

Wang, W., Liu, W., Zeng, Y., Han, Y., Yu, M., Lu, X., et al. (2015). A Novel Exfoliation Strategy to Significantly Boost the Energy Storage Capability of Commercial Carbon Cloth. *Adv. Mater.* 27, 3572–3578. doi: 10.1002/adma.201500707

Wang, X., Ding, X., and Zou, H. (2020). Mesoporous Silica Nanosheets with Tunable Pore Lengths Supporting Metal Nanoparticles for Enhanced Hydrogenation Reactions. *Catalysts* 10:12. doi: 10.3390/catal10010012

Wang, X., Wu, D., Song, X., Du, W., Zhao, X., and Zhang, D. (2019). Review on carbon/polyaniline hybrids: design and synthesis for supercapacitor. *Molecules* 24:2263. doi: 10.3390/molecules24122263

Wei, D., Grande, L., Chundi, V., White, R., Bower, C., Andrew, P., et al. (2012). Graphene from electrochemical exfoliation and its direct applications in enhanced energy storage devices. *Chem. Commun.* 48, 1239–1241. doi: 10.1039/C2CC16859F

Wei, W., Mi, L., Gao, Y., Zheng, Z., Chen, W., and Guan, X. (2014). Partial Ion-Exchange of Nickel-Sulfide-Derived Electrodes for High Performance Supercapacitors. *Chem. Mater.* 26, 3418–3426. doi: 10.1021/cm5006482

Wei, X., Jiang, X., Wei, J., and Gao, S. (2016). Functional Groups and Pore Size Distribution Do Matter to Hierarchically Porous Carbons as High-Rate-Performance Supercapacitors. *Chem. Mate.* 28, 445–458. doi: 10.1021/acs.chemmater.5b02336

Weingarth, D., Noh, H., Foelske-Schmitz, A., Wokaun, A., and Kotz, R. (2013). A reliable determination method of stability limits for electrochemical double layer capacitors. *Electrochim. Acta* 103, 119–124. doi: 10.1016/j.electacta.2013.04.057

Wen, Z., Wang, X., Mao, S., Bo, Z., Kim, H., Cui, S., et al. (2012). Crumpled Nitrogen-Doped Graphene Nanosheets with Ultrahigh Pore Volume for High-Performance Supercapacitor. *Adv. Mater.* 24, 5610–5616. doi: 10.1002/adma.201201920

Winkless, L. (2014). Carbon nanotube supercapacitors for portable electronics. *Mater. Today* 17, 266–266. doi: 10.1016/j.mattod.2014.06.013

Wong, S., Kitaev, V., and Ozin, G. A. (2003). Colloidal crystal films: advances in universality and perfection. *J. Am. Chem. Soc.* 125, 15589–15598. doi: 10.1021/ja0379969

Worsley, M. A., Pauzauskie, P. J., Olson, T. Y., Biener, J., Satcher, J. H., and Baumann, T. F. (2010). Synthesis of graphene aerogel with high electrical conductivity. *J. Am. Chem. Soc.* 132:14067. doi: 10.1021/ja1072299

Wu, H., Xu, M., Wang, Y., and Zheng, G. (2013). Branched Co 3 O 4/Fe 2 O 3 nanowires as high capacity lithium-ion battery anodes. *Nano Res.* 6, 167–173. doi: 10.1007/s12274-013-0292-z

Wu, Z. S., Winter, A., Chen, L., Sun, Y., Turchanin, A., Feng, X., et al. (2012). Three-dimensional nitrogen and boron co-doped graphene for high-performance all-solid-state supercapacitors. *Adv. Mater.* 24, 5130–5135. doi: 10.1002/adma.201201948

Xia, X., Chao, D., Fan, Z., Guan, C., Cao, X., Zhang, H., et al. (2014a). A new type of porous graphite foams and their integrated composites with oxide/polymer core/shell nanowires for supercapacitors: structural design, fabrication, and full supercapacitor demonstrations. *Nano Lett.* 14:1651. doi: 10.1021/nl5001778

Xia, X., Zhu, C., Luo, J., Zeng, Z., Guan, C., Ng, C. F., et al. (2014b). Synthesis of Free-Standing Metal Sulfide Nanoarrays via Anion Exchange Reaction and Their Electrochemical Energy Storage Application. *Small* 10, 766–773. doi: 10.1002/smll.201302224

Xia, X., Tu, J., Zhang, Y., Wang, X., Gu, C., Zhao, X.-B., et al. (2012). High-quality metal oxide core/shell nanowire arrays on conductive substrates for electrochemical energy storage. *ACS Nano* 6:5531. doi: 10.1021/nn301454q

Xia, X. H., Tu, J. P., Zhang, J., Xiang, J. Y., Wang, X. L., and Zhao, X. B. (2010). Cobalt Oxide Ordered Bowl-Like Array Films Prepared by Electrodeposition through Monolayer Polystyrene Sphere Template and Electrochromic Properties. *ACS Appl. Mater. Interf.* 2, 186–192. doi: 10.1021/am900636g

Xiao, J., Wan, L., Yang, S., Xiao, F., and Wang, S. (2014). Design Hierarchical Electrodes with Highly Conductive NiCo 2 S 4 Nanotube Arrays Grown on Carbon Fiber Paper for High-Performance Pseudocapacitors. *Nano Lett.* 14, 831–838. doi: 10.1021/nl404199v

Xie, X., Zhang, C., Wu, M.-B., Tao, Y., Lv, W., and Yang, Q.-H. (2013). Porous MnO 2 for use in a high performance supercapacitor: replication of a 3D graphene network as a reactive template. *Chem. Commun.* 49, 11092–11094. doi: 10.1039/c3cc46867d

Xiong, X., Ding, D., Chen, D., Waller, G., Bu, Y., Wang, Z., et al. (2015). Three-dimensional ultrathin Ni(OH)2 nanosheets grown on nickel foam for high-performance supercapacitors. *Nano Energy* 11, 154–161. doi: 10.1016/j.nanoen.2014.10.029

Xu, C., Xu, B., Gu, Y., Xiong, Z., Sun, J., and Zhao, X. S. (2013). Graphene-based electrodes for electrochemical energy storage. *Energy Environ. Sci.* 6, 1388–1414. doi: 10.1039/c3ee23870a

Xu, K., Li, W., Liu, Q., Li, B., Liu, X., An, L., et al. (2014). Hierarchical mesoporous NiCo 2 O 4 @MnO 2 coreshell nanowire arrays on nickel foam for aqueous asymmetric supercapacitors. *J. Mater. Chem. A* 2, 4795–4802. doi: 10.1039/c3ta14647b

Yamaguchi, I., Watanabe, M., Shinagawa, T., Chigane, M., Inaba, M., Tasaka, A., et al. (2009). Preparation of Core/Shell and Hollow Nanostructures of Cerium Oxide by Electrodeposition on a Polystyrene Sphere Template. *ACS Appl. Mater. Interf.* 1, 1070–1075. doi: 10.1021/am900040c

Yan, D., Guo, Z., Zhu, G., Yu, Z., Xu, H., and Yu, A. (2012). MnO.sub.2 film with three-dimensional structure prepared by hydrothermal process for supercapacitor.(Report). *J. Power Sour.* 199:409. doi: 10.1016/j.jpowsour.2011.10.051

Yan, J., Liu, J., Fan, Z., Wei, T., and Zhang, L. (2012). High-performance supercapacitor electrodes based on highly corrugated graphene sheets. *Carbon* 50, 2179–2188. doi: 10.1016/j.carbon.2012.01.028

Yan, J., Sumboja, A., Khoo, E., and Lee, P. S. (2011). V2O5 Loaded on SnO2 Nanowires for High-Rate Li Ion Batteries. *Adv. Mater.* 23, 746–750. doi: 10.1002/adma.201003805

Yang, C.-M., Kim, Y.-J., Endo, M., Kanoh, H., Yudasaka, M., Iijima, S., et al. (2007). Nanowindow-regulated specific capacitance of supercapacitor electrodes of single-wall carbon nanohorns. *J. Am. Chem. Soc.* 129:20. doi: 10.1021/ja065501k

Yang, X.-H., Wang, Y.-G., Xiong, H.-M., and Xia, Y.-Y. (2007). Interfacial synthesis of porous MnO 2 and its application in electrochemical capacitor. *Electrochim. Acta* 53, 752–757. doi: 10.1016/j.electacta.2007.07.043

Yang, H., Ye, S., Zhou, J., and Liang, T. (2019). Biomass-derived porous carbon materials for supercapacitor. *Front. Chem.* 7:274. doi: 10.3389/fchem.2019.00274

Yang, S., Lohe, M. R., Müllen, K., and Feng, X. (2016). New-generation graphene from electrochemical approaches: production and applications. *Adv. Mater.* 28, 6213–6221. doi: 10.1002/adma.201505326

Yang, X., Zhu, J., Qiu, L., and Li, D. (2011). Graphene assembly: bioinspired effective prevention of restacking in multilayered graphene films: towards the next generation of high-performance supercapacitors (Adv. Mater. 25/2011. *Adv. Mater.* 23, 2771–2771. doi: 10.1002/adma.201190093

Yang, Y., Fei, H., Ruan, G., Xiang, C., and Tour, J. M. (2014). Edge-Oriented MoS2 Nanoporous Films as Flexible Electrodes for Hydrogen Evolution Reactions and Supercapacitor Devices. *Adv. Mater.* 26, 8163–8168. doi: 10.1002/adma.201402847

Yao, B., Chandrasekaran, S., Zhang, H., Ma, A., Kang, J., Zhang, L., et al. (2020). 3D-Printed Structure Boosts the Kinetics and Intrinsic Capacitance of Pseudocapacitive Graphene Aerogels. *Adv. Mater.* 32:1906652. doi: 10.1002/adma.201906652

Ye, Y.-J., Huang, Z.-H., Song, Y., Geng, J.-W., Xu, X.-X., and Liu, X.-X. (2017). Electrochemical Growth of Polyaniline Nanowire Arrays on Graphene Sheets in Partially Exfoliated Graphite Foil for High-Performance Supercapacitive Materials. *Electrochim. Acta* 240, 72–79. doi: 10.1016/j.electacta.2017.04.025

Yenny, H., Valeria, N., Mustafa, L., Fiona, M. B., Zhenyu, S., Sukanta, D., et al. (2008). High- yield production of graphene by liquid- phase exfoliation of graphite. *Nat. Nanotechnol.* 3:563.

Yoon, Y., Lee, K., Baik, C., Yoo, H., Min, M., Park, Y., et al. (2013). Anti-Solvent Derived Non-Stacked Reduced Graphene Oxide for High Performance Supercapacitors. *Adv. Mater.* 25, 4437–4444. doi: 10.1002/adma.201301230

You, B., Wang, L., Yao, L., and Yang, J. (2013). Three dimensional N-doped grapheneCNT networks for supercapacitor. *Chem. Commun.* 49, 5016–5018. doi: 10.1039/c3cc41949e

Younesi, S. R., Veith, G. M., Johansson, P., Edström, K., and Vegge, T. (2015). Lithium salts for advanced lithium batteries: Li-metal. Li-O2, and Li-S. *Energy Environ. Sci.* 8, 1905–1922. doi: 10.1039/C5EE01215E

Yu, M., Han, Y., Cheng, X., Hu, L., Zeng, Y., Chen, M., et al. (2015a). Holey tungsten oxynitride nanowires: novel anodes efficiently integrate microbial chemical energy conversion and electrochemical energy storage. *Adv. Mater.* 27, 3085–3091. doi: 10.1002/adma.201500493

Yu, M., Huang, Y., Li, C., Zeng, Y., Wang, W., Li, Y., et al. (2015b). Building Three-Dimensional Graphene Frameworks for Energy Storage and Catalysis. *Adv. Funct. Mater.* 25, 324–330. doi: 10.1002/adfm.201402964

Yu, M., Qiu, W., Wang, F., Zhai, T., Fang, P., Lu, X., et al. (2015c). Three dimensional architectures: design, assembly and application in electrochemical capacitors. *J. Mater. Chem. A* 3, 15792–15823. doi: 10.1039/C5TA02743H

Yu, M., Patrick, H., Annette Von, J., and Alexandre, Y. (2019). Current Li-Ion Battery Technologies in Electric Vehicles and Opportunities for Advancements. *Energies* 12:1074. doi: 10.3390/en12061074

Yu, M., Zhai, T., Lu, X., Chen, X., Xie, S., Li, W., et al. (2013). Manganese dioxide nanorod arrays on carbon fabric for flexible solid-state supercapacitors. *J. Power Sour.* 239, 64–71. doi: 10.1016/j.jpowsour.2013.03.083

Yu, M., Zhang, Y., Zeng, Y., Balogun, M. S., Mai, K., Zhang, Z., et al. (2014). Water Surface Assisted Synthesis of Large-Scale Carbon Nanotube Film for High-Performance and Stretchable Supercapacitors. *Adv. Mater.* 26, 4724–4729. doi: 10.1002/adma.201401196

Yu, Z., and Thomas, J. (2014). Energy storage: energy storing electrical cables: integrating energy storage and electrical conduction (Adv. Mater. 25/2014. *Adv. Mater.* 26, 4400–4400. doi: 10.1002/adma.201470172

Yuan, P., Zhang, N., Zhang, D., Liu, T., Chen, L., Liu, X., et al. (2014). Fabrication of nickel-foam-supported layered zinccobalt hydroxide nanoflakes for high electrochemical performance in supercapacitors. *Chem. Commun.* 50, 11188–11191. doi: 10.1039/C4CC05057F

Yun, Y. S., Cho, S. Y., Shim, J., Kim, B. H., Chang, S. J., Baek, S. J., et al. (2013). Microporous Carbon Nanoplates from Regenerated Silk Proteins for Supercapacitors. *Adv. Mater.* 25, 1993–1998. doi: 10.1002/adma.201204692

Yuxi, X., Zhaoyang, L., Xing, Z., Xiaoqing, H., Nathan, O. W., Yu, H., et al. (2014). Holey graphene frameworks for highly efficient capacitive energy storage. *Nat. Commun.* 5:4554. doi: 10.1038/ncomms5554

Zhai, T., Lu, X., Ling, Y., Yu, M., Wang, G., Liu, T., et al. (2014). A New Benchmark Capacitance for Supercapacitor Anodes by Mixed-Valence Sulfur-Doped V 6 O 13- x. *Adv. Mater.* 26, 5869–5875. doi: 10.1002/adma.201402041

Zhai, T., Lu, X., Wang, H., Wang, G., Mathis, T., Liu, T., et al. (2015). An Electrochemical Capacitor with Applicable Energy Density of 7.4 Wh/kg at Average Power Density of 3000 W/kg. *Nano Lett.,* 15, 3189–3194. doi: 10.1021/acs.nanolett.5b00321

Zhang, C., Mahmood, N., Yin, H., Liu, F., and Hou, Y. (2013a). Synthesis of Phosphorus-Doped Graphene and its Multifunctional Applications for Oxygen Reduction Reaction and Lithium Ion Batteries. *Adv. Mater.* 25, 4932–4937. doi: 10.1002/adma.201301870

Zhang, F., Tang, J., Shinya, N., and Qin, L.-C. (2013b). Hybrid graphene electrodes for supercapacitors of high energy density. *Chem. Phys. Lett.* 584, 124–129. doi: 10.1016/j.cplett.2013.08.021

Zhang, F., Yuan, C., Zhu, J., Wang, J., Zhang, X., and Lou, X. W. (2013c). Flexible Films Derived from Electrospun Carbon Nanofibers Incorporated with Co 3 O 4 Hollow Nanoparticles as Self-Supported Electrodes for Electrochemical Capacitors. *Adv. Funct. Mater.* 23, 3909–3915. doi: 10.1002/adfm.201203844

Zhang, L., Zhang, F., Yang, X., Long, G., Wu, Y., Zhang, T., et al. (2013d). Porous 3D graphene-based bulk materials with exceptional high surface area and excellent conductivity for supercapacitors. *Sci. Rep.* 3:1408. doi: 10.1038/srep01408

Zhang, F., Liu, T., Hou, G., Kou, T., Yue, L., Guan, R., et al. (2016). Hierarchically porous carbon foams for electric double layer capacitors. *Nano Res.* 9, 2875–2888. doi: 10.1007/s12274-016-1173-z

Zhang, F., Liu, T., Li, M., Yu, M., Luo, Y., Tong, Y., et al. (2017). Multiscale Pore Network Boosts Capacitance of Carbon Electrodes for Ultrafast Charging. *Nano Lett.* 17:3097. doi: 10.1021/acs.nanolett.7b00533

Zhang, X., Gong, J., Zhang, K., Zhu, W., Li, J.-C., and Ding, Q. (2019). All-solid-state asymmetric supercapacitor based on porous cobalt selenide thin films. *J. Alloys Compounds* 772, 25–32. doi: 10.1016/j.jallcom.2018.09.023

Zhang, X., Shi, W., Zhu, J., Kharistal, D. J., Zhao, W., Lalia, B. S., et al. (2011). High-power and high-energy-density flexible pseudocapacitor electrodes made from porous CuO nanobelts and single-walled carbon nanotubes. *ACS Nano* 5:2013. doi: 10.1021/nn2020453

Zhang, Z., Xiao, F., Qian, L., Xiao, J., Wang, S., and Liu, Y. (2014). Facile Synthesis of 3D MnO 2 -Graphene and Carbon Nanotube-Graphene Composite Networks for High-Performance, Flexible, All-Solid-State Asymmetric Supercapacitors. *Adv. Energy Mater.* 4:1400064. doi: 10.1002/aenm.201400064

Zhao, C., and Zheng, W. (2015). A Review for Aqueous Electrochemical Supercapacitors.(Report)(Author abstract). *Front. Energy Res.* 3:23. doi: 10.3389/fenrg.2015.00023

Zhao, M. Q., Ren, C. E., Ling, Z., Lukatskaya, M. R., Zhang, C., Van Aken, K. L., et al. (2015). Flexible MXene/Carbon Nanotube Composite Paper with High Volumetric Capacitance. *Adv. Mater.* 27, 339–345. doi: 10.1002/adma.201404140

Zhao, X., Hou, Y., Wang, Y., Yang, L., Zhu, L., Cao, R., et al. (2017). Prepared MnO 2 with different crystal forms as electrode materials for supercapacitors: experimental research from hydrothermal crystallization process to electrochemical performances. *RSC Adv.* 7, 40286–40294. doi: 10.1039/C7RA06369E

Zhao, Z., Richardson, G. F., Meng, Q., Zhu, S., Kuan, H.-C., and Ma, J. (2016). Pedot-based composites as electrode materials for supercapacitors. *Nanotechnology* 27:042001. doi: 10.1088/0957-4484/27/4/042001

Zhong, C., Deng, Y., Hu, W., Qiao, J., Zhang, L., and Zhang, J. (2015). A review of electrolyte materials and compositions for electrochemical supercapacitors. *Chem. Soc. Rev.* 44, 7484–7539. doi: 10.1039/C5CS00303B

Zhou, C., Zhang, Y., Li, Y., and Liu, J. (2013). Construction of High-Capacitance 3D CoO@Polypyrrole Nanowire Array Electrode for Aqueous Asymmetric Supercapacitor. *Nano Lett.* 13, 2078–2085. doi: 10.1021/nl400378j

Zhou, M., Wu, H. B., Bao, J., Liang, L., Lou, X. W., and Xie, Y. (2013). Ordered Macroporous BiVO 4 Architectures with Controllable Dual Porosity for Efficient Solar Water Splitting. *Angewandte Chem. Int. Edn.* 52, 8579–8583. doi: 10.1002/anie.201302680

Zhou, Y., Ghaffari, M., Lin, M., Parsons, E. M., Liu, Y., Wardle, B. L., et al. (2013). High volumetric electrochemical performance of ultra-high density aligned carbon nanotube supercapacitors with controlled nanomorphology. *Electrochim. Acta* 111:608. doi: 10.1016/j.electacta.2013.08.032

Zhou, W. (2019). Reversed Crystal Growth. *Crystals* 9:7. doi: 10.3390/cryst9010007

Zhu, C., Liu, T., Qian, F., Han, T. Y.-J., Duoss, E. B., Kuntz, J. D., et al. (2016). Supercapacitors Based on Three-Dimensional Hierarchical Graphene Aerogels with Periodic Macropores. *Nano Lett.* 16:3448. doi: 10.1021/acs.nanolett.5b04965

Zhu, H., Peng, S., and Jiang, W. (2013). Electrochemical Properties of PANI as Single Electrode of Electrochemical Capacitors in Acid Electrolytes. *Sci. World J.* 2013:940153. doi: 10.1155/2013/940153

Zhu, J., Cao, L., Wu, Y., Gong, Y., Liu, Z., Hoster, H. E., et al. (2013). Building 3D Structures of Vanadium Pentoxide Nanosheets and Application as Electrodes in Supercapacitors. *Nano Lett.* 13, 5408–5413. doi: 10.1021/nl402969r

Zongping, C., Wencai, R., Libo, G., Bilu, L., Songfeng, P., and Hui-Ming, C. (2011). Three-dimensional flexible and conductive interconnected graphene networks grown by chemical vapour deposition. *Nat. Mater.* 10:424. doi: 10.1038/nmat3001

**Conflict of Interest:** The authors declare that the research was conducted in the absence of any commercial or financial relationships that could be construed as a potential conflict of interest.

# Advantages of publishing in Frontiers

**OPEN ACCESS**
Articles are free to read
for greatest visibility
and readership

**FAST PUBLICATION**
Around 90 days
from submission
to decision

**HIGH QUALITY PEER-REVIEW**
Rigorous, collaborative,
and constructive
peer-review

**TRANSPARENT PEER-REVIEW**
Editors and reviewers
acknowledged by name
on published articles

**Frontiers**
Avenue du Tribunal-Fédéral 34
1005 Lausanne | Switzerland

**Visit us:** www.frontiersin.org
**Contact us:** info@frontiersin.org | +41 21 510 17 00

**REPRODUCIBILITY OF RESEARCH**
Support open data
and methods to enhance
research reproducibility

**DIGITAL PUBLISHING**
Articles designed
for optimal readership
across devices

**FOLLOW US**
@frontiersin

**IMPACT METRICS**
Advanced article metrics
track visibility across
digital media

**EXTENSIVE PROMOTION**
Marketing
and promotion
of impactful research

**LOOP RESEARCH NETWORK**
Our network
increases your
article's readership